Electromagnetic pump and hardware development for organs-on-chips

by

Brij M. Bhushan

B.Tech., Indian Institute of Technology (2012)

Submitted to the Department of Mechanical Engineering
in partial fulfillment of the requirements for the degree of

Master of Science in Mechanical Engineering

at the

MASSACHUSETTS INSTITUTE OF TECHNOLOGY

February 2018

Author .....
Department of Mechanical Engineering
January 15, 2018

Certified by .....
David L. Trumper
Professor
Thesis Supervisor

Accepted by .....
Rohan Abeyaratne
Chairman, Department Committee on Graduate Theses
Graduate Officer

Electromagnetic pump and hardware development for organs-on-chips

by

Brij M. Bhushan

Submitted to the Department of Mechanical Engineering
on January 15, 2018, in partial fulfillment of the
requirements for the degree of
Master of Science in Mechanical Engineering

Abstract

MicroPhysiological Systems (MPS), also called organs-on-chips, attempt to mimic the relevant human multi-organ physiology in-vitro. They have potential applications in drug development and personalized medicine by enabling more accurate testing of physiological drug response earlier in the development cycle. On-platform pumps provide greater flexibility and design freedom and are a key feature of such platforms. One approach to multi-organ MPS platforms has been developed in our lab and uses an open-well system to culture tissues of various organs. A common fluid-media circulates between the organs using on-platform pneumatic diaphragm micro-pumps. These pumps require significant effort in setup and depend on external pressure and vacuum sources. An independent, portable pump with low power consumption is desirable. There are also on-going efforts in the field to make sterile platform components low-cost and single use, to reduce user setup time and sterilization effort.

This thesis describes a scaled-up version of an ElectroMagnetic (EM) pump. The pump uses a teeter-totter EM actuator having a low energy consumption of about 1 mJ/stroke. The EM actuator minimizes energy by a latching design that requires a short pulse of energy only to switch its state and its springs store energy which is recovered in the reverse stroke. This thesis also describes injection-molded, single-use platforms with onboard pneumatic diaphragm micro-pumps. It describes various valve and pump geometries and a model to predict large deflections of polymer diaphragms. We integrate the EM actuators with these platforms, demonstrating temperature rise of less than 0.1 °C, valve sealing up to 60 kPa, and a pumping frequency of 1 Hz, limited by diaphragm behavior. In addition, we improve platform features using spillways which allow for better passive leveling of fluid height between MPSes. This thesis also presents the selection of polymer tubing to resolve condensation issues in pneumatic channels of an MPS platform inside a cell culture incubator.

Thesis Supervisor: David L. Trumper
Title: Professor

Acknowledgments

I am most grateful to my advisor Professor David Trumper for his inspiration, guidance, and support. He introduced me to electromechanical design and control and nurtured my thinking on design and how to do good research. I'm particularly grateful for his wisdom, patience, and his willingness to share his knowledge. From him, I have learned the importance of both looking at the big picture and go into the details in any situation. In every meeting with him, I learn something new from his vast experience and his perspectives on tackling research problems. I'm also very grateful to Professor Linda Griffith for her vision in the area. With her incredible energy, she has brought together researchers from diverse backgrounds and I'm grateful for the opportunity to work in her lab.

I worked with Dr. Jun Young Yoon, on the electromagnetic (EM) actuator design. He shared his expertise on designing electromagnetic systems and his attention to detail is remarkable. He also gave very useful feedback on thesis writing. Dan Rathbone gave very useful suggestions for the mechanical design and manufacturing of the EM Actuator. Through numerous lunchtime conversations, I have learned a lot about design thinking and prototyping to test an idea. I really enjoyed working with him on the design of the injection molded platforms. I'm grateful to Timothy Kassis for his useful perspective and advice on grad school and research. He is always a source for wonderful, thought-provoking conversations. Collin Edington helped me learn the ropes when I first joined the lab. I'm grateful for his kindness and patience. He did a great job of leading the hardware team from the front during the DARPA project. Luis Soenksen and I worked together on the DARPA project and on the spillway designs. He is one of the most creative people I know and is a great teammate. I still don't understand how he manages to keep track of so many projects and side-projects he works on at the same time.

I'm also grateful to Lei, Minkyun, and Tyler. Their helpful nature creates a caring lab environment, which is a wonderful place to work in. They are so approachable and always ready to help. I still remember the great time together at the ASPE

student challenge in 2016! I'm grateful to Mark Belanger at the Edgerton machine shop for his help with fabrication and training me on various machine tools.

I'm grateful to my parents and my sister Nandini, for their love and support. They have been a constant source of motivation through my journey. My parents taught me the value of sincerity, working hard and being a good human being. I'm very grateful to my wife, Summy, for her unconditional love and spiritual support. She inspires the best in me and brings beauty into my life.

And finally, I'm grateful to everyone at MIT. It has been a great learning experience and I have grown tremendously, academically and as a person. Thank you for all your encouragement!

Contents

List of Figures

List of Tables

Chapter 1

Introduction

1.1 Introduction

The costs associated with developing a new drug are constantly increasing [1]. The inability to translate pre-clinical drug testing to the drug response in humans in terms of safety and efficacy is a major cause [2]. Pre-clinical drug testing is typically done on in-vitro cell cultures and with animal models. In-vitro cell cultures suffer from a lack of complexity to simulate the complex morphology and function of human tissues and organs [3]. Although animal models exhibit complex biology, their ability to accurately predict human response is limited at best [4]. There is a need to accurately predict human response to a drug earlier in the development cycle to better screen potential drugs. MicroPhysological Systems (MPS) offer a potential solution. They use 3D *in vitro* human tissue cultures with multiple interacting cell types, to reproduce desirable aspects of the human physiology [2].

One approach to multi-organ MPS platforms has been developed in our lab. An example of a 7-organ MPS platform is shown in Figure 1-1. Each organ is housed in open wells and a common fluid media circulates among the organs transporting nutrients and other chemicals from a central reservoir (mixing chamber) to each organ as well as among organ systems. Thereby, the platform mimics the physiological circulation between those organ systems [2]. The transport of fluid from the mixing chamber to the organs is by on-platform pneumatic diaphragm micro-pumps [5].

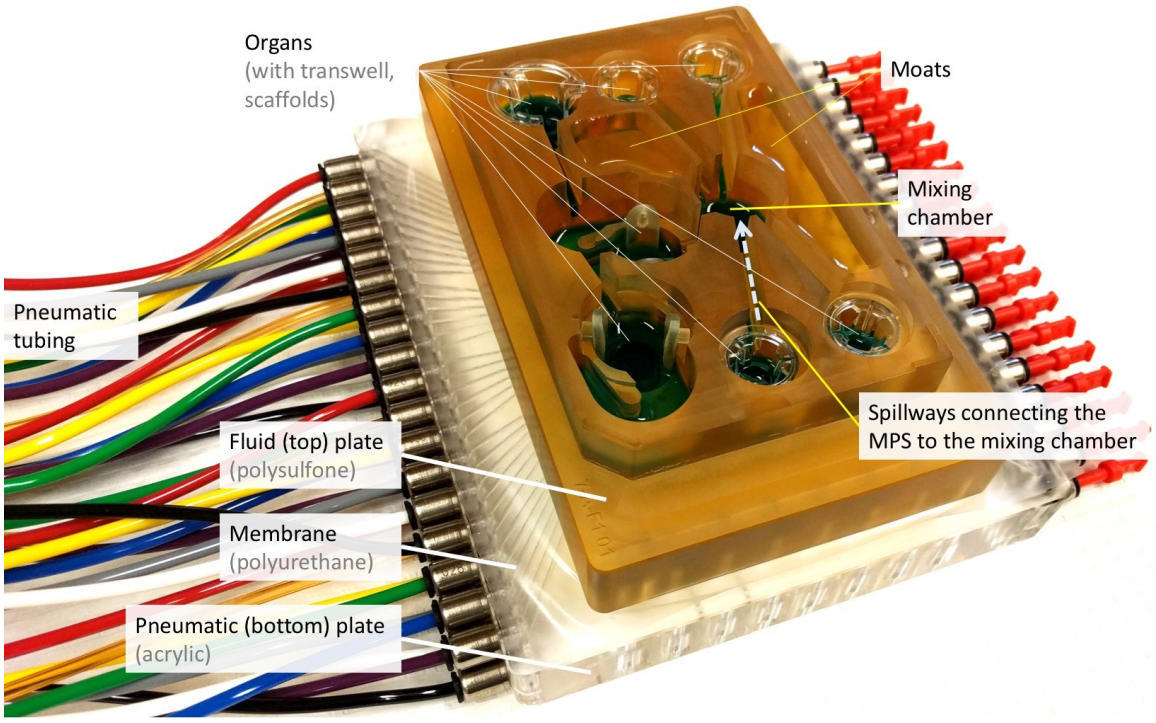

Figure 1-1: MPS platform with capability for seven organ tissues. The platform consists of a polyurethane membrane sandwiched between a machined polysulfone top plate and a machined acrylic bottom plate. The pump and valve features (not shown) are machined at the bottom surface of the top plate and at the top surface of the bottom plate. Platform is shown with no tissues and with blue-dyed media in the organ wells. Moats provide a sacrificial source for evaporative loss.

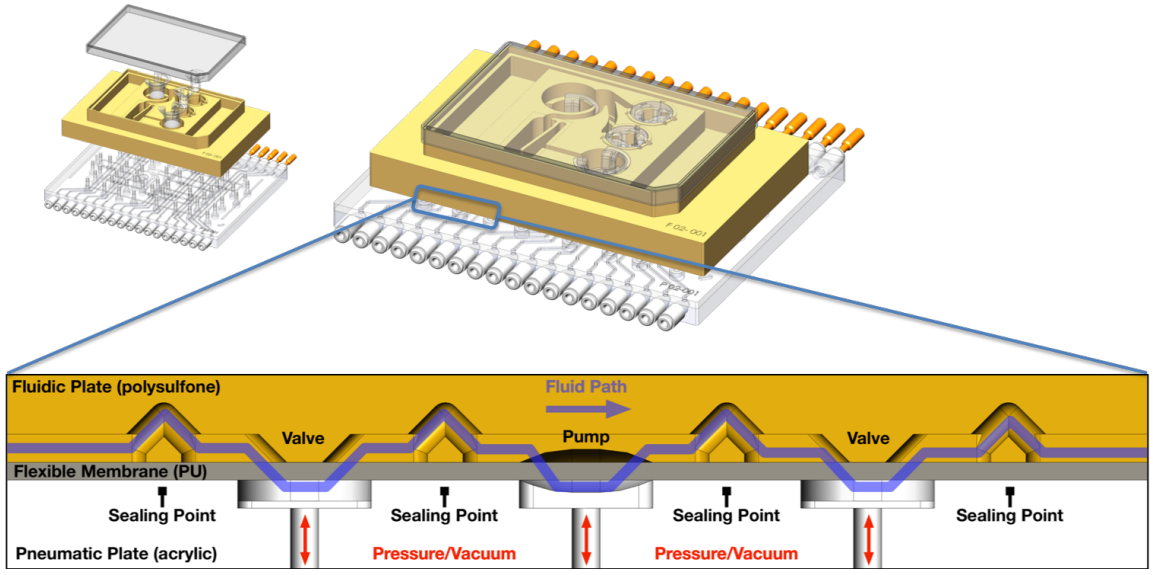

Figure 1-2: Existing platforms - exploded view and cross-section of pumps. Image courtesy of Collin Edington, a Post-Doc in our lab.

Spillway features between the MPSes maintain fluid leveling and thus maintain volume in each organ and return excess fluid back to the mixing chamber. The platform consists of the following layers (top to bottom) — a standard microtiter plate lid, transwells and scaffolds for the tissue systems, fluid (top) plate machined out of a monolithic block of polysulfone, polyurethane membrane which acts to seal the fluid channels at the bottom of the fluid plate and as the diaphragm for the micro-pumps, pneumatic (bottom) plate machined out of acrylic and bonded together to make the internal pneumatic channels. Fluid channels machined into the bottom of the fluid plate establish connections from the mixing chamber to the various organs, and for recirculation within the organs. The remaining area on the top surface of the top plate is used to create water containing reservoirs, called *moats*, which provide sacrificial fluid to reduce the evaporation from the organ wells during operation in the cell-culture incubator. The pneumatic diaphragm micro-pumps consist of three linked valve-pump-valve chambers embedded into these fluid channels (Figure 1-2) [5]. The acrylic bottom plate acts as a pneumatic manifold, delivering pressurized air and vacuum locally to each pump and valve chamber. The polyurethane diaphragm sandwiched between the top and bottom plate is actuated by setting pressure or vacuum under the diaphragm. Sequential actuation of the valve and pump chambers transports fluid in the forward or reverse direction. These pumps are a type of positive displacement pump, transporting an approximately constant volume volume per stroke over a range of back-pressures. The top and bottom plates are clamped together using an array of screws and spring washers to evenly distribute the clamping force throughout the platform area in order to get sealing across all the fluid elements.

On-platform pumps provide greater flexibility and design freedom and are a key feature of the MPS platforms developed in our lab. They transport fluid with low dead volumes which is important for concentration studies of various analytes. In addition, on-platform pumps allow easy interfacing with closed and open microfluidic devices. In the MPS platforms developed in our lab, on-platform pumps transport fluid not only from the mixing chamber to the various organs but also provide recirculation flow to mix the media within an MPS, enhancing nutrient and oxygen transport.

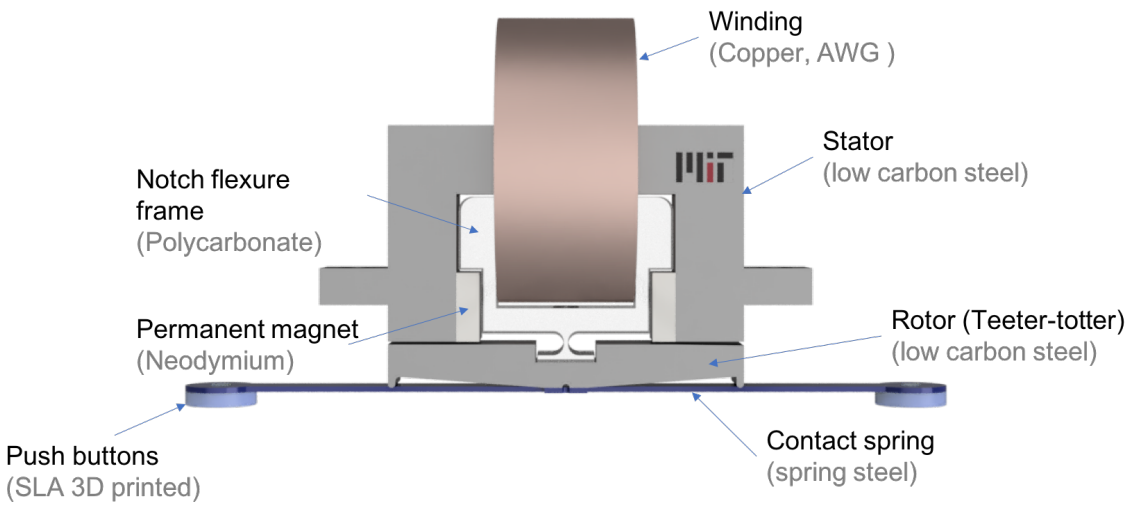

Figure 1-3: EM actuator module showing the various parts as well as the materials used. The teeter-totter rotor rotates about the notch flexure making contact with either side of the stator pole face. The push-buttons make contact with the membrane through an elastomer layer (not shown). The contact springs help bound the force of contact of the push-buttons with the membrane and store some of the actuator kinetic energy, which is recovered in the opposite stroke.

A downside of the current pumps is that they require significant effort in setup, and depend on external pressure and vacuum sources for their operation. This is especially challenging, given the sterily requirements of the platform after assembly. Thus, an independent, portable pump with low power consumption is desirable. For greater adoption of these platforms by the wider community, there is a thrust in the field to make these platforms low-cost and single-use, so as to further reduce the sterilization and setup time and effort.

1.2 Thesis overview

This thesis describes the design and development of a scaled-up version of an electromagnetic (EM) pump (Chapter 5). A CAD model is shown in Figure 1-3. It uses electrical energy which can be supplied by a battery and is therefore portable. The EM pump uses a teeter-totter EM actuator having a low energy consumption of about 1 mJ/stroke. Running at 1 Hz pumping frequency, that translates to a

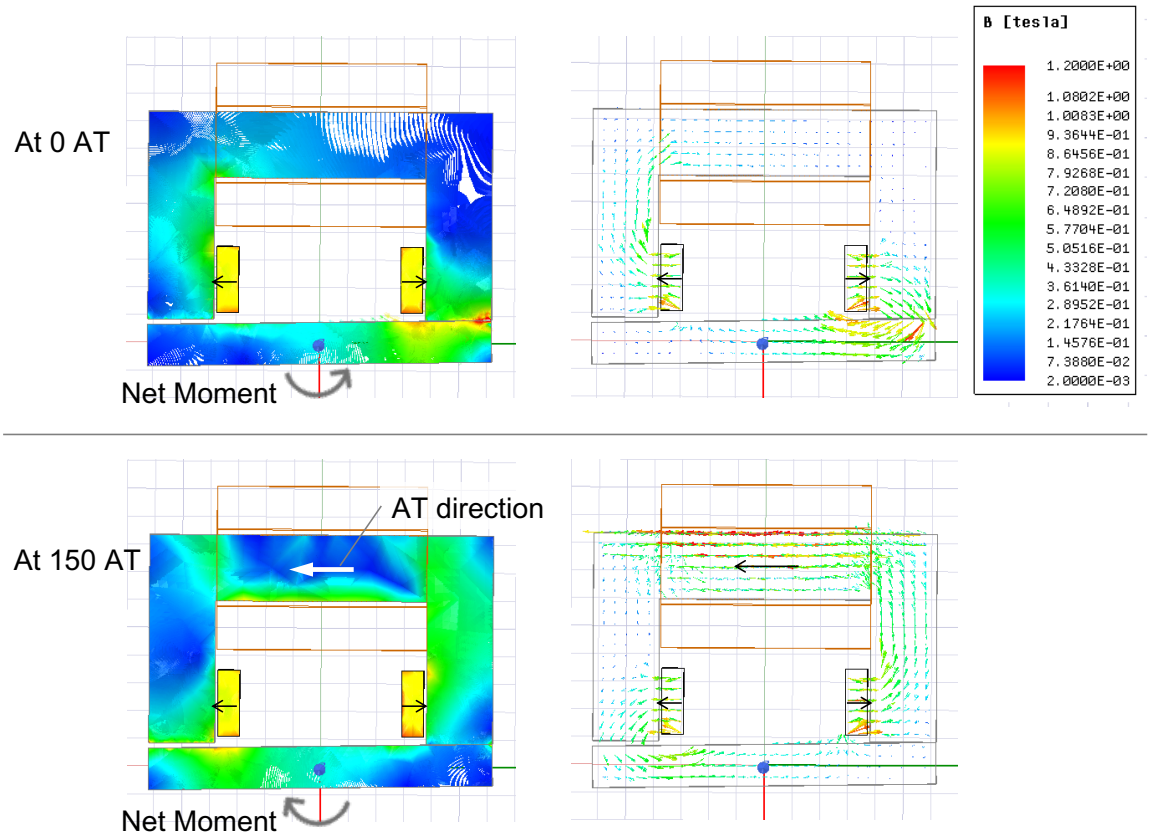

Figure 1-4: Magnetic flux density (B) plots as a color map on the left and as a vector plot on the right depicting magnitude and direction of the B-field. The top plot represents no current through the winding and the bottom plot represents 150 Amp-turns of current through the winding. When latched with no current, the field from permanent magnet makes a short loop through the contacting pole face, thence into the rotor and then closes back to the permanent magnet by travelling through air. With 150 AT of current, the total B-field on the right stator pole face is reduced and the field on the left side of the stator increases to flip the rotor from the right to the left. When on, the current AT vector by right hand rule is shown in the figure. The net moment on the rotor is also shown in the figure.

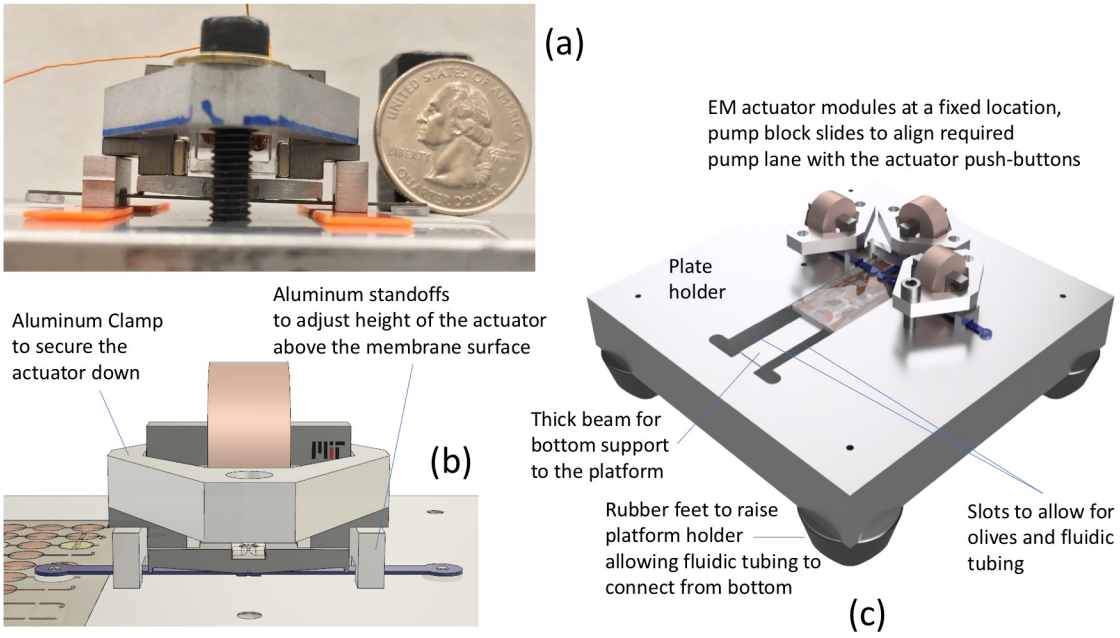

Figure 1-5: Integration of the EM actuator modules into the EM pump. (a) front view of the assembled actuator with the stator resting on aluminum standoffs. An aluminum clamp secures them to the plate holder using two bolts. (b) CAD model showing standoffs and clamps for clarity. (c) CAD model of the assembly showing the plate holder, the actuators and the fluidic top-plate

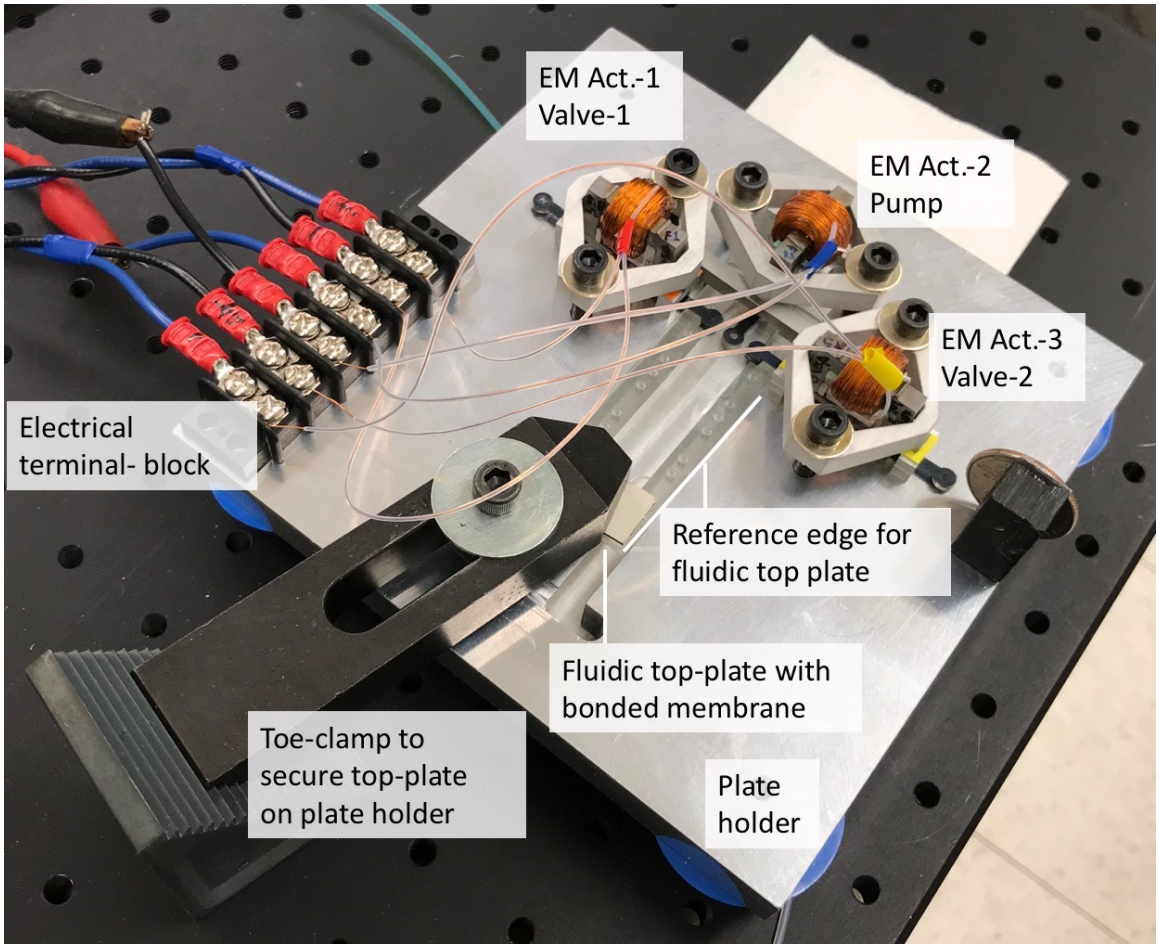

Figure 1-6: Assembled EM pump showing the plate holder, actuator modules, fluidic top-plate secured by a toe-clamp and electrical terminal blocks

power consumption of 6 mW (total) for 3 actuators, one each for a set of valve-pump-valve. We experimentally verified the steady-state actuator coil temperature rise to be less than 0.1 C, confirming negligible heating in the winding due to this low power consumption. This makes the actuator suitable for use within a cell-culture incubator with very small effects on the nominal 37 °C temperature of the cell-culture medium, even for a platform using multiple actuators. The actuator's low energy consumption is achieved by a latching design which requires only a short pulse of energy to switch its state and where springs store some of the actuator kinetic energy, which is then recovered in the reverse stroke. Figure 1-4 shows a B-field plot of the EM actuator in operation.

In addition, in this thesis, we explore concepts for pumping and valving (Chapter 4). This thesis also describes the development of injection-molded, single-use platforms with on-board diaphragm micro-pumps (Chapter 3). A CAD model of the injection molded pump test-blocks currently under manufacturing and testing is shown in Figure 1-7. This thesis also describes a model to predict large deflections of polymer diaphragms (Chapter 2). The model is in close agreement with FEA simulations (Figure 1-8) and experimental results. We integrate the EM actuators with the injection-molded platforms, demonstrating pumping at a flowrate of 0.45 µL/stroke, temperature rise of less than 0.1 °C, valve sealing up to 60 kPa, and a pumping frequency of 1 Hz, limited by diaphragm behavior (Chapter 5). The assembly of the EM actuators into an EM pump is shown in Figure 1-5 and Figure 1-6.

Further, this thesis describes improvements in passive leveling between MPSes on a platform using improved spillway designs (Chapter 6). The new design of spillways is shown in Figure 1-9. This thesis also presents a method to fluidically interconnect two platforms and maintain an interconnect flow and fluid level between them (Chapter 7). It also describes the selection of polymer material for pneumatic tubing to resolve the condensation issue in pneumatic channels of the diaphragm micro-pumps (Chapter 8).

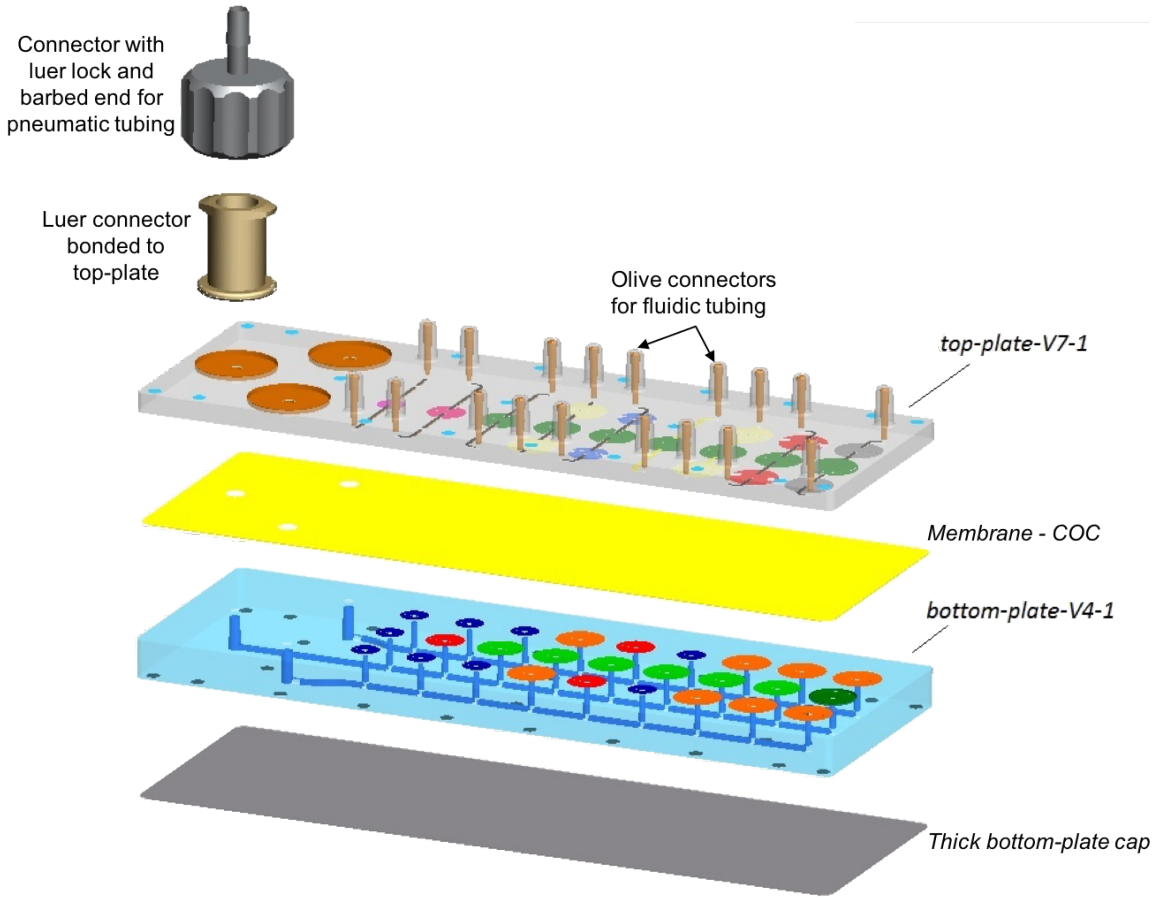

Figure 1-7: Exploded view of the disposable injection molded pump test-block. The top (fluid) plate, membrane, bottom (pneumatic) plate and the thick bottom cap are made of Cyclic Olefin Copolymer (COC). There are 9 lanes of pneumatic diaphragm micro-pumps (valve-pump-valve chambers) with different pump and valve geometries. This pump test-block is designed to demonstrate on-platform pumping and to evaluate feasible pump and valve geometries for future integration with injection-molded MPS platforms. Image by microfluidic ChipShop GmbH, our manufacturing partner for this project.

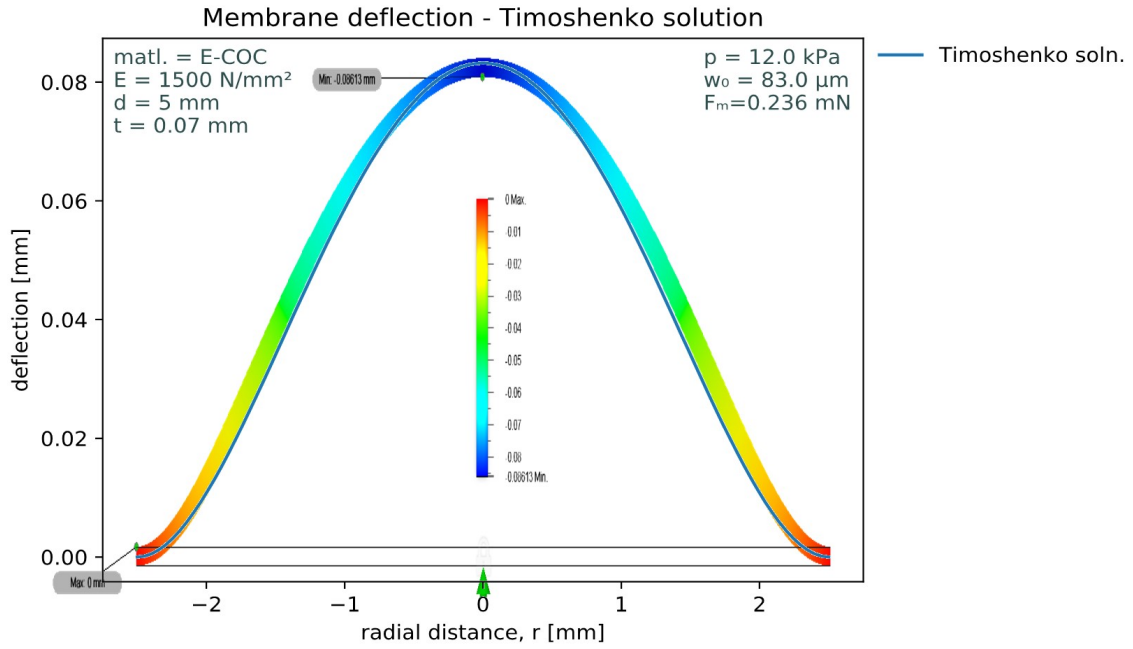

(a) Vertical displacement profile - Timoshenko solution overlapped with FEA result.

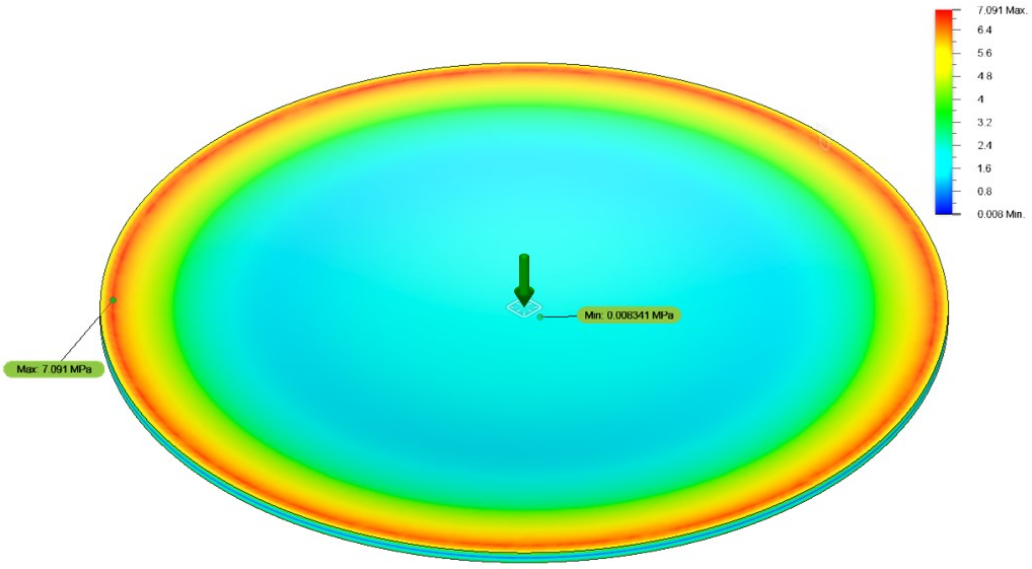

(b) Von-Mises stress.

Figure 1-8: Comparison of model and FEA simulation results for thickness = 0.070 mm, diameter = 5 mm, and pressure = 12 kPa. (a) Vertical displacement profile with model and FEA solutions overlapped. The maximum deflection (83 µm) is close to the value predicted from the analytical model gven by the Timoshenko curve. (b) Maximum von-mises stress is 7 MPa is at the edge of the diaphragm. This stress value is lesser than 1/3 times the yield stress of the Cyclic Olefin Copolymer (COC) diaphragm material. We measured the yield stress of the COC diaphragm on an Instron material tester and found it to be 24 MPa.
Simulations were run in Autodesk Fusion 360, nonlinear static stress analysis mode.

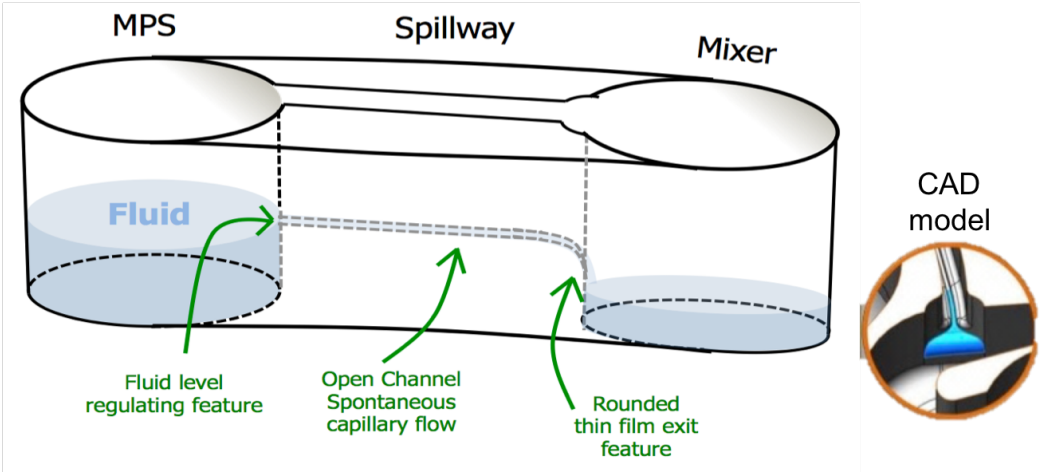

Figure 1-9: Our new design with rounded spillway geometry at the exit. In normal operation there is a fluidic connection from the entry well through Spontaneous Capillary Flow (SCF) until the fluid film breaks at the rounded exit feature. The fluid thins at the exit due to the larger area, and this thin film is unstable due to surface tension and thus breaks up into droplets and sheds into the sink well. Thereby, it transports media into the sink well, but without a fluid coupling between the source and the sink well.

Chapter 2

Diaphragm design for micro-pumps

2.1 Introduction

Peristaltic diaphragm micro-pumps, as described in Chapter 3 and 5 and also in [5], consist of a fluidic layer bounded by a diaphragm. The diaphragm is deformed by some means to either seal the fluid flow in valves or to transfer energy to the fluid in the pump chambers and is therefore the active part of the peristaltic micro-pump. Being able to predict the behavior of the diaphragm against actuation forces is critical to designing the the pump and valve geometries. In this chapter, we describe the design considerations for use of diaphragms in such micro-pumps. We describe a model that approximates the diaphragm deflection and predicts the displaced volume for a given actuation pressure. This allows us to determine the feasible geometry of the diaphragm and get a bounding for the displaced volume per stroke. We verify the model using Finite Element Analysis (FEA) and also experimentally validate it. At the end of the chapter, we select feasible geometries of the diaphragm for use in the disposable test pump blocks which are discussed in Chapter 3.

For the injection molded disposable platforms, as described in Chapter 3, the diaphragm is bonded between the pneumatic and the fluidic plate, as shown in Figure 2-1. Due to the constraints in manufacturing and a different diaphragm material, the designs need to be modified compared to the existing pump and valve geometries as shown in Figure 2-2. The existing pump and valve geometries have a spherical

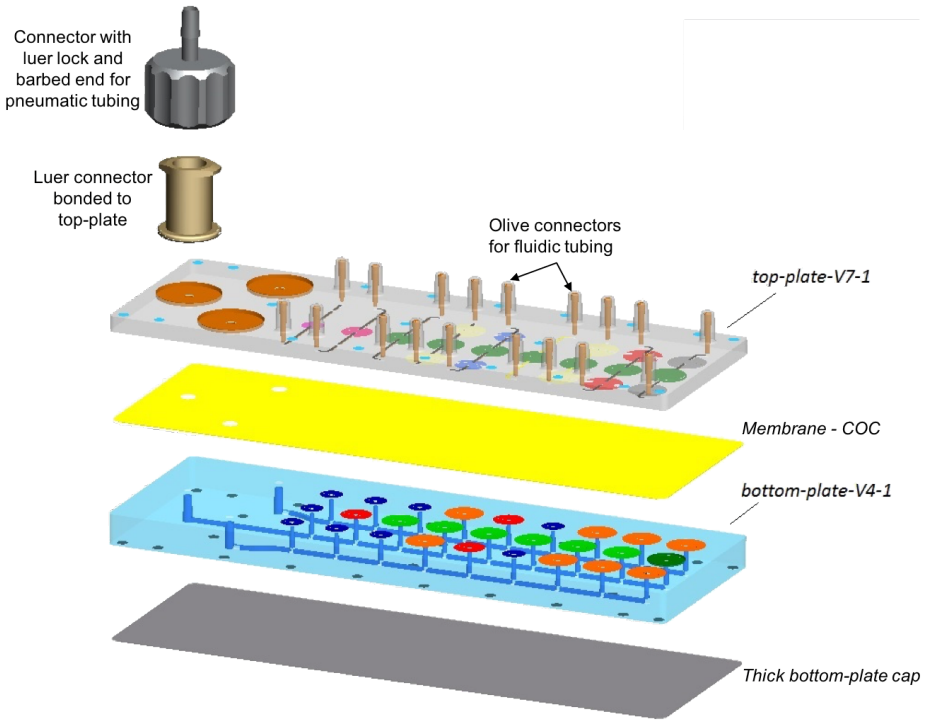

Figure 2-1: Exploded view of the single-use injection-molded platform showing various layers which are bonded together. Design details for each component are discussed in Chapter 3. Image by microfluidic ChipShop GmbH.

chamber geometry and use a 0.050 mm polyurethane sheet as the diaphragm material. They are described in greater detail in Chapter 4 and also in [5]. In the disposable platforms, the pneumatic and fluidic plates are made of Cyclic-Olefin-Copolymer (COC) and the diaphragm is also made of 0.065-0.075 mm sheet of COC. We need to predict the impact of various factors such as the the actuation pressure and diaphragm area on the deflection of the diaphragm to design the pump and valve chamber geometries. The deflection behavior of the diaphragm within the pump and valve chambers is responsible for the pressure vs. volume-flow-rate characteristics such as volume-per-stroke, back-pressure capability, and sealing pressures for these micro-pumps. Therefore, it is important to understand the membrane behavior in the design phase.

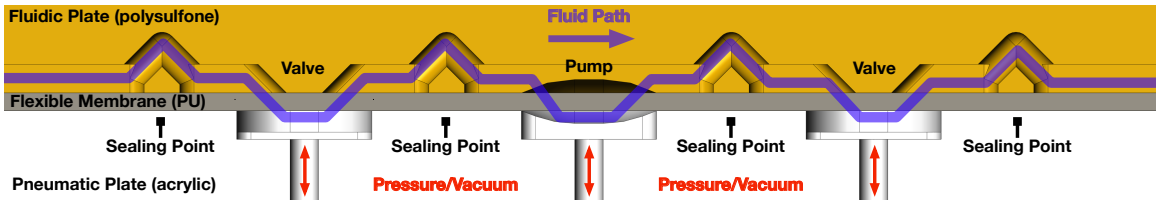

Figure 2-2: Cross-section of the existing diaphragm micro-pump. It is described in more detail in Chapter 5 and in [5].

2.1.1 Design of diaphragms using polymer materials

Generally, polymer manufacturing is a variable process in which it is challenging to achieve tight consistency in the composition at reasonable prices, especially for low volume manufacturing. In our existing pumps, as described in Section 5, we use polyurethane (PU) diaphragms, the physical properties of which were found to be varying stock to stock for the same specification, from the same manufacturer. Therefore, based on the recommendation by the supplier, a larger lot quantity was purchased and is being used to cut the diaphragms for the platforms to maintain assembly to assembly consistency. Our manufacturing partner for microfluidic devices for this project is microfluidic ChipShop GmbH. They had a large quantity of a particular thickness of COC sheet - 0.065-0.075 mm (thickness variation of 10 µm) and hence, that was fixed as the working thickness of the diaphragm. Thus, we have to work with the diaphragm parameters as a fixed part of the design and work on other aspects of the system to make it all work together.

It is important to limit the working range to within the linear elastic regime of the diaphragm material so that the diaphragm returns back to its initial position every actuation. Otherwise, if the material yields, it will have some permanent deformation set into the diaphragm which will cause it to slack leading to non-deterministic volumes. This means, the strain in the diaphragm should be limited to below the yield strain in normal operation.

For pneumatically actuated diaphragms, the ideal would be a diaphragm which requires almost zero force for deflection. This means that all the pressure at the input on the pneumatic side is seen by the fluid and the pressure required to maintain a

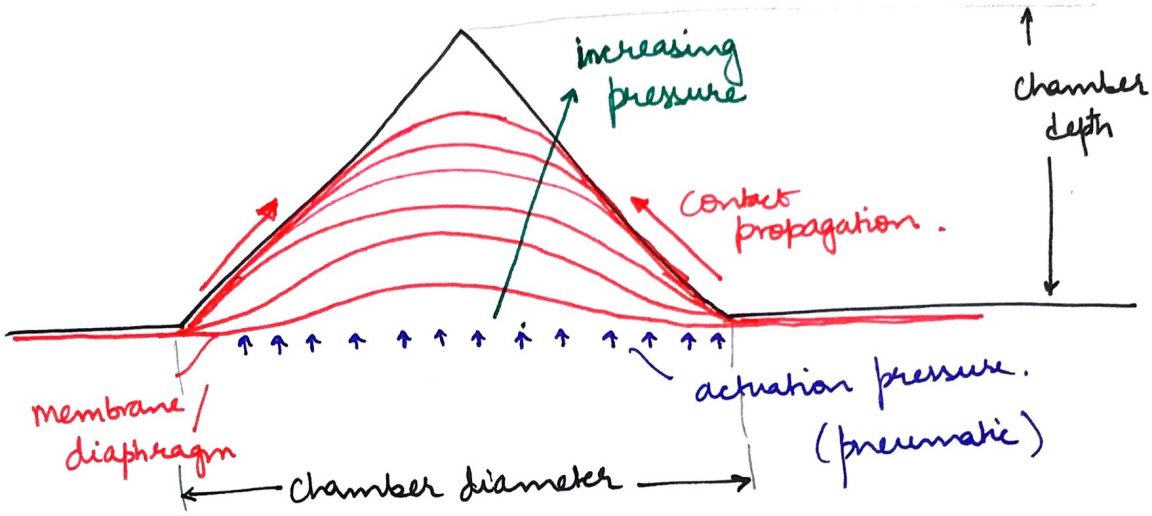

Figure 2-3: Propagation of diaphragm deflection in a conical chamber. The contact with the wall linearly propagates upwards with increasing pressure. As that happens, the effective diameter of the diaphragm reduces and the diaphragm stiffness increases approximately quadratically.

certain deflection state on the membrane is negligible. All the applied pressure then, is used to oppose the fluidic back-pressure.

For the disposable platforms, as described in Chapter 3, we decided to use conical pump and valve chambers to have a well-defined propagation front of the diaphragm when it comes in contact with the chamber walls, as shown in Figure 2-3. We have to decide the diameter and depth of the pump and valve chambers. There are two modes of pneumatic actuation commonly used for diaphragm micropumps - (i) symmetric bidirectional actuation which uses both pressure and vacuum and (ii) unidirectional actuation which uses pressure only. The maximum operating pressure using symmetric bi-directional actuation mode, is limited to around ± 80 kPa(g), mostly limited by the line vacuum which cannot be lower than -15 psi(g) (-103.4 kPa(g)). Here "(g)" denotes that the pressure values are in gauge pressure, i.e. gauge pressure = absolute pressure - atmospheric pressure (absolute). An alternative would be to use only pressure to compress the fluidic chambers and use the stiffness of the diaphragm to retract and create the suction necessary to fill the pump chambers and open the valves. This would enable us to use much larger pressures as the line pressures are generally higher, up to +300–400 kPa(g), which is a common mode of operation with

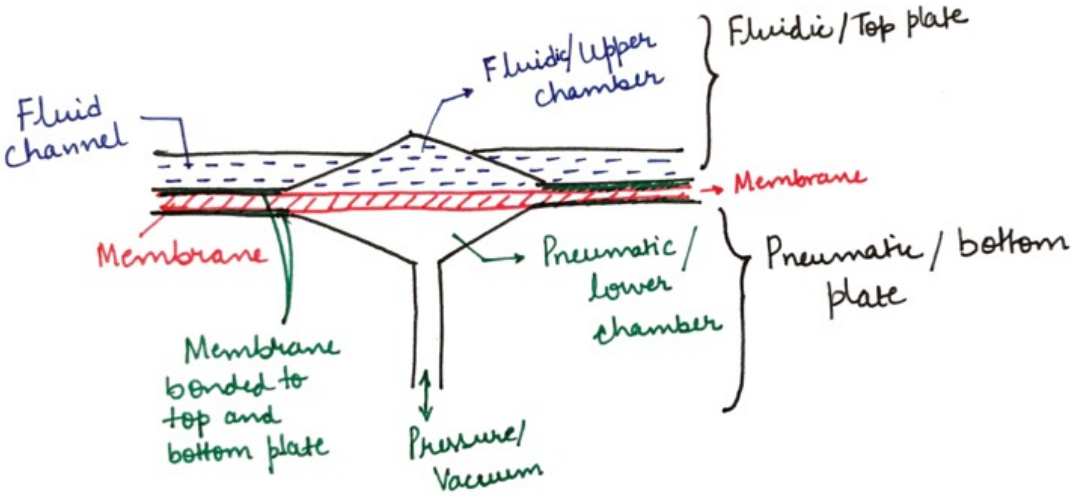

Figure 2-4: Pump chamber cross-section showing the conical chamber shape and the fluidic channels

very stiff diaphragms due to the larger pressure and hence larger force available for actuation.

The diaphragm stiffness varies non-linearly with deflection, having very low stiffness when the deflection is small and the stiffness increases at a faster rate (approximately as the square of the deflection, as the deflection varies as the cube root of pressure for large deflections) [6] as the deflections become larger. Therefore, to increase the stiffness at zero deflection, one solution is to have some initial tension in the diaphragm before bonding. The diaphragm would need to retain this tension stress in operation and not creep with time and with actuation stresses. Another solution would be to modify the membrane shape to have wavy undulations which make the membrane response more linear with pressure and increase the stiffness around zero deflection point. Although the manufacturing process becomes more complicated. Since stability in the uni-directional mode of operation still needs to be evaluated for the COC diaphragm, we decided to pursue the symmetric bi-directional mode of actuation by switching between pressure and vacuum for our project.

The pump chambers are of similar conical geometry on both sides of the diaphragm as shown in Figure 2-4. For the valves, on the pneumatic side chambers are of a

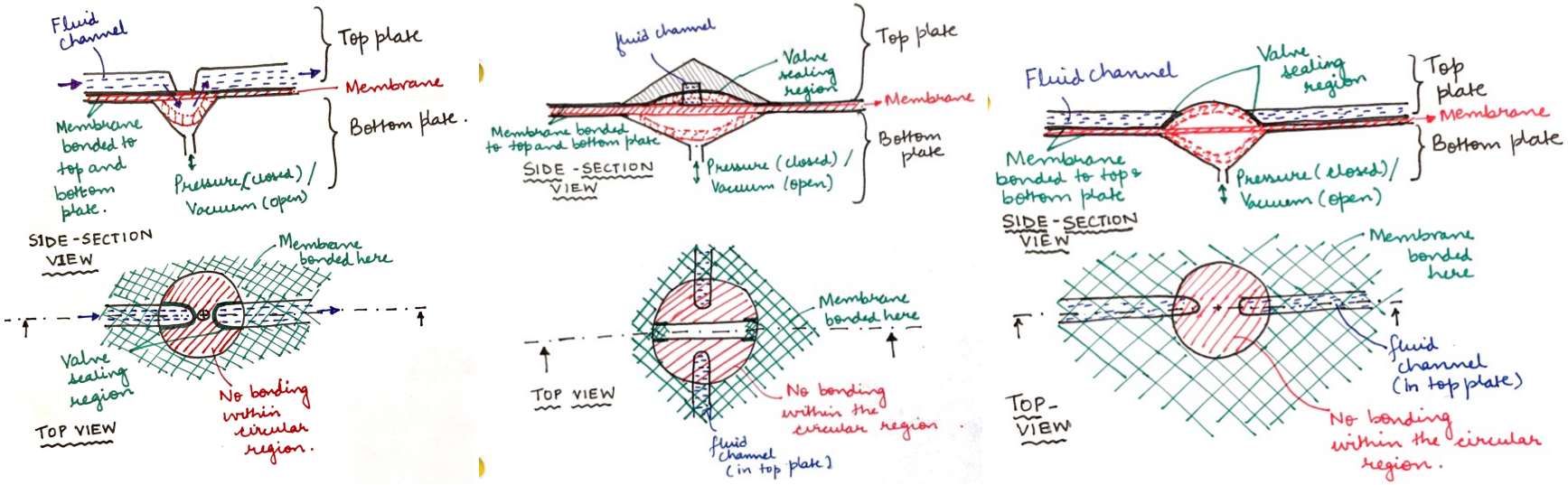

(a) Doormat valve **(b)** Mid-wall valve **(c)** Rounded valve

Figure 2-5: Valve cross-sections showing the various geometries

conical geometry with a pneumatic port connection of 0.5 mm diameter connecting to the pneumatic channels. On the fluidic side, we have 3 geometries, as described in Section 3.6.2 — the doormat, mid-wall and rounded valves also shown in Figure 2-5.

It is important to have a depth of at-least 1-2 times larger than the thickness of the diaphragm to provide enough gap during bonding of the diaphragm. Otherwise, the diaphragm can touch the valve and pump chamber walls and get bonded to them which are called "bonding touchdowns". Based on the thickness of the diaphragm, we decided on a chamber depth of 0.075-0.150 mm. Another consideration is that there is typically a ±2% geometrical error in most micro-manufacturing processes for microfluidics [7]. Therefore, the deeper the pump chambers, the smaller the contribution of these random errors on the total stroke-volume variance. Deeper pump chamber also increases the pressure requirement for deflection and increases the strain in the diaphragm, which can cause yield.

Once the diaphragm comes in contact with the chamber walls, the diaphragm deflection behavior changes, and that needs to be taken into account. After contact, the diaphragm acts much stiffer and there is a smaller increase in deflection for large increases in pressure beyond that point, thereby saturating the displaced chamber volume beyond a certain pressure. We would like to limit the deflection of the diaphragm in the pump chamber at around 10-15 kPa(g) below the actuation pressure so that we have a constant stroke-volume up to 10-15 kPa of back-pressure capability, i.e. the pressure head against which the pump can pump at the same volume flow-rate. For example, if the membrane touches the chamber wall at 20 kPa(g) and we are actuating at 40 kPa(g), then the additional 20 kPa is the back-pressure capability of the pump within which it will still pump out a deterministic stroke volume for a back-pressure between 0-20 kPa(g).

2.2 Modeling the deflection behavior of diaphragms

We need a model to predict the diaphragm deflection for a given pressure difference across it, with a bonded (fully clamped) boundary condition at the edges. We also

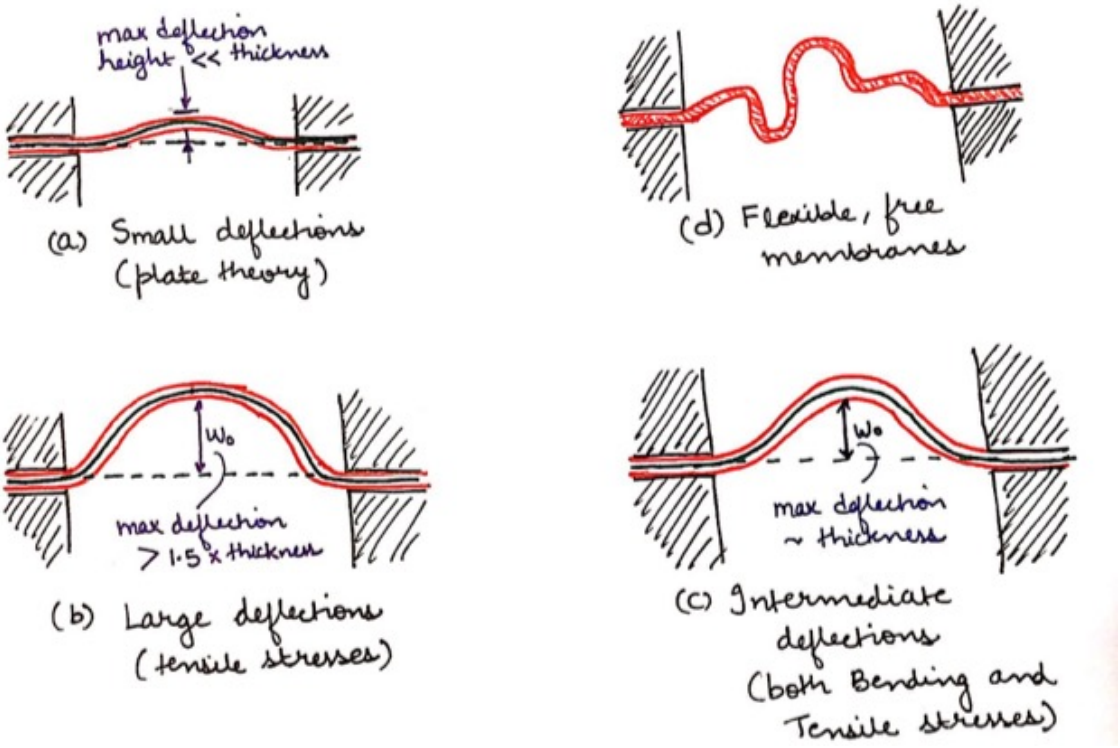

Figure 2-6: Categorization of diaphragm deflection. Details are given in Section 2.2.

should be able to predict approximately the pressure at which the diaphragm makes contact with the wall for the pumps and valves.

Diaphragm deflections can be categorized into three categories, as also shown in Figure 2-6:

1. Small deflections

   In these, the diaphragm deflection is limited to be smaller than the diaphragm thickness. The stress state within the diaphragm is primarily bending-dominated. These are usually analyzed using von-Kármán plate theory as the boundary conditions are easier to resolve and exact analytical solutions exist. [8]

2. Large deflections

   In these, the diaphragm deflection is larger than 1.5 times the diaphragm thickness. The stress state is dominated by tensile stresses in the diaphragm. These are also called membrane deflections. A spherical deflection shape is assumed and these are analyzed using solutions for thin spherical shells. [6]

3. Intermediate deflections

   In these, the diaphragm deflections are of the order of the diaphragm thickness. Both bending moments and tensile stresses contribute significantly to the stress state. This is a general case and the solutions to this should lead to the small deflection solution for the limit of small deflections and the large deflections solutions at the upper limit. We use this solution in our analysis as the chamber depth and hence our deflection range of interest is of the order of the membrane thickness. This is further discussed in the subsequent sections.

4. Flexible, free diaphragms

   In these, as noted in [9] the diaphragm is so flexible that bending moments and tensile stresses are negligible. There is slack in the diaphragm to accommodate the deflections of interest with almost zero stress in the diaphragm until all the slack is removed, beyond which the diaphragm stiffness suddenly increases. The diaphragm acts as a partition between the two sides and allows for the net transfer for pressure from one side to another with minimal pressure difference across the membrane. The diaphragm shape at equilibrium is undetermined, and at equilibrium, the pressures on both sides of the diaphragm are equal.

2.2.1 Prior work

For small deflections of plates, the classic text by Timoshenko [8] has a thorough analysis of the modeling of such deflections. For large deflections, Small and Nix [6] assume a spherical shape and derive equations based on the formulae for stress in thin-walled spherical shells. They later also describe a more refined model, derived by curve fitting of FEA data. Lin and Senturia [10] use the energy minimization method and give an approximate solution for large deflections. Timoshenko and Woinowsky-Krieger [8] and Way [11] give an approximate solution for plate deflection in the intermediate to large deflection range. Zhang [12] has tabulated many of the different equations developed, which shows a historic progression in the development of analytical solutions to predict the deflections clamped circular plates in literature.

In our analysis, we use the solutions developed by Timoshenko [8] with slight modifications to include the initial stress state and keep the Poisson's ratio as a variable.

2.2.2 Problem Definition

The thickness of the diaphragm is fixed (0.065 - 0.075 mm), the range of deflection depths (0.075 - 0.150 mm) is fixed and the range of pressures is also fixed ($\pm 20 - \pm 100\,\text{kPa(g)}$). Therefore, the problem is to find the feasible range of diameters which will work for these parameters. The diaphragm parameters used for modeling are given in Table 2.1.

Table 2.1: Diaphragm physical parameters used for modeling. Details of measurement of measured values are given in Section 2.3.1.

Parameter	Symbol	Value	Units
Young's modulus (measured)	E	1300-1500	MPa
Density	ρ	940	kg/m^3
Poisson's ratio	ν	0.41	-
Yield strength (measured)	Y	24	MPa

2.2.3 Modeling the diaphragm deflection

Assumptions and Considerations

The assumptions are:

1. The diaphragm thickness is much smaller than the chamber diameter.
2. The diaphragm is always within the linear proportionality limit of the material, i.e., below the yield stress, and
3. The diaphragm material is isotropic.

For the diaphragm design, an analytical model is ideal during the initial design phase compared to an FEA solution because it gives us insight into the design rules and how various parameters affect the stiffness helping us identify feasible designs.

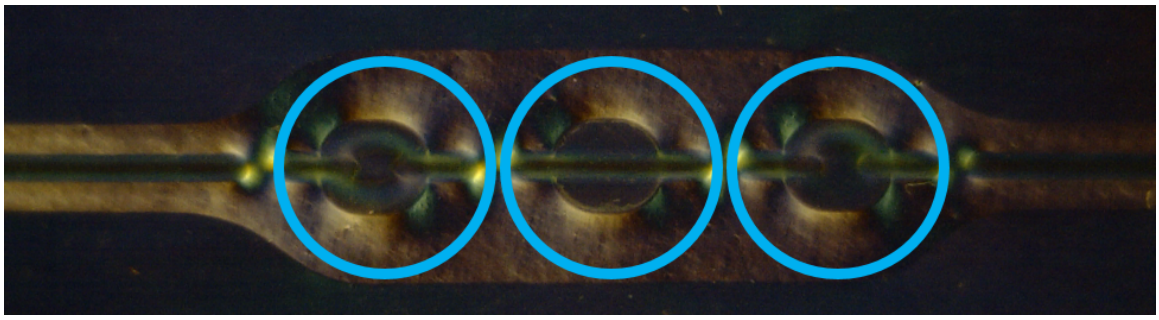

Figure 2-7: Birefringence imaging of the diaphragm. Visible buckling which presents as wrinkling at the clamped edges of the diaphragm, inside the blue circles. Diaphragm material is polyurethane with a thickness of 0.050 mm. Image courtesy of Luis Soenksen, a PhD student in our lab.

Then, we can use FEA over these feasible designs to further refine the design. We develop analytical expressions to predict the diaphragm deflection profile and the volume displaced in the pump chamber and then verify them using FEA and experiments. For FEA, we need a non-linear FEA solver to solve for the large deformations, which are generally time and resource intensive.

Boundary conditions for the diaphragm deflection

The boundary conditions at the edge of the chambers are an important consideration to model the deflection of the diaphragm. In the current platforms, the polyurethane diaphragm is clamped between the fluidic and the pneumatic plates. This clamping by vertical compression generates horizontal compressive stresses at the edge of the diaphragm. For thin diaphragms with diameters an order of magnitude greater than the thickness, the buckling stiffness is very small and the diaphragm buckles [6]. This can be seen as wrinkles near the edges, as shown in Figure 2-7. This makes the analysis of deflection of such diaphragms challenging as it is difficult to know the exact state of of the diaphragm before actuation [6]. In currently used designs, the membrane is pre-tensioned before clamping, to guarantee net tension after clamping. This is implemented by mounting the membrane on grip rings (Ultron Systems 10 UGR-12) to provide uniform tension.

In the present case, the diaphragm is bonded and therefore, the compressive

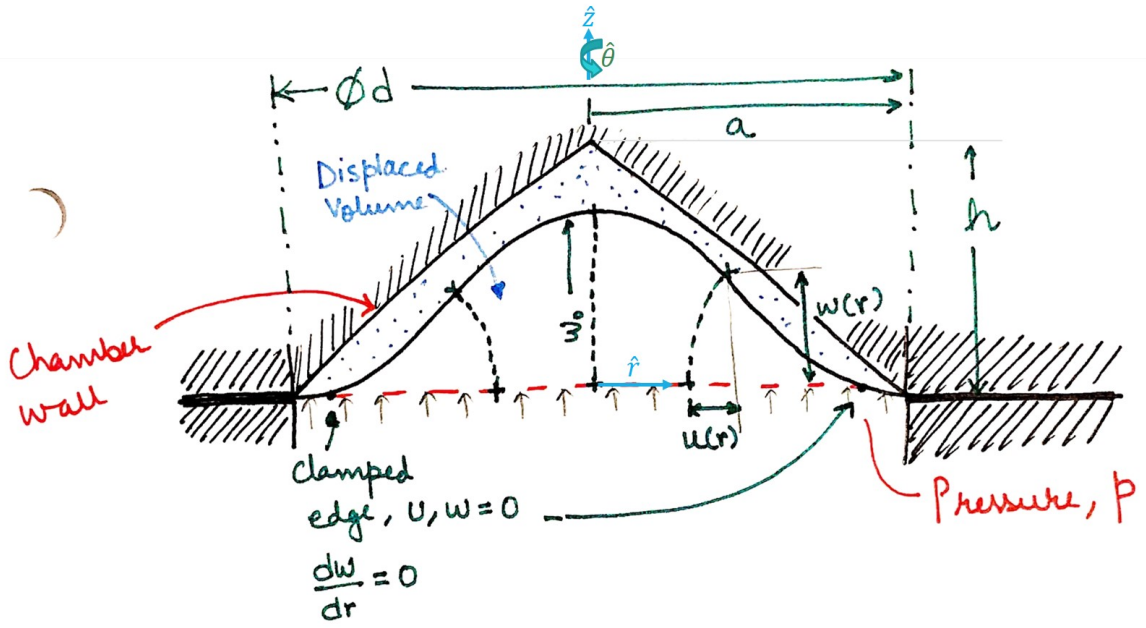

Figure 2-8: Diaphragm deflection parameters. The coordinate axes $\hat{r}, \hat{\theta}, \hat{z}$ are shown in the figure.

stresses are negligible. The initial stress state in the diaphragm is assumed to be constant with a value σ_0 (symmetric and equal in radial and tangential directions) with the corresponding in-plane strain of ϵ_0 related by,

$$\epsilon_0 = \frac{1-\nu}{E}\sigma_0 \tag{2.1}$$

where, E is the Young's modulus and ν is the poisson's ratio for the diaphragm.

Approximate solutions for the deflection shape

The diaphragm parameters used for modeling are listed in Table 2.2 and also shown in Figure 2-8. From the boundary conditions, we can ascertain the state of stress and strain in the diaphragm, which is also described in [6]. At the boundary, due to the clamped condition, the tangential strain (ϵ_θ) should be zero, and at the center, the tangential and the radial components of stress and strain should be equal due to axisymmetry.

The radial displacement ($u(r)$) and the vertical displacement ($w(r)$) vary with

Table 2.2: Parameters used for modeling the diaphragm deflection

Parameter	Symbol	Units	Value
diaphragm diameter	d	mm	<to be found>
diaphragm radius	a	mm	d/2
diaphragm thickness	t	mm	0.065-0.075
Height of chamber	h	mm	0.075-0.150
Actuation pressure	p	kPa	±20–±80

changing pressure and give rise to the deformed profile of the diaphragm and corresponding stresses. Due to the axisymmetric nature of the displacements, the radial and the vertical displacements uniquely define the displacement of any point on the diaphragm as a function of the radius, as shown in Figure 2-8. The boundary conditions are given below. Here, r is the radial coordinate and a is the radius, $a = d/2$, of the diaphragm.

$$u = 0 \qquad \frac{dw}{dr} = 0 \qquad at\ r = 0, \tag{2.2}$$

$$u = 0 \qquad w = 0 \qquad \frac{dw}{dr} = 0 \qquad at\ r = a. \tag{2.3}$$

To get an exact solution using plate theory for these deflections which are of the order of diaphragm thickness, we need to use numerical methods.[8]. The difficulty comes from the complexity of solving the von-Kármán equations with the boundary conditions. We can get an approximate solution for the deflection shape by using energy methods (Principal of virtual work). Timoshenko and Woinowsky-Krieger [8] assume the following deflection shapes for the radial, u and vertical, w displacements. They assume that the shape of the deflected surface for deflections of the order of the diaphragm thickness can be represented by the same equation as in the case of small plate deflections. Thus, for the vertical deflections, we get,

$$w = w_0 \left(1 - \left(\frac{r}{a}\right)^2\right)^2 \tag{2.4}$$

where w_0 represents the maximum deflection at the center point of the diaphragm.

For the radial deflection we have,

$$u = r(a - r)(C_1 + C_2 r + C_3 r^2 + ...). \tag{2.5}$$

Both these equations satisfy the radial and vertical boundary conditions. It is very difficult to take all the terms for the radial deflection into account and for the approximation, we only take the first two terms in the series. Therefore, u becomes,

$$u = r(a - r)(C_1 + C_2 r). \tag{2.6}$$

The unknown variables, w_0, C_1, C_2 are cosntants which are found by minimizing the total strain energy, which is the sum of strain energy due to bending and tensile stretching, with respect to each of these variables. This gives us 3 equations for three unknowns. Zhang [12] solves the Timoshenko and Woinowsky-Krieger [8] equations including the term for the initial stretching and expresses the equations in terms of the Poisson's ratio, ν while Timoshenko and Woinowsky-Krieger [8] use ν as 0.25 or 0.3 for their derivation. Therefore, we get, from [12],

$$w_0 + \left\{ \frac{3}{4} \left(\frac{a}{t} \right)^2 (1 + \nu)\epsilon_0 \right\} w_0 + (0.4319 + 0.2411\nu - 0.1808\nu^2)\frac{w_0^3}{t^2} = \frac{pa^4}{64D}, \tag{2.7}$$

where D is the flexural rigidity of the diaphragm, given by,

$$D = \frac{Eh^3}{12(1 - \nu^2)}. \tag{2.8}$$

The first term in the left-hand side of Eq. 2.7 is due to bending, the second term is due to the initial stretching of the diaphragm and the third term is due to the further stretching from the tensile stress due to the pressure. Finding the real root to this equation, we get the value of w_0. The value of C_1 and C_2 can be found from the following equations, again from [12],

$$C_1 = [8.75(0.146 - 0.2603\nu) + 11.25(0.0127 + 0.13968\nu)]\frac{w_0^2}{a^3} \tag{2.9}$$

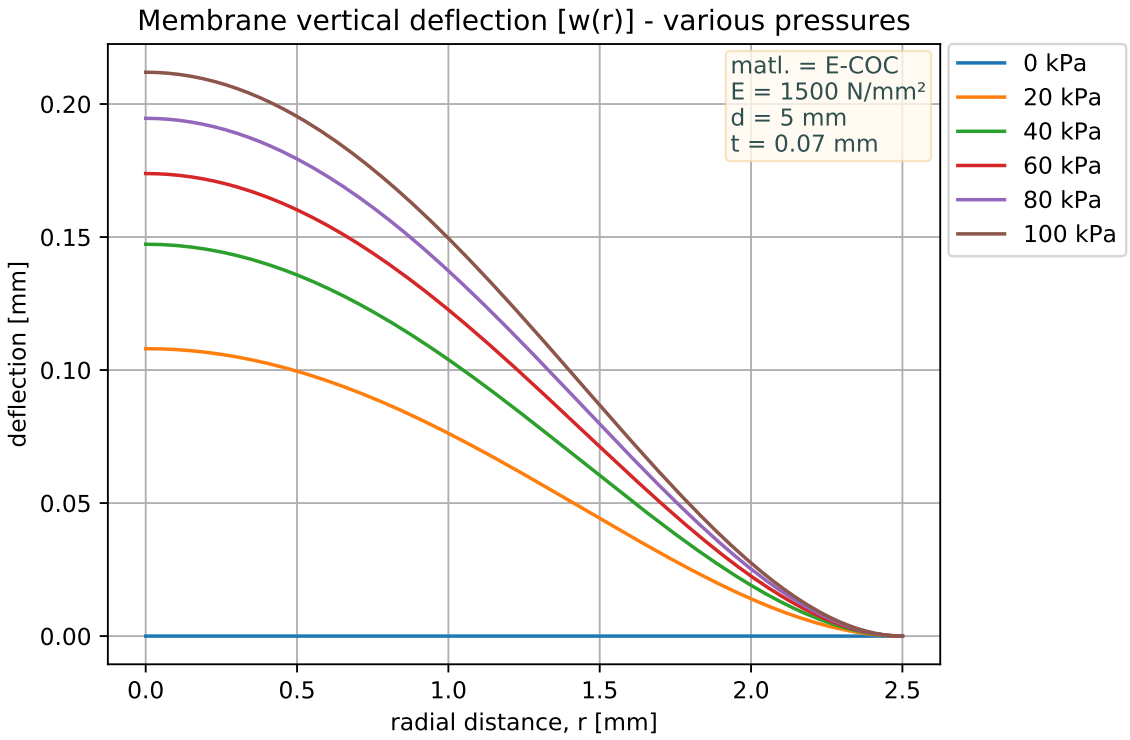

Figure 2-9: Diaphragm vertical deflection profile for 5mm dia. COC diaphragm. The curve is modeled using the Timoshenko solution as described in the previous section. The membrane solution satisfies the boundary condition for deflection value and slope at the center and the edges. The initial tension in the diaphragm is assumed to be 0.

and,

$$C_2 = [-11.25(0.146 - 0.2603\nu) - 18.75(0.0127 + 0.13968\nu)]\frac{w_0^2}{a^4} \tag{2.10}$$

We now have all the terms required to evaluate u and w for the diaphragm. We cannot estimate the diaphragm stress and strain from this equation as they require second order derivatives of the displacements and from the assumed shape, we are not solving those boundary conditions which come from force and moment balance. We use this analysis to find the diameters which satisfy our deflection requirements within the actuation pressure range and then use FEA to verify that the stresses are within the yield limit. For long life of the diaphragms, it is recommended that the stresses be within 1/3 times the yield strength.

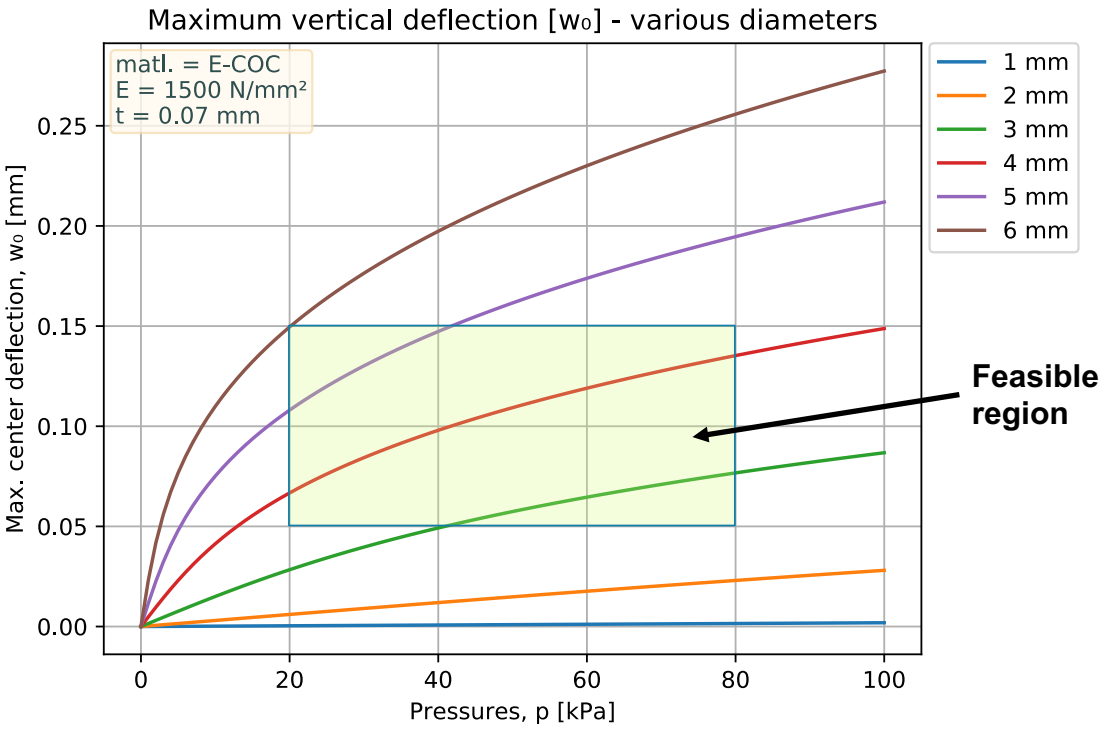

Figure 2-10: Maximum center deflection vs. pressure for various diameters. The feasible region is that which encompasses the pressure actuation range and the allowable maximum deflection, limited by the chamber depth. For our case, 3-5 mm is the feasible range for chamber diameters. The initial tension in the diaphragm is assumedto be 0.

Modeling Results

Using the analysis described above, we calculate the deflection profiles for the Timoshenko solution. The modeled vertical deflection ($w(r)$) profiles of the diaphragm for a diameter of 5 mm is shown in Figure 2-9. We can see that the deflection profile satisfies the boundary conditions of zero slope at the center and at the edge as well as zero deflection at the edge. Figure 2-10 shows the variation of the mid-point vertical deflection vs. pressure for various diameters. From this, we can extract the range of chamber diameters that would be feasible for our purpose based on the chamber height and actuation pressures. For our case, the diameters within 3-5 mm are feasible. The maximum deflection of the diaphragm shows a variation approximately as pressure to the power 1/3 for larger diameters (d $\geq$ 4 mm) and linearly with pressure for smaller diameters (d $\leq$ 2 mm).

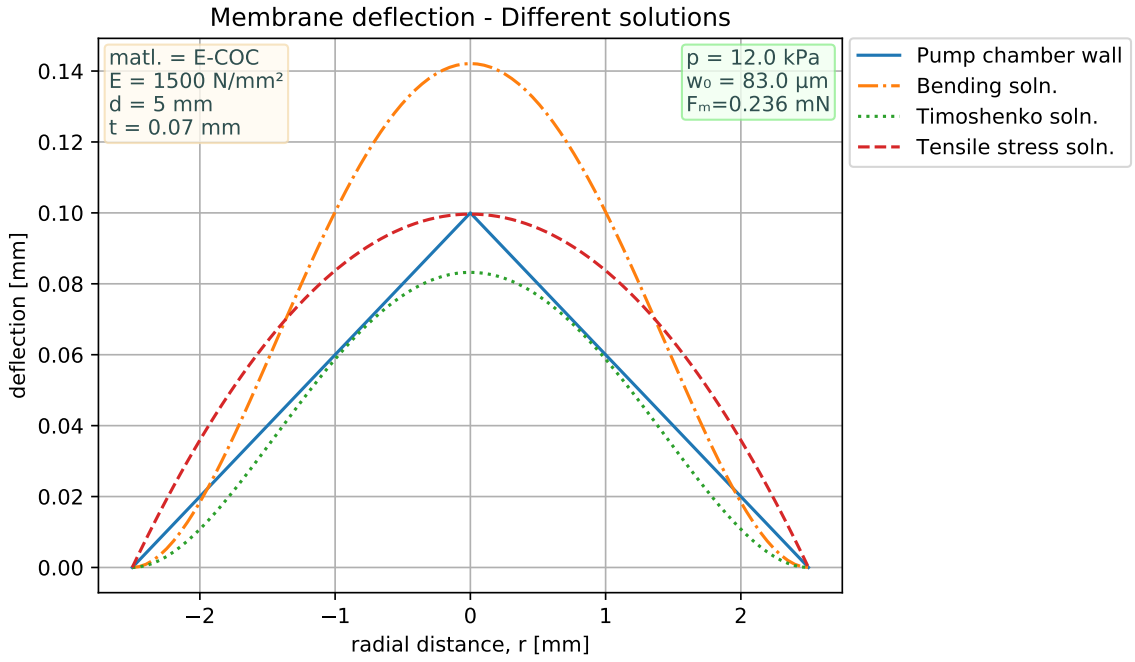

Figure 2-11: Modeling chamber profile and different deflection solutions. Bending solution only considers the bending stresses and therefore overestimates the deflection (orange dash-dot line). Tensile stress solution only considers the tensile stresses and ignores bending and it also overestimates the deflection for small values of pressure (red dash line). The Timoshenko solution incorporates both the tensile and bending stresses and are most representative of the actual deflection (green dotted line). In this particular case, the diaphragm touches the chamber walls at a pressure of 12 kPa, beyond which the diaphragm becomes much stiffer and thus there will be a much smaller change in volume with increasing pressure.

We also model the chamber profile and vary the pressure to see at what value the diaphragm makes contact with the chamber walls as shown in Figure 2-11. In addition, we model other solutions for comparison: (1) a bending solution which only considers the the bending stresses and therefore overestimates the deflection, and (2) a tensile stress solution which only considers the tensile stresses and ignores bending and it also overestimates the deflection for small values of pressure. Timoshenko solution incorporates both the tensile and bending stresses and is thus most representative of the actual deflection over a wide range of deflections of the diaphragm. For a diaphragm diameter of 5 mm, we predict the contact with the chamber walls occurs at a pressure of 12 kPa. Beyond this pressure, the diaphragm becomes much stiffer and there will be a much smaller change in deflection with increasing pressure.

The displacement profiles were verified by FEA, as shown in Figure 2-12. The displacement profile shows good agreement with the analytical data presented in Figure 2-9 for 5 mm diameter, 40 kPa actuation. The maximum stress in the case of the 5 mm diaphragm diameter is 16.86 MPa, which is less than the yield stress of 24 kPa, reported in Table 2.1. For a chamber depth of 0.1 mm, the diaphragm makes contact with the walls at 12 kPa, when the stresses would be smaller, including the edge. Beyond that, the net force due to increase in pressure is balanced by the reaction forces from the chamber walls. Therefore, the stress state shouldn't increase much greater beyond that point. Therefore, the diaphragm is expected to have a long life over a large number of cycles in operation, which should be tested in the final injection molded platforms containing these pump features.

In addition, we compare the model and FEA profiles for 5 mm diameter diaphragm with 12 kPa actuation as shown in Figure 2-13. The Timoshenko solutions matches quite well with the FEA results and the maximum stress in the diaphragm is found to be 7 MPa, which is less than 1/3 times the diaphragm yield stress.

In our analysis, we have assumed that the diaphragm is free to deflect at the edges as long as it satisfies the zero vertical deflection and zero slope boundary condition. In practice, the manufactured pump chamber profile will have some radius at the base, which would modify the end boundary conditions as shown in Figure 2-14. There will

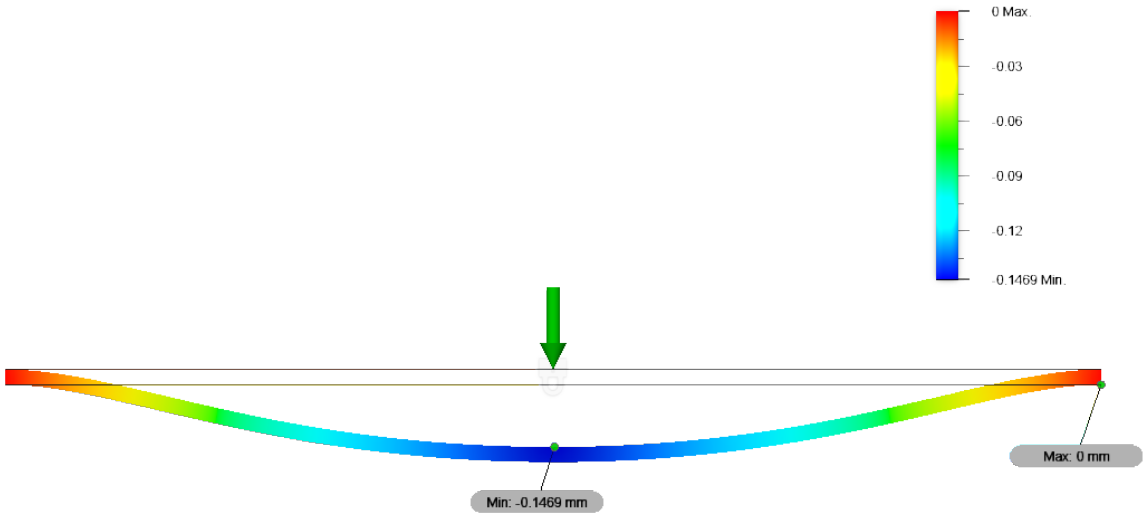

(a) Vertical displacement profile

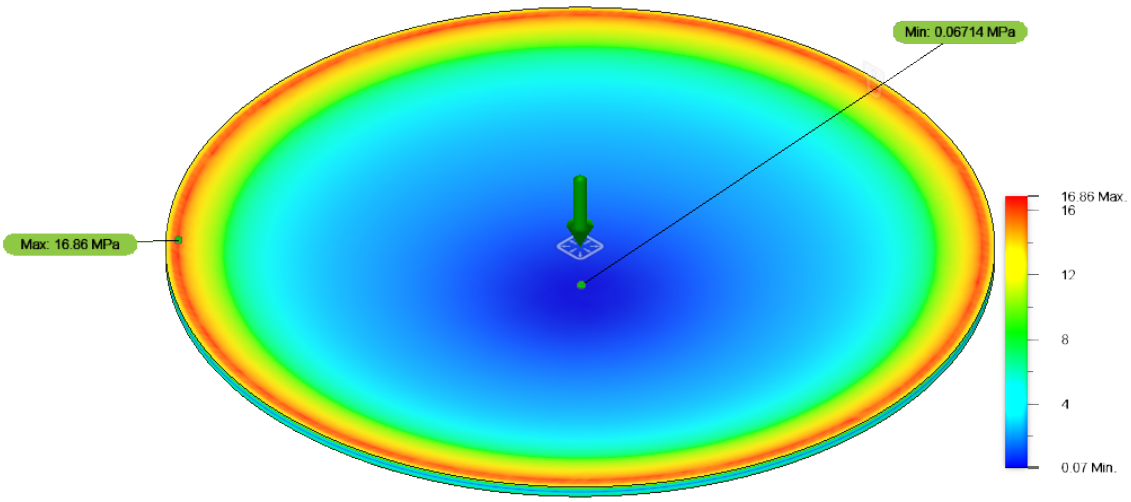

(b) Von-Mises stress

Figure 2-12: FEA simulation results for thickness = 0.070 mm, diameter = 5 mm, pressure = 40 kPa.
(a) Vertical displacement profile, the maximum deflection (147 µm) is close to the value predicted from the analytical model as shown in Figure 2-9.
(b) Von-Mises stresses distribution. The maximum stress (17 MPa) is at the edge, and is lesser than the yield stress of the diaphragm.
Simulations were run in Autodesk Fusion 360, Nonlinear Static Stress analysis mode.

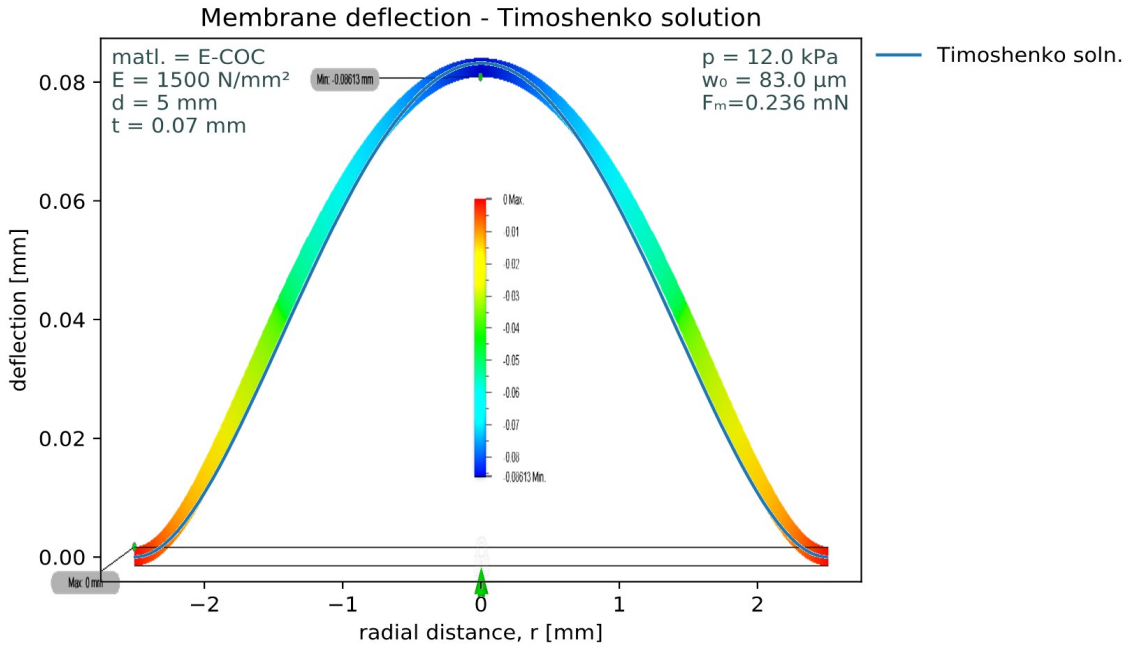

(a) Vertical displacement profile - Timoshenko solution overlapped with FEA result.

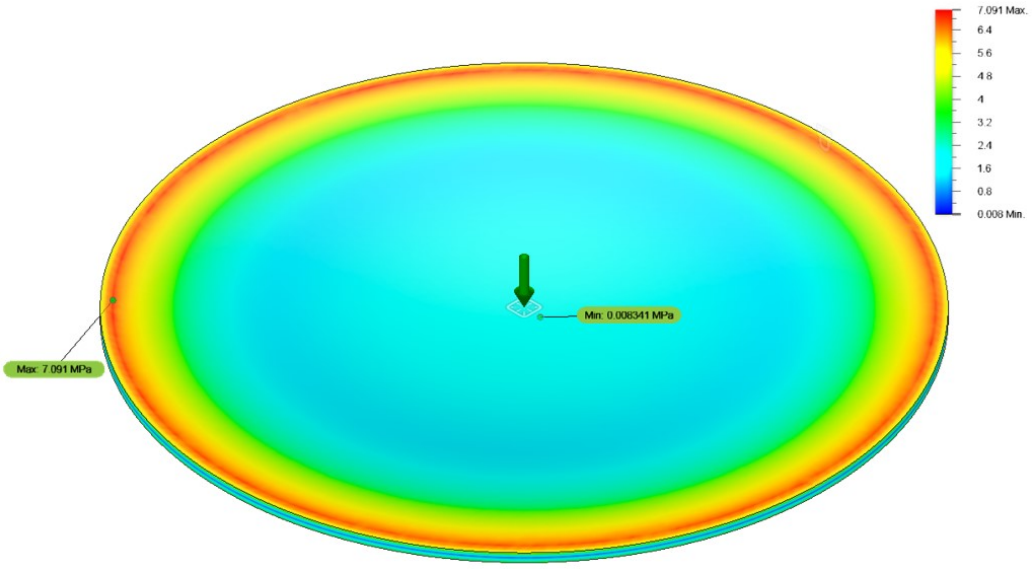

(b) Von-Mises stress.

Figure 2-13: Comparison of model and FEA simulation results for thickness = 0.070 mm, diameter = 5 mm, and pressure = 12 kPa. (a) Vertical displacement profile with model and FEA solutions overlapped. The maximum deflection (83 µm) is close to the value predicted from the analytical model gven by the Timoshenko curve. (b) Maximum von-mises stress is 7 MPa is at the edge of the diaphragm. This stress value is lesser than 1/3 times the yield stress of the Cyclic Olefin Copolymer (COC) diaphragm material. We measured the yield stress of the COC diaphragm on an Instron material tester and found it to be 24 MPa.
Simulations were run in Autodesk Fusion 360, nonlinear static stress analysis mode.

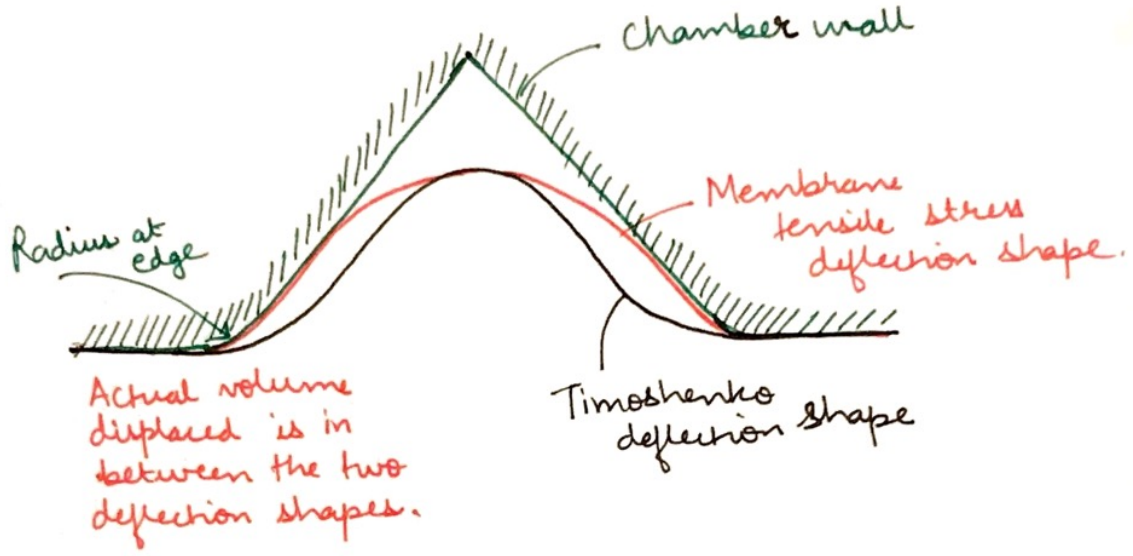

Figure 2-14: Volume displaced by the diaphragm within the pump chamber. The volume displaced would be bounded between the shapes of the Timoshenko deflection and the Tensile stress deflection shape when considering a radius at the edge of the pump chamber.

be a higher stress concentration at the radius which will modify the slope at other end of the edge radius to a non-zero value. The maximum deflection would still be close to the Timoshenko solution as both bending and tensile stresses are significant. Therefore, the diaphragm deflection profile will be of an intermediate shape between the Timoshenko solution and the tensile stress solution shape with nearly the same maximum deflection as shown in Figure 2-14.

Thus, the volume displaced by the diaphragm deflection when the diaphragm has not touched the chamber walls would lie between the volume given by under the Timoshenko displacement curve and under the tensile stress displacement curve with the same maximum deflection. In the manufacturing of the mold, the tip of the cone will also have a radius and that will also modify the actual volume displaced for large deflections of the diaphragm. The volume of a conical pump chamber of diameter d and depth h is given by the equation for volume of a cone,

$$V_{cone} = \frac{\pi}{12} d^2 h. \tag{2.11}$$

The volume displaced under the Timoshenko profile is given by,

$$V_{timoshenko} = \int_0^a 2\pi w_0 r \left(1 - \left(\frac{r}{a}\right)^2\right)^2 dr = \frac{\pi}{3} a^2 w_0. \tag{2.12}$$

And the volume displaced by the diaphragm tensile stress solution, which is a spherical cap as given in [13],

$$V_{tensile} = \frac{\pi}{6} w_0 (3a^2 + w_0^2). \tag{2.13}$$

These give the bounds for the fluid volumes when the diaphragm is not in contact with the chamber walls. $V_{timoshenko}$ is the lower bound while $V_{tensile}$ is the upper bound for the displaced volume.

2.3 Experiments

2.3.1 Measurement of uni-axial Young's modulus of the COC diaphragm

The first step in evaluating the model is knowing the physical parameters of the diaphragm. Since the physical properties such as Young's modulus and the yield stress can have a large variation manufacturing lot-to-lot, we need to measure them. The Young's modulus of the diaphragm was measured as per the ASTM D882-12 standard [14]. The Young's modulus was measured for multiple trials and found to be in the range of 1300-1500 MPa. Figure 2-15 shows the setup and Figure 2-16 shows the plots of data obtained for one of the tests.

2.3.2 Testing of the volume displaced vs. actuation pressure

- The work described in this section was done jointly with Daniel R. Rathbone.

To verify the model and to roughly evaluate the pump chambers before finalizing the design for molding, an acrylic test block of the pump chamber is machined as shown in Figure 2-17. The diaphragm is pneumatically actuated from the port below and fluid is filled in the chamber above the diaphragm. The displaced fluid volume

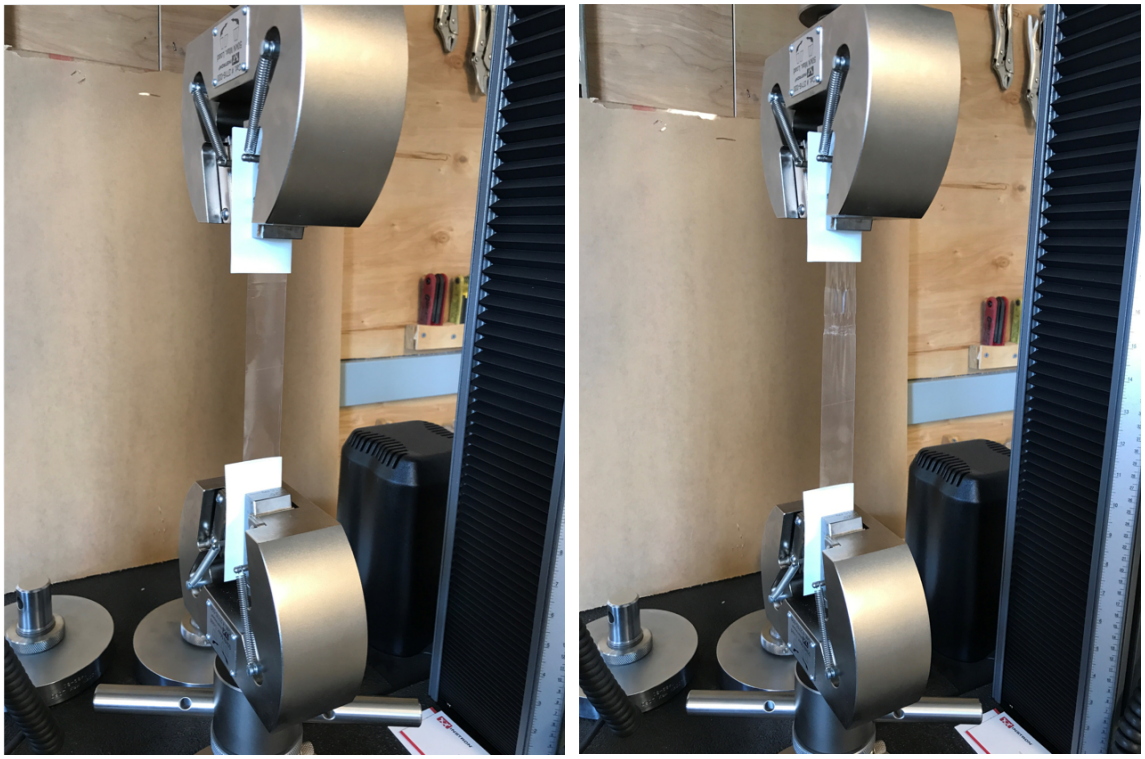

(a) Initial setup **(b)** At the end of experiment

Figure 2-15: Young's modulus measurement of the diaphragm on an Instron machine.

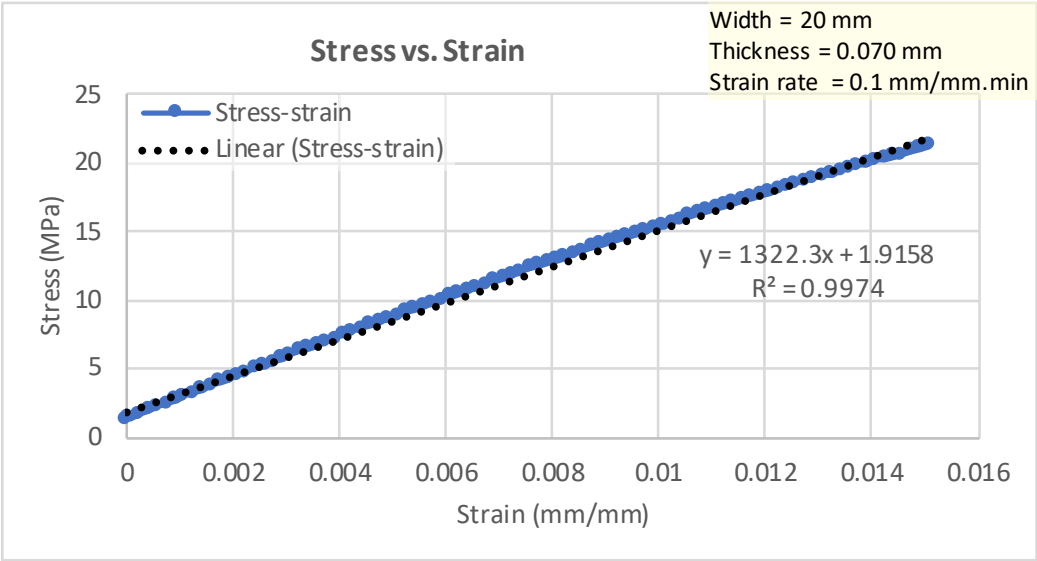

(a) Stress-Strain curve in the linear deflection range for the COC diaphragm.

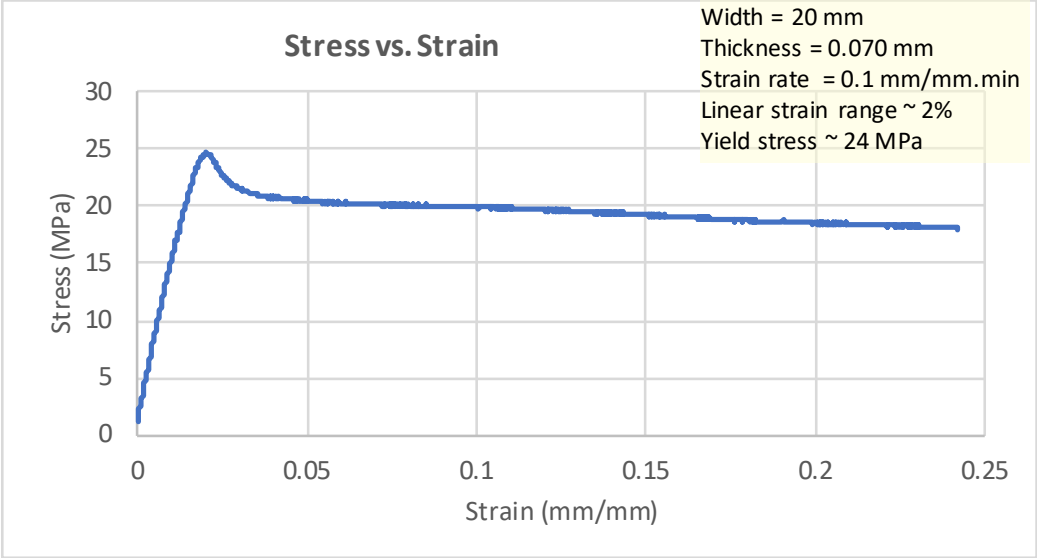

(b) Stress strain curve showing the linear range and the past the Yield point.

Figure 2-16: Stress-strain curve obtained for the COC diaphragm with Young's modulus measurement.
(a) Calculation of Young's modulus with a linear fit line for the linear regime. The slope is the Young's modulus and the value is found to be 1322 MPa. In the regions of lower strain, the slope is slightly higher with a maximum value of 1500 MPa. Thus, the Young's modulus is 1300-1500 MPa
(b) Stress-strain curve much beyond the yield stress. The yield stress is 24 MPa and the corresponding strain at yield is about 2%.
The measurements were conducted on an Instron 5960 series material tester as per ASTM D882-12 standard.

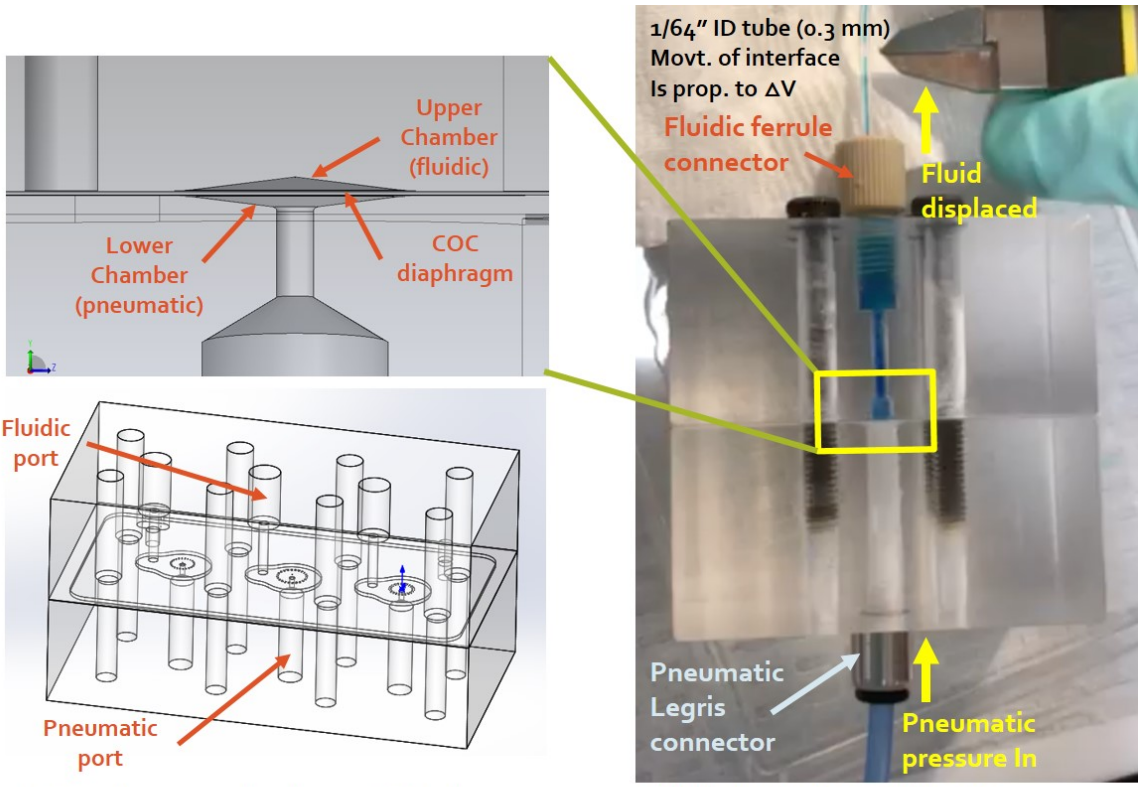

(a) Acrylic pump chamber test block

(b) Method of measuring the displaced fluid volume

Figure 2-17: Pump chamber test block to evaluate the volume displaced vs. actuation pressure
(a) CAD model of the pump chamber test block.
(b) Measurement method for the displaced volume. The pneumatic pressure from the bottom causes diaphragm deformation and displacement of volume. The displaced volume is the volume of the cylinder swept by the moving meniscus in the tube.

is measured from the displacement of the meniscus in a tube from a port connected to the upper chamber as shown in Figure 2-17. The tested chamber diameters and chamber depths on the fluidic side are - (3 mm, 150 um), and (5 mm, 250 um) for pressures ranging from 20 kPa(g) to 80 kPa(g).

Modeling predicts that for the pressures actuated, the maximum deflection for the 3 mm diameter is 0.08 mm and for 5 mm diameter is 0.2 mm. Thus, the diaphragm should not touch the chamber walls. Hence, the volume upper and lower bounds as described in Section 2.2.3 can be used to compare the model with the experiments. Figure 2-18 shows the stroke volume vs. pressure for the 3 mm and 5 mm diameter

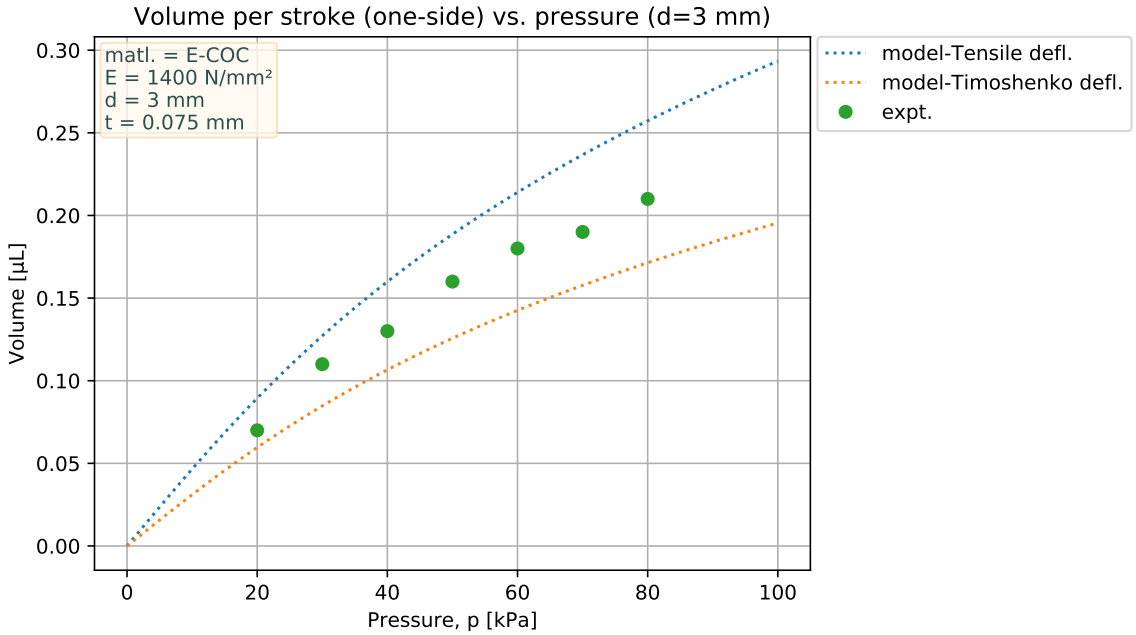

(a) 3 mm chamber diameter, 0.15 mm depth

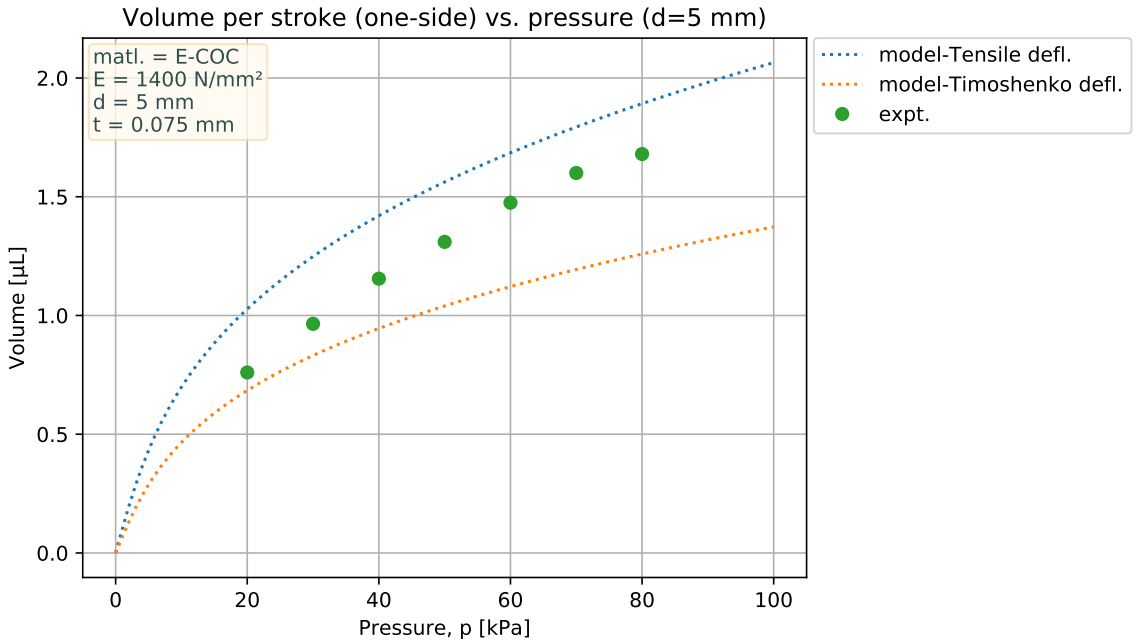

(b) 5 mm chamber diameter, 0.25 mm depth

Figure 2-18: Comparison of experimental data and model for the volume displaced per stroke vs. pressure.
Considering uncertainties of the model and the experiments, the model bounds the displaced volume per stroke reasonably well.

Table 2.3: Parameters of the pump chamber geometries selected for manufacturing. Diaphragm material is COC, of thickness 0.065-0.075 mm.

Dia. (mm)	Height (mm)	Stroke vol. (one-sided) µL	Stroke vol. (two-sided) µL	$P_{wall-contact}$ (kPa)	$F_{diaphragm}$ (mN)
5	0.1	0.65	1.30	10	200
4	0.1	0.42	0.84	25	325
3	0.1	0.24	0.42	75	525

pump chambers. Considering the manufacturing tolerances (± 20 µm) and the modeling uncertainties as described above, this shows that the model reasonably bounds the displaced volume.

2.4 Results and Conclusions

Based on the above analysis, and manufacturing considerations, 3,4, and 5 mm chamber diameters were chosen with a chamber depth of 0.1 mm. The selected configuration is summarized in Table 2.3. The details of the pumps and valves with these diameters, designed for manufacturing, are described in Section 3.6. In operation, as the pressure is increased, the diaphragm deflects and then makes contact with the chamber walls. Further increase in pressure only slightly increases the deflection and consequently, the displaced volume. Therefore, the volume displaced per stroke is almost constant beyond that pressure. The additional pressure gives rise to the back-pressure capability of the pump. A depth of 0.1 mm is chosen as it is almost 1.5 times the diaphragm thickness, within the linear deflection range of the diaphragm and feasible for bonding. Larger depths would require a larger actuation pressure for the diaphragm to make contact with the chamber walls while with shallower chambers the chances for bonding touchdowns increase.

Being able to predict the diaphragm deflection behavior is a essential for the design of pneumatic diaphragm micro-pumps. In this chapter, a model for the diaphragm deflection profile and displaced volumes was developed and the methodology of how to approach such problems was described. It was found that the Timoshenko deflection solution, which incorporates the contributions due to bending and the tensile

stresses, approximates the deflection profile reasonably well. The model was verified using FEA and experiments measuring the displaced volume. The performance considerations of diaphragms for pumping were described. The model developed allows us to speedily ascertain the feasible geometry of the diaphragm and gives a bounding for the displaced volume per stroke. Though not discussed, it was found that the Timoshenko solutions also reasonably predict large deflections for the 0.050 mm polyurethane membrane, which is the deflection case for our existing micropumps [5]. The approach from this work can be used to model a wide range of pneumatically actuated diaphragm deflection scenarios - from small to large deflections. With polymer diaphragms, there can be a significant variation in the physical properties and it is very important to measure the physical parameters, especially the Young's modulus and the yield stress and strain of the actual material sample before they can be fed into the model.

Chapter 3

Injection-molded, single-use pump test blocks

- The work described in this chapter was done jointly with Daniel Rodion Rathbone, an SM student in our lab.

3.1 Introduction

Our existing MPS platforms consist of a fluidic, top-plate layer made of polysulfone and a pneumatic, bottom-plate layer made of acrylic with a 0.050 mm polyurethane membrane sandwiched and clamped in between [2]. The top-plate contains the fluidic channels and fluid-side valve and pump features. The bottom plate contains the pneumatic-side valve and pump features connected to the pneumatic channels.

These pumps require significant time and effort for sterilization and assembly before an experiment. Injection-molded, disposable platforms can help eliminate the need for sterilization and drastically reduce the setup time and effort. The change in the materials involved and the manufacturing process, require changes in the pump and valve geometries. For example, using stiffer Cyclic Olefin Copolymer (COC) diaphragm material requires using larger diameter and shallower depth pump and valve chambers. We design and manufacture a prototype pump test block to evaluate the feasibility of injection molded platforms with on-board pumps (Figure 3-4).

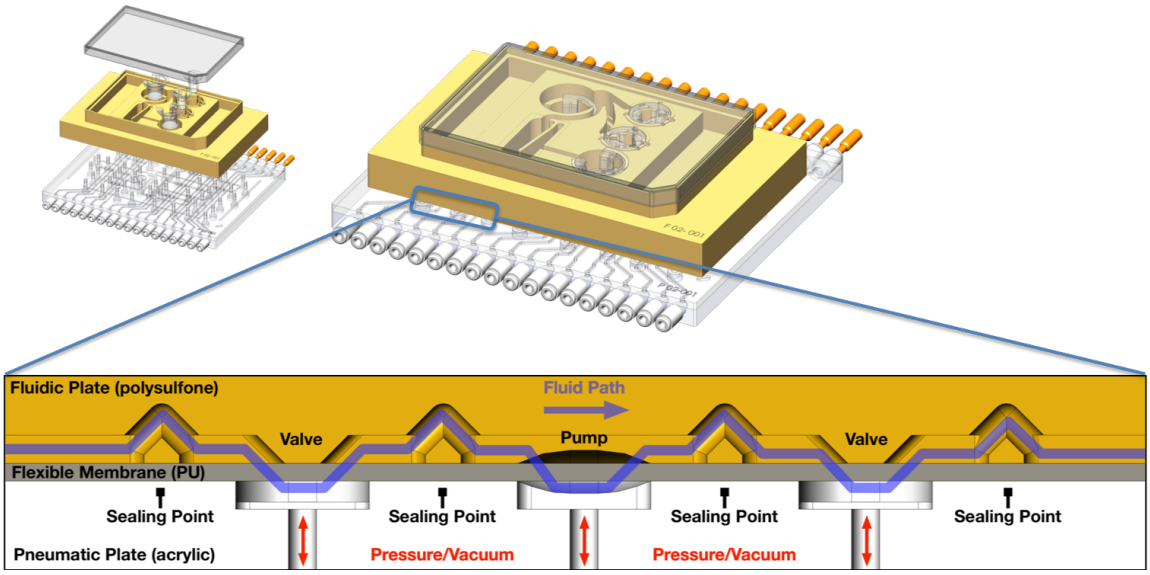

Figure 3-1: Existing platforms - exploded view and cross-section of pumps. Image courtesy of Collin Edington, a Post-Doc in our lab.

This chapter briefly describes the existing pneumatic diaphragm micro-pump. We discuss the motivation for injection-molded, single use platforms. We study the feasibility of injection-molded on-platform pumps by designing a pump test block with 9 lanes of pump and valve variants (Figure 3-4) . We describe the design considerations and details of the pump and valve geometries. Two versions are manufactured: (1) fully integrated platform with pneumatic actuation, and (2) just the membrane bonded to the fluidic top plate for actuation with the electromagnetic (EM) actuator described in Chapter 5. The manufacturing and testing of these plates are in progress. Preliminary valve sealing tests of the EM actuator with the membrane bonded plates show encouraging results.

3.2 Existing pneumatic diaphragm micro-pumps

As shown in Figure 3-1, the pneumatic diaphragm micro-pump consists of three linked valve-pump-valve features. These pump and valve chambers are interconnected with square cross-section fluidic channels, which run though them and connect the valve and pump chambers and also the whole pump to source and destination points

on the platform. The valve geometry, called the doormat valve, consists of a flat region on the top-plate which provides the sealing area around two fluidic channel ports on the inlet and outlet side of the valve chamber. This geometry was included in the pumps designed by Inman et al. [5]. When the chamber on the bottom-plate side is pneumatically pressurized, the membrane pushes onto the flat region of the valve sealing it closed. When the actuation is changed to vacuum, the valve opens by pulling the membrane towards bottom-plate side, thereby establishing fluidic continuity between the two ports.

A modification of using the *v-cuts* on either side of the valves - between the valve and the pump chamber and the valve and the subsequent fluidic channel is described in [2]. The v-cuts are two 45° holes drilled into the top-plate which join within the material at 90°, creating a continuous conduit for the fluid. The flat surface of the top-plate below the v-cuts acts as a sealing surface for the pneumatic pressure and vacuum such that the pneumatic actuation of a pump or a valve does not travel along the underside of the membrane and thus affect the state of subsequent pumps and valves. Without the v-cuts, a pneumatic actuation in a valve, for example, could affect a nearby pump chamber by the travelling pressure/vacuum signal under the fluid channels by deflection of the membrane.

The fluid channels are of a square cross-section with 0.4 mm sides. The pump chamber consists of an oblong elliptical dome shaped chamber on both top and bottom plates. The diameter (major–1.9 mm, minor–1.5 mm) and depth (0.19 mm) are chosen such that the pump chamber has a stroke volume of 0.5 µL. Volume determinism is established by actuating at a pressure greater than 15-20 kPa, which is the pressure at which the 0.050 mm polyurethane membrane deflects and conforms to the domed chamber walls. The deflection is geometrically bounded such that the deflection, and hence the volume displaced, does not significantly increase on further increase of pressure and vacuum. In operation, these pumps are actuated at a pressure of +40 kPa(g) and vacuum of -40 kPa(g). Therefore, these pumps provide a constant volume per pump stroke up to at-least 15 kPa of back-pressure as is experimentally shown in [5]. Concurrently, these pumps also have the capability of pumping with

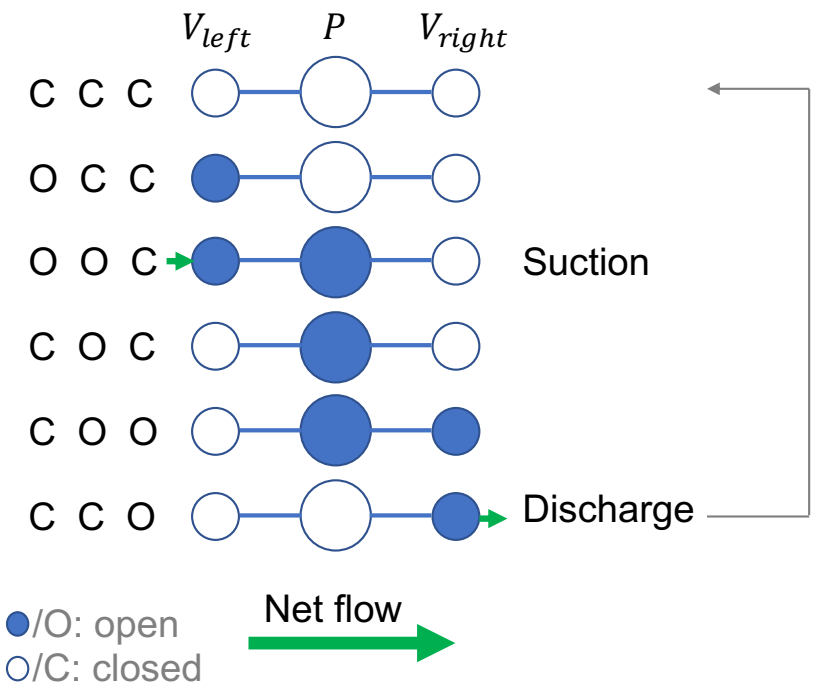

Figure 3-2: 6-step pump sequence for peristaltic diaphragm pumps with active valves. This sequence causes fluid flow in direction of valve-left to valve-right. To reverse the flow, we can reverse the pumping sequence or equivalently switch the states between valve-left and valve-right.

a negative suction head at the inlet of at-least 10-15 kPa. It is important to ensure that the membrane deflection does not seal off the fluid entry or exit into the pump chamber before the entire volume of the chamber can be discharged. For this, a 0.4 mm square cross-section fluid channel runs across the pump chamber in the top-plate and the bottom-plate. These channels also slightly increase the volume displaced with increase in pressure which increases the variance of pump stroke volume.

The diaphragms are actuated in the sequence shown in Figure 3-2 to cause fluid to flow from left to right. Reversing the actuation sequence reverses the flow direction.

3.3 Motivation for injection-molded platforms

On-platform pumping makes these platforms versatile, but also adds complexity in design and usage. Currently, the platforms require careful assembly of the polyurethane membrane sandwiched between the fluidic top-plates and the pneumatic

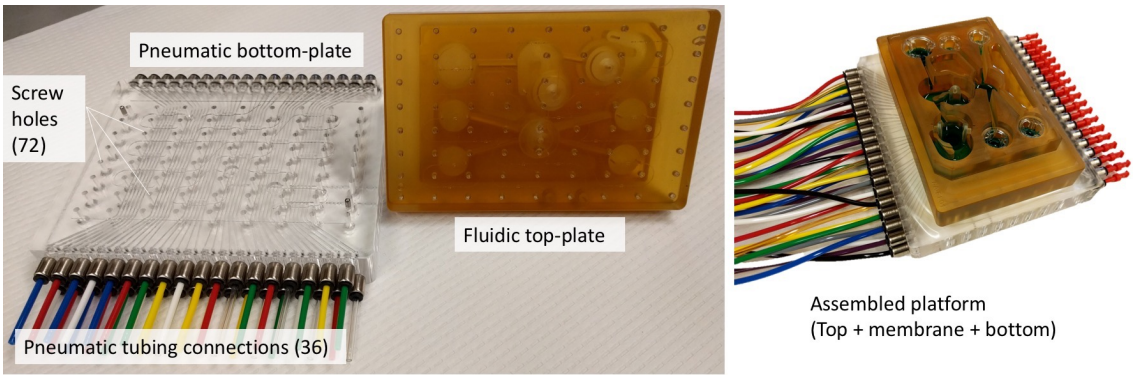

Figure 3-3: Existing platform assembly requires careful assembly of the top and bottom plate with the membrane sandwiched in between. The clamping is by 72 screws. Each pump degree of freedom (dof) requires 3 pneumatic connections and 12 dof on the platform require 36 pneumatic connections.

bottom plates. These platforms require significant effort in setup, which is especially challenging given the sterility requirements during and after assembly. Each pump degree of freedom requires 3 pneumatic connections (1 each for valve, pump and valve). The 7-way platform, which has 7 MPSs on-board, has 12 pump degrees-of-freedom and therefore 36 tubing connections. In addition, the top and bottom plates are clamped together with 72 screws (Figure 3-3). For wider adoption of these platforms by other labs and industry, it is important to reduce the setup and assembly overhead, and also implement reliable sterility.

One solution is the use of injection-molded platforms in which the different layers including the membrane are bonded together, and which are used only once. Injection molding presents a one-time cost of making the mold, which is relatively expensive. After the upfront investment, the additional cost per part is small, provided there are larger numbers of parts used, so as to amortize the mold investment cost. This low cost per part makes these platforms amenable for one-time use. In a typical usage scenario, the single-use platforms arrives sterile, in a sealed package, and the user just needs to remove the platform from the package, plug in the connections and run the platforms. No prior sterilization or assembly steps, which consume significant time and effort, would be required. In addition, with bonded platforms, we can explore the use of better bio-compatible materials. For example, in the existing platforms, we use

a polyurethane membrane as the diaphragm material. Polyurethane is an elastomer and absorbs small molecule, high log-D drugs and is therefore not an ideal material for drug studies with such classes of drugs. Commonly used thermoplastic materials for injection molding such as Cyclic Olefin Co-polymer (COC) are stable and do not significantly interact with such drugs. It is also optically transparent, which allows for easy imaging for biology experiments and for inspection. Therefore, COC was chosen as the material for the injection molded platforms described below.

Another potential benefit of a new design is to achieve improved repeatability of the pumping volume per stroke. Our existing pumps have a variance of about ±10 % in the pumped volume per stroke. One of the major reasons for the variance in pumped volume per per stroke is the manufacturing tolerances of the milling operations, which is on the order of 25-50 µm. This leads to variation in pump chamber geometry and hence to a variance in the stroke volumes, pump to pump on the same platform as well as between platforms. The dimensional tolerances of features in precision injection molding can be as low as 2-5 µm part to part. Therefore, with injection molding, the variation in volume per stroke can potentially be brought down to the order of ±2-5 %.

3.4 Injection molded, single-use platforms

There are significant differences in the design and manufacturing considerations of injection-molded vs. machined platforms. For injection-molded platforms, multiple injection-molded layers are bonded together as opposed to the assembled layers in our present design. The simplest system for diaphragm micro-pumps consists for 4 layers as shown in Figure 3-4 - a fluidic top-plate, a membrane (diaphragm for pumps and valves), a pneumatic bottom plate and a thick bottom cap plate to seal the pneumatic channels. In this configuration, the fluid and pneumatic plates can be molded with relatively simple mold geometries.

The COC membrane material has a Young's modulus of 1500 MPa, which is 2 orders of magnitude greater than the 4 MPa modulus of the polyurethane membrane.

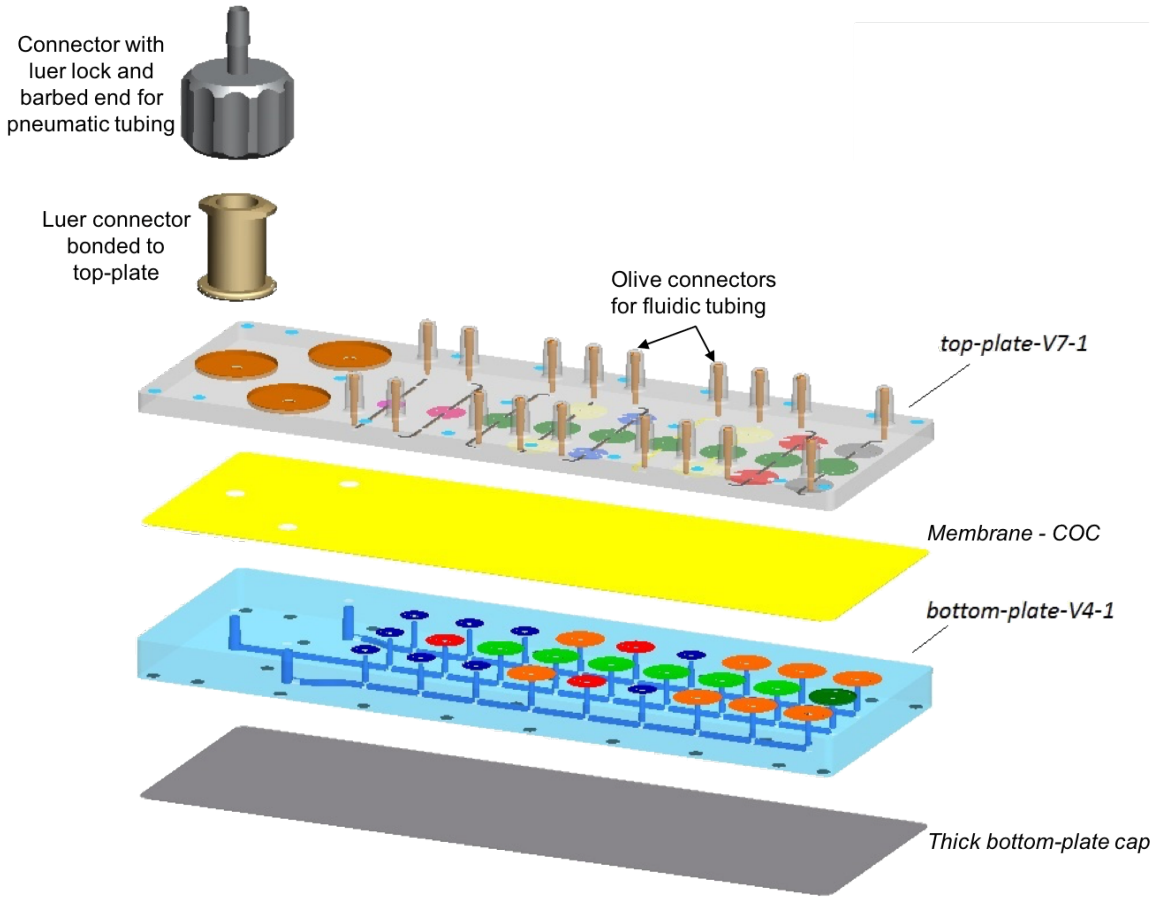

Figure 3-4: Exploded view of the disposable injection molded pump test-block. The top (fluid) plate, membrane, bottom (pneumatic) plate and the thick bottom cap are made of Cyclic Olefin Copolymer (COC). There are 9 lanes of pneumatic diaphragm micro-pumps (valve-pump-valve chambers) with different pump and valve geometries. This pump test-block is designed to demonstrate on-platform pumping and to evaluate feasible pump and valve geometries for future integration with injection-molded MPS platforms. Image by microfluidic ChipShop GmbH, our manufacturing partner for this project.

This much larger stiffness requires changes to the diaphragm diameter and deflection ranges to stay within a reasonable actuation pressure range below 100 kPa(g). We predict the diaphragm deflections using the model developed in Chapter 2. We thus require larger diaphragm diameters and shallower depths for the pump and valve geometries.

For the first prototype, we limit our designs to a single layer each of fluidic and pneumatic plate. An additional fluidic layer, for example, would enable vertical fluid ports for the valves which would then have a more deterministic sealing contour. Every additional layer adds a part that needs to be molded and then aligned and bonded. This increases the cost per platform significantly, although it can provide greater design freedom.

For the manufacturing of these platforms, we worked with microfluidic ChipShop GmbH as our manufacturing partner. In the subsequent sections, we describe the considerations and design of pump and valve geometries suitable for injection-molding.

3.5 Considerations for pneumatic diaphragm micropumps

3.5.1 Valves

For closed valves, the minimum pressure to seal against the sealing lands (P_{min}) should be low enough to give a high back-pressure capability ($P_{back-pressure}$). For an actuation pressure (P_{act}) greater than P_{min}, $P_{back-pressure}$ is defined as,

$$P_{back-pressure} = P_{act} - P_{min}. \tag{3.1}$$

For open valves, the fluidic resistance should be low and the resistance to flow should be negligible compared to the upstream and downstream fluid channels. During the switching between closed and open, valves should minimize the displaced volume as these are seen as pulses in the pump flow profile.

3.5.2 Pumps

For deterministic volume displacement per stroke, the actuation pressure (P_{act}) should be greater than the minimum pressure required to drive the diaphragm deflection into contact with the chamber walls (P_{min}). The back-pressure capability is then also given by Eq. 3.1. The geometry of the chamber walls and the shape taken by the membrane together determine the volume displacement per pump stroke.

Both pumps and valves should avoid situations where the diaphragm deflection can get self-locked. For example, when actuated with vacuum, the diaphragm can seal off the pneumatic port and the diaphragm deflection becomes undetermined. A similar situation can happen if the diaphragm deflection seals off the fluid channel entering the valve or pump chamber. In addition, stiction of the diaphragm with the chamber walls or sealing lands should also be avoided. There should always be regions in the contact region where the fluid (media or air) can displace the diaphragm from such a state when actuated. For *e.g.*, if the diaphragm is stuck to the pneumatic chamber walls when under vacuum, since the pneumatic port is at the bottom of the chamber (Figure 3-9) during the next pressure stroke, the diaphragm can get dislodged again. Stiction depends on the surface properties of the materials in contact and the presence of fluids can modify the stiction forces significantly.

3.5.3 Fluid channels

The fluid channels connect the pump to the source and delivery points, and also between the valves and the pumps. These play an important role in determining pump behavior. During pumping, especially for pulsatile flows, the flow resistance and inertance of the channels can be significant. In addition, the fluid channels hold a certain volume captive that needs to be evacuated before the media introduced at the source point reaches the delivery point. This introduces a time delay in operation which must be taken into account.

3.5.4 Pneumatic actuation system

The pneumatic actuation system can introduce additional dynamics into the system. To switch between pressure and vacuum we use 3 port solenoid switching valves (SMC S070B-6CG) which have a switching time of 5 ms and consume 0.35 W in operation. The pneumatic tubes which connect from the solenoids to the platform act as pneumatic capacitors which introduces some lag between switching of pressure at the solenoid and the pressure being felt at the pneumatic ports of the diaphragms.

In Chapter 5, we describe the design of an EM actuator to actuate the diaphragm for platforms with the diaphragm bonded to the fluidic plate with a single-sided actuation scheme, as an alternative to this pneumatic approach.

3.6 Designs of pump test-block elements

Prediction of the diaphragm deflection for a given actuation pressure is pivotal for effective design of pump and valve features for such diaphragm micro-pumps. The modeling of diaphragm deflection is described in Chapter 2. The subsequent sections describe the design of various elements of the pump test-block.

3.6.1 Connecting channels

At the entrance and exit to the pumps and valves, the channels should be greater than the chamber depth. A smaller channel depth could be sealed off by the membrane, causing self-locking (Figure 3-5). However, deeper channels running across the pump chamber increases the chance of membrane deflection into the channels leading to an uncertainty of the displaced volume and possible membrane damage due to the channel sharp corners. Therefore, we chose a channel depth of 0.1 mm which is the maximum chamber depth of the pumps and valves.

A sufficiently large hydraulic diameter (cross-sectional area/perimeter) leads to a low fluidic resistance. At the same time, the cross-sectional area should be small to minimize the captive volume within the fluid channels. Using the Darcy-Weisbach

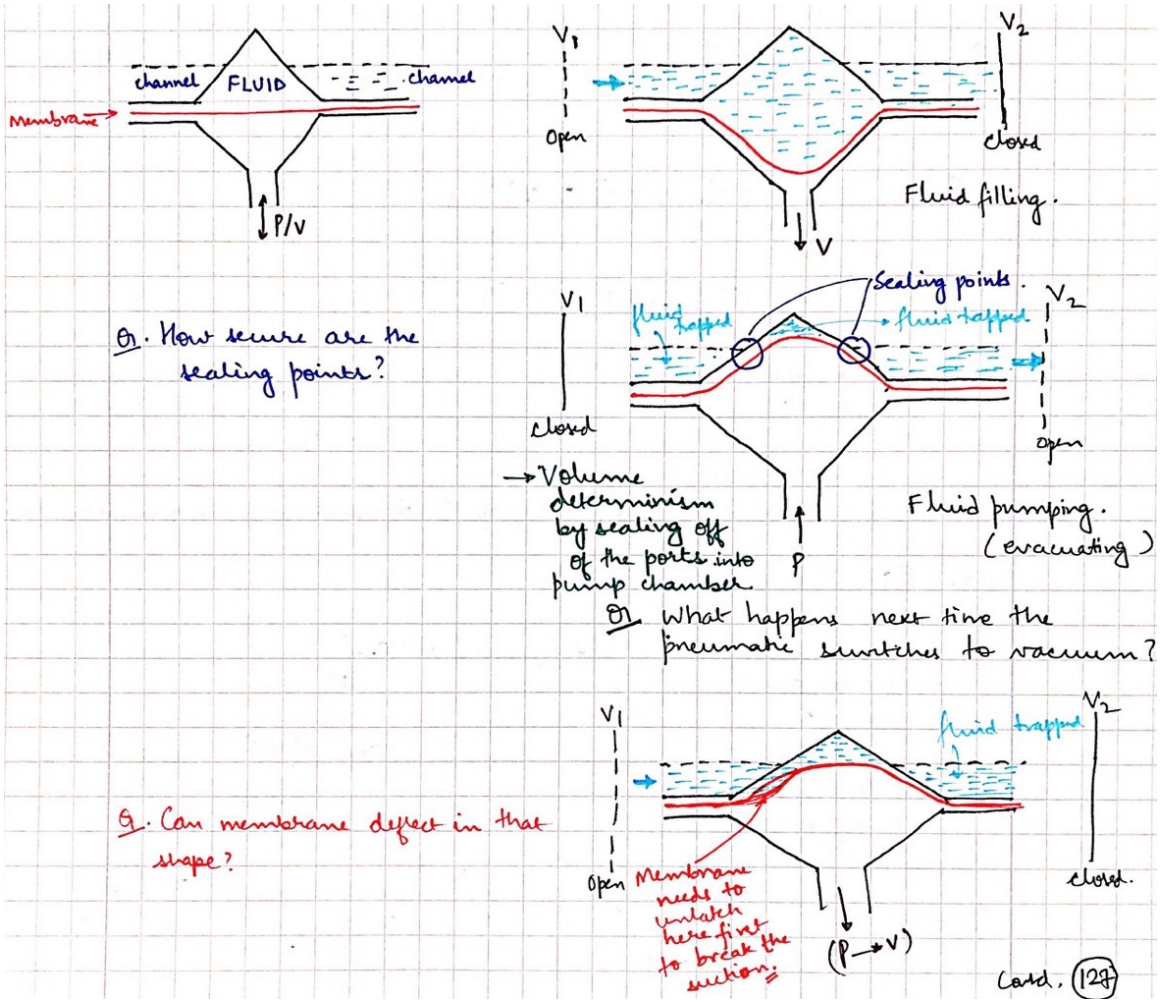

Figure 3-5: Shallower inlet/outlet channels lead to a potential sealing point where the diaphragm can seal of either the entry or the exit to the pump chamber. This can cause non-deterministic fluid volumes per pumping stroke.

equations for flow in a laminar regime, we evaluate the flow resistance for various channel dimensions. We select a fluid channel 0.4 mm wide and 0.1 mm deep. This channel has a fluid pressure drop of 0.03 kPa/mm for a flowrate of 1 µL/s and a captive volume of 0.04 µL/mm.

3.6.2 Valves

Valves should displace minimal volume in operation. When closed, they should seal up to a certain pressure, and when open they should add negligible resistance to the fluid flow path. Since the flow regime is laminar, the flow is viscous-dominated

on the average flow-rate and the flow resistance comes from friction at the walls. In operation, as long as it provides greater cross-sectional area for flow compared to the fluid channel, the relative fluid resistance by the valve should be small. At the same time, we also try to minimize the volume displaced by the valves. Theoretically, the net volume displaced by the valves across a pump cycle is 0. Each valve undergoes a suction and discharge stroke within one pump cycle, pushing or pulling the same amount of fluid each stoke from a side of the pump. In operation, the volume displaced when the valve opens or closes will be seen as a flow pulse. The amplitude of the pulse becomes smaller as the volume displaced by the valve reduces, which is desirable.

For normally closed valve geometries such as the doormat valves, vacuum pulls the diaphragm opening the valve (Figure 3-6 (a), 3-7 (a)). Since the valves do not contribute to the net volume per stroke of the pump, bounding of the diaphragm deflection is not necessary for the valves. In operation, opening the valves such that the cross-sectional area is more than the fluid channel is adequate. Based on these considerations, a 3 mm doormat valve was selected. The spacing between the channels on each side of the valve was selected nominally as the width of the channel, i.e., 0.4 mm. The model, described in Chapter 2 predicts that it requires 25 kPa to deflect the membrane to have the same cross-sectional area as the fluid channel ($0.4 \times 0.1 = 0.04$ mm^2). We nominally actuate at 40 kPa where the deflection would be 0.06 mm and the volume displaced would be 0.2 µL (Table 3.1). Since the diaphragm is bonded on both sides, it does not require additional sealing lands which are facilitated by V-cuts like the machined pumps, as discussed in Section 3.2.

For the normally open geometries such as the mid-wall valves (Figure 3-6 (b)), pressure pushes the diaphragm against the sealing land and closes them. At the neutral position of the diaphragm, they should have cross-sectional area more than than that of the channels. When open, the selected valve dimensions of 4 and 5 mm diameter have a larger cross sectional area than the fluid channels. Table 3.1 compares the volume displaced by various valve configurations. Providing a gentle valve seat curvature is important so that the membrane doesn't have points of high stress concentration. Two variants are designed as shown in Figure 3-8. Mid-wall valve

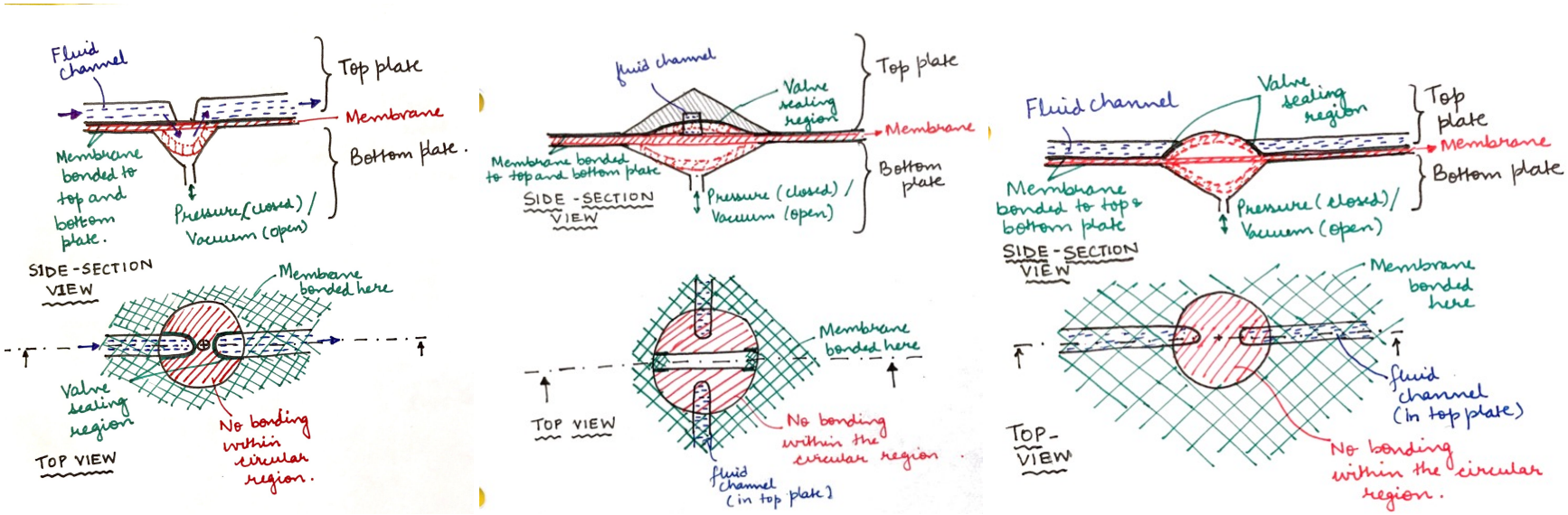

(a) Doormat valve **(b)** Mid-wall valve **(c)** Rounded valve

Figure 3-6: Valve cross-sections showing the various geometries we considered.

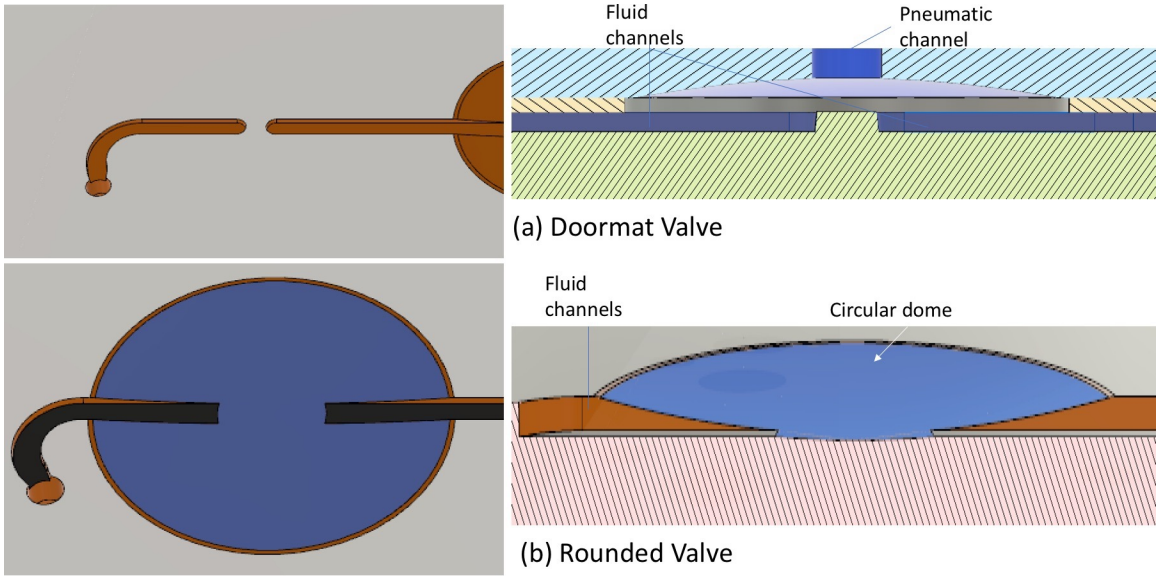

Figure 3-7: Doormat and Round Valve Geometries. Left side shows an isometric view on the fluidic side and the right side shows a vertical section view through the center of the fluid channel.

configurations have a larger volume displaced per stroke, especially for bi-directional pneumatic actuation. This volume can potentially be reduced if we reduce the chamber depth on the pneumatic side. Due to concerns with bonding touchdowns (unintended bonding of the diaphragm with the fluidic plate at the active pump and valve features), the depth was kept at 0.1 mm on the pneumatic side.

The rounded valve geometry (Figure 3-6 (c), 3-7) requires much larger pressures for actuation as the sealing surfaces have a sharper curvature. Therefore a larger

Table 3.1: Valve actuation parameters. The minimum pressures and forces required to actuate the diaphragm to open (doormat) and seal the valves are tabulated. The volume displaced per stroke on each side (F: fluidic side, P: pneumatic side) for a nominal 40 kPa actuation are also given. The doormat valve would be ideal in terms of minimum volume displaced during actuation.

Valve	Dia. [mm]	Height (min.) [mm]	Press. (min.) [kPa]	Force (min.) [N]	$\Delta Vol.$ (one-sided) [µL]	$\Delta Vol.$ (two-sided) [µL]
Doormat	3	0.025	25	200	0.15(P)/0.0(F)	0.15
Midwall	4	0.075	20	250	0.4(P)/0.2(F)	0.60
	5	0.075	10	200	0.6(P)/0.4(F)	1.00

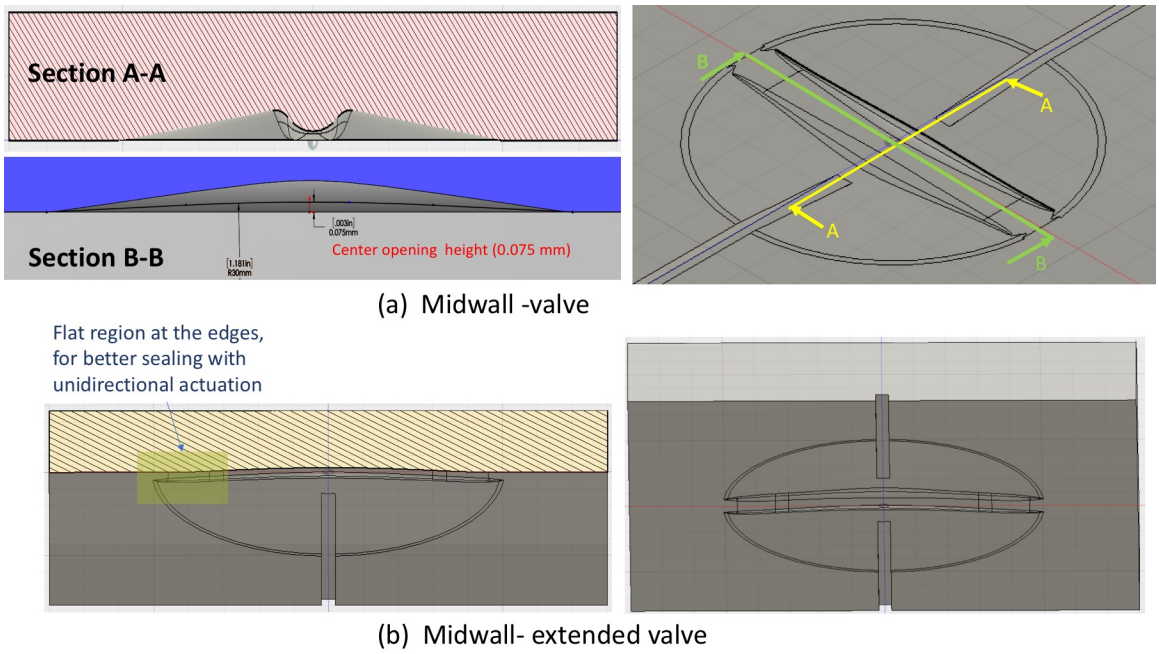

Figure 3-8: Mid-wall valve designs have a central wall containing a sealing land. When under pneumatic pressure, the diaphragm makes contact with the wall and thereby creates a seal. It is important to have gentle curvatures to allow for the diaphragm to make uniform contact with the wall.

diameter, 5 mm was selected with a chamber depth of 0.1 mm.

Manufacturing Considerations

The doormat valve requires masking of the flat sealing-land region of the top-plate during bonding, so that the diaphragm is not bonded at that region and is free to actuate (Figure 3-6 (a)). This is a more complex process and has a higher risk of failure in manufacturing. The mid-wall and the rounded valves have recessed sealing lands which makes it easier to bond the diaphragm to the top plate. Therefore, all the three types of valves were selected for evaluation with the test pump block.

3.6.3 Pumps

The pump designs use a conical chamber geometry which makes the diaphragm have a well-defined contact propagation with the chamber walls and ensures that the diaphragm can never go into a self-locked state. It touches the slant wall of the cone

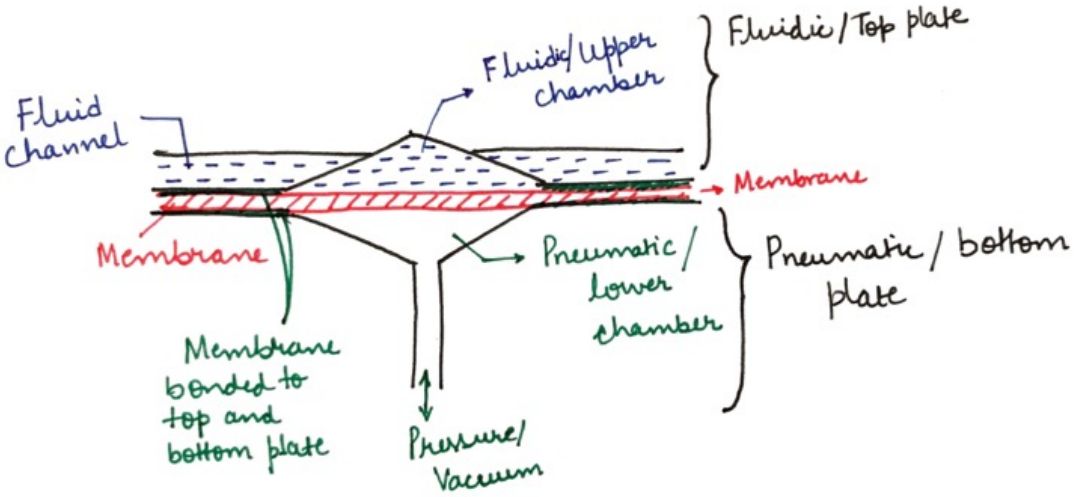

Figure 3-9: Pump chamber cross-section showing the conical chamber shape and the connecting fluidic channels.

Table 3.2: Parameters of the pump chamber geometries selected for manufacturing. Diaphragm material is COC, of thickness 0.065-0.075 mm. Modeling details are in Chapter 2.

Dia. [mm]	Height [mm]	Stroke vol. (one-sided) [µL]	Stroke vol. (two-sided) [µL]	Pressure (wall-contact) [kPa]	Force (wall-contact) [mN]
5	0.1	0.65	1.30	10	200
4	0.1	0.42	0.84	25	325
3	0.1	0.24	0.42	75	525

at first contact. Further deflections bring more of the diaphragm in contact with the walls, with the diaphragm sequentially progressing towards the pneumatic port.

As discussed in Section 2.1.1, as the diaphragm comes in contact with the chamber walls, it becomes much stiffer, and the volume displaced almost saturates. The difference between the actuation pressure and the minimum pressure for contact is approximately the back-pressure capability of the pumping chamber.

To preventing a state of self-locking, the fluid channels which enter the pump chamber have a depth of 0.1 mm. Therefore, there is always a pathway for the fluid to get evacuated, and no fluid can get trapped as shown in Figure 3-5. The COC membrane has a relatively low coefficient of friction with COC and maintains surface

integrity under contact stresses. Therefore, it exhibits low stiction with the chamber walls in operation.

3.7 Integration of pump and valve designs

3.7.1 Manufacturing considerations

Our manufacturing partner, microfluidic ChipShop GmbH has processes well-established for manufacturing of fluidic devices with a footprint of the standard microscopy slide, i.e., 75×25 mm. We adjusted the length of the fluid channels to create a valve-pump-valve triplet within the footprint (Figure 2-1).

For fluid connections, ChipShop has standard connectors called "olives" [15] which are molded in with the rest of the plates. They have a forward taper which is amenable to in-molding (Figure 3-4). For the pneumatic connectors, we bond luer connectors onto the top-plates after molding (Figure 3-4). The luer-connectors cannot be molded-in vertically due to their side projections. A barbed luer-lock connector attaches onto the luer connector and connects to the pneumatic tubing for actuation.

3.7.2 Pump and valve variants on the test pump block

Figure 3-10 shows the variants designed to be tested for manufacturing feasibility and pumping performance. Lanes-1 to 3 test the doormat valves with 3 mm diameter and different pump chamber diameters. Lanes-4, 5 test the mid-wall valves. Lane 6 tests the same configuration as in Lane-3 but with shallower fluid channels connecting them. Lane-7 tests the same configuration as in Lane-4 with shallower fluid channels. Lane-8 tests a slightly modified mid-wall valve in which there is a region with zero slope at the edge of the circle to provide a better stress state to the deflecting diaphragm (Midwall-extended valve, Figure 3-8 (b)). Lane-9 tests a rounded valve geometry with a cylindrical pump chamber which would help visualize the deflection state of the membrane.

All pump chambers, except in Lane-9 are conical with a depth of 0.1 mm and

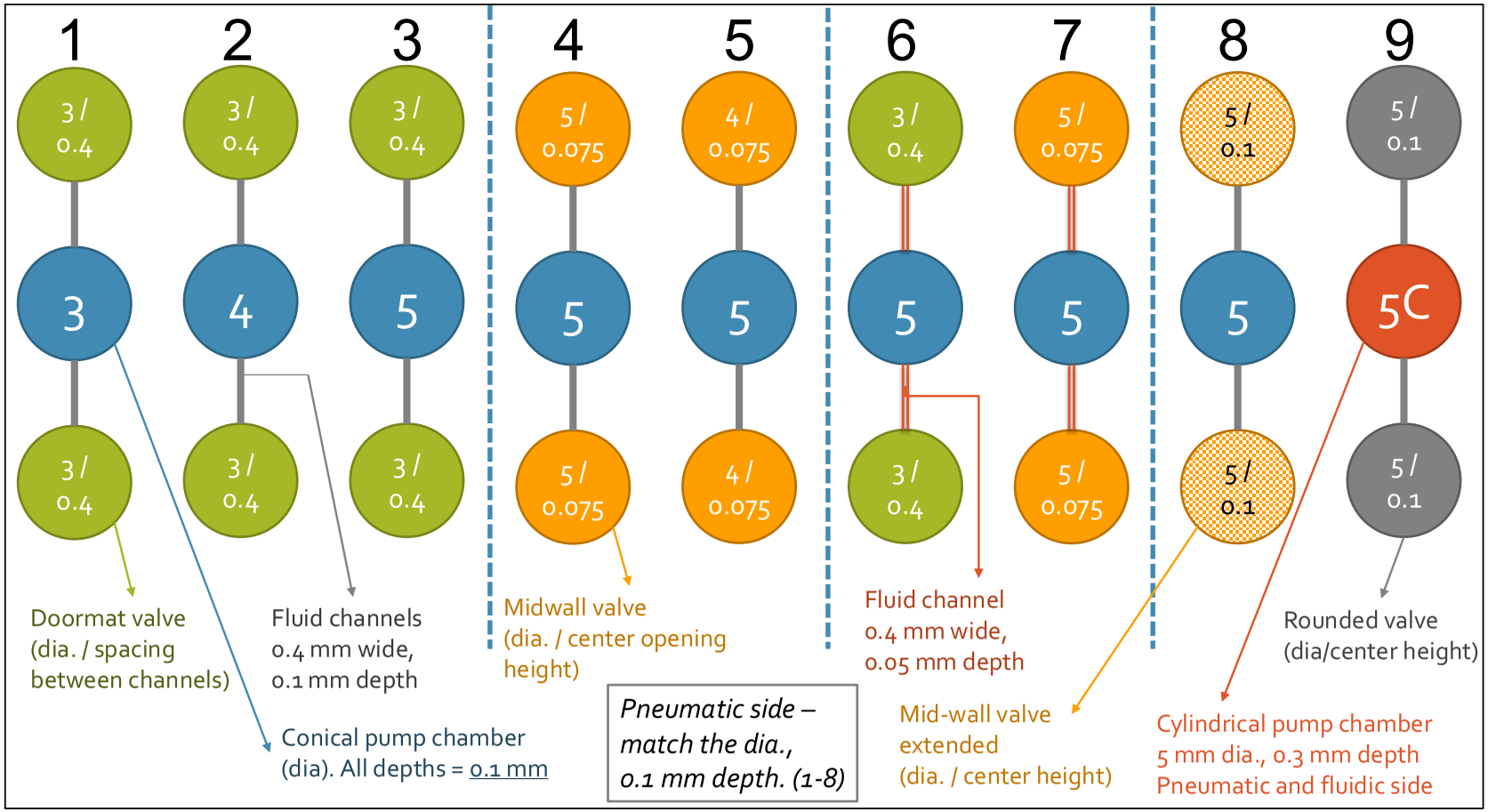

Figure 3-10: Variants of pumps and valves to be evaluated. Each pump lane consists of a sequence of valve-pump-valve.

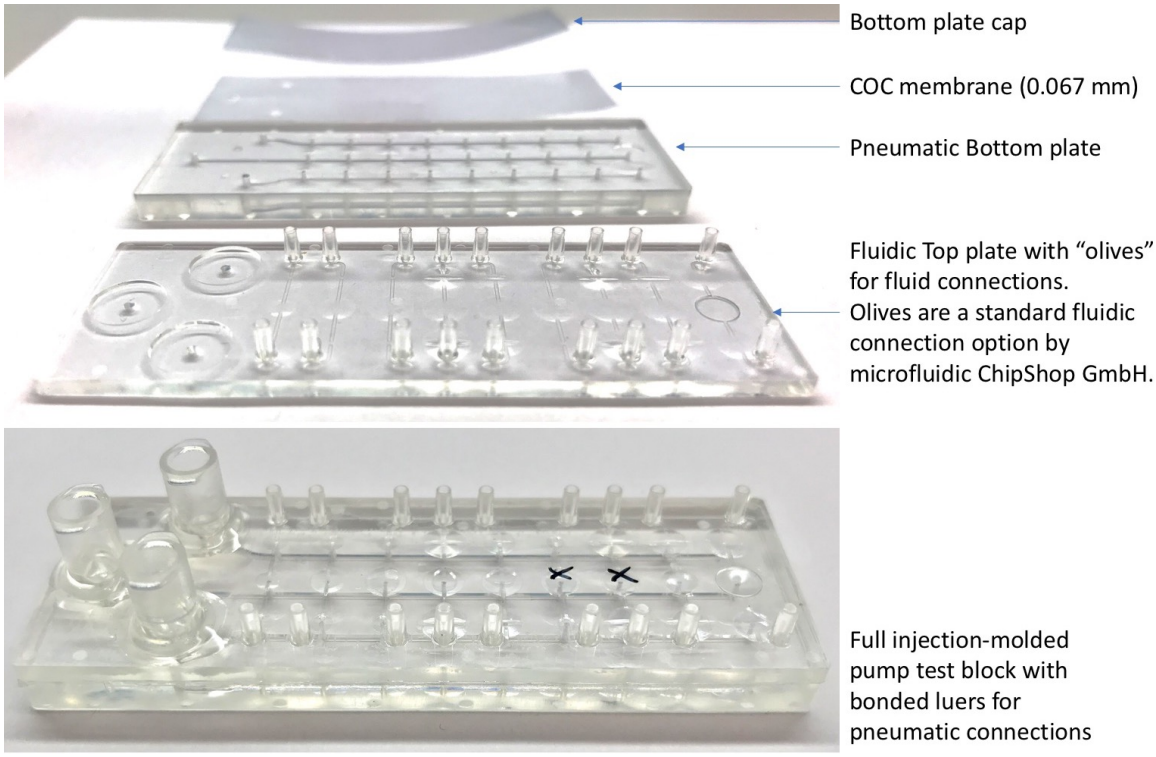

Figure 3-11: Preliminary samples of the manufactured injection-molded platforms manufactured in collaboration with microfluidic ChipShop GmbH.

respective diameters. The shallower fluidic channels in Lane-6, 7 help evaluate if self-locking would be a concern even with stiff diaphragms.

3.8 Manufacturing and testing of injection-molded platforms

The manufacturing of the injection molded platforms is in progress. A few preliminary samples received are shown in Figure 3-11. We faced two major challenges in the bonding process of the platforms,

1. Bonding touchdowns in the shallow pump and valve geometries. These either seal off the valve or pump completely or are bonded at a few points on the pump and valve chambers. Even if the membrane is only bonded at a few points, the diaphragm at the pump and valve chambers do not deflect when actuated with pressure and vacuum.

2. Sealing of pneumatic channels around with the bottom cap. For the pneumatic channels to seal well, the bond around the channels have to be sealed through their length, from the luer connectors to each of the valve and pump chambers. Sealing this large area has been challenging.

The issues in manufacturing are being addressed and we are testing the platforms in tandem.

We also got a few plates manufactured with the membrane bonded to the fluidic top plate to evaluate pumping and valve sealing with electromagnetic actuators (Chapter 5). Preliminary valve sealing and pumping tests have been successful and further testing is under way.

3.9 Conclusions

Injection molded platforms have the potential to significantly reduce platform setup time and effort. This chapter describes the designs of alternate pump and valve geometries which are feasible for injection molding. We evaluate 9 pump variants on a pump test block (Figure 2-1).

Once on-board pumping is proven with these injection molded platforms, we can explore design and manufacturing of mult-organ MPS platforms. There are many injection-molded organs-on-chip devices in the literature and on the market that use external pumping sources to drive flow. On-board pumping provides greater flexibility and design freedom for the MPSes and their interactions and reduced dead volumes associated with external pumps. In addition, with focus in the field on reducing fluid volumes, these manufacturing technologies are suitable for closed volume microfluidics as well. On-board pumping also allows the coupling of open and closed microfluidics on a single platform.

The pump chambers designed with the COC membranes have volumes of about 1 µL. Large volumes displaced create larger pulsations in the flow profile of the pumps. To reduce the volumes, we need to go to smaller diaphragm diameters which will require a more flexible membrane. One option is elastomeric COC, which has a

Young's modulus of 50 MPa. We are exploring options to use elastomeric COC as the membrane material in future designs.

Chapter 4

Pumping designs for MPS platforms

4.1 Introduction

MicroPhysiological Systems (MPS) attempt to mimic the relevant human multi-organ physiology in-vitro.[2]. They have potential applications in drug development and personalized medicine by enabling more accurate testing of physiological drug response earlier in the development cycle. On-platform pumps provide flexibility and greater design freedom and are a key feature of such platforms. One approach to multi-organ MPS platforms has been developed in our lab and uses an open-well system to culture various tissue organs. A common fluid-media circulates between the organs using on-platform pneumatic diaphragm micro-pumps [5]. These pumps require significant effort in setup and depend on external pressure and vacuum sources. An independent, portable pump with low power consumption is desirable.

This chapter reviews the literature in the field and describes pumping concepts and ideas which were considered. We also describe ideas for valve sealing and contact between elements. Sterility considerations make diaphragm pumps attractive and are the focus of our design.

For the new pump, we use diaphragm pumps with active valves. The pumps have a conical geometry and the valves have a mid-wall geometry (Figure 4-9). We develop an electromagnetic (EM) pump to interface with the injection-molded platforms containing the pumps. The platform consists of a Cyclic Olefin Copolymer (COC) fluidic

plate with a bonded COC diaphragm and is described in Chapter 3. The development of the EM actuator and its integration into an EM pump is given in Chapter 5.

4.2 Literature Review

Organs-on-chip are devices with feature sizes ranging from meso to micro-scale and are used to manipulate small fluid volumes to achieve the desired objectives in a wide variety of fields such as biological, chemical, environmental and medical applications.

Over the years, there has been great emphasis on microfluidic devices for organs-on-chip, primarily due to their small footprint, which provides the potential for high throughput and automation [16]. To address these needs, a large variety of microfluidic systems have been developed over the years, both in terms of device development, such as fluid pumping, flow manipulation, fabrication, as well as their applications in various fields.

One of the long-running challenges in this field has been that of micro-fluidic pumping systems [17]. With respect to organs-on-chip, the requirements from such pumping systems are that they should be integrated into the biological systems for ease of use [18], have a low foot-print and be of the same scale as the microfluidic system, be scalable in terms of the volume flow rates required and providing power and controlling the degrees of freedom as the number of pumps are increased. The ability to precisely control flow-rates and flow-profiles [19], be reliable, low power, bio-compatible and of low cost is a huge thrust of one-time use, disposable systems [19].

There are many reviews over the years of microfluidic pumping systems, each with a slightly different emphasis [16, 17, 18, 19, 20]. Of late, there have been reviews focusing specifically on cell culture systems [16]. The selection of pumping techniques for organs-on-chip application is dependent on the integrated application as a whole and in addition to the pump requirements described above, system level considerations such as integration scale, flexibility, and operation independent of human intervention need to be considered.

Pumps can be classified into two main categories, along the lines of classifications in other reviews (Figure 4-1) [17, 18, 19, 20]:

1. Mechanical displacement micro-pumps exert oscillatory or rotational pressure forces on the working fluid through a moving solid-fluid (vibrating diaphragm, peristaltic, rotary pumps), or fluid-fluid boundary (ferrofluid, phase change, gas permeation pumps).

2. Electro-kinetic and magneto-kinetic micropumps provide a direct energy transfer to pumping power and generate constant/steady flows due to the continuous addition of energy (electroosmotic, electrohydrodynamic, magnetohydrodynamic, electrowetting).

At the scale of milli-, and microfluidics, the surface to volume ratio is much larger than that on a macro scale, which leads to high viscous forces and restricts downscaling of well-known macro-scale mechanical pump principles. In addition, surface energy effects can become dominant and need to be considered.[20]

Typically, micropumps have flowrate range from a few µL/s to several mL/s [20]. With these flow rates, most of the micropumps work in the range of Reynolds number from 1-100, and are therefore in a laminar regime.[20]

For pump selection, the major considerations are given below: Good reference charts and tables can be found in [16, 18, 19, 20] :

1. Pump material– the portion of the pump that comes most in contact with the pumped fluid needs to be evaluated in terms of sterility, bio-compatibility and drug absorption. Manufacturing considerations also play a vital role.

2. Mean and maximum flow-rates and flow profiles.

3. Maximum back-pressure the pumps have to pump against

4. Size and scalability (ability to be multiplexed)

5. Bidirectional capability

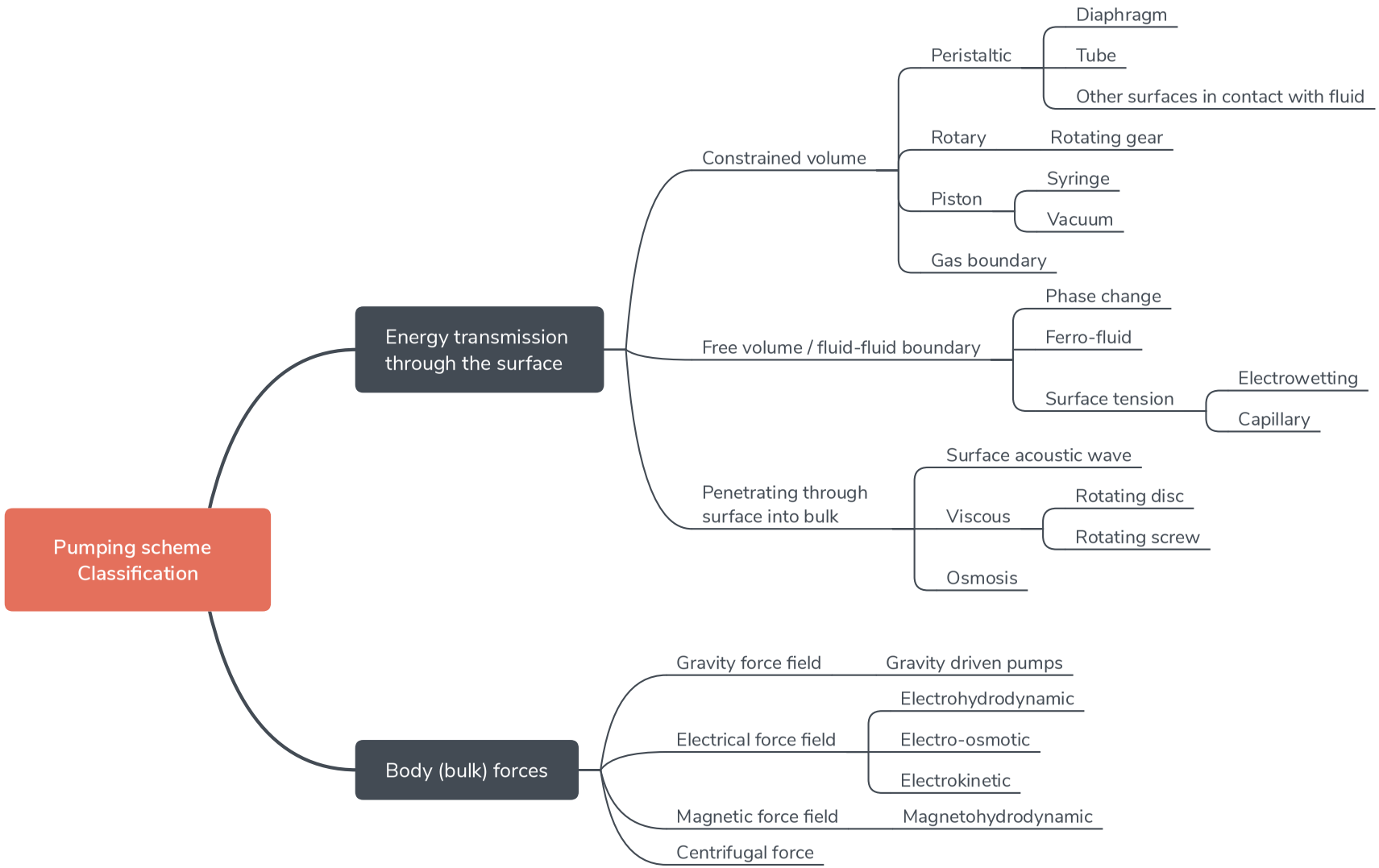

Figure 4-1: Pumping schemes can be divided into: (a) Energy transmission though the surface. The force is applied through the fluid boundary which increases pressure within the fluid or imparts momentum to the fluid; and (b) Energy transmission through body forces. The forces directly act on the bulk of the fluid particles and transfer momentum.

6. Power requirements

7. Media recirculation or single flow-through

8. Other considerations such as clogging, bubble clearance can become important on a case-to-case basis.

There has been considerable progress in the area of pumping systems for organs-on-chips in recent years, but many challenges remain. A continuing area of opportunity and need is the development of active pumps that are user-friendly, compact, have low power requirements, and are capable of producing a wide range of flow rates and flow patterns. There is also a need for integrating various pumping systems with other aspects of system integration such as fluid manipulation, sensing and control, keeping in mind the scaling aspects. As further developments in manufacturing are taking place, there is scope for unique fabrication methodologies that improve current systems and also make new pump types possible.

4.3 Prior work on micro-pumps in our lab

The major focus of the labs work has been on development of pneumatic diaphragm pumps for the MPS platfroms. These pumps are integrated on-platform, provide reliable long-term operation. Recently, for more flexibility to transport liquid through smaller microfluidic systems, a pumping system using commercially available piezoelectric microfluidic pumps have been developed.

4.3.1 Pneumatic actuated diaphragm micropumps

Early work on pneumatic actuated pump was done by Inman et. al. [5], where a polyurethane membrane was sandwiched between a polysulphone fluidic top-plate and an acrylic pneumatic bottom-plate. This pump is discussed in more detail in Section 3.2. An improved version of this pump, with V-cuts for better valve sealing and pump chamber volume of 0.5 µL is used our existing MPS platfoms and is described in [2].

These pumps provide a constant volume per pump stroke up to at-least 15 kPa of back-pressure which is shown experimentally in [5].

4.3.2 Pumping system using commercially microfluidic pumps

Kassis et al., in [21] describe an integrated pumping system that utilizes two commercially available piezoelectric pumps, the Bartels mp6 pumps (Bartels Mikrotechnik GmbH). They present an integrated system, with a Raspberry Pi controller controlling the mp6 pumps and is capable of producing dynamic flow profiles ranging from 1 to 3,000 uL/min. They use this device to replace macro-scale syringe and peristaltic pumps and can be fludically connected to microfluidic chips using flexible tubing. The mp6 pumps have an inversely linear relationship between pressure and volume-flow-rate.

4.4 Motivation for a new pumping system

The pneumatic diaphragm pumps have been used successfully in our lab to demonstrate up to 10-organ interactions and are very versatile. These pumps require significant effort in setup and depend on external pressure and vacuum sources. An independent, portable pump with low power consumption is desirable. Such a portable pump should enable quick setup and deployment and also potentially be more energy efficient.

4.5 Functional requirements of the pumping system

The requirements of on-platform pumps for the MPS systems in our lab are given in Table 4.1.

Table 4.1: Functional requirements for on-platform pumps to transport biological fluids.

Parameter	Value	Description
Flowrate precision	$\leq \pm$ 5 %	Deterministic flow volume against varying back-pressures allows to use the pumps in dosing applications and where precise amounts of fluids need to be transported. In our MPS systems [2], accurate flow control against varying conditions is critical for multi-organ interaction studies.
Flow-rate range	0.001–0.01 (or) 1–5 µL/s	There are two distinct ranges for the flow-rates. The flow from the mixer to various MPS occurs at low flowrates while the perfusion and recirculation occurs at the higher range of flowrates. Low pulsation flow profiles are preferred.
Back-pressure capability	20 kPa	Pump a constant volume flowrate for given actuation condition, up till the back-pressure rating.Back-pressure arises due to resistance from internal channels and destination wells, and the tissue-scaffold support structures. These values are determined experimentally.
Bio-compatibility, and no drug-adsorption	—	Do not modify the physical or chemical properties of the media or cells. All the fluid surfaces that the fluid comes in contact with should be sterile and bio-compatible. Lipophilic (high logD), small molecule drugs should not be adsorbed to maintain accurate low concentrations in the system.
Self-priming, and bubble-tolerant	—	Evacuate air inside and create enough suction to fill with fluid even when started dry. Bubbles should not affect the pump performance.
Energy efficiency, and Bi-directionality of flow	—	For portable systems, energy efficiency should be minimized. Bi-directional pumping is desirable, especially while seeding cells on the tissue scaffolds.
Long-term reliability, and Scalability	—	The platforms run in the incubator for up to 4 weeks at a time and should be capable of multiple such runs at the same performance. They should be small enough to assemble multiple pumps on a single platform.

4.6 Concept exploration of pumping designs

The requirement of sterility places severe restrictions on the types of pumping schemes that can be used. A clear method of containing the biological media and acting through a membrane or directly using body forces seems to be the most feasible path.

Using body forces requires manipulation of a field which can act directly on the fluid at a distance. For contact volume flow-rates under back-pressure, we would still need some form of valving. Therefore diaphragm pumps are considered as they intrinsically have valves in the valve-pump-valve design. A comparison between the characteristics of pumps and valves are given in Table 4.2. Another consideration is the mode of operation as a pump-pump-pump or a valve-pump-valve design, described in Table 4.3. In our design exploration, we mostly consider various details of valve-pump-valve designs.

The figures below detail designs of the pumping system. The captions explain the contents of the figure in greater detail. There are 3 ways a diaphragm can be actuated, as shown in Figure 4-2. Methods by which energy can be transferred to a fluid through a mechanical boundary is described in Figure 4-3. One of the challenges is the bi-directional actuation of the membrane with a mechanical contact, and concept solutions are described in Figure 4-8. We discuss considerations of sealing of clamped membranes in Figure 4-24 and 4-25.

Table 4.2: Pumps and valves have different requirements

	Pumps	Valves
Action time	Controlled motion for low pulsatility while discharge. Suction should be fast.	Fast action for opening and closing.
Displaced volume	Most of the pumped volume per stroke should come from discharge of the pump chamber.	Minimize volume displacements during actuation.
Force	The force required to deflect the diaphragm subtracted from the actuation force is the force into the fluid. Volume determinism required bounding of the pump diaphragm deflection	Force required to deflect the diaphragm till it seals the sealing lands is the minimum actuation force to seal the valve.

Table 4.3: Pump-pump-pump vs. valve-pump-valve configuration of pumping

	Pump-pump-pump	Valve-pump-valve
Design considerations	Multiplexed design requirements. For deterministic volume flow rate, each chamber needs to seal as well as displace significant fluid volume.	Specialized design requirements. For deterministic volume flow rate, valve chambers seal and rectify the flow while pump chambers transfer energy into the fluid.
Manufacture	Relatively easier due to only one chamber profile	More complex manufacturing due to different profile.
Power efficiency	For deterministic volume flow rates, only the volume displaced by the last pump chamber is important. If valves consume lesser energy, then this is less efficient.	Potential for lower power consumption if efficient valves can be designed.

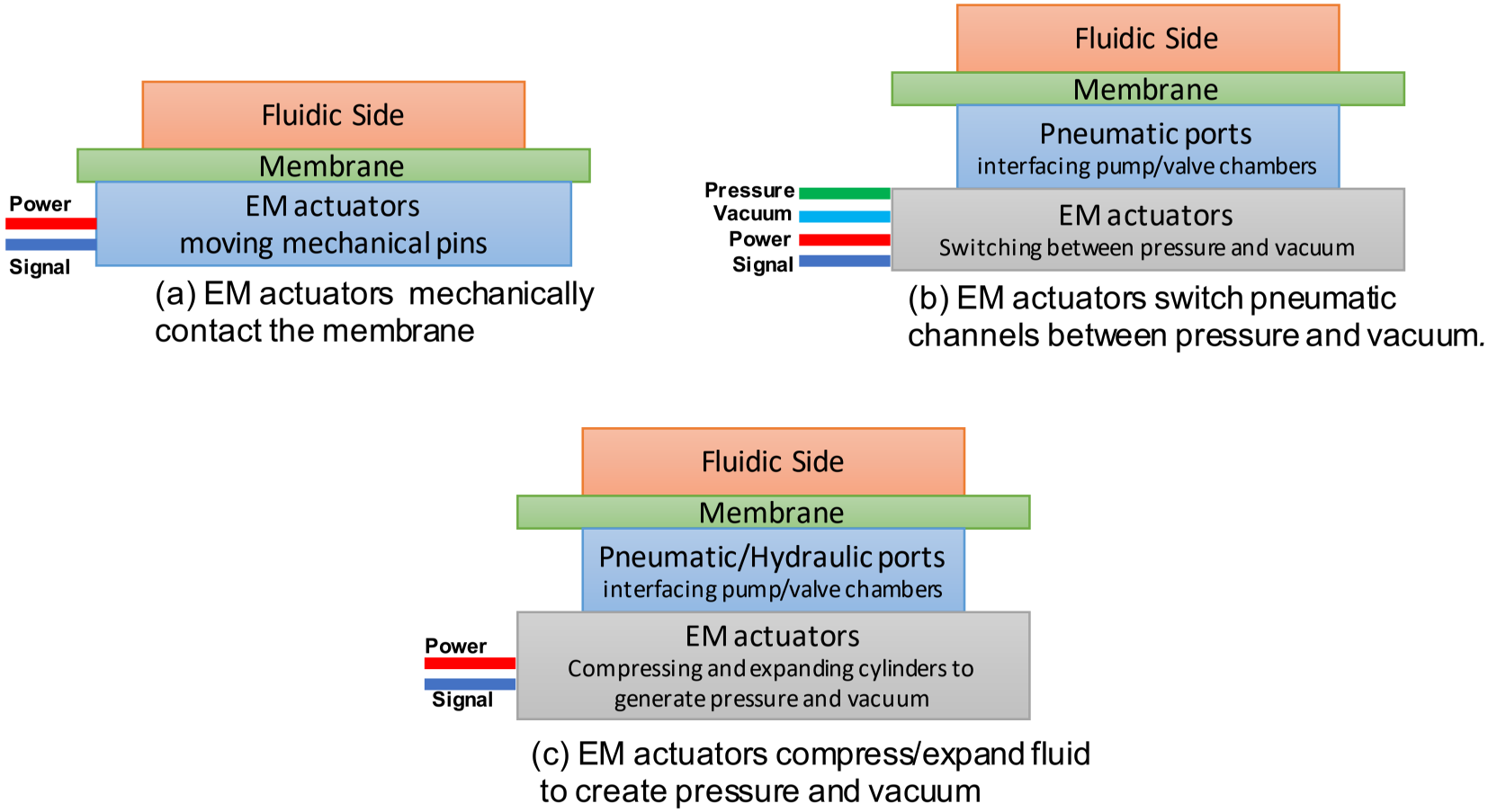

Figure 4-2: Pumping schemes with EM actuators. (a) EM actuators are in mechanical contact with the membrane. Placement of actuators in close proximity can be difficult. (b) EM actuators switch the pneumatic channels between pressure and vacuum. This pressure switching changes the pressure under the membrane and actuates the pump and valve chambers. This is our existing mode of operation in the MPS platforms. The EM actuators can be physically close to or separated from the platform. (c) EM actuators compress/expand an intermediate fluid to create pressure and vacuum. The fluid can be air or hydraulic fluid. The EM actuators can be physically close to or separated from the platform.

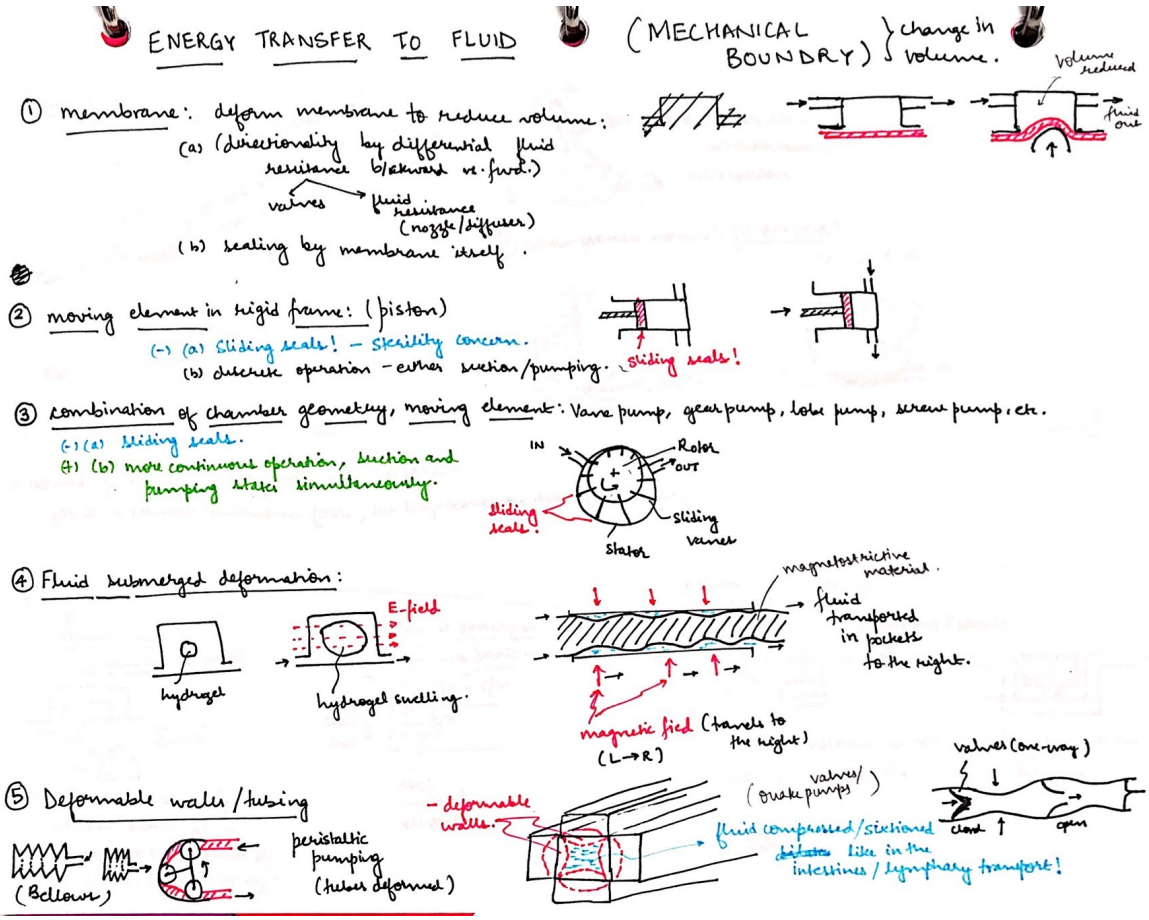

Figure 4-3: Some methods to transfer energy into fluid to cause pumping. The flow is rectified using valves. (1) Through deforming a membrane, (2) Sliding element like a piston, (3) Constrained volume where the chamber geometry moves and at the same time changes shape and size, causing pumping, (4) Deformation of some element submerged in the fluid volume. The element can be activated thermally (bubbles), magnetically (Magnetostritive materials - Magnetic Shape Memory Alloys), or electrically (electroactive polymers) (5) Deformation of walls of the chamber like in peristaltic pumps.

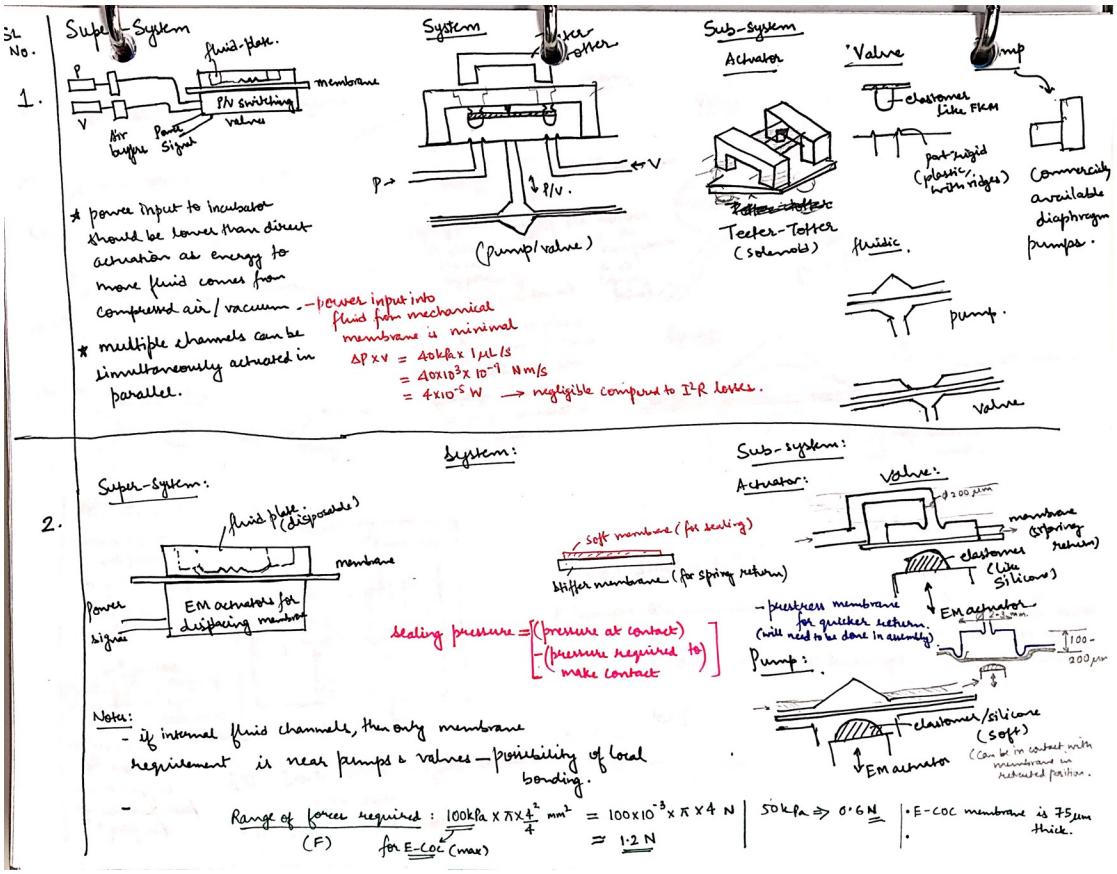

Figure 4-4: Diaphragm pump design concepts.
(Top) The upper half describes diaphragm actuation by switching between pressure and vacuum. Such pumps are currently used in our MPS platforms. An advantage is that the pneumatic channels can be placed with a high density on the platform and one pressure switching actuator can actuate many diaphragms at the same time in parallel. The actuators to switch between pressure and vacuum are commercially available 3-port pneumatic solenoids in the current MPS platforms. These solenoids have a relatively high power consumption and hence are not suitable for operation inside the incubator due to concerns of temperature rise. A solution is the use a bi-stable EM actuator, with low power consumption, to switch between pressure and vacuum.
(Bottom) The lower half describes direct mechanical contact with the membrane to actuate the diaphragm. The membrane makes contact with the sealing lands, closing them. It shows an elastomeric pusher in contact with the diaphragm. A challenge is to restore the diaphragm state after deflection. One way is to rely on the diaphragm stiffness. Other concepts are described in Figure 4-8.

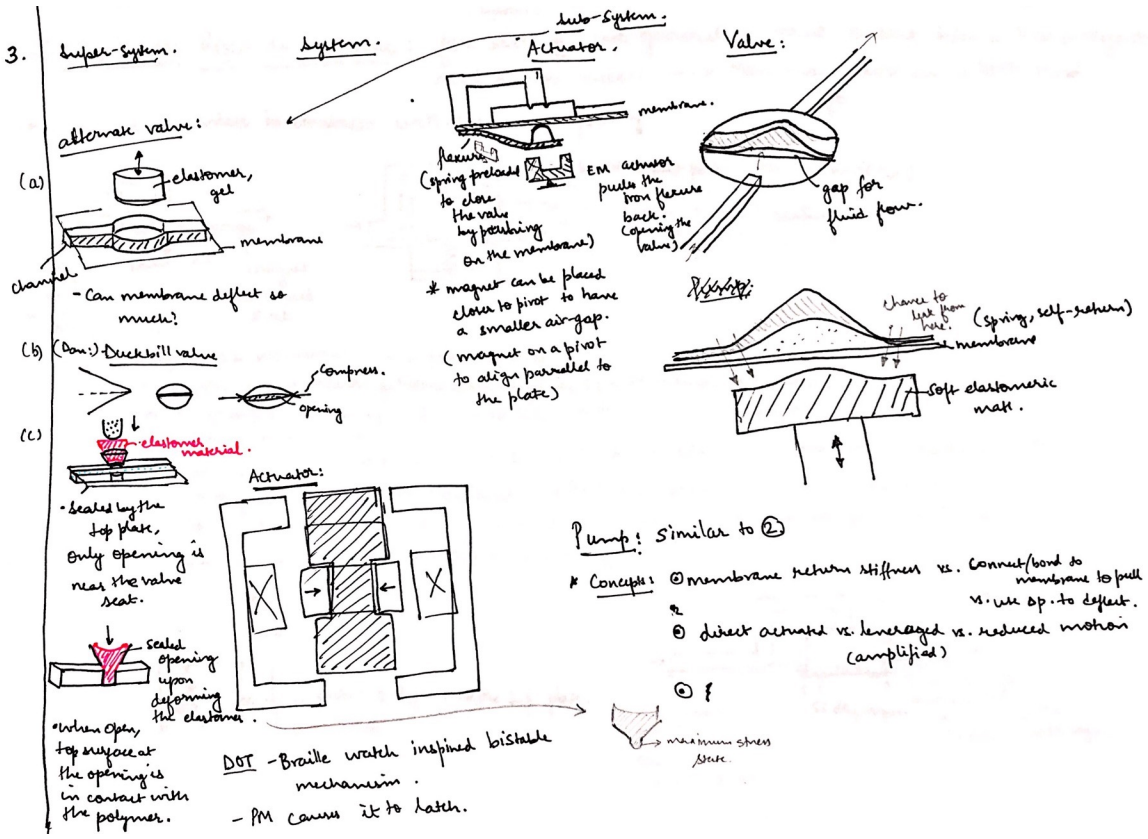

Figure 4-5: Diaphragm pump design concepts. On the left, alternate valve concepts which would not use a membrane are described. (a) Elastomer gel conforming to the cavity and sealing the channel. (b) A duckbill geometry, which is normally closed and opens when actuated. (c) Using an elastomer as a hydraulic piston. Pushing from the top loads the elatomer in a hydrostatic stress state and causes longer deformation at the bottom, sealing the channel. These designs try to address the issue of large volume displaced during actuation of diaphragm valves. A concern is the sealing of the biolgical fluid and material of elastomer in contact with the fluid. The right part of the figure elaborates further on the valve actuation for the valves described in Figure 4-4.

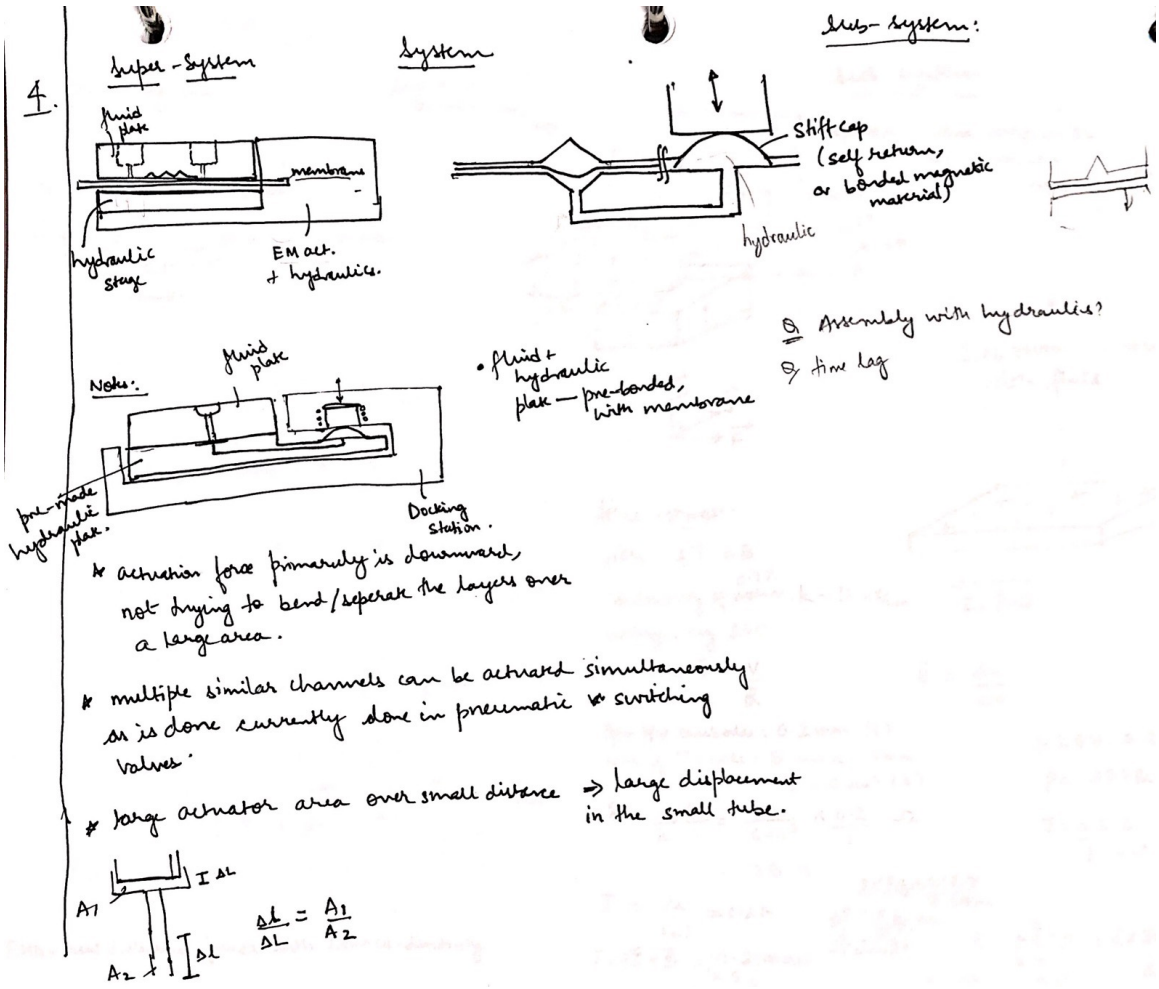

Figure 4-6: Diaphragm pump design concepts. This is a hybrid between the concepts described in Figure 4-4. We use a stiff plastic blister pack which contains hydraulic fluid. The spherical cap is pushed down and pressurizes the hydraulic fluid within the system which actuates the diaphragm at pumps and valves. The return of the diaphragm is by its own stiffness or we can use any of the concepts described in Figure 4-8. A benefit is higher packing density of the pneumatic ports and the actuation of multiple diaphragms in parallel. A challenge is the sealing of hydraulic fluid under pressure.

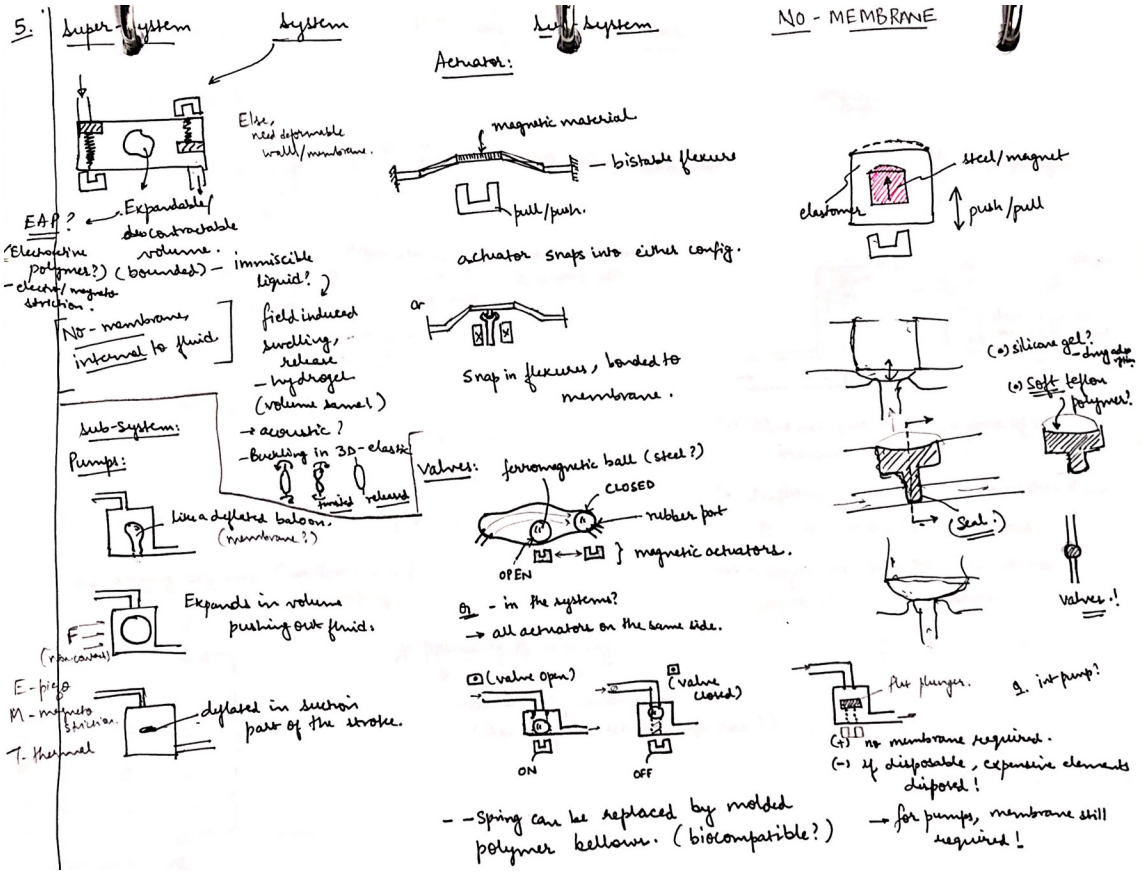

Figure 4-7: Pump design concepts. We explore options of not using a membrane. In the right-most column, a magnetic material embedded in an elastomer can be acted upon from a distance to produce force and deflection in the elastomer. Another way is to push an elastomer in a large area region and amplify that deflection over a smaller area. At the right bottom corner, we show concepts for valve actuation by elements inside the fluid. The left-most column shows a pump using internal elements. A field like temperature, or electric/magnetic field acts at a distance and causes deformation in the pump chamber material. Valves rectify the flow to cause net pumping of fluid volume.

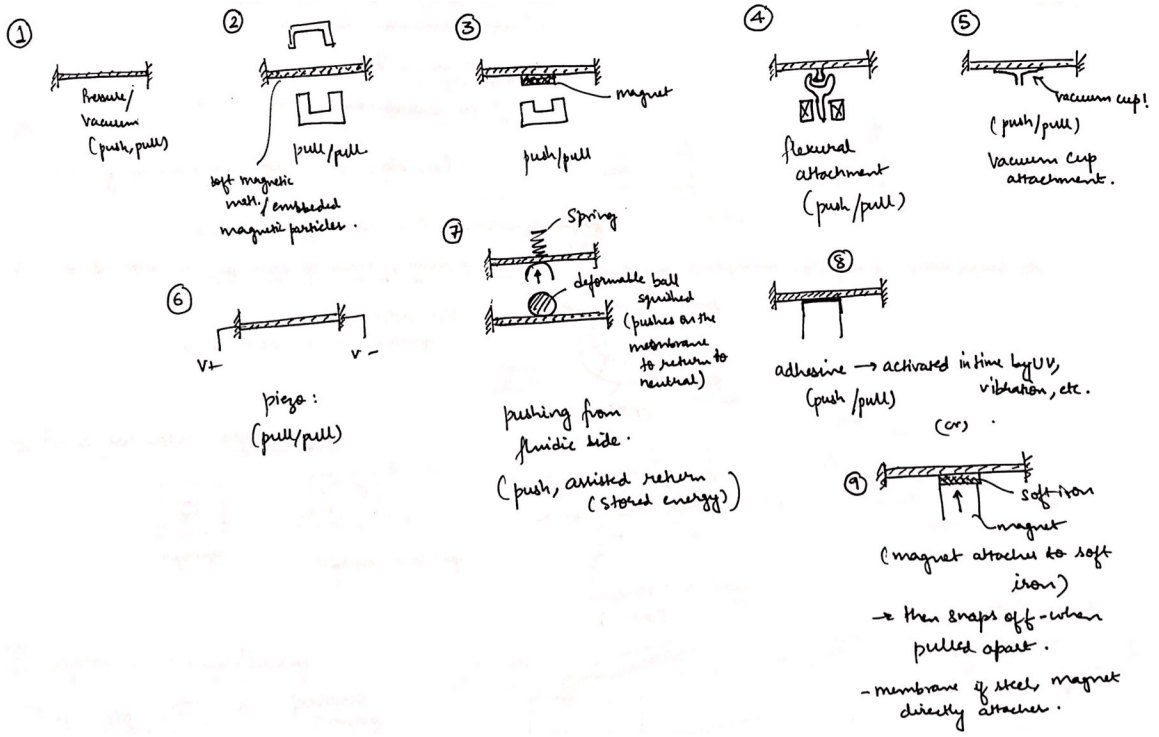

Figure 4-8: Concepts for bidirectional actuation of membrane. (1) Biasing with pressure or vacuum can allow to push or pull the membrane, (2) If the membrane material is magnetic or it is coated or embedded with magnetic particles, a varying electromagnetic field can be used to push or pull on the membrane, (3) Is similar to 2, with magnet attached to the membrane, (4) A clamp clamps onto the holding structure on the membrane and makes the membrane move along with the actuator, (5) A vacuum cup makes a temporary bond with the membrane, (6) Piezo-actuators can actuate in either direction by modulating the sign of the actuation signal, (7) Some spring element placed within the fluidic side stores energy and assists the membrane return, (8) Temporary bonding such as the ones which are activated by UV light could bond the pusher with the membrane, (9) Hybrid between 2, 3, and 4, a soft-magnetic material in the membrane attaches to a permanent magnet on the pusher giving a temporary bond.

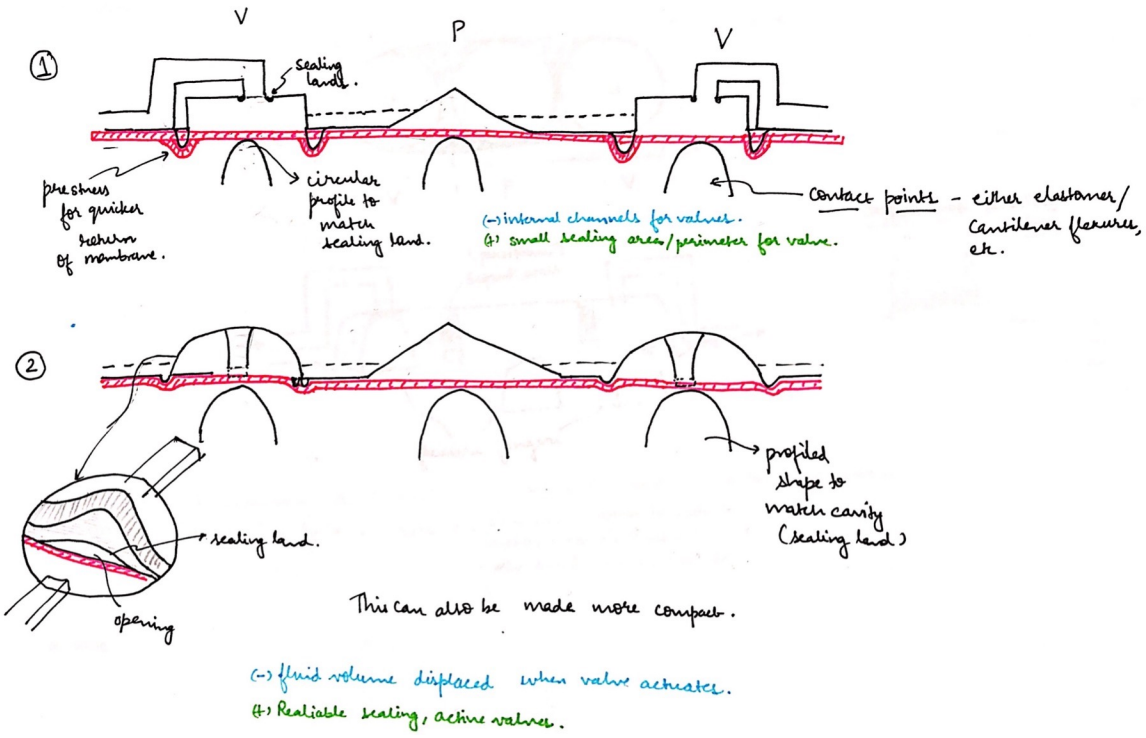

Figure 4-9: Section views of valve and pump features for diaphragm actuation with mechanical contact. Conical pump chamber allows for a progressive, determined deflection front of the membrane. (1) Valve with a fluid port from the top which acts as the sealing surface, (2) Mid-wall valves with a middle wall extending downwards which provides a well-defined region of sealing with lower fluid volume displacement per stroke compared to 1.

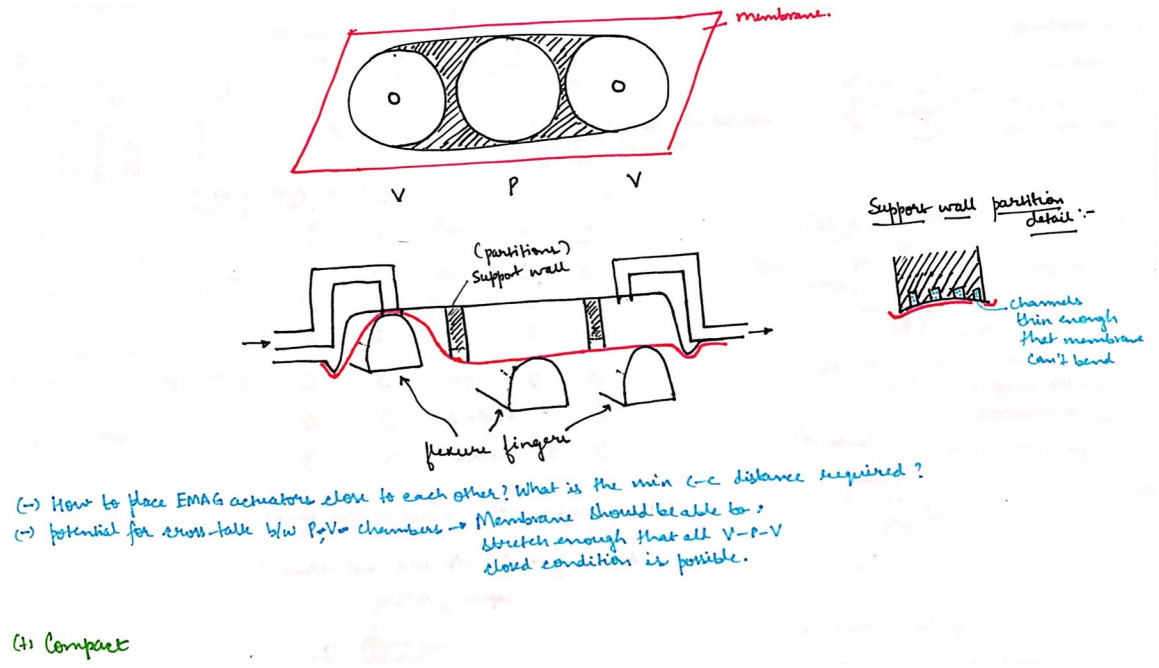

Figure 4-10: A compact embodiment of the pump and valve features shown in Figure 4-9. Instead of fluid channels, there are slots in the walls partitioning the valve and pump chambers which allow fluid flow but also prove a boundary to the membrane during deflection. Placement of actuators so close to each other is however a challenge.

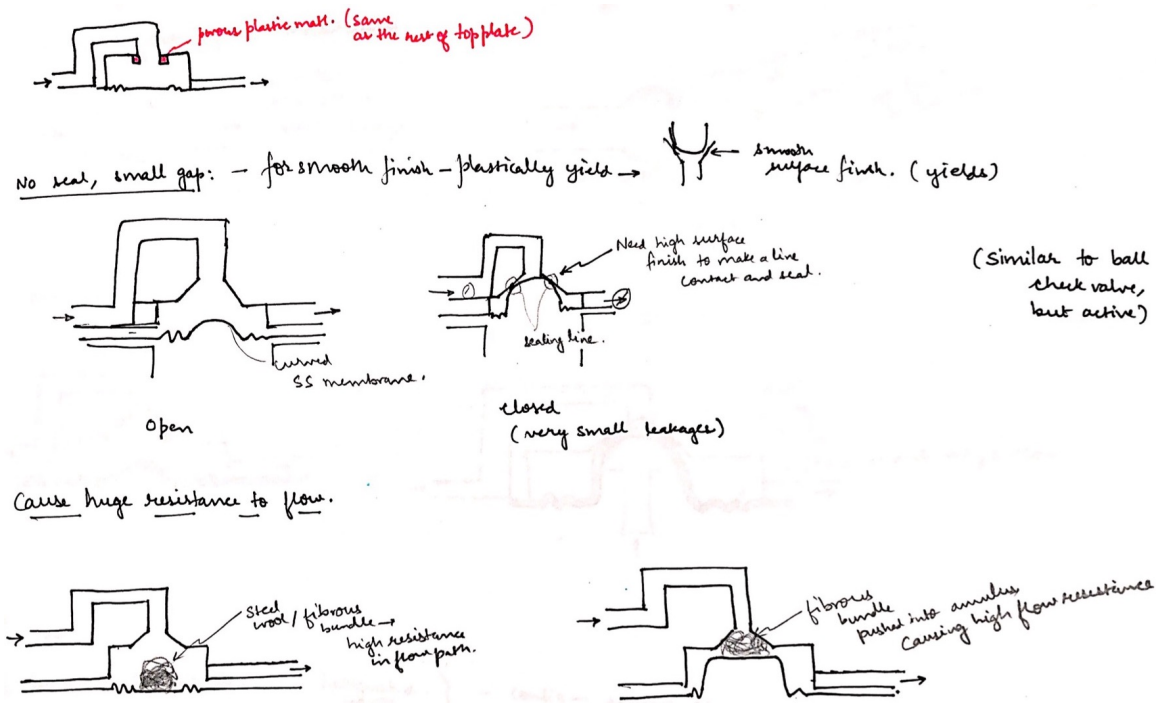

Figure 4-11: Valve concepts. When open, a valve allows free flow of fluid and when closed, seals the fluid flow. Sealing can be accomplished either by contact with sealing lands (top, middle) or by greatly increasing the flow resistance through the valves (bottom). For sealing by local deformation at the contact, a combination of soft and hard material (top) or two smooth surfaces (middle) are ideal.

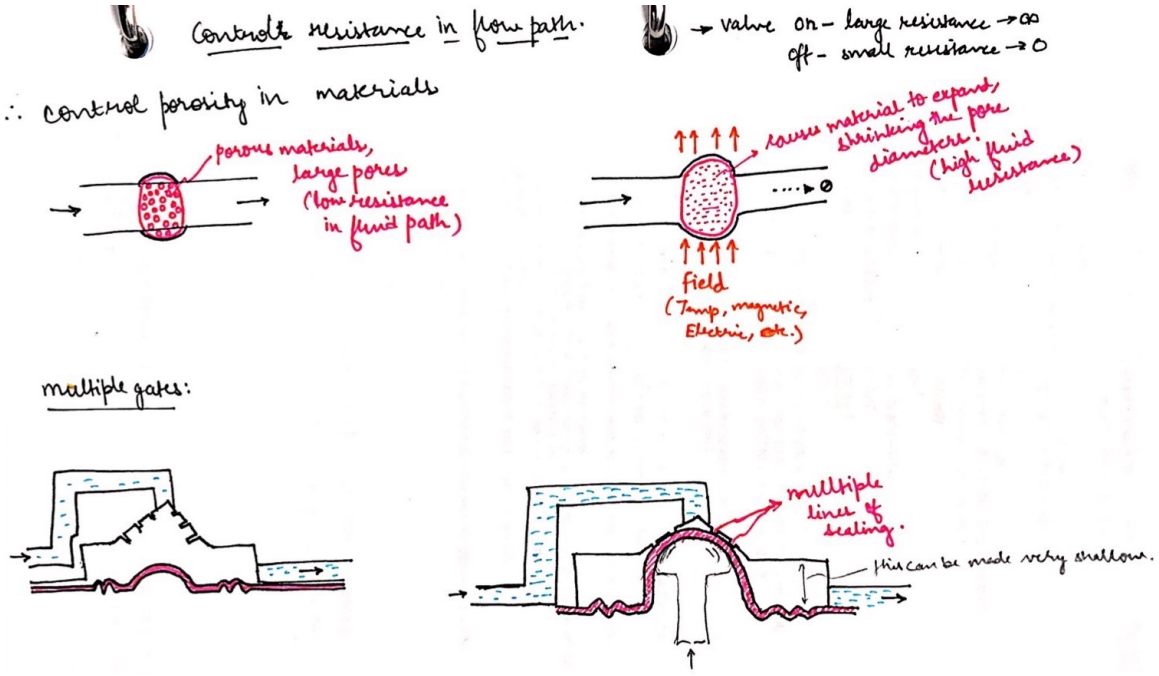

Figure 4-12: Valve concepts.
(Top) A porous material allows fluid to flow through with low resistance. When acted upon by a field, such as temperature or electromagnetic fields, it swells thereby shrinking the pores and the flow-through stops.
(Bottom) Valve sealing with multiple sealing lands. Concentric rings at which the membrane makes contact with the sealing lands, and thus establish valve sealing.

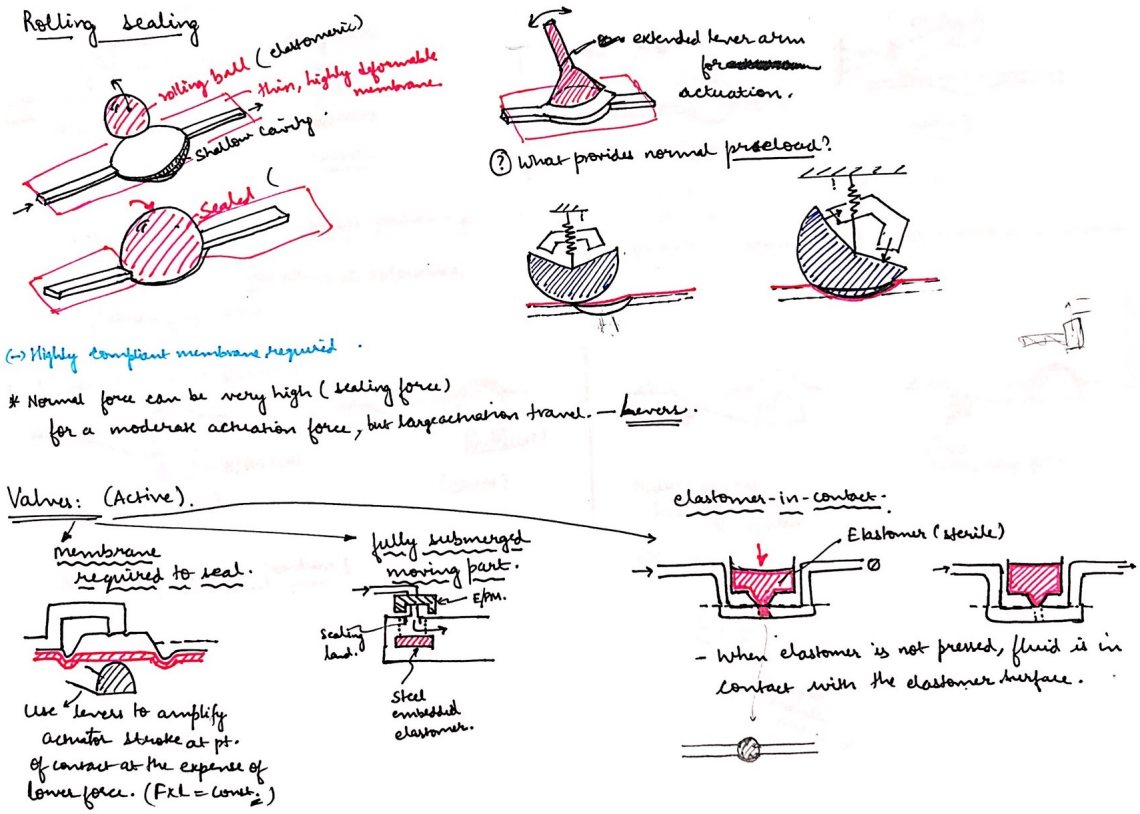

Figure 4-13: Valve concepts. Alternate configurations for the valves.
(Top) The active element rolls into the sealing cavity and seals by pushing the membrane against the sealing lands.
(Bottom) Sealing can be done either through a membrane, some element within the fluid, or by deforming an elastomer.

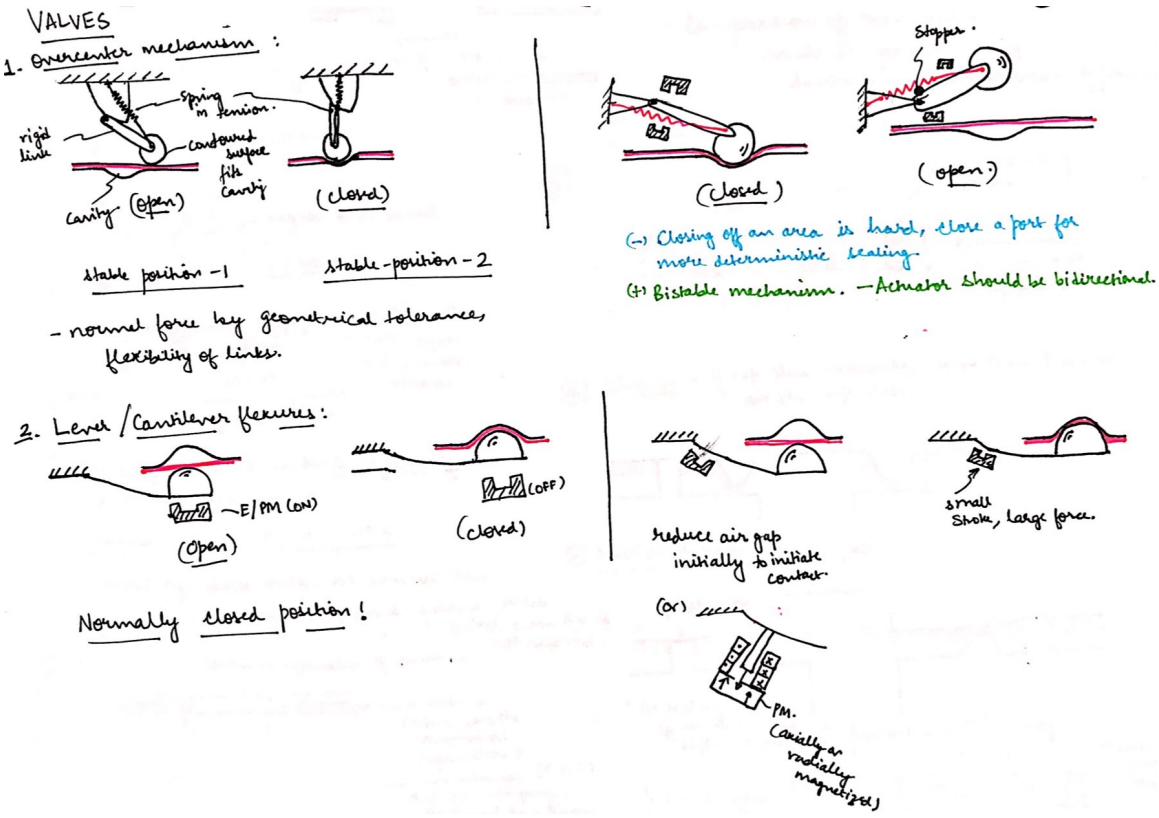

Figure 4-14: Valve concepts.
(Top) For latching of valves, we can potentially use over-center mechanisms which latch into position and which thus only require energy to switch their state.
(Bottom) Stiffness of the metal cantilever flexure pushes the membrane down by default and is pulled up EM force. Latching can either be achieved fluidically as in macroscale pilot valves, or using a coined membrane which flips to either side, or within the actuator mechanism.

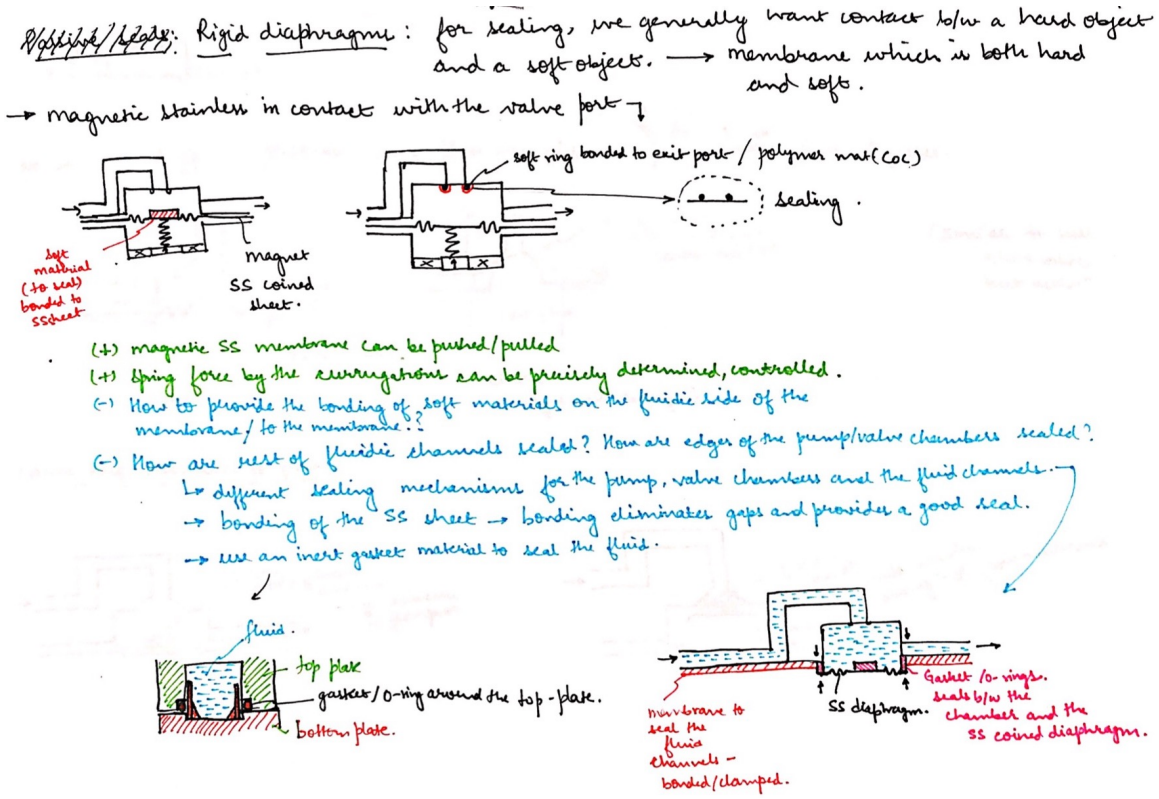

Figure 4-15: Using coined rigid diaphragms has the advantage that the spring force can be precisely determined by the curved sections. However, such diaphragms have significant stiffness at the neutral position as compared to a flat diaphragm. A challenge is fluidic sealing with the fluid channels and the valve and pump chambers. This is potentially addressed by bonding the membrane with the fluidic side or using another softer material (such as a gasket) for sealing and using the diaphragm only for force transmission to the fluid.

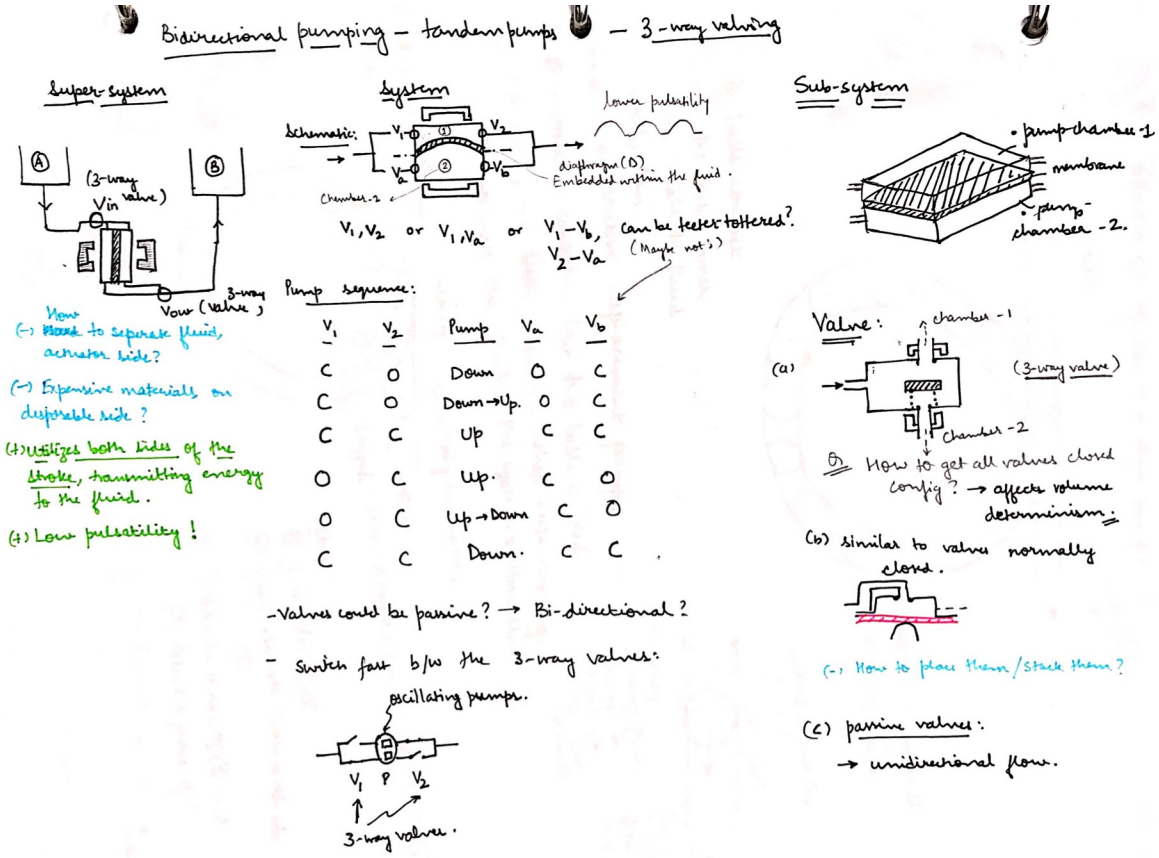

V_1	V_2	Pump	V_a	V_b
C	O	Down	O	C
C	O	Down→Up.	O	C
C	C	Up	C	C
O	C	Up.	C	O
O	C	Up→Down	C	O
C	C	Down.	C	C

Figure 4-16: Tandem pumps in which both directions of the diaphragm actuation are utilized. The valving can be passive (uni-directional flow) or active (bi-directional flow). A benefit is a smoother flow-profile due to tandem operation. During each half of the stroke, one side of the chamber is pumping while the other is in suction. This reduces the gap between subsequent pulses in the flow profile, thereby reducing the overall pulsatility. Material compatibility is however a challenge. Coated piezoelectric diaphragms can potentially be used. Right-most column shows the design of a 3-way valve.

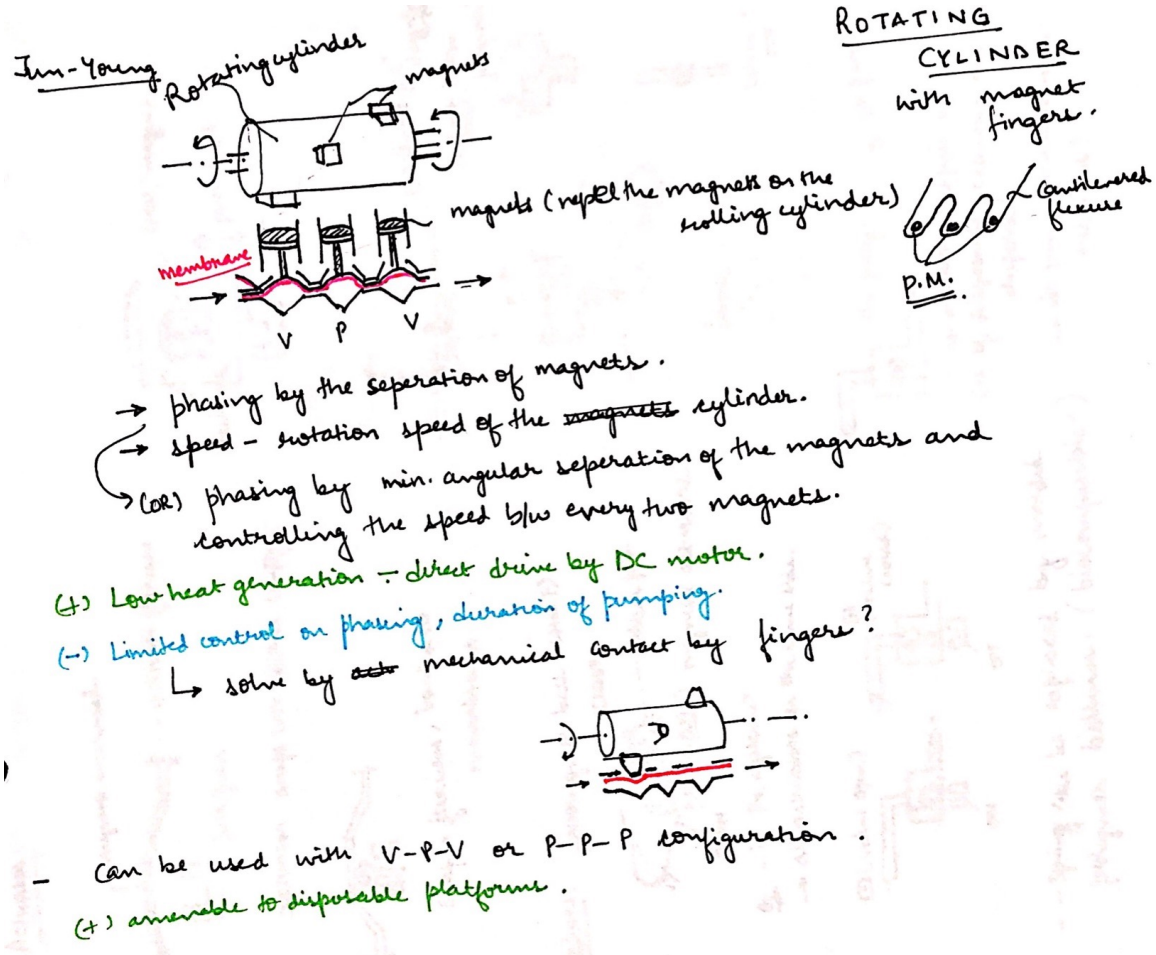

Figure 4-17: Rotating cylinder pump. Motors can be power-efficient, and small motors are commercially available. Force can happen at a distance through magnets or by direct mechanical contact. The actuation frequency of the pump is determined by the rotation speed of the cylinder and the phasing is determined by the relative placement of the magnets and fingers around the circumference.

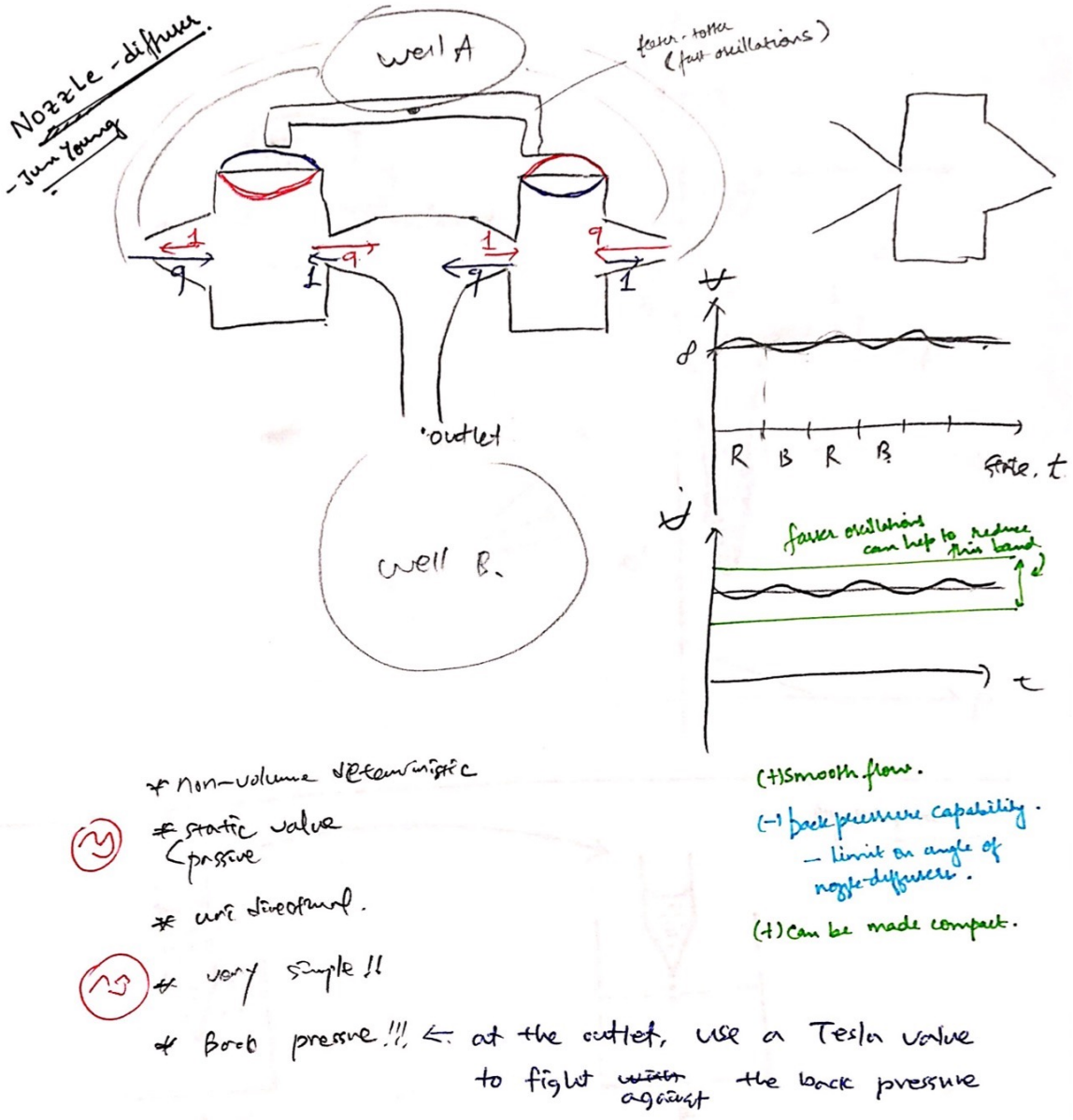

Figure 4-18: A tandem nozzle-diffuser pump. In each stroke of an oscillating actuator, there is net fluid flow at the outlet. This helps reduce the pulsations and the two pump diaphragms are the only active elements. A challenge is that there will always be some back-flow and the volume is non-deterministic. The operation of the pump is uni-directional.

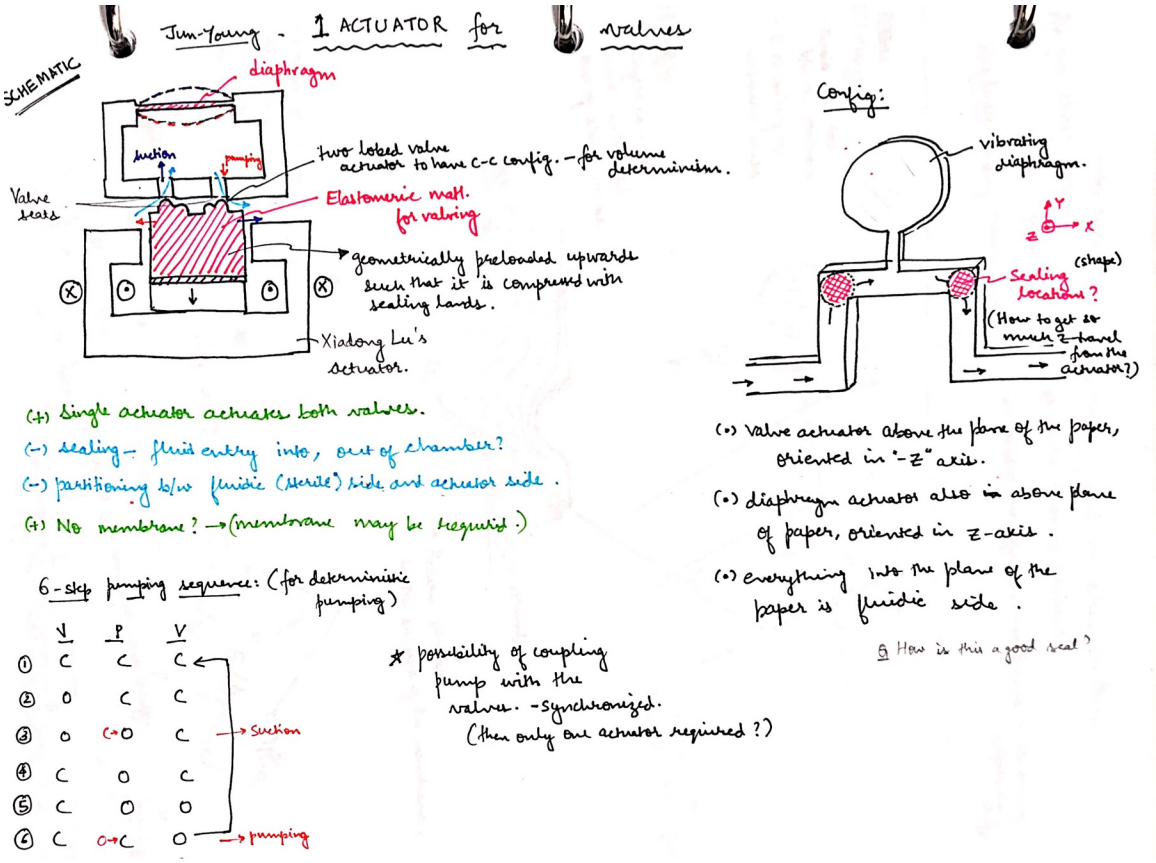

Figure 4-19: Single actuator for sealing both valves. A shaped elastomeric material facing two side-by-side valve ports. When the elastomer is to the left it seals the left valve and opens the right. When the elastomer is to the right, it opens the left valve and closes the right. Figure on the right is an embodiment where the fluid channels and the pump diaphragm are in a plane and the valve sealing actuator described above acts perpendicular to this plane and seals at the sealing locations. The benefit is that it reduces the requirement of the number of actuators. Potentially, the pump can be actuated by a single actuator if the valves and the pump diaphragm can be synchronized. A challenge is the effective sealing of the valves and undetermined valve states when the valve actuator switches state which can cause back-flow.

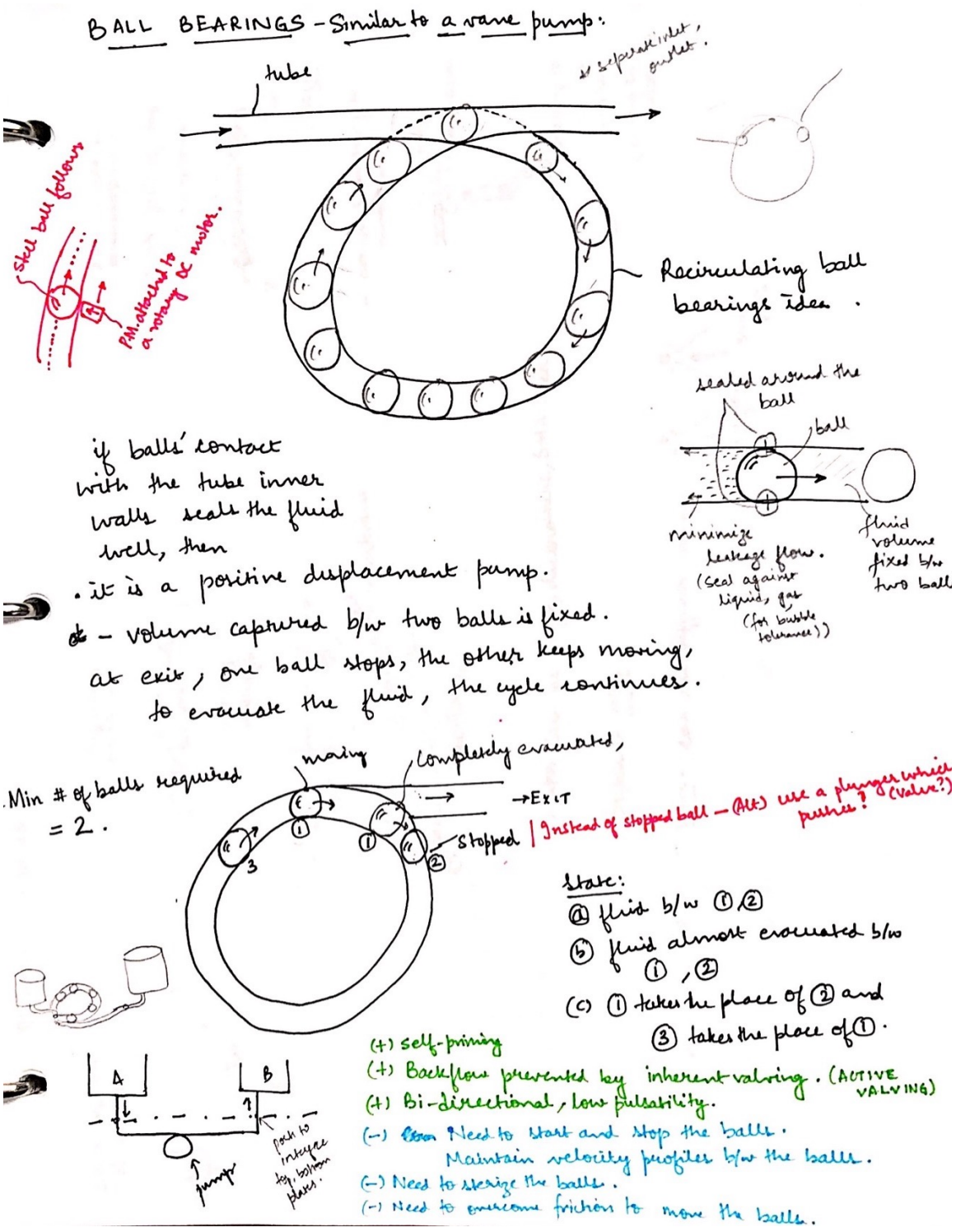

Figure 4-20: A concept for a ball-bearing pump. Volume determinism comes from the fixed spacing between the balls. Benefits are that no valves are required and potentially a single actuator with magnets from the outside can actuate the balls. Sealing is a challenge. One potential solution could be to slightly oversize the balls with respect to the inner diameter of the tubing.

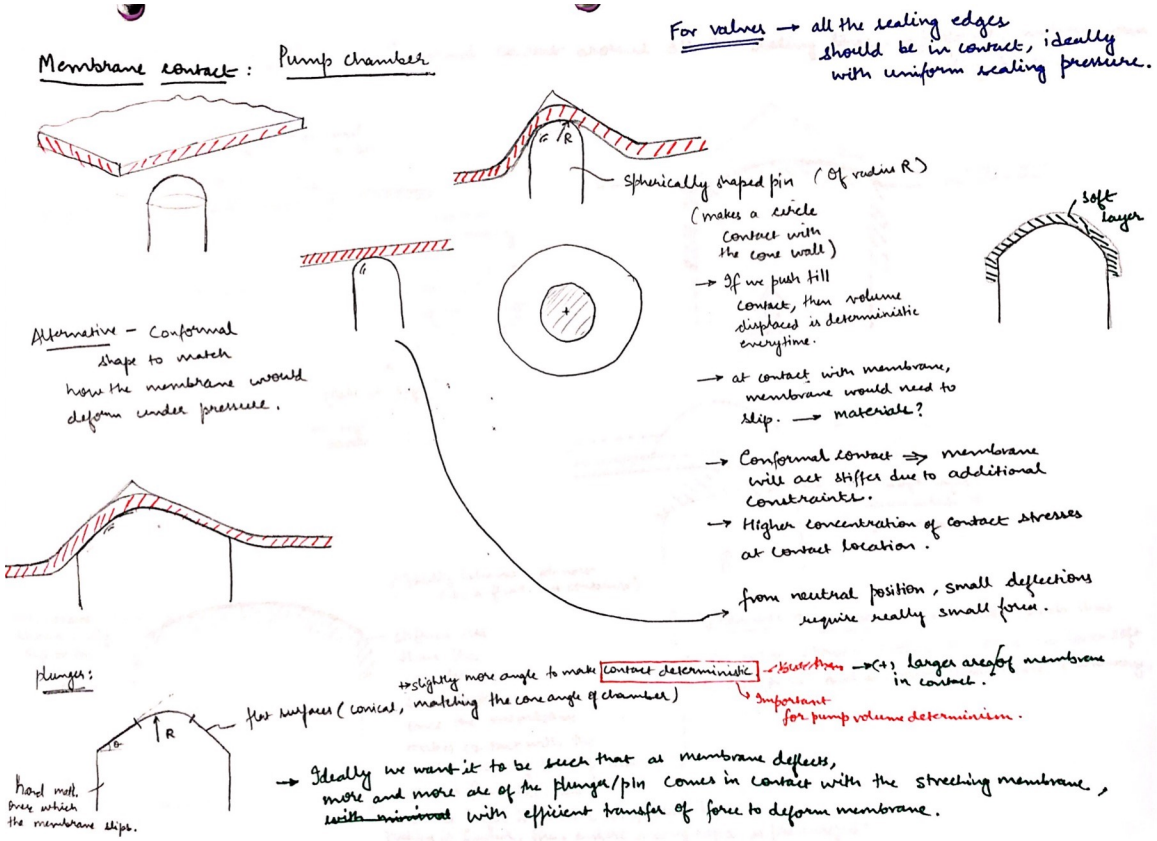

Figure 4-21: Membrane contact - pump chamber. The contact mechanics of the pushing element is an important consideration. A circular shaped pin for the pump geometry such that when the membrane bottoms out, the geometry is well defined, and so is the displaced volume. Stress concentrations at the contact point can be avoided by a thin layer of soft elastomeric material between the pusher and the membrane which gets loaded in a hydro-static stress state and helps distribute the pressure more evenly.

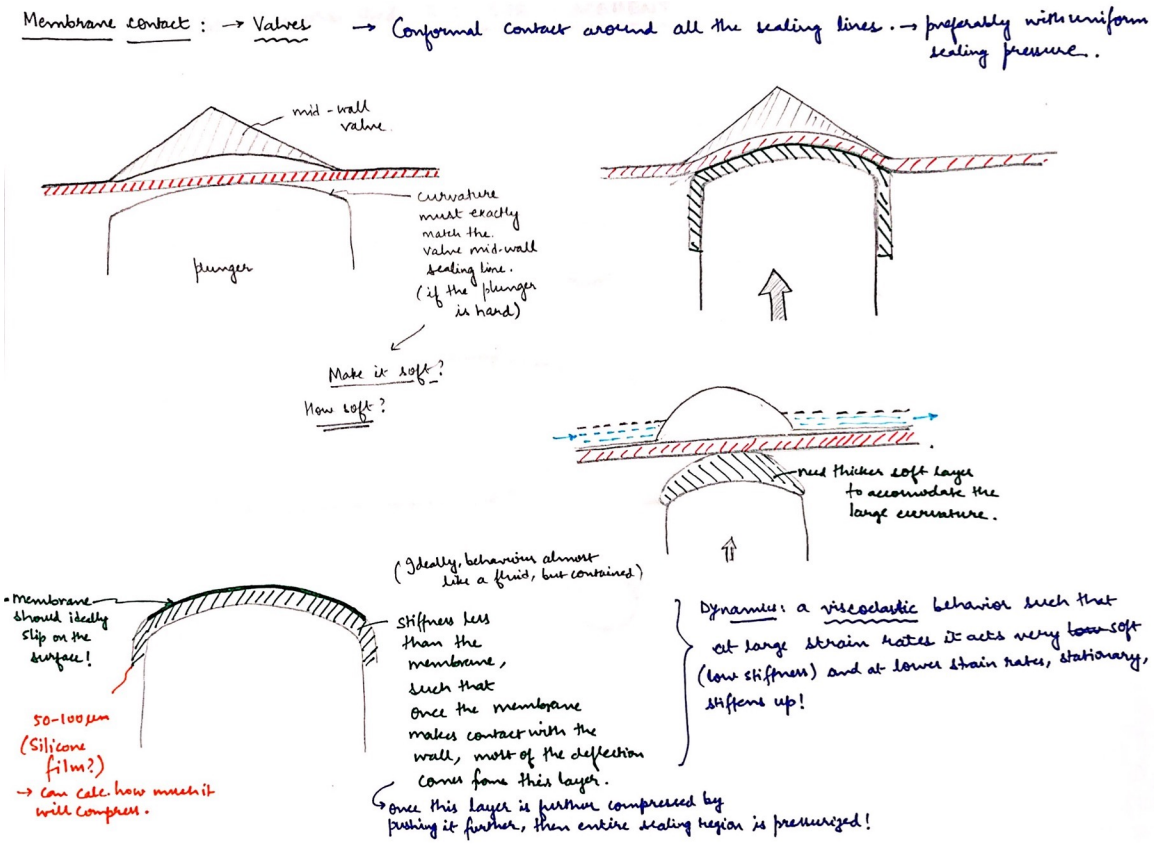

Figure 4-22: Membrane contact - valve chamber. Sealing of valve chambers is potentially more challenging. The membrane needs to make contact with the sealing lands and deform locally at the contact point to seal. For this, ideally, there should be an even pressure from the other side of the membrane pushing towards the sealing lands. This is achieved by placing a relatively thick layer of soft elastomer between the pusher and the membrane. In operation, the elastomer gets loaded in a hydro-static stress state and helps distribute the pressure evenly to cause sealing.

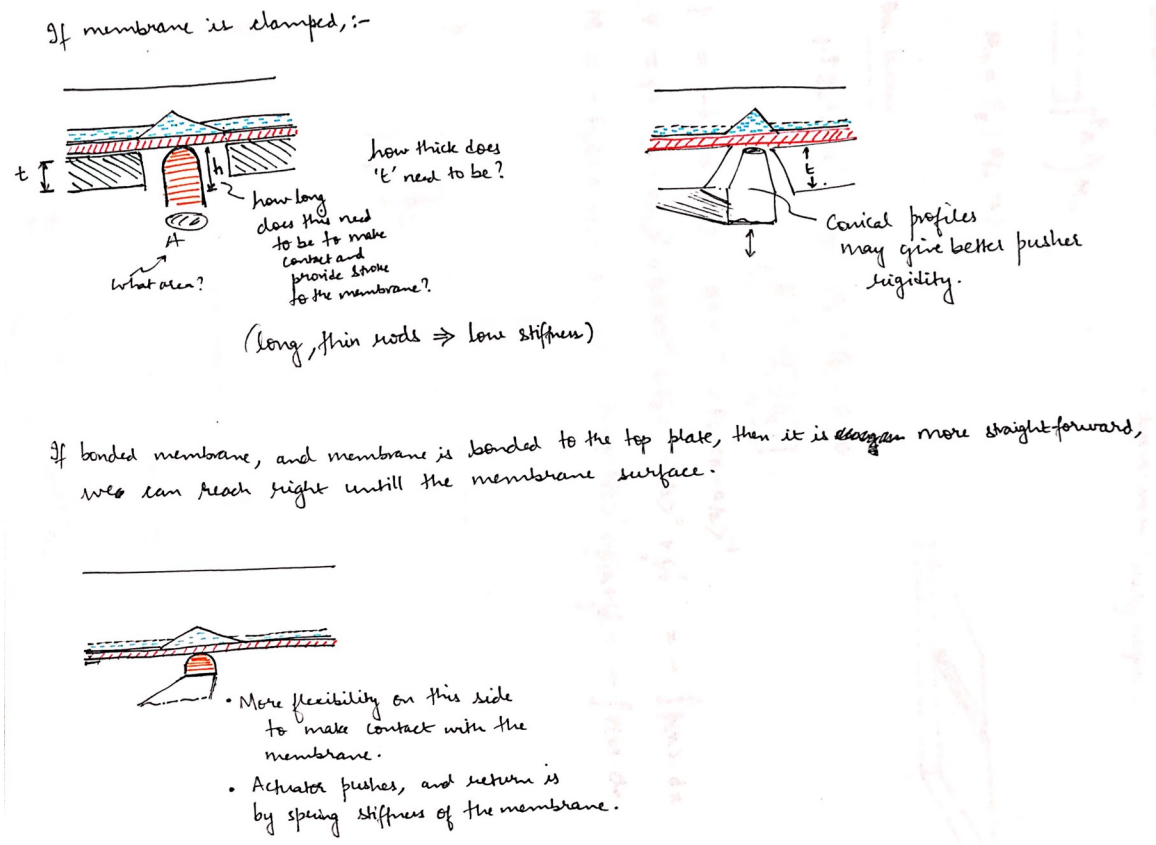

Figure 4-23: Actuator interfacing with the membrane. (Top) If the membrane is clamped, then the pushing pin needs to clear the thickness of the lower clamped layer. If the pushing pin becomes too long, it will be slender. Potentially, the pusher can be made more rigid by giving it a conical shape. (Bottom) If the membrane is bonded to the fluidic side, it gives more flexibility for the actuators on the other side of the membrane.

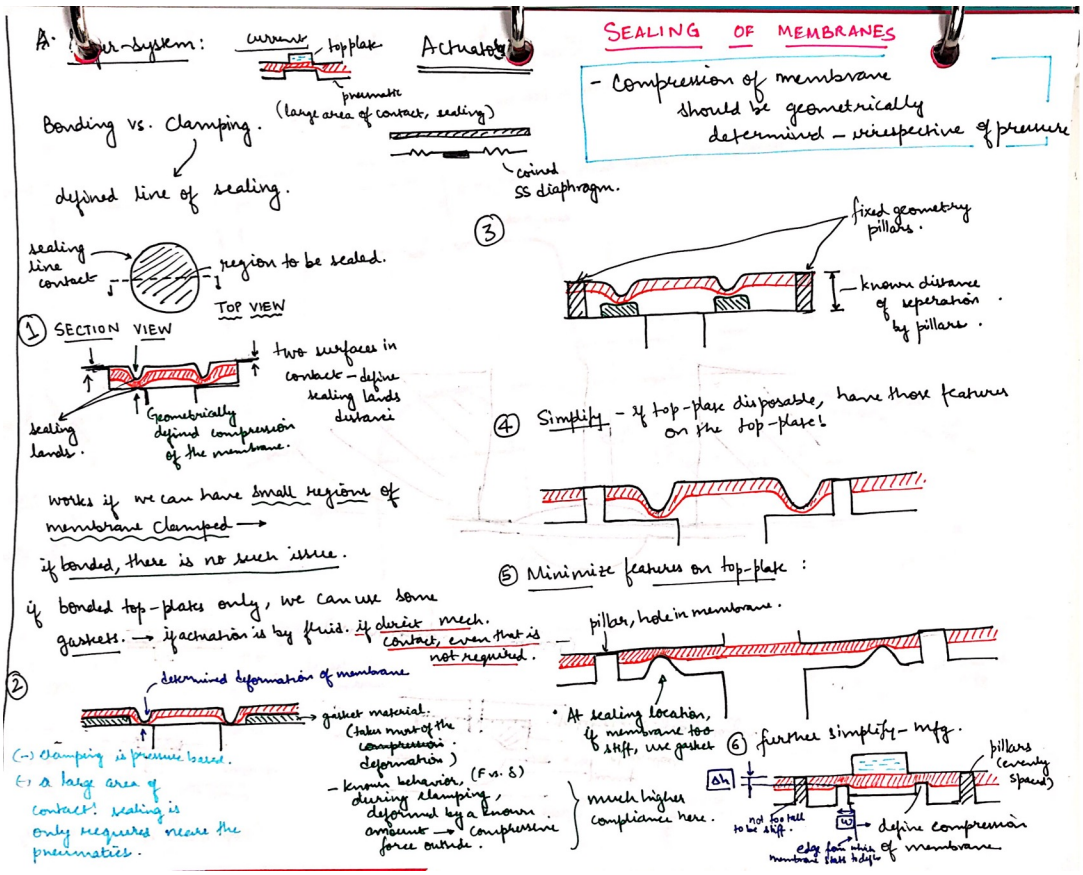

Figure 4-24: Membrane sealing. The sealing of membranes is an important consideration, especially in clamped membranes. Sealing of large flat areas is challenging. A well defined sealing line should be defined. Compression of the membrane should be geometrically determined and the sealing force comes out from the deformation of the membrane by hooke's law. ①–⑥ show various embodiments of this idea.

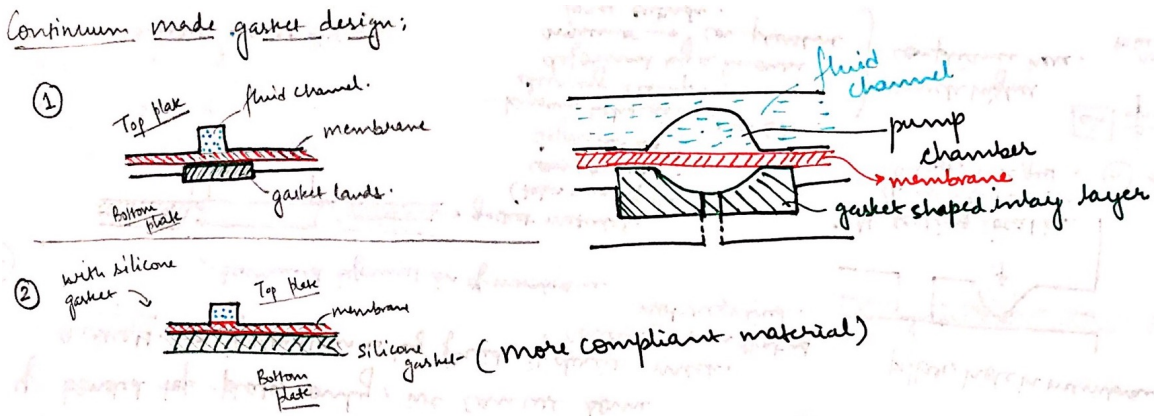

Figure 4-25: Membrane sealing with gaskets. Gaskets take most of the compression are a feasible option in case of rigid and stiff membranes. The total clamping force = deformation of gasket × gasket stiffness.

4.7 Selection of pump design for further exploration

Diaphragm pumps with active valves are a feasible configuration to provide volume deterministic flow-rates over a range of back-pressures. Sterility considerations place severe restrictions on the materials that can be used for the diaphragm.

Small scale electromagnetic (EM) pumps with active valves are relatively unexplored in the literature. Therefore, we decided to pursue the development of EM actuator pump which is described in Chapter 5. The fludidic platform used with the EM actuators is an injection-molded, single-use platform described in Chapter 3. It consists of an injection-molded Cyclic Olefin-Copolymer (COC) top-plate with a COC membrane bonded to it. We used the pump lane with conical pump chambers and the mid-wall valve configuration as described in Figure 4-9. More details about the platform can be found in Chapter 3.

Chapter 5

Electromagnetically actuated diaphragm micro-pump

-The work described in this chapter was done jointly with Dr. Jun Young Yoon - a PostDoc in our lab.

5.1 Introduction

MicroPhysiological Systems (MPS) attempt to mimic the relevant human multi-organ physiology in-vitro.[2]. These systems have potential applications in drug development and personalized medicine by enabling more accurate testing of physiological drug response earlier in the development cycle. On-platform pumps can provide flexibility and greater design freedom and are a key feature for enabling such platforms. Approaches to multi-organ MPS platforms developed in our lab primarily use an open-well system to culture various tissue organs. A common fluid-media circulates between the organs as driven by on-platform pneumatic diaphragm micro-pumps [5]. These pumps require significant effort in setup and depend on external pressure and vacuum sources. An independent, portable pump with low power consumption and thus low heat generation is desirable.

Electromagnetic pumping at the micro-scale is a relatively unexplored area. A significant challenge is the energy efficiency of these actuators on the micro-scale.

For easier and faster fabrication and assembly, in this research we created a scaled up version of electromagnetic pump drivers. This design uses a *teeter-totter* EM actuator having a low energy consumption of about 1 mJ/stroke. At a 1 Hz cycle rate (2 strokes/sec), this results in a power dissipation of 2 mW per actuator. By *teeter-totter* we mean that the magnetic element tilts back and forth on a hinge, much like a playground teeter-totter. Such low energy consumption is achieved by a latching design which only requires a short pulse of energy to switch its state and stores some of the kinetic energy in springs which is then recovered in the reverse stroke. The force by the deflected springs assists the EM when the airgap is large and help to reduce the time of switching. Details of this design are given below.

This chapter first gives the design overview (Section 5.2) of the EM actuator and details the design considerations (Section 5.2.1). Further, the chapter describes models to predict the electromagnetic (Section 5.3.1) and mechanical (Section 5.3.2) behavior of the EM actuator, and describes the manufacturing, assembly, and integration (Section 5.4) of the actuator with a fluidic assembly. Finally, the chapter presents preliminary test results (Section 5.5).

5.1.1 Design Requirements

The design requirements for the pump and valve chambers are described in Chapter 3. For the electromagnetic actuator, the design requirements are:

1. Force capability of 1 N for a stroke of 0.4 mm

   As described in Section 5.3.2, the pump and valve chambers are designed such that the membrane deflects by 0.1 mm, against a back-pressure of 20 kPa for a force of around 1N. This force is dominated by the membrane stiffness for our typical dimension and material parameters. We need additional stroke for gaps and for spring deflection. Larger stroke allows to accommodate greater manufacturing errors and assembly tolerances. At the contact point with the membrane, the actuator should have this much force (1 N) and stroke availability (0.4 mm) to deflect the membrane till it touches the chamber walls.

2. Minimize energy consumption

   These pumps have to run within a cell culture incubator which has an ambient temperature of 37 °C. As is the case with our bodies, the cells are very sensitive to temperature. Therefore, we need to minimize the heat generation and remove the excess heat away from the fluid so that the temperature of the cells and cell-culture fluid fluid does not rise above 37.5 °C.

3. Long life of actuator elements

   The micro-pumps should be able to operate in the incubator for up to 4 weeks of non-stop operation for a given experiment. The diaphragm life and the life of the actuator elements determine the life of the micro-pump. For an actuation frequency of 4 Hz, running for 4 weeks, we have 10 million (1×10^7 strokes) strokes. To be able to run numerous such experiments, and have a life-time of years, they must operate successfully over about 1×10^9 strokes. The actuator elements should not fail for less than these number of strokes.

5.1.2 Prior work

Most macro-scale pumps are electrically driven. Most designs commonly use electric motors which use electromagnetic interactions to drive an interface in contact with the fluid, thereby increasing the fluid energy at the pump-outlet.

At the micro-scale, there has been lot of interest to develop electromagnetic pumps. The reviews [18, 19, 22, 17, 20] on micro-pumps give a good summary of the different types of micro-pumps in literature. The major categories of pumping systems using electromagnetic conversion of electricity into forces and motion are: [18, 19, 22, 17, 20]

1. Rotary micro-pumps with a rotating rotor which transfers momentum to the fluid.

2. Diaphragm micro-pumps in which an electromagnetic actuator pushes a diaphragm, increasing the fluid pressure.

3. Electro- and magneto-kinetic pumps which continuously transfer energy to the fluid directly. These require special fluid or substrate properties for their operation.

Of these, at the micro-scale, only the diaphragm micro-pumps with active valves have been shown to have a deterministic flow-rate against a range of back-pressures. In the literature, electromagnetically actuated diaphragm micro-pumps with active valves are hard to find. The reasons commonly cited are thermal problems due to the large electric currents [20]. Tandon et al. describe an electromagnetic micro-diaphragm pump with active valves [23, 24] although they do not report the energy consumption and show a varying stroke volume with back-pressure. There are numerous diaphragm micro-pumps with active valves using other actuation schemes such as piezoelectric and electrostatic actuation described in literature. As an example, Geipel et al. [25] describe a piezoelectrically actuated membrane diaphragm micro-pump with active valves. They achieve a constant volume flow-rate per stroke up to a frequency of 0.5 Hz and up to a back-pressure of 20 kPa. Although power efficient, a challenge with piezoelectrically actuated membranes is the reduced life of the piezoelectric diaphragm due to the large strains during actuation and complex manufacturing. This is typically addressed in operation by reducing the deflections limiting the strain and therefore, typically operating these actuators at higher actuation frequencies to compensate to achieve a long life-time of operation.

An example of commercially available micro-pumps capable of recirculation flow, which requires the pump to be flow-through, are the Bartels mp6 pumps (Bartels Mikrotechnik GmbH). They use two piezo diaphragm actuators with passive flap type check valves. The wetted parts are manufactured using PolyPhenylSulfone (PPSU) which is a bio-compatible material. These pumps have a low power consumption of 50 mW and an inversely linear relationship between pressure and volume-flow-rate, with a maximum flowrate of $7\,\mathrm{mlmin}^{-1}$ and back-pressure of 60 kPa. They typically operate at frequencies above 100 Hz have an operating life of 5000 hours (208 days), which translates to about $\sim 1 \times 10^9$ strokes. An example of a pumping system that uses the mp6 pumps are given in [21]. There are similar piezo-electric pumps available

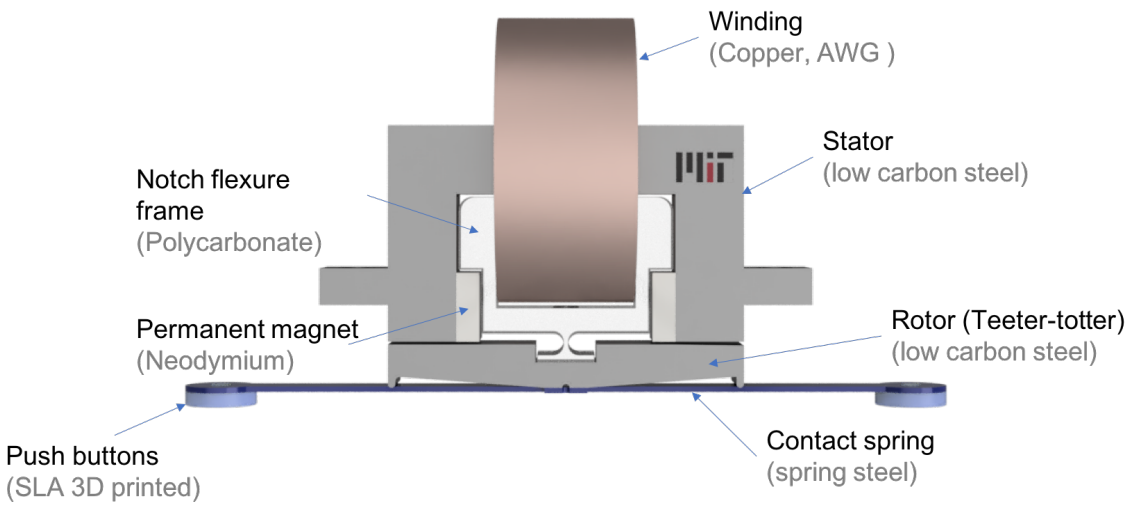

Figure 5-1: EM actuator module showing the various parts as well as the materials used. The teeter-totter rotor rotates about the notch flexure making contact with either side of the stator pole face. The push-buttons make contact with the membrane through an elastomer layer (not shown). The contact springs help bound the force of contact of the push-buttons with the membrane and store some of the actuator kinetic energy, which is recovered in the opposite stroke.

from Takasago Fluidic Systems. Takasago also has miniature rotary peristaltic pumps such as the RP-TX which is a positive displacement pump and can pump volumes from 0.1–40 µL/min up to a back-pressure of 30 kPa. They have a power consumption of 350 mW which is relatively higher and have a larger foot-print.

In this chapter, we describe the design of a power efficient electromagnetic actuator to actuate a diaphragm micro-pump with active valves.

5.2 Design overview of the EM actuator pump

The EM actuator, as shown in Figure 5-1 consists of a low-carbon steel stator, with neodymium permanent magnets attached on each side to provide the magnetic latching force for the rotor, which we refer to as a *teeter-totter*. The rotor is made out of low-carbon steel. In operation, the rotor flips contact with the pole face on either side of the stator leg. It switches between the two stable equilibria, switching between left and right side contact like a playground teeter-totter. Current through

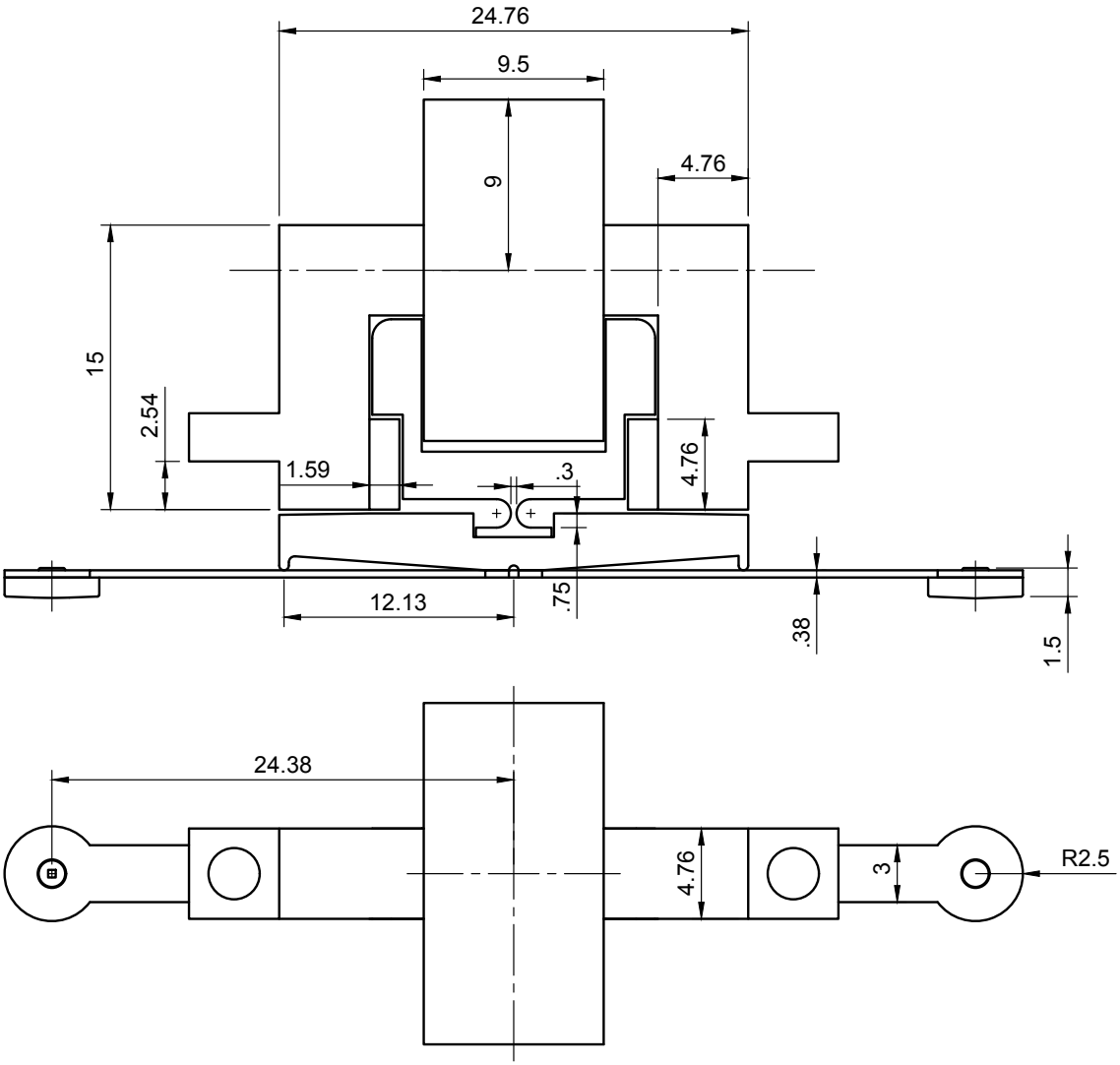

Figure 5-2: Detailed dimensions of the EM actuator elements. The labels for each item are given in Figure 5-1. All dimensions are in mm.

copper winding of AWG-30 wire with 300-500 turns is the actuation input signal. This current generates a magnetic field though the magnetic circuit creating a net differential of magnetic flux between the two ends of the rotor causing the rotor to flip. The magnetic fields of the actuator are shown in Figure 5-10a. The bearing and pivot for rotation of the rotor is provided by a polycarbonate notch flexure. Polycarbonate is used due to its low modulus and high strain limits as compared with metal. A spring steel flexure with push-buttons makes contact with the diaphragm to deflect the diaphragm. Its low stiffness and mass help to bound the contact force with the diaphragm. The push-buttons have a geometry matching the pump and valve geometries and are stereolithography (SLA) 3D-printed.

5.2.1 Design considerations for each element

This section lists each of the major elements and their broad design considerations. Detailed design and calculations follow in subsequent sections.

1. **Stator**

   The stator is U-shaped, a square of 3/16" (4.763 mm) side was chosen as the cross-section for the stator as the pump diameters are 4-5 mm. To avoid cross-talk between the magnets, the legs are spaced at a width of 5 times the leg width. The permanent magnet should have most of the flux going through the stator and the rotor. It should minimize the closing of magnetic flux from the permanent magnet through air before reaching the stator leg on the other side (Figure 5-10a). Therefore, the length of the legs was decided to be around 3 times the width of the magnet so that the connecting segment of the "U" is far away from the PM compared to the rotor.

2. **Permanent Magnets**

   The permanent magnets provide the latching force at each pole face of the stator to hold the rotor in contact without any additional power input. The permanent magnets therefore, lead to bi-stability of the actuator. They are bonded to

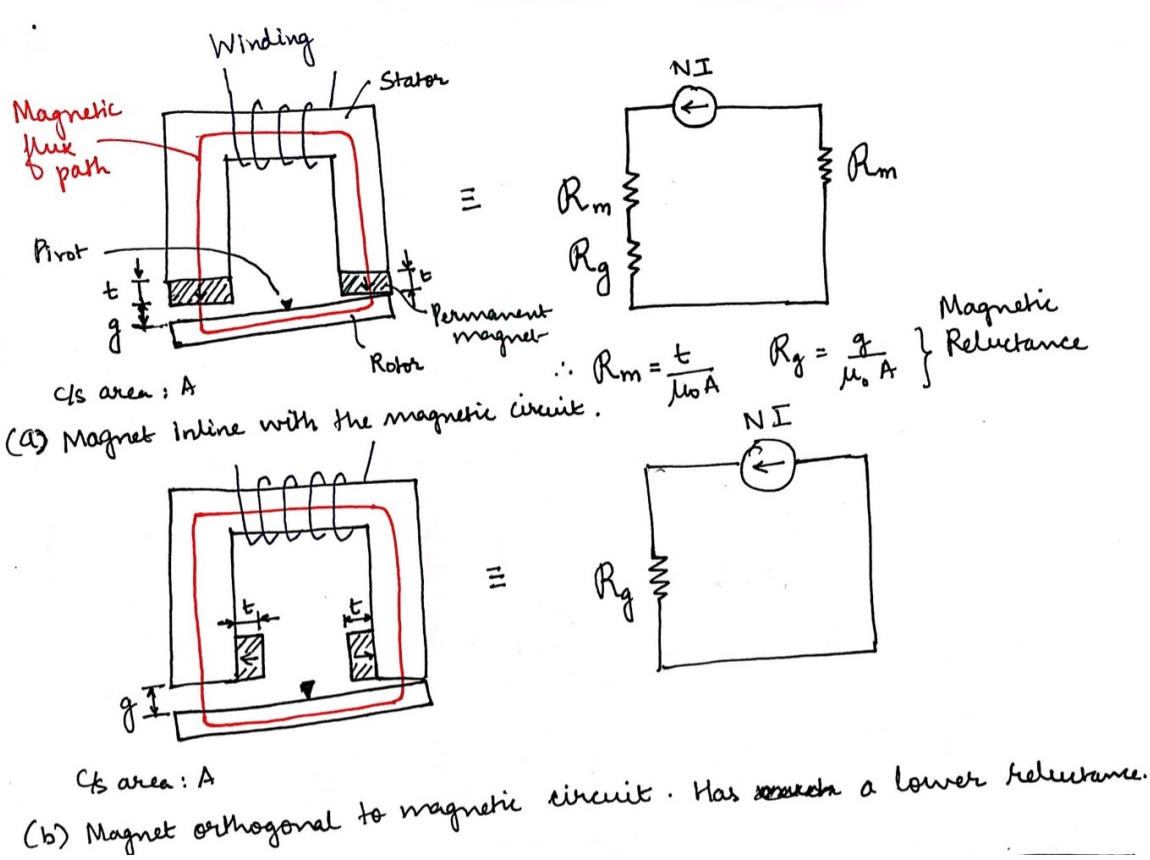

Figure 5-3: Permanent magnets inline in the magnetic circuit (a) cause additional reluctance from the permanent magnets which is eliminated if the magnets are placed by the side (b).

the stator using cyanoacrylate (Henkel Loctite 408) adhesive. The permanent magnets are attached to the side of the stator legs so that the permanent magnet itself doesn't become a part of the main magnetic circuit. This is a good feature since the permanent magnet has an incremental permeability of μ_0, and thus acts as an air-gap, which would increase the reluctance in the circuit. Ideally, we want most of the reluctance in the magnetic circuit to come from the working air-gap between one end of the rotor and the stator pole face. Figure 5-3

3. **Rotor**

The rotor rotates about the notch flexure and switches by making contact with pole face on either leg of the stator. The rotor incorporates features to locate the notch flexure, locate the contact spring as well as a pushing element for

the contact spring (Section 5.4.1). A thickness of 3 mm was selected to avoid magnetic field saturation within the rotor as a part of the magnetic circuit. The maximum air-gap of 0.4 mm on the other side when the rotor is latched to one of the sides is chosen. This is because the maximum required deflection of the diaphragm is 0.1 mm, i.e., the depth of the pump chambers. Having a deflection of 4 times that value gives us buffer to accommodate the deflection of the spring flexure, air gaps and manufacturing and assembly tolerances.

4. **Winding**

   The coil is the source of input magnetomotive force (MMF) into the actuator. Current through the winding creates a differential in the magnetic field between the pole faces at each side of the stator. This results in a net torque on the rotor causing it to flip. AWG30 insulated copper wires are used for the winding. The number of turns varies from 350-500 in the prototypes we constructed.

5. **Notch flexure**

   The notch flexure provides mechanical support for the rotor and a pivot point around which the rotor rotates to make contact with a pole face of the stator. The notch flexure provides a relatively high-stiffness bearing in the vertical direction, and a short force-loop as shown in Figure 5-4. Polycarbonate is chosen as the polymer material as it has a high toughness and yield stress value and therefore can sustain a larger number of cycles of switching of the rotor. On the other hand, metal notch flexures are relatively more stiff and a large fraction of the actuation force would thus go into the deflection of the metal notch. The notch is designed such that the axis of rotation of the notch is fixed at the intersection of the plane parallel to the stator pole faces passing through the neutral position of the rotor (0.2 mm air-gap on each side) and the vertical plane between the stator legs (Figure 5-2).

6. **Contact spring**

   The contact spring ensures that independent of the diaphragm deflection, the

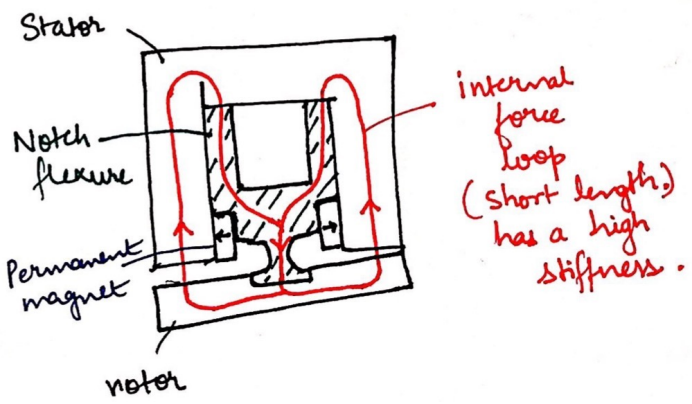

Figure 5-4: The notch flexure allows for a shorter force loop. The forces travel internally and the whole loop is much stiffer compared to an external pivot.

rotor always can always go into a latched state. It also helps bound the impact force with the diaphragm and fluidic platform, due to the relatively low inertia of the mass of the push buttons as compared to the rotor. After contact has been made, the force on the diaphragm is a result of the net deformation of the contact spring, as the rotor moves independently. The contact spring also stores energy from the actuation of the rotor, and helps reduce the acceleration of the rotor thereby reducing the impact force between the rotor and the stator pole face on the other side. This stored energy can then be used in the return stroke, providing a larger initial acceleration of the rotor compared to without the spring for the same Amp-turns of current through the winding. The magnetic force is weaker at a large air gap and the spring force assists in the initial acceleration of the rotor. More details of this operation are given in Section 5.3.2. At the contact location with the diaphragm, we want to convert deterministic and limited motion (0.4 mm) but undetermined and impulsive force (when rotor contacts stator pole face) of the rotor into undetermined and excessive motion (deflection of spring) and deterministic and limited force (limited maximum force) of the contact spring at the push-button–diaphragm interface.

7. **Push buttons**

Stereolithography (SLA) 3D-printed push buttons are attached to the contact

spring and make contact with the diaphragm. These buttons have a curved surface which is designed to conform to the the valve and pump chamber slopes. The valve geometries are as described in Section 2.1.1. There needs to be some tolerance at the push-button–diaphragm contact interface to accommodate for geometrical and alignment errors. For valve sealing, we also need to conformally deflect the membrane to the sealing lands. This is accomplished by using a layer of highly deformable elastomer such as sorbothane or natural rubber between the push button and the membrane. The elastomer acts to create a hydro-static stress state pushing onto the membrane and accommodates variations in depth in the deflection direction.

The dimensions of the EM actuator elements are given in Figure 5-2. The design details are presented in the sections below.

5.3 Design and modeling of various elements of the EM actuator pump

This section describes the detailed electromagnetic and mechanical design of the actuator.

5.3.1 Electromagnetic design and modeling

In this section, the design considerations described in Section 5.2.1 are elaborated, developing the design in detail. The magnetic analysis is done using ANSYS Maxwell software package.

The permanent magnet (PM) near the air-gap makes it challenging to analyze this problem analytically due to leakage paths. That is significant flux goes from the rotor through air, back to the PM (Figure 5-10a). Therefore, we use Finite Element Analysis (FEA) to analyze this system with experiments to verify its validity. 3D FEA was chosen because the shallow dimensions of the actuator don't lend themselves well to be modelled in 2D where an infinite depth assumption would be made.

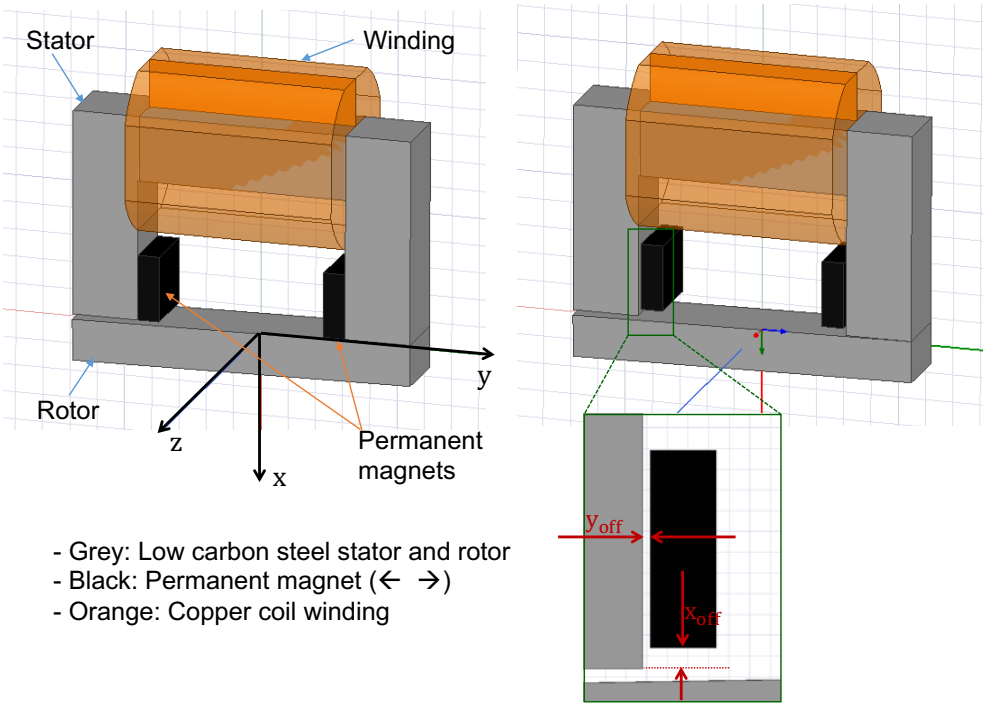

Figure 5-5: 3D FEA model showing the stator, winding, permanent magnets and the rotor. Due to coating of the magnet and the adhesive bonding and alignment and tolerances in assembly, there will be an offset in position, which is shown as y_{off} and x_{off}.

The FEA model is shown in Figure 5-5. The model shows the stator, winding and the permanent magnets. Approximate materials that were available in the ANSYS Maxwell material library are used. This is acceptable, as the main objective is to get approximate estimates for the actuator design . Details of the material specifications used are given below:

1. Permanent magnet

   For the FEA, we used an N35 grade of the magnet from the ANSYS library. The magnet is sold by K&J Magnetic Inc. with a magnetic coercivity of 8.9×10^5 A/m (11.2 kOe). The magnet used to build the prototype was of grade N42, which has a coercivity of greater than 11 kOe. The actual coercivity will have a range but be close to 11 kOe. The relative permeability used is 1.00998.

2. Stator and Rotor

   Steel 1010 from the material library was used for FEA with the default non-linear properties. The material used for the prototype is low carbon steel from McMaster Carr. The actual material properties are close to the values used for FEA.

Due to coating of the magnet and the adhesive bonding and alignment of the magnet to the stator in assembly, there will be an offset in position which is shown as y_{off} and x_{off}. This is the setup of the model used for further analysis.

At the neutral position, i.e., at the position where the air-gap is equal to 0.2 mm on both poles of the stator, the magnetic flux from the permanent magnets is symmetric on both sides and there is no net torque. As the rotor tilts and moves closer to one pole, the magnetic flux through that side increases and correspondingly decreases through the other side, resulting in a net torque about the z-axis in the direction of the closer pole face as shown in Figure 5-5. The net torque increases as the rotor gets close to the pole face until it finally makes contact. This process depends upon the fluxes from both the PM and the coil The maximum air gap on the side not in contact with a stator pole face is then 0.4 mm and the rotor has tilted by an angle of about 1°.

Further, we describe the modeling of latching forces (rotor touching stator pole face on one side) in the state with no current in the winding as well as the force on the rotor as the Amp-turns are increased when flipping the rotor.

0 current through the winding

Figure 5-6 shows a plot of net torque vs. rotor angle for 0 current through the winding and thus depending only on the permanent magnets. The plot on the right shows the difference of the forces on each side vs. the air-gap at the right pole face of the stator-rotor combination. We see a significant change in the forces and torques due to the x_{off} and y_{off} values. This is due to high intensity of B-field close to the permanent magnets which result in large forces. At small air-gaps, the forces are high and even small offsets modify the air-gap and hence significantly modify the forces. The maximum force difference when the x_{off} and y_{off} are zero is around 5.5 N.

Figure 5-7 shows the total attractive force, which is the sum of the forces on the right and left side on the rotor at various rotor angles. The notch flexure bearing experiences this load in operation. Again, there is no current through the winding. Magnetic force is very sensitive to air-gap and therefore the highest when the rotor is in contact with the stator pole face. When the rotor is in contact with the pole faces, the total vertical force increases and is the lowest at the neutral position. The maximum vertical force, when x_{off} and y_{off} are zero is around 7.5 N.

Amp-turns through the winding:

Figure 5-8 shows the torque and force difference for various coil Amp-Turns (AT). The actuator configuration is such that for the assumed coil polarity, the magnetic field due to current in the winding adds to the magnetic field from the permanent magnet and increases the total magnetic field and the force on the left leg. On the other side, the field from the winding current counteracts the magnetic field from the permanent magnet and reduces the total magnetic field and force on the right side. The result is a net force which is greater on the left side and will cause the rotor to tilt in the opposite direction and make contact with the left pole face.

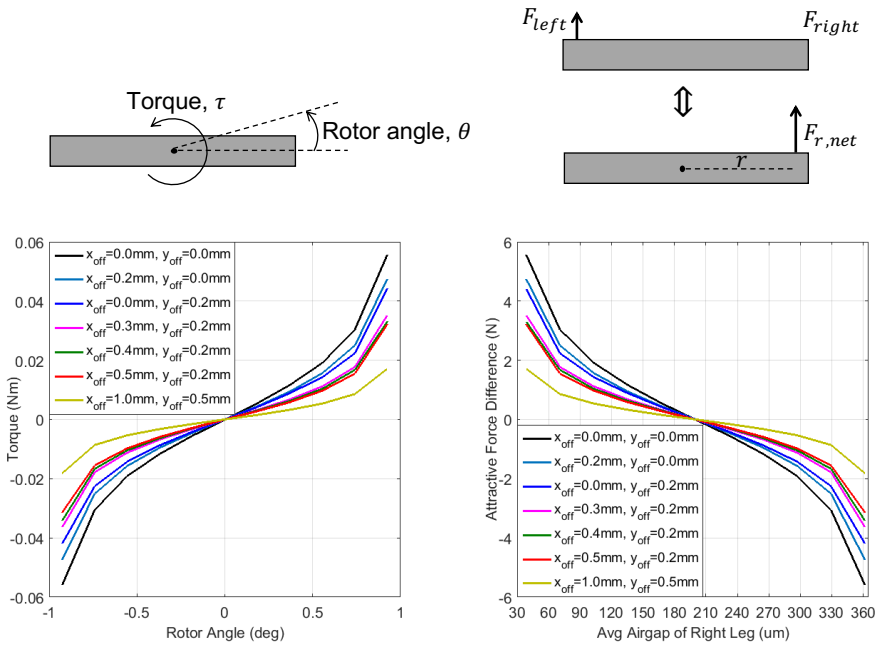

Figure 5-6: The right-side plot shows the net force, $F_{r,net}$ on the rotor. When multiplied with the radial distance, this gives the net torque as shown in the left-side plot. These plots are for 0 Amp-turns through the winding. Positive rotor angle is defined as corresponding to the right side of the rotor being closer to the pole face than the left side. Values for different magnet offsets x_{off} and y_{off} are evaluated and are shown in the plots. At neutral position of the rotor (rotor angle = 0°, air-gap = 0.2 mm) the torque and the net force is 0

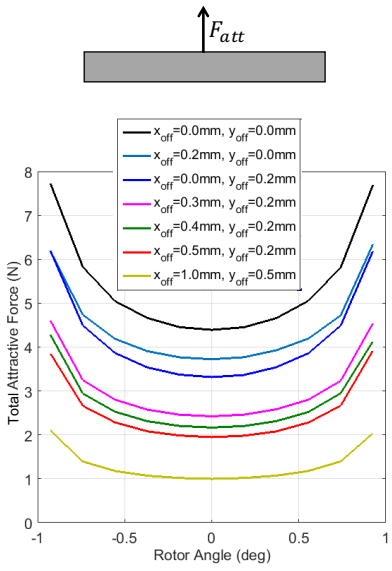

Figure 5-7: Total attractive force on the rotor at various rotor angles, for no current through the winding. This is the load carried by the hourglass notch flexure due to the PMs until rotor pole face contact. Magnetic force is very sensitive to air-gap and therefore maximum when the rotor is in contact with the stator pole face.

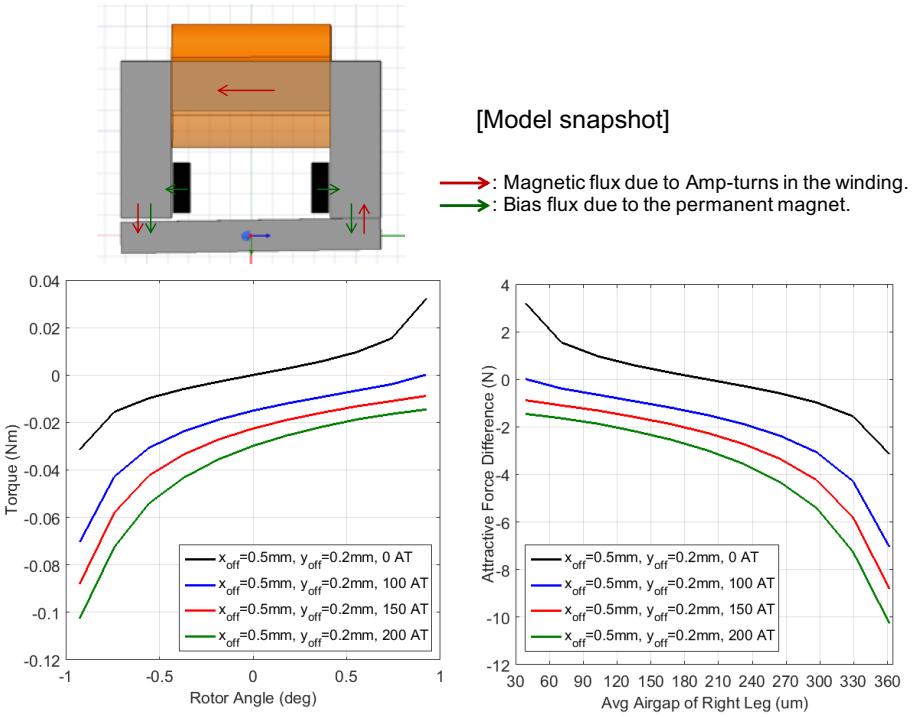

Figure 5-8: Winding driven flux density adds to the magnetic field on the left side, while subtracting from the magnetic field on the right side, thereby creating a force differential and a net torque tilting the rotor to contact the left pole face. Positive rotor angle corresponds to the right side of the rotor being closer to the pole face than the left side. Positive attractive force difference corresponds to a greater force on the right side as described in Figure 5-6

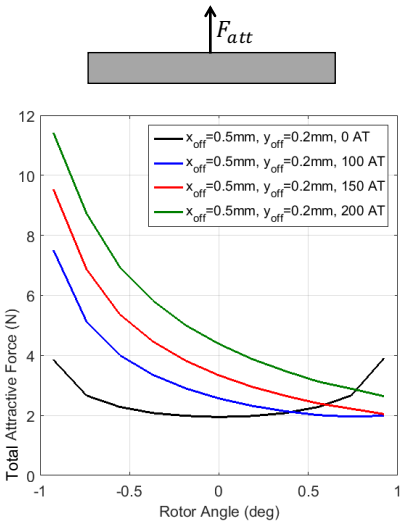

Figure 5-9: When the rotor is in contact on the right side, the total force reduces as Amp-turns are increased and reaches a minimum force at around 100 Amp-turns beyond which it increases again. This is the vertical load carried by the notch flexure in operation when the rotor is switching, before contacting the pole face.

We find approximately 100 Amp-turns to be the minimum threshold current in the winding to cause the flipping of the rotor. Thus, if we provide a current greater than 100 Amp-turns, we should cause the rotor to flip. An interesting thing to note here is that since even with 0 Amp-turns, once the rotor crosses the neutral point there is net force on the left side. This means, if the current is switched off after the rotor crosses the neutral point, the net force is still on the left side which will bring the rotor to make contact on the left pole face. This latching behavior is due to the permanent magnets and is used to reduce power consumption in the actuator.

Figure 5-9 shows the total attractive force, which is the sum of the forces on the left and the right side of the pole faces for the actuator when current flows through the winding. This is the total bearing force experienced by the notch flexure in operation. It is interesting to note that when the rotor is in contact on the right side, the total force reduces as Amp-turns are increased and reaches a minimum force at around 100 Amp-turns beyond which it increases again. At that minimum point, the total vertical force is almost zero as the magnetic flux from the winding almost completely cancels the magnetic flux from the permanent magnet on the right side. On the left side, due to the comparatively large air-gap, the forces due to the permanent magnet and the winding magnetic flux are much weaker.

Magnetic field distribution within the stator and rotor during operation

Figure 5-10 shows the magnetic flux density (B) plots as a color map on the left and as a vector plot depicting magnitude and direction of the B-field on the right. The top plots represent the case with no current through the winding. The bottom plots represent the case with 150 Amp-turns of current through the winding. These plots give us an insight into the behavior of the actuator. We can see in Figure 5-10a-top that when the rotor is contacting the right pole face, the field from the permanent magnet on the right side makes a short loop through the pole face, into the rotor on the right side and closes back on the right permanent magnet travelling through air. This results in a strong latching force. On the left side, a smaller fraction of the magnetic flux goes through the rotor on the left side. The majority of flux from the

left side permanent magnet goes through the stator to the right leg and returns to the left permanent magnet through the rotor and through air. There is slight saturation at some regions on the right side of the stator and rotor, but majority of the stator and rotor are not saturated.

When current is switched on in the winding with an associated flux direction shown by the arrow (Figure 5-10a bottom), the winding B-field counteracts the permanent magnet B-field on the right side while it adds to the permanent magnet B-field on the left side. There is no saturation of B-field in most regions in this case as well. This results in a net torque on the rotor and the rotor starts tilting to make contact with the left side pole face (Figure 5-10b bottom, 5-10c bottom). When the rotor makes contact on the left side pole face, the magnetic field is saturated on the left side near the pole face in the stator and the rotor. When the current is switched off (Figure 5-10c top), the system return to a state which is the mirror image about the vertical axis of the actuator with rotor contacting the right side with no current in the winding (Figure 5-10a top). When the rotor is in the neutral position, with equal air gap on both sides with no current in the winding (Figure 5-10b top), the magnetic field pattern is symmetric on both left and right sides and therefore there is negligible net torque on the rotor. When the coil is actuated (Figure 5-10b bottom), there is considerable B-field on both the left and the right pole faces. The field on the left side is much greater than the field on the right side and therefore, there is a net torque on the rotor titling it towards the left pole face.

In practice though, due to asymmetry in the manufacturing, there will be a net torque on the rotor even in the neutral position, but its value would be small compared to the net torque when the rotor makes contact with either pole face.

Summary

The simulations show that that we can achieve a latching force n the range of 2-4.5 N. The latching force is defined as the minimum force required to tilt the rotor to the other side when the rotor is in contact with a stator pole face. There will be a vertical force in the range of 2-8 N which will be supported by the notch flexure

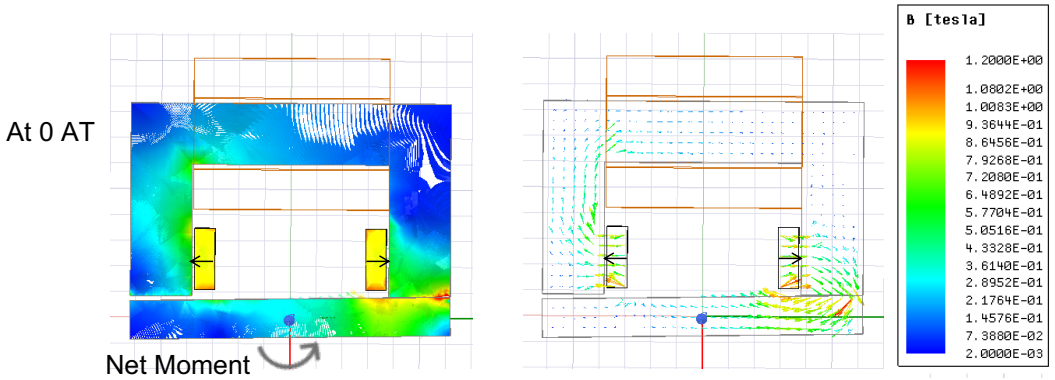

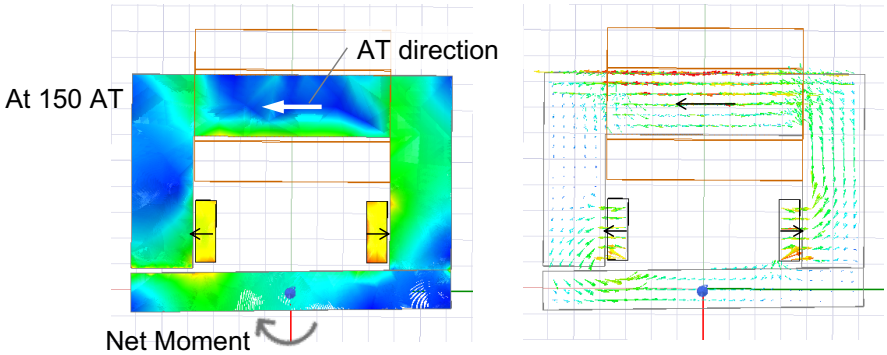

(a) Right latch

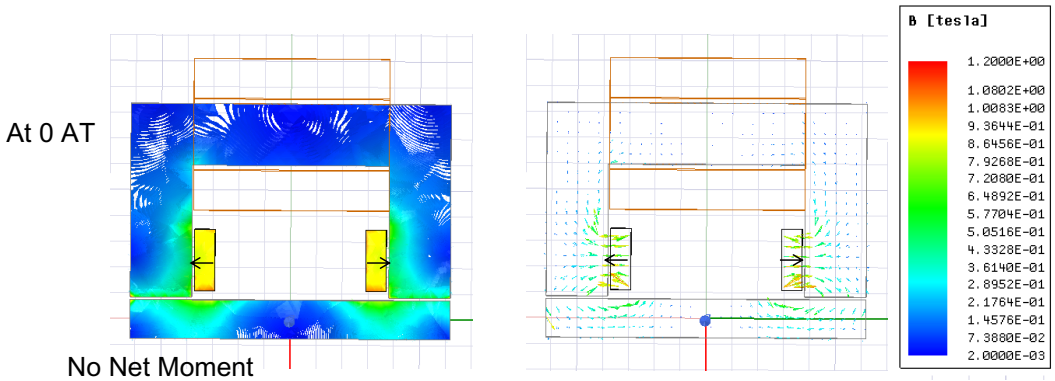

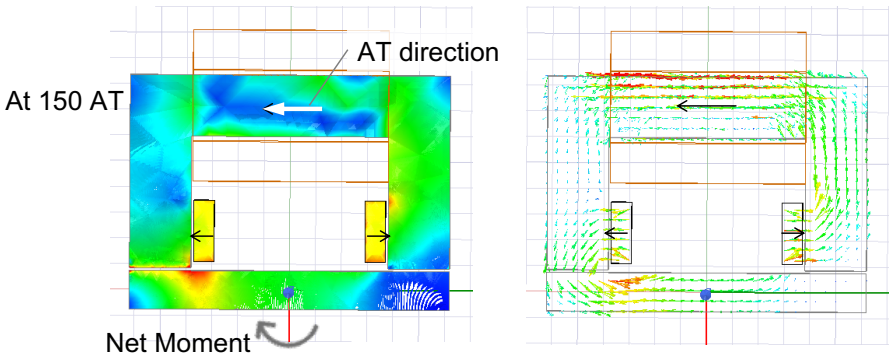

(b) Neutral position

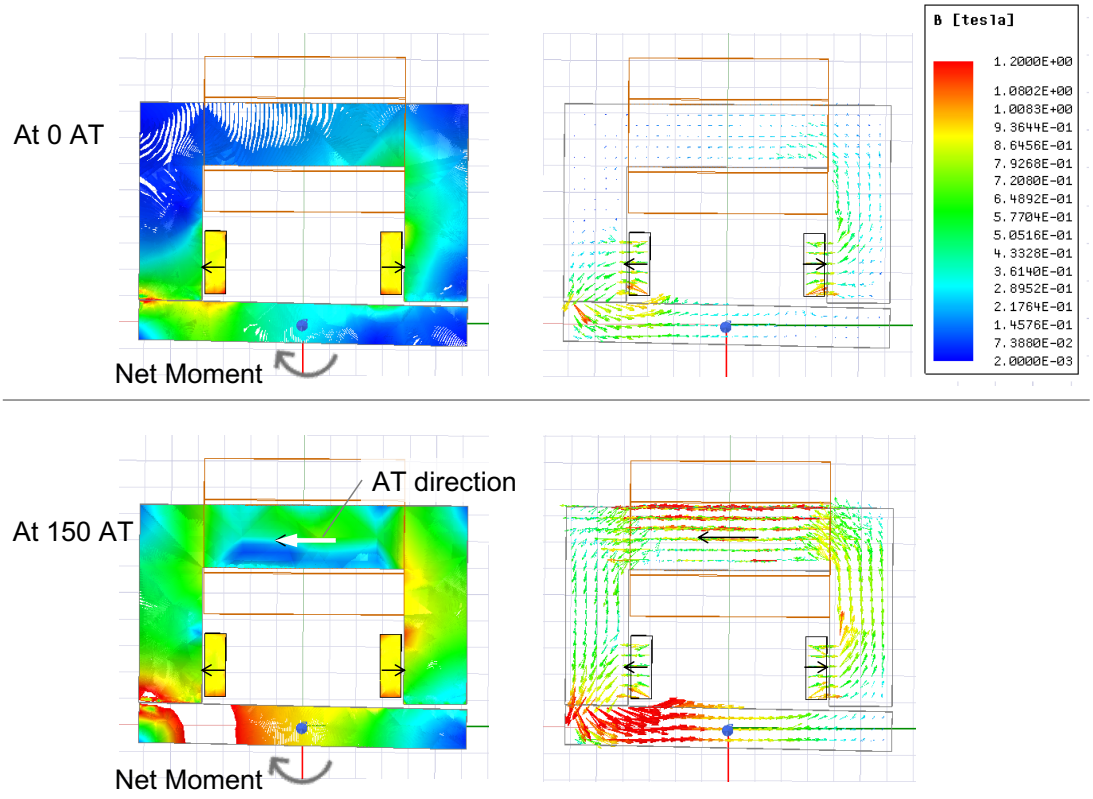

(c) Left latch

Figure 5-10: Magnetic flux density (B) plots as a color map on the left and as a vector plot on the right depicting magnitude and direction of the B-field. The top plot represents no current through the winding and the bottom plot represents 150 Amp-turns of current through the winding. When latched (Figures a,c) with no current, the field from permanent magnet makes a short loop through the contacting pole face, thence into the rotor and then closes back to the permanent magnet by travelling through air. With 150 AT of current, the total B-field on the right stator pole face is reduced and the field on the left side of the stator increases to flip the rotor from the right to the left. When on, the current AT vector by right hand rule is shown in the figure. The net moment on the rotor is also shown in the figure.

bearing. Flipping of the state of the rotor requires a current greater than about 100 Amp-turns.

5.3.2 Mechanical design and modeling

Here, we describe the modeling of the mechanics of actuator switching and the force and deflection of various spring elements in the mechanical loop. We also describe the dynamics of the actuator when it switches.

Force required to deflect the membrane

We decided to use the fluidic plates with the bonded COC membrane manufactured by microfluidic ChipShop GmbH as the platform to demonstrate pumping by these actuators. These fluidic plates are described in more detail in Chapter 3. This was motivated by the fact that COC has a Young's modulus of 1.3-1.5 GPa. This translates to a reasonably high stiffness value and can therefore generate a modest amount of suction pressure to fill the pump chamber during the suction phase as well as to open the valves. The various pump and valve geometries are described in Section 3.6. Chapter 2 describes the design of diaphragms for these platforms, and Chapter 3 describes the design of the injection-molded, single use platforms from ChipShop.

Chapter 2 gives an approximation of the force required to actuate the membrane. Table 2.3 summarizes the pressure required for a conical chamber of various diameters and depth of 0.1 mm for the diaphragm to make contact with the chamber walls. We find that the force for deflecting a 3 mm diaphragm is around 525 mN. To achieve a back-pressure capability of around 15-20 kPa, that pressure should be added to actuation. For a 5 mm diameter diaphragm which is as large as we are contemplating, a 20 kPa pressure translates into a force (pressure times area) of around 400 mN. Therefore, the total force at the contact point between the contact push button and the membrane will be about 1 N. The stiffness of the diaphragm, as described in Section 2.1.1 is non-linear, with a small value for small forces and then the stiffness

increases at an increasing rate as the force increases. For simplified analysis of the forces and deflections in the actuator elements, the stiffness is linearized. It takes 1 N for the push-button to deflect the membrane by 0.1 mm, including the back-pressure, so the linearized stiffness of the membrane is about 10 N/mm.

Forces and deflections in the actuator elements

When the rotor rotates about the notch, the displacement of the rotor at each pole face is distributed between the contact spring, and the membrane which act as springs in series as shown in Figure 5-11. The notch flexure in parallel with the contact spring and membrane and has the same total deflection. The rotor is assumed to be rigid compared to the other elements in the system. The sum of the deflections in the contact spring and the membrane add up to the total displacement of the rotor, while the notch flexure deflection is the same as the rotor displacement. Therefore, the force is the same through the contact spring and membrane and the total force from the rotor is distributed between the notch flexure and the contact spring and the membrane.

There are limits to deflection of the rotor and the notch flexure by the stator pole faces, shown by green rectangles in the upper part of the figure and the membrane deflection is limited by the chamber walls which are shown by green rectangles in the lower part of the figure. The maximum membrane deflection allowed is 0.1 mm. The maximum rotor deflection is 0.4 mm. We have an estimate of the membrane stiffness from 5.3.2 . The objective here is to get an estimate of the stiffness and deflection range for the contact spring to have enough force (approximately 1N) and deflection capability at the point of contact with the diaphragm.

We want most of the force from the rotor to be exerted at the contact with the membrane. Therefore, we try to minimize the stiffness in the notch flexure which results in a low force in the notch flexure for a given deflection. In operation, the notch flexure is always engaged with 0 deflection at the neutral position of the rotor. During operation, for example, when the rotor is flipping after being latched with the right side pole face, the push button on the right side is initially not in contact

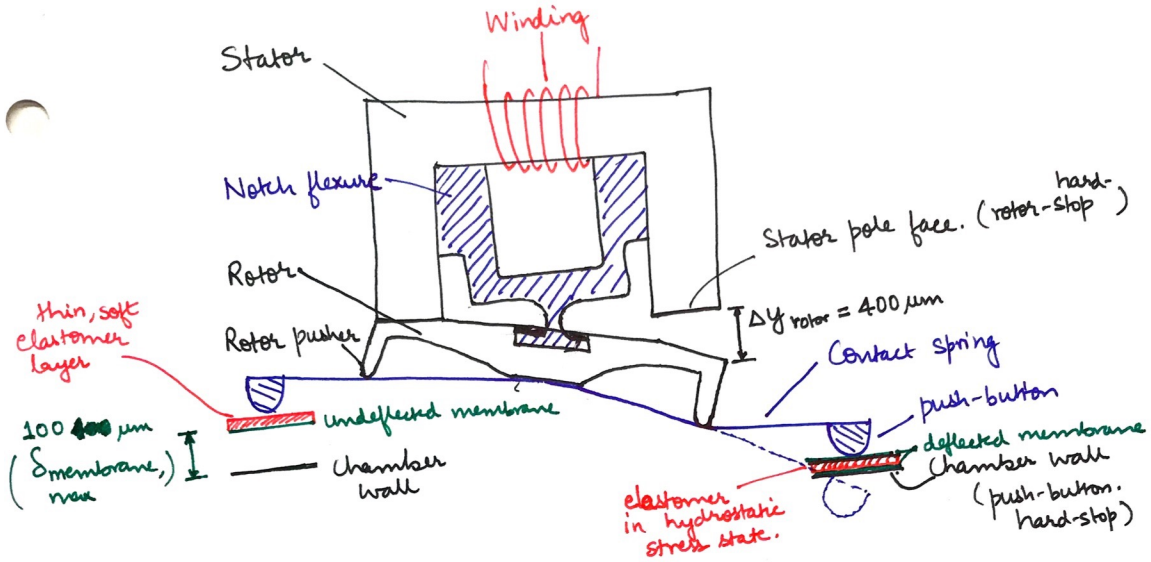

(a) Schematic of the actuator deflecting the membrane on the right and no contact with the membrane on the left. The right side membrane is fully deflected and is in contact with the pump/valve chamber walls. The left side membrane is undeflected. The maximum stroke of the rotor at the pole face is 400 µm. The maximum membrane deflection is 400 µm. The elastomer gets loaded in a hydrostatic state to uniformly distribute the pressure on the valve sealing lands and seal.

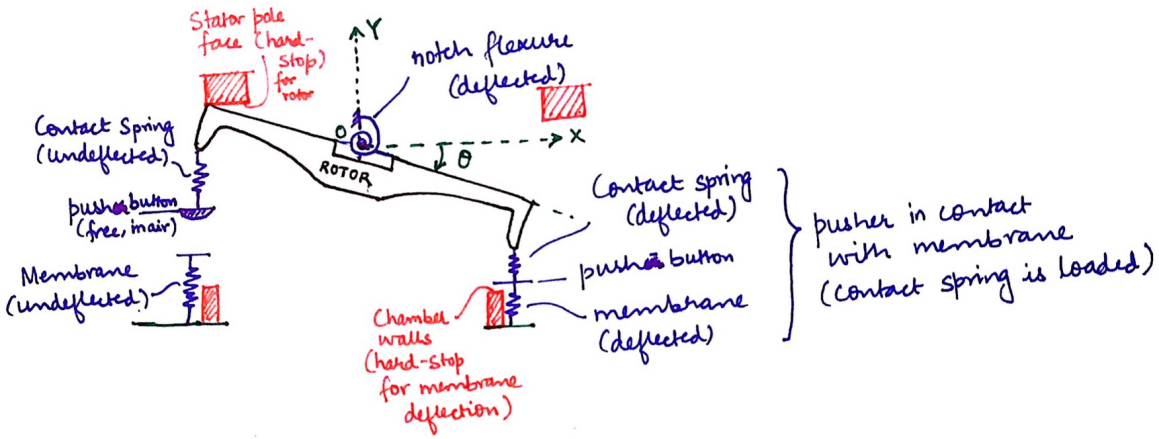

(b) Simplified schematic with springs connected to the rotor. Rotor is in contact with the left stator pole face. The hard-stops in red limit the deflection of various elements. The stator pole faces limit the deflection at the top of the rotor. The membrane deflection is limited by the chamber walls. Once the contact spring and membrane come in contact, they act as springs in series.

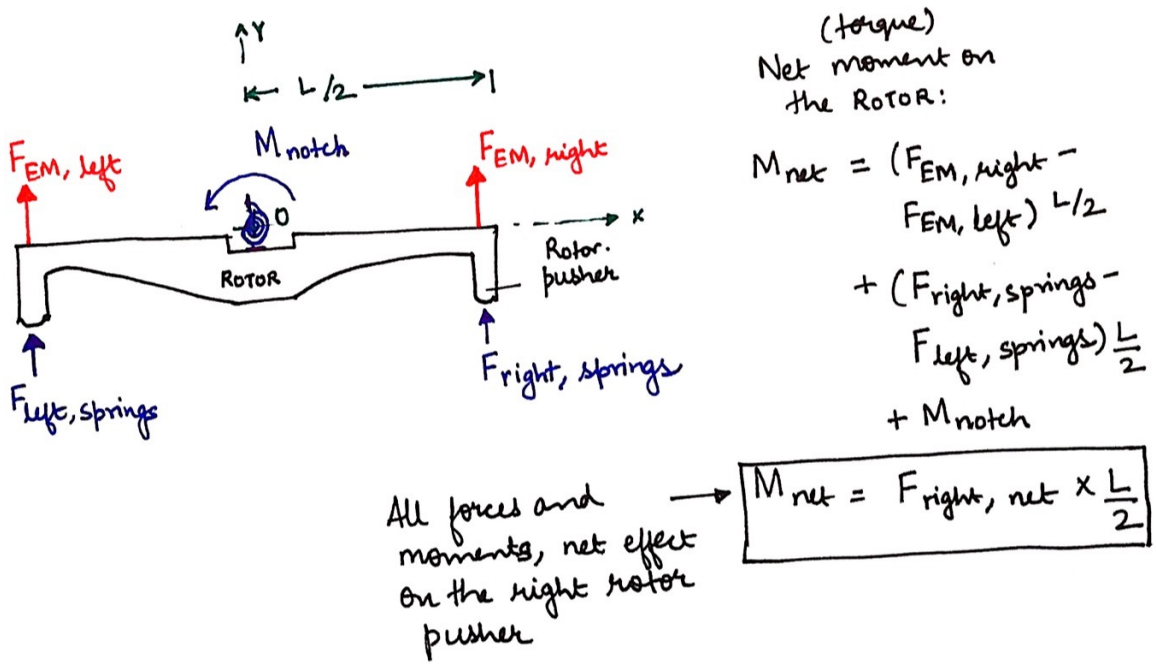

(c) Free-body diagram of the rotor showing the forces acting on the rotor. The EM forces, shown in red are from the permanent magnet and the winding current. The spring forces the force from the contact spring onto the pusher.

Figure 5-11: Schematic used for modeling the dynamics of the EM actuator.

with the membrane. The rotor has to move a certain distance before the push-button makes contact (Figure 5-11 right side). After the push-button makes contact with the membrane, the contact spring and the membrane are in series and further deflections of the rotor are distributed between them in the inverse ratio of their stiffnesses. Once the membrane bottoms out at the chamber wall, the membrane deflection stops and all further deflection of the rotor is accommodated only by the contact spring. Finally, the rotor deflection stops rapidly when the rotor comes in contact with the pole face on the left side.

Design of the notch flexure

The notch flexure is the bearing and the hinge for the rotor. In operation, it has to carry the preload from the permanent magnets as well as the net vertical force when the rotor switches to the other side. In addition, some fraction of the latching force is taken by the notch flexure while the remaining portion of the force is taken

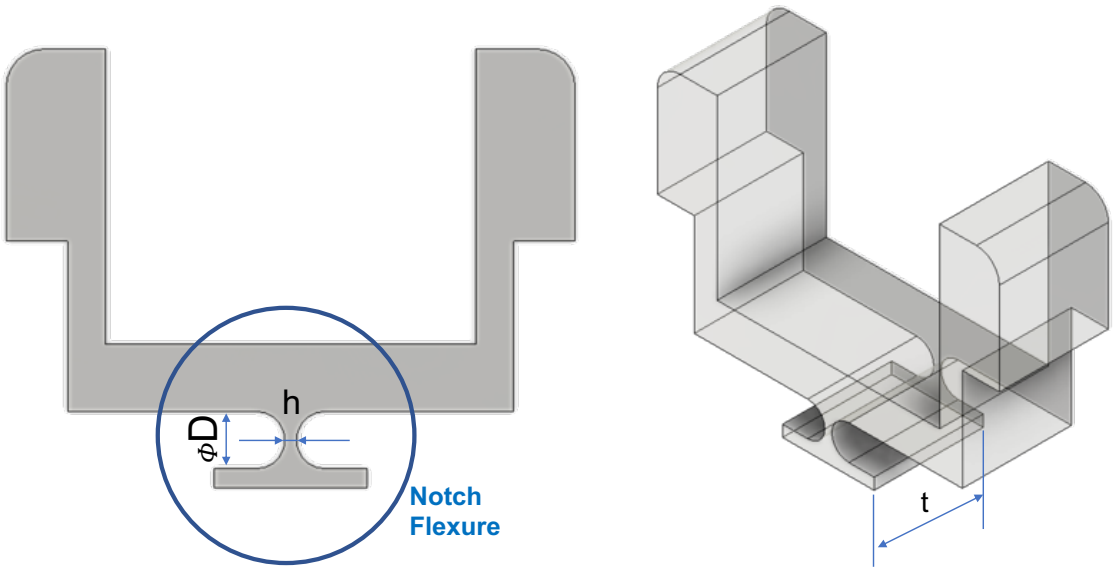

Figure 5-12: Polycarbonate notch flexure used in the EM actuator as the vertical bearing and hinge for the rotor. Dimensions of the notch flexure are labelled.

up by the contact spring and membrane combination.

Herman Soemers, in Section 3.7, page-112 of [26] gives the design charts and rules for designing notch flexures for small rotation angles of up to 1°, which is the case for our system. An excel spreadsheet was made to easily evaluate various materials and actuation conditions. The important geometrical dimensions of the notch flexure, shown in Figure 5-12, are the notch height h, notch diameter D and the thickness t. We found a feasible design is a notch flexure made of poly-carbonate, with h=0.3 mm, D=1.5 mm and t=4.763 mm (same as thickness of the stator). For such a notch, the stiffness in the vertical direction is around 2000 N/mm which results in a vertical deflection of approximately 5 µm for a vertical load of 10 N, which is much smaller compared to the membrane deflection of 100 µm, and the maximum actuator air gap of 400 µm. Since there is further motion of the rotor after the membrane bottoms out, this deflection can be accommodated in that extra motion. The rotational stiffness of the notch flexure along the notch axis is around 80 Nmm/rad. For a rotation angle of approximately 1°, the torque required is thus around 1.5 Nmm. This translates to a linearized stiffness of 0.8 N/mm at the rotor edge. The pole faces are approximately 10 mm away from the notch center and therefore, the force at the pole face taken

by the notch flexure when the rotor is latched is around 0.15 N. This is less than 10% of the latching force of 2-4.5 N, and hence we can neglect the force in the notch flexure when designing the contact spring. The maximum stress in the notch flexure is around 10-15 MPa, which is less than 1/3rd of the yield strength of polycarbonate - around 60 MPa (nominal). Therefore, the poly-carbonate notch flexure should have a long life in operation. In future work, we plan to test this experimentally.

We also verified the deflection of the notch flexure using mechanical FEA (Figure 5-13). Due to the contribution of the vertical force in addition to the moment, the deflections and forces are higher than calculated above, but still remain within an acceptable range. The beam supporting the notch has a bending deflection of around 10 µm which can be reduced by reinforcing the beam against the winding and the permanent magnets (Figure 5-1), as will be the case if the actuator is potted in epoxy or some other material as a part of the manufacturing process.

Design of the contact spring

As described in Section 5.2.1, the contact spring helps bound the contact force with the membrane due to its lower stiffness and low mass of the push-button. It also ensures that independent of the exact membrane deflection, the rotor always goes into a latched state. In addition, the spring stores energy which serves to decelerate the rotor into contact, and which can be used on the return stroke to assist in faster switching of the actuator.

The kinematics of contact is an important consideration. The required deflection of the membrane is in the vertical direction into the pump and valve chambers. When the rotor tilts along the pivot axis, it creates a horizontal component of the motion along with vertical which can cause sliding of the push-button on the membrane surface (Figure 5-14). In addition, the push button in contact with the membrane is also tilted with respect to the vertical. This tilting is potentially problematic as the displaced volume would then be limited to the intersection of the tilted push button geometry when the membrane comes in contact with the walls of the pump chamber. This volume is lower than if the push-button comes down vertically into the chamber.

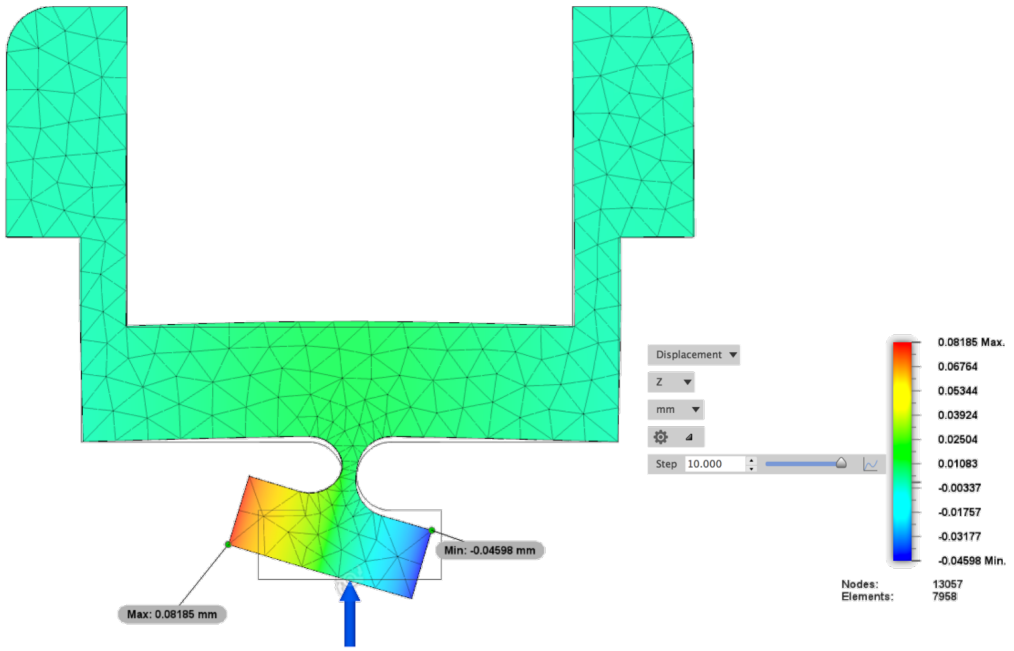

(a) Vertical displacement

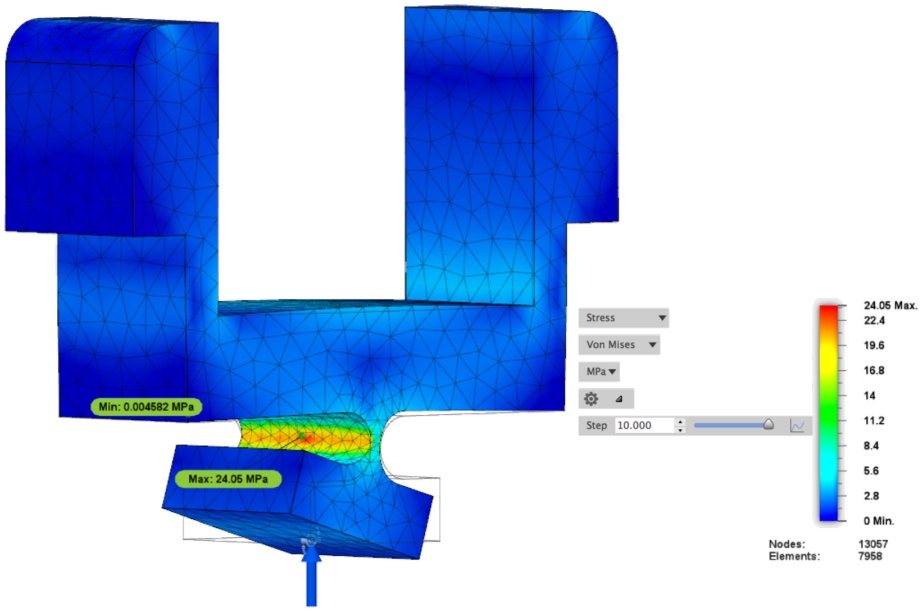

(b) Von-mises stress

Figure 5-13: FEA of the notch flexure. The displacement and the stresses are within acceptable range. Since the stresses are within 1/3 times the yield stress, the notch flexure is expected to have a long life in operation.
Autodesk Fusion 360 in non-linear simulation mode was used for the FEA

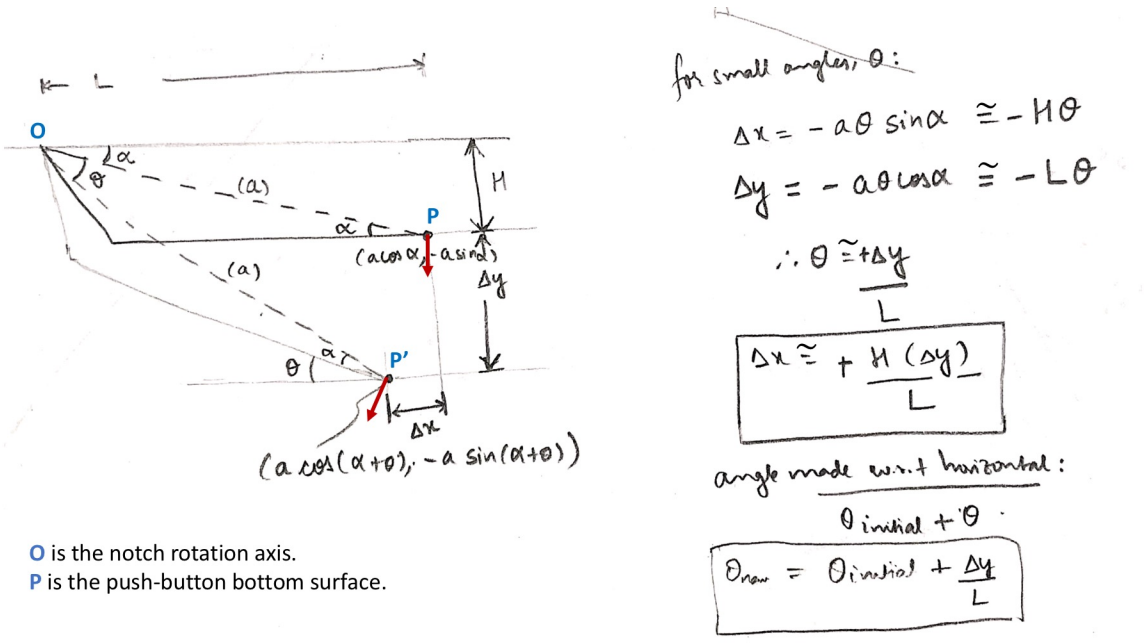

Figure 5-14: When the rotor rotates and the tip moves down by Δy, there is a horizontal component of the displacement, Δx and also a tilt angle, θ.

For valves, this is potentially more problematic as we need a conformal contact of the diaphragm against the sealing lands to create a seal and the tilted push button will increase chances of gaps between the diaphragm and the sealing lands.

To accommodate these deviations, we use an elastomeric layer between the push-button and the membrane (Figure 5-11a). The thicker the elastomeric layer, the larger deviations it can accommodate, but in return it reduces the vertical stroke of the actuator acting to deflect the membrane or to store energy. Hence, we need to minimize these deviations by minimizing the tilt and horizontal motion of the push-button. Therefore, we design the contact spring such that it can deflect and transmit force to the membrane as the rotor rotates and at the same time, minimizes the horizontal travel and the tilt at the point of contact of the push-button when the membrane is in its fully deflected condition.

Figure 5-14 shows the rotation of point P about a point O. Point O corresponds to the center of the pivot flexure. Point P corresponds to the tip of the push-button, which would lie at the end of the contact spring. Point P is located at a vertical distance H below and horizontal distance L to the right of O. When the rotor

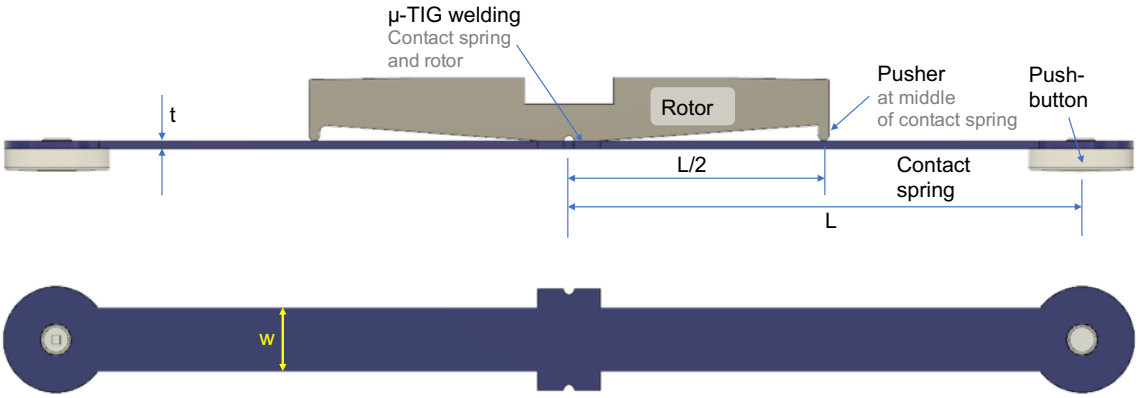

Figure 5-15: Contact spring design. The pusher at the edge of the rotor engages with the contact spring after the push-button makes contact with the membrane. It deflects the contact spring at the middle and removes the tilt from the push-button after membrane contact. The spring is micro-TIG welded to the rotor at the center point, as indicated. Thank you to Dan Rathbone for suggesting this fabrication method.

rotates, point P moves to P'. The distance moved vertically is Δy. The corresponding distance moved in the horizontal direction, to the left is Δx. As shown in the figure, the horizontal motion is,

$$\Delta x = \frac{H}{L}\Delta y. \tag{5.1}$$

For a vertical motion of $\Delta y = 0.2$ mm downwards, and nominal $L = 12$ mm (the horizontal distance between the vertical mid-plane to a stator pole face) and nominal $H = 6$ mm (the vertical distance between the pivot center point and the bottom of the push-button), we get Δx=0.1 mm to the left and a $\theta = \Delta y/L = 1^\circ$ tilt to the left with respect to the vertical. This horizontal motion is a fraction H/L times the vertical motion. Since the chambers are shallow, the push-button can potentially accomodate this motion by moving into position by sliding on the membrane. The tilt is potentially more problematic and therefore we need to remove the tilt and minimize the horizontal motion for a given vertical motion of the push-button and at the same time allow the rotor to rotate about the pivot center and make contact with the pole faces. As described earlier, further deviations are accommodated by the elastomeric layer below the push-button.

One of the solutions to resolve this is to have a force acting vertically between

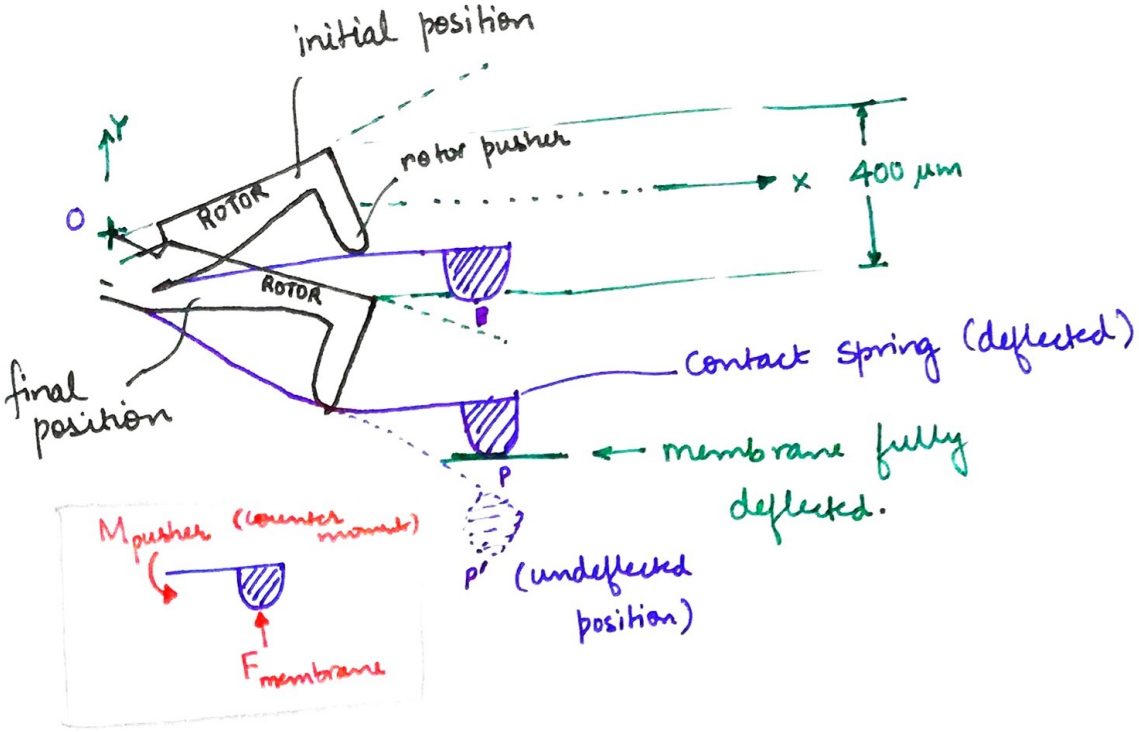

Figure 5-16: The design of the contact spring. The rotation center of the contact spring is close to the rotation axis of the rotor. The pusher pushes at the middle of the contact spring. The contact spring gets loaded once the contact spring push-button comes in contact with the membrane. The vertical heights are maintained such that the contact spring is parallel to horizontal at the final position of the rotor (rotor latched to the left side pole face).

points O and P to provide a counter moment in between the O and P to remove the tilt once the push-button makes contact with the membrane. This is accomplished as shown in Figure 5-16. The rotor is modified to have a contact point at the mid-point of the contact spring and thus pushes in the middle of the contact spring as shown in Figure 5-15. When the contact spring makes initial contact with the membrane, the effective length of the contact spring is from the center of the rotor to the push button. After contact with the membrane, due to the membrane resistance, the pusher engages with the contact spring. Consequently, the effective length is reduced by half, to the distance between the pusher to the push-button. Therefore, the contact stiffness at the time of contact is around 8 times smaller than the stiffness after contact. This is because the vertical stiffness of a loaded beam is inversely proportional to cube of the

length. The reduction of effective length by 2 times, increases the stiffness by 8 times after contact. This minimizes the impact forces on the membrane. Once the pusher is engaged, it also provides a counter moment which removes the tilt from the pusher as shown in Figure 5-16. The modified design of the rotor with the pusher at the middle of the contact spring is shown in Figure 5-15. The contact spring is attached to the rotor by micro-TIG welding at the center since the joint will bear significant moments which try to peel the contact spring away from the rotor. Welding gives a joint which is strong in all directions whereas bonding is typically weak in peeling and cleavage directions.

An alternative solution could have been to attach a cantilevered beam at the end of the rotor (Figure 5-17). The downside is that it would have a higher stiffness (almost 8 times) during impact compared to one described above. In addition, as the rotor edge moves down, the cantilever at the push-button will move horizontally to accommodate the reduction in vertical height at the rotor. Our solution minimizes the vertical downward motion by keeping the other end close to the pivot point and consequently minimizes the horizontal motion. Other flexure spring designs could be made which keep the push-button vertical as the rotor edge moves down but they would be more complex than the solution described earlier and were therefore not utilized.

Contact spring deflections

After membrane contact, the region from the pusher to the push-button acts as a cantilever beam with spring stiffness given by

$$k_{contact-spring} = \frac{F}{\delta} = \frac{3EI}{(L/2)^3}, \tag{5.2}$$

where F is the force on the push-button, δ is the deflection of the cantilever beam (contact spring deflection), E is the Young's modulus of the contact spring material, I is the beam bending moment of inertia, and L is the length of the contact spring from the rotor center to the push-button.

The contact spring and the membrane act like springs in series, as shown in

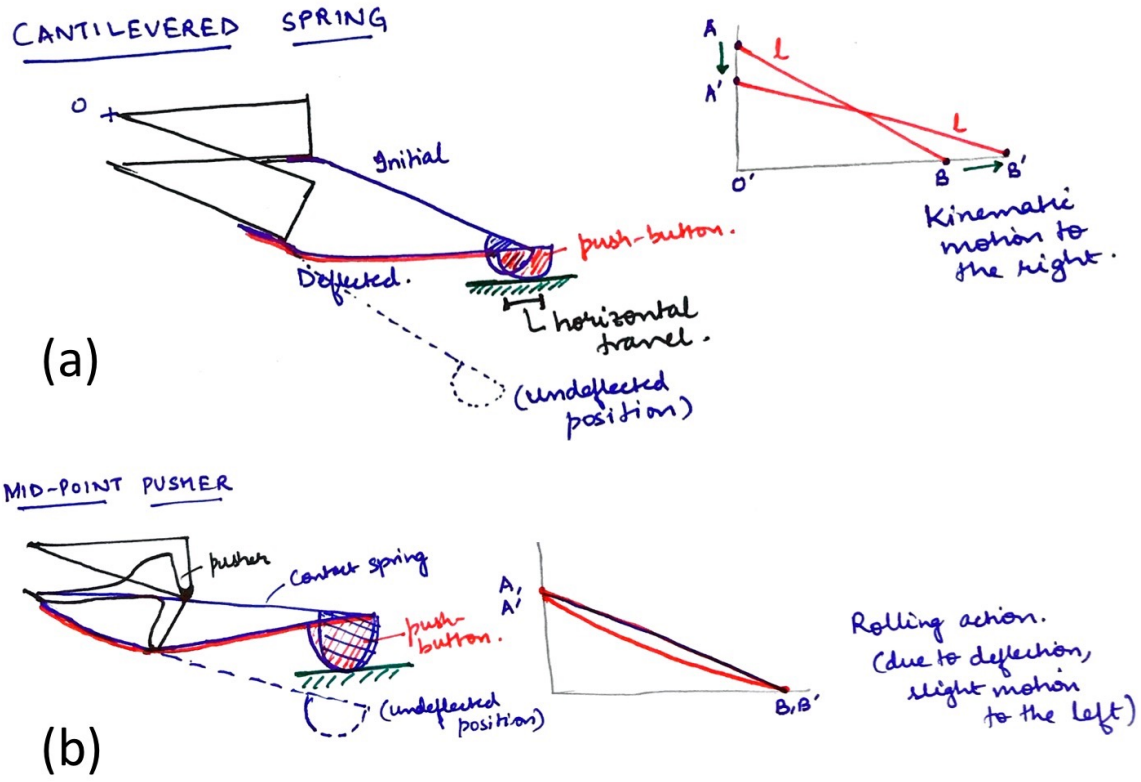

Figure 5-17: Comparison between (a) a cantilevered pusher, and (b) a mid-point pusher. Kinematically, the cantilever at the push-button will move horizontally to accommodate the reduction in vertical height at the rotor. The mid-point pusher minimizes the vertical downward motion by keeping the other end close to the pivot point and consequently minimizes the horizontal motion. In addition, the contact stiffness of the cantilevered spring is almost 8 times the contact stiffness of the mid-point pusher design.

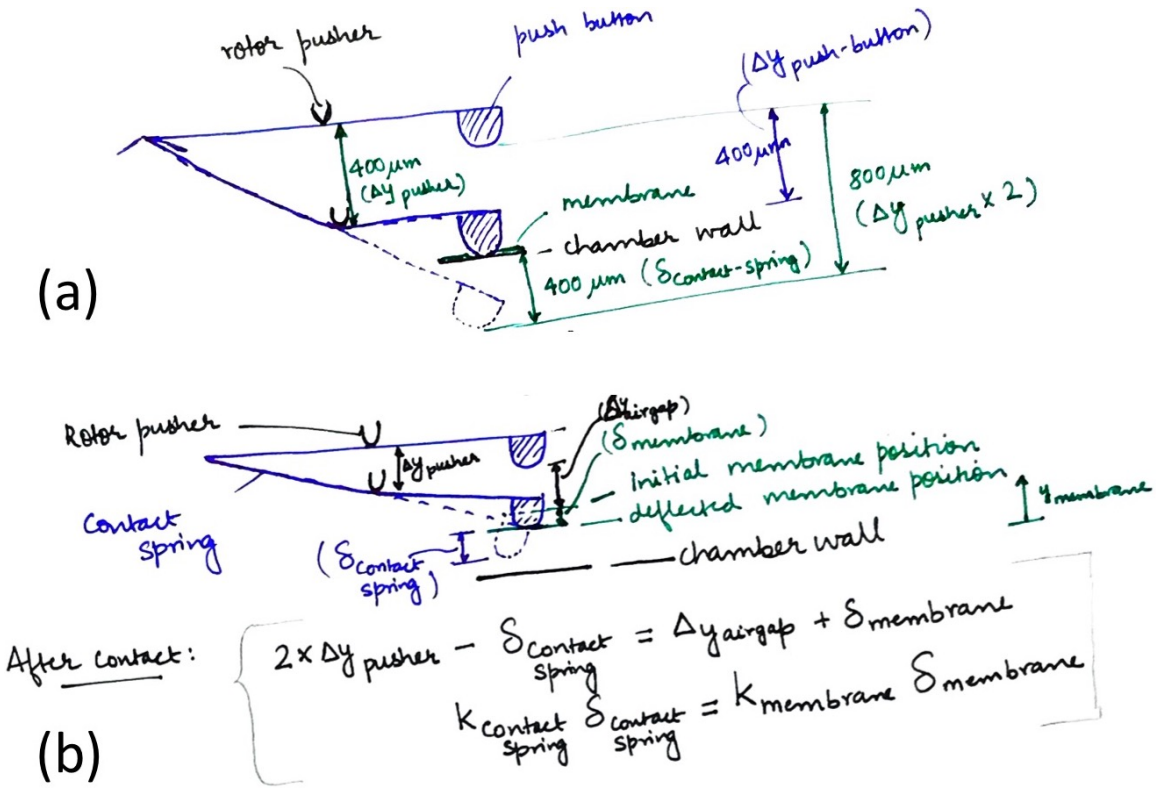

Figure 5-18: Deflection of contact spring with the pusher pushing at the middle of the contact spring.
(a) Final deflection state. The rotor is latched on the left side stator pole face and the pusher moves down by 400 µm, fully deflecting the membrane to make contact with the chamber walls. The undeflected position of the push-button would have been 800 µm below its initial position. The deflected contact spring is parallel to horizontal due to the upwards force from the membrane and then the pump chamber walls at the push-button. Then, the deflection of contact spring is 800 µm - 400 µm = 400 µm.
(b) Intermediate deflection state of the contact spring and the membrane. The push-button travels a vertical distance Δy_{airgap} before making contact with the membrane. The unonstructed displacement of the push-button would have been $2 \cdot \Delta y_{pusher}$. After contact, the membrane resists the push button displacement. The membrane deflects down by $\delta_{membrane}$. The push-button displacement after contact with the membrane is $\Delta y_{airgap} + \delta_{membrane}$. The deflection in the contact spring is then given by the difference between the unobstructed displacement and the actual displacement, that is, $\delta_{contact-spring} = 2 \cdot \Delta y_{pusher} - (\Delta y_{airgap} + \delta_{membrane})$. The contact spring and the membrane act as springs in series.

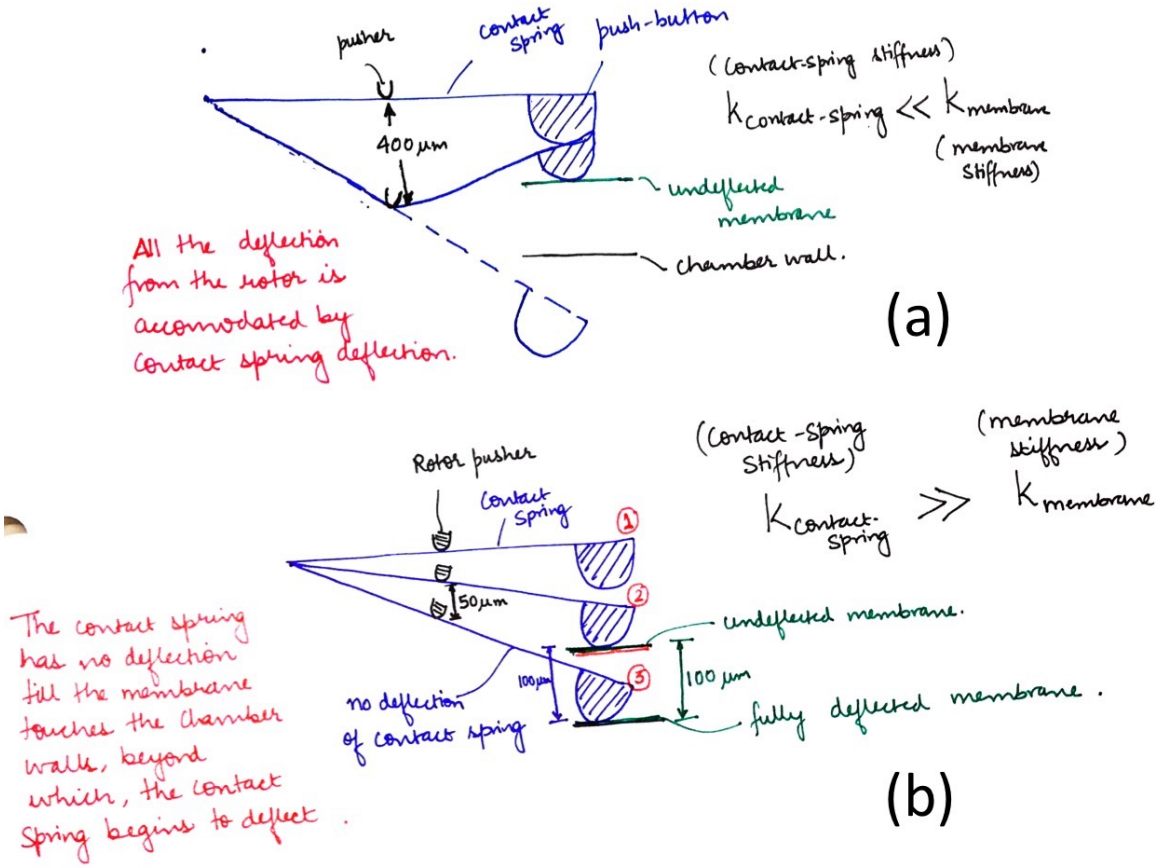

Figure 5-19: Two limiting cases of the deflection of contact spring and membrane. (a) The membrane is much stiffer than the contact spring. Then, the displacement of the rotor (pusher) is accommodated by the deflection of the contact spring. Membrane hardly deflects.
(b) The contact spring is much stiffer than the membrane. Then, the displacement of the rotor (pusher) is accommodated by the deflection of the membrane. Then the membrane deflects twice the displacement of the pusher after contact. Contact spring hardly deflects.

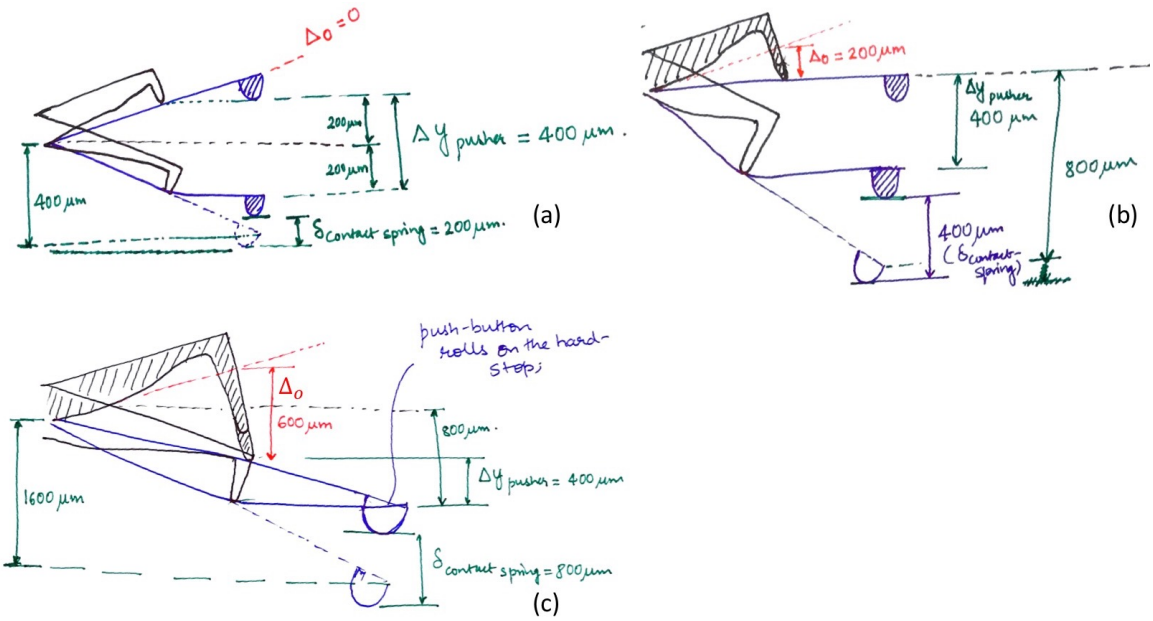

Figure 5-20: Increase pusher length to increase contact spring deflection.
(a) No offset (Δo). The maximum deflection of the contact spring is 200 µm.
(b) $\Delta o = 200$ µm. The maximum deflection of the contact spring is 400 µm.
(c) Limiting case, $\Delta o = 600$ µm. Maximum deflection of the contact spring is 800 µm.

Figure 5-18. As the pusher moves down by a certain amount, Δy_{pusher}, the push-button moves down by $2 \cdot \Delta y_{pusher}$ if unobstructed. The actual motion would be smaller due to resistance by the membrane. At the end of motion, when a side of the rotor (pusher) is in the lower-most position, $\Delta y_{pusher} = 400$ µm, the contact spring should be parallel to horizontal, as shown in Figure 5-18 (a). This position would be the lowermost position of the pump/valve chambers and hence is a hard-stop for the membrane and the contact spring deflection. If unobstructed, the position of the push-button would be at 800 µm, but due to being stopped by the chamber walls, it is at 400 µm, keeping the slope 0. Hence the contact spring deflection is 800 µm - 400 µm = 400 µm. Figure 5-19 shows the limiting cases for the relative stiffnesses of the contact spring and the membrane.

This spring deflection can be increased by giving an offset deflection in the vertical direction by increasing the length of the pusher by Δo, as shown in Figure 5-20. In our electromagnetic design, we considered a $\Delta o = 200$ µm. The maximum spring deflection achievable then is $\delta_{contact} = 400$ µm. In this configuration, the contact

spring is at the neutral position line when the rotor is at the top most position. In manufacturing, we can implement the pusher length offset, Δo either by increasing the length of the pusher or by using thin shim strips of the required thickness between the pusher and the contact spring.

After contact of the push-button with the membrane, the contact spring and membrane have the same force F and distribute the deflections (Figure 5-18). Let the membrane deflection be $\delta_{membrane}$ (maximum value = 0.1 mm), and the deflection of the contact spring be $\delta_{contact-spring}$. Further, define the total deflection at the push-button as δ_{cm}. The equation describing the forces and deflections is then,

$$F = k_{contact-spring}\delta_{contact-spring} = k_{membrane}\delta_{membrane} = k_{series}\delta_{cm}, \tag{5.3}$$

where k_{series} is the series spring-stiffness of the contact spring and the membrane together given by,

$$k_{series} = \frac{k_{contact-spring}k_{membrane}}{k_{contact-spring} + k_{membrane}}. \tag{5.4}$$

The deflections are related as,

$$\delta_{cm} = \delta_{contact} + \delta_{membrane} \tag{5.5}$$

We can then estimate the stiffness required of the contact spring. For a deflection value of the contact spring, $\delta_{contact-spring} = 0.4$ mm, the membrane should deflect by $\delta_{membrane} = 0.1$ mm. Since the force in the contact spring and the membrane is the same (Eq. 5.4), the stiffness of the contact spring is,

$$k_{contact} = \frac{k_{membrane}\delta_{membrane}}{\delta_{contact-spring}}. \tag{5.6}$$

Substituting the values, with $k_{membrane} = 10$ N/mm, we get, $k_{contact} = 2.5$ N/mm. This is the lower bound of $k_{contact}$ and is determined by the ability to deflect the membrane within the deflection range allowed (1 N for 0.4 mm deflection). The upper limit of $k_{contact}$ is determined by the force available from the electromagnetic

latching force between the rotor and the stator pole faces.

As shown in Figure 5-21 and 5-22, the elastomer below the push-button has negligible stiffness till a critical deflection. Once the critical deflection is crossed, the stiffness drastically increases and the elastomer acts like a rigid body. This critical deflection is assumed to be equal to half the thickness. For our analysis, the overall effect of the elastomer at the end of the rotor stroke is that is reduces the total availabe deflection of the contact spring by half the thickness of the elastomer.

If the contact spring is stiffer, the membrane bottoms out by touching the chamber walls before the rotor has completed its stroke. Once that happens, the additional displacement of the rotor is accommodated by the deflection of the contact spring. If we have a large excess latching force, then making the contact spring stiffer helps increase the energy storage in the spring. This stored energy is released in the reverse stroke and increases the speed of latching. Conversely, for a given speed of latching, the Amp-turns required would be reduced. The storage of energy in the springs also reduces the force on the rotor when it is neat the permanent magnets and helps reduce the velocity of impact of the rotor with the stator pole face.

For sizing the contact spring, the length is twice the distance between the rotor center to edge, i.e., $L = 25$ mm. We use spring steel as it has a high yield strength of 400 MPa. It has a young's modulus, $E = 200$ GPa. To get a stiffness greater than 2.5 N/mm, a thickness, $t = 0.015$ in (0.381 mm), and width, $w = 3$ mm was chosen (Figure 5-15). The resulting bending moment of inertia, I is 1.4×10^{-2} mm^4, and the stiffness of the contact spring, $k_{contact-spring}$ is 4.2 N/mm.

EM actuator elements during motion: Forces, deflection and dynamics

To simplify the dynamic modeling, we estimate a linear force displacement curve for each of the spring elements and derive the stiffness values. We do the same for the force due to the permanent magnets, which behave like springs with negative stiffness. When there is current though the winding, we approximate that the forces go up or down with a constant offset of 2N (Figure 5-23). This is obtained by fitting a linear curve to the attractive magnetic force difference vs. rotor position with and

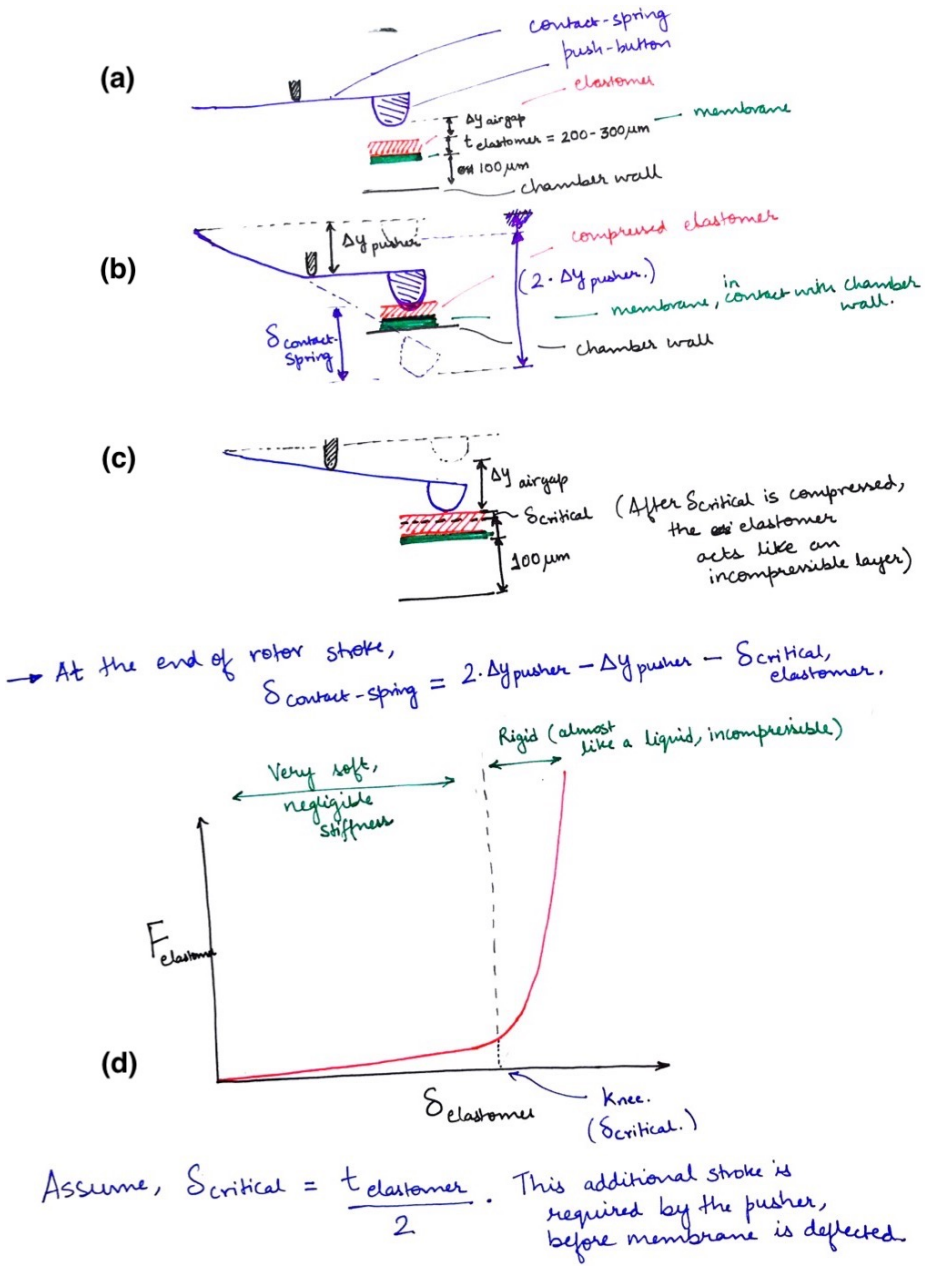

Figure 5-21: Details of the elastomer between the push-button and diaphragm. (a) Beginning of the stroke. (b) End of stroke, contact pin is horizontal. The elastomer is deflected. (c) Push-button just contacts the membrane, after air-gap motion. (d) A model of elastomer layer deflection. Till a critical deflection value, the elastomer acts very soft with negligible stiffness. Once the critical deflection is crossed (assumed to be half the elastomer thickness), the stiffness drastically increases and the elastomer acts almost like a rigid body.

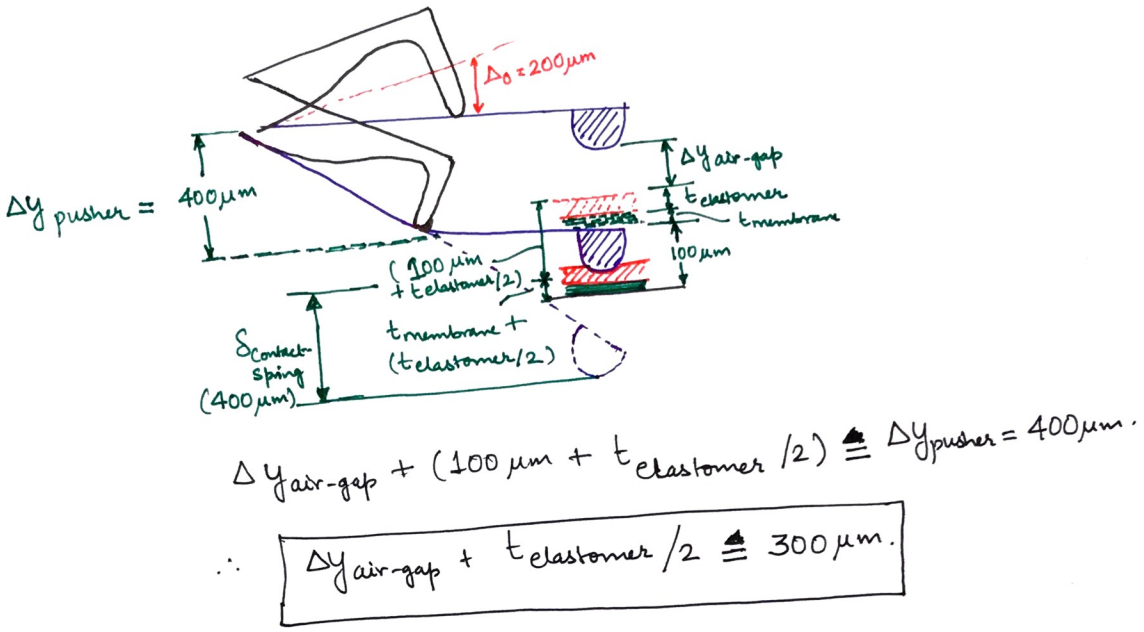

Figure 5-22: Pusher offset along with elastomer considerations. As shown in Figure 5-21, the critical deflection of the elastomer is assumed to be half the thickness. This consideration places a limit on the airgap (the displacement of the push-button for which there is no contact of the push-button with the elastomer) displacement.

without Amp-turns, shown in Figure 5-6 and 5-8 for the case of x_{off} of 0.5 mm and y_{off} of 0.2 mm. The stiffness values used are tabulated in Table 5.1. The model neglects frictional forces in the system.

Table 5.1: Linearized stiffness [N/mm] used for dynamics modeling. All stiffnesses are referenced to act at the pusher (rotor contact point with the contact spring).

Permanent magnet	-15
Membrane	10
Contact spring	4.2
Notch flexure	0.8

As shown in Figure 5-18, once the push-button makes contact with the membrane, the contact spring and membrane are like springs in series and the force is the same in both springs. The push-button moves twice the amount of the rotor if unobstructed (Section 5.3.2).

In the discussions below, the stroke considered is the switching of the rotor from contacting the right pole face to making contact with the left pole face. All forces

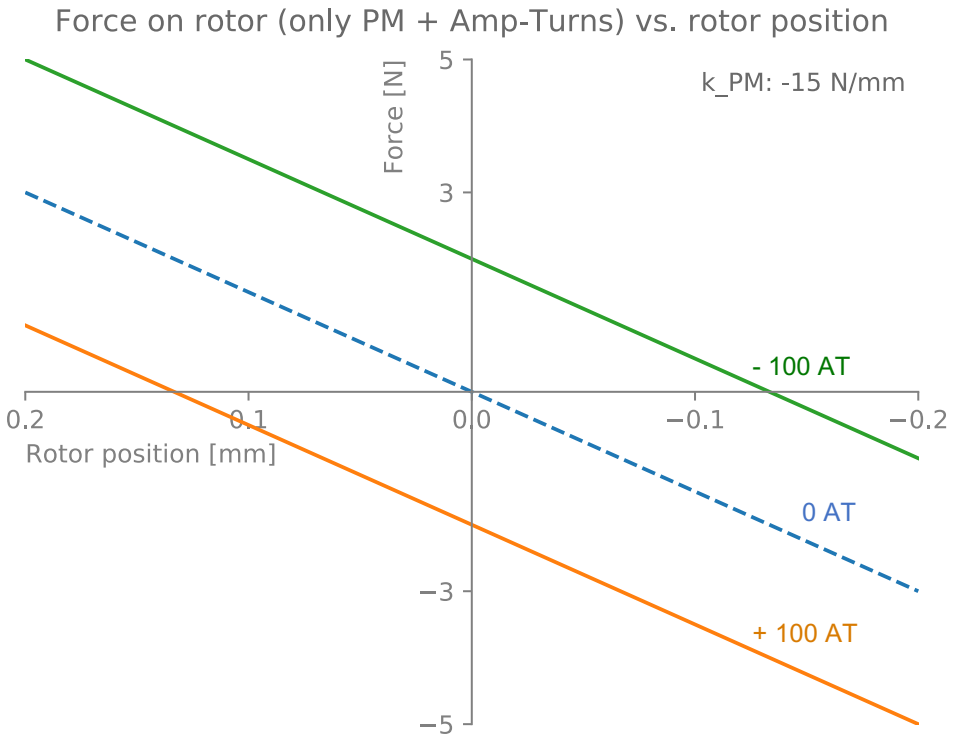

Figure 5-23: Net force on the rotor right-side due to the permanent magnet (PM) as it depends on the winding current vs. rotor position. Positive force is in the upward direction on the rotor right-side. The rotor position is the vertical displacement of the rotor right-side from the neutral position. When there is no current in the winding, the latching force is 3 N at ± 0.2 mm displacement associated with pole face contact. The addition of ± 100 Amp $-$ turns of current offsets the force due to the PM by ± 2 N, thus causing almost enough force to switch the rotor. Spring forces have not yet been taken into account in this plot.

and displacements are referred to the right pusher of the rotor. The corresponding displacement of the right rotor (pusher) is from +0.2 mm to -0.2 mm. When the push-button is in air, the force on the push-button is negligible and therefore, as the rotor moves down by an amount Δy_{pusher}, the push-button moves down by an amount of $2 \cdot \Delta y_{pusher}$.

Referring to Figure 5-22, total rotor stroke is 0.4 mm. The maximum displacement of the push-button is limited to 0.4 mm by the chamber walls once the membrane is fully deflected. When the rotor latches to the left side, the contact spring should be parallel to horizontal (Section 5.3.2). The membrane, when it is not deflected, sits 0.1 mm above the chamber walls. Once the push-button comes in contact with the membrane, the contact spring and the membrane come in series and the deflection gets distributed. The displacement of the push-button, $y_{push-button}$ is,

$$y_{push-button} = \min(\Delta y_{airgap} + \delta_{membrane}, 0.4). \tag{5.7}$$

where, Δy_{airgap} is the airgap motion, and $\delta_{membrane}$ is the membrane deflection. The push-button displacement is limited to a maximum value of 0.4 mm.

The deflection in the contact spring is then the difference between the total displacement ($2 \cdot \Delta y_{pusher}$) and the push-button displacement ($y_{push-button}$).

$$\delta_{contact-spring} = 2 \cdot \Delta y_{pusher} - y_{push-button} \tag{5.8}$$

The relation between the membrane deflection and the contact-spring deflection, from Equation 5.6 is,

$$\delta_{membrane} = \min\left(\frac{k_{contact-spring}}{k_{membrane}} \delta_{contact-spring}, 0.1\right) \tag{5.9}$$

where, $k_membrane$ and $k_{contact-spring}$ are the membrane and contact-spring stiffnesses.

We now have all the relations to calculate $y_{push-button}$, $\delta_{membrane}$ and $\delta_{contact-spring}$ as a function of rotor (right pusher) displacement, Δy_{pusher}.

The modeled push button displacement and the membrane and the contact spring

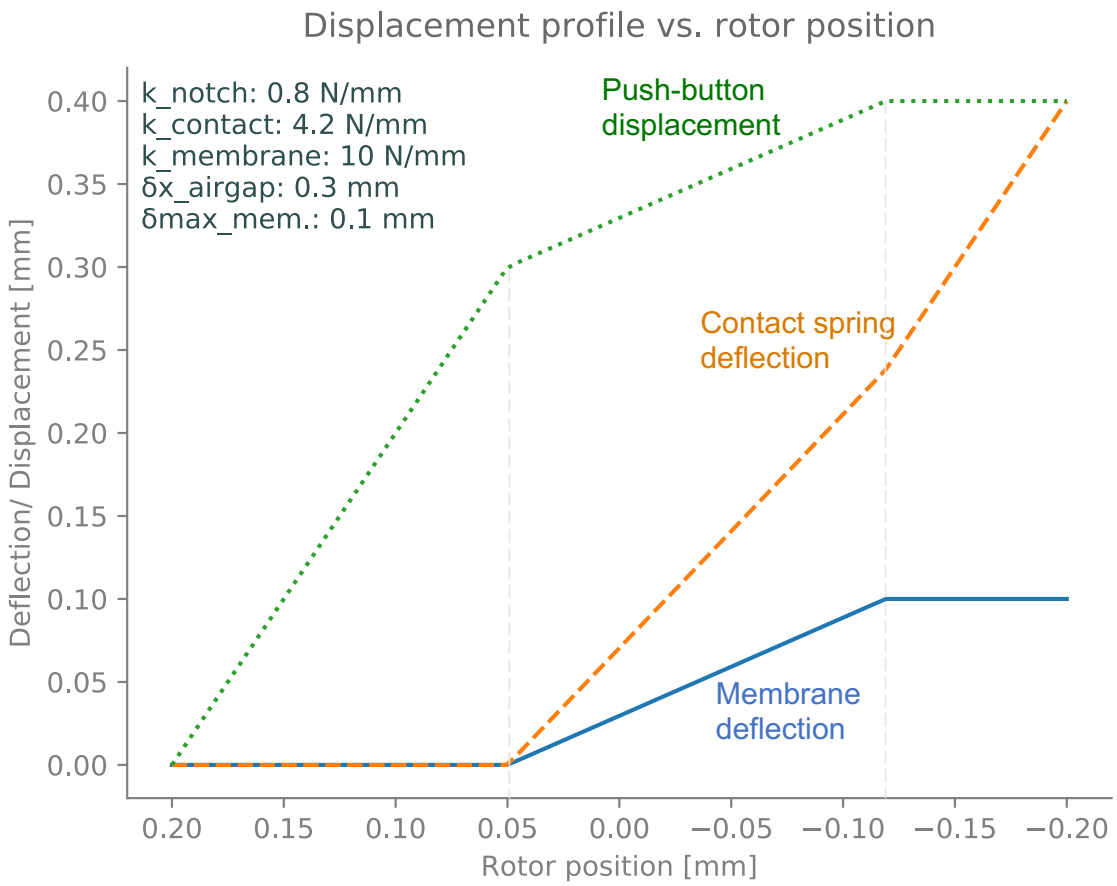

Figure 5-24: Displacement of push-button, and deflection of contact-spring and membrane during rotor switching. The push-button moves freely through the air-gap until it comes in contact with the membrane. Then the displacement slope reduces due to resistance by the membrane and by the chamber walls after the membrane bottoms out, at which point the displacement is saturated at 0.4 mm.

deflections are shown in Figure 5-24. When the push-button is traveling in air, till 0.3 mm, the deflection in the membrane and the contact spring is 0 (Figure 5-25). After contact, the membrane and the contact spring deflect together until the membrane touches the chamber wall. After that, the push-button stays at the same vertical position due to the rigid chamber wall and the contact spring continues to deflect until it reaches a maximum deflection of 0.4 mm.

As shown in Figure 5-25, when the rotor is latched on the right, the contact spring on the left side is in its maximum deflected state. The deflection of the membrane, contact spring, and notch flexure is given in Figure 5-26. The corresponding forces

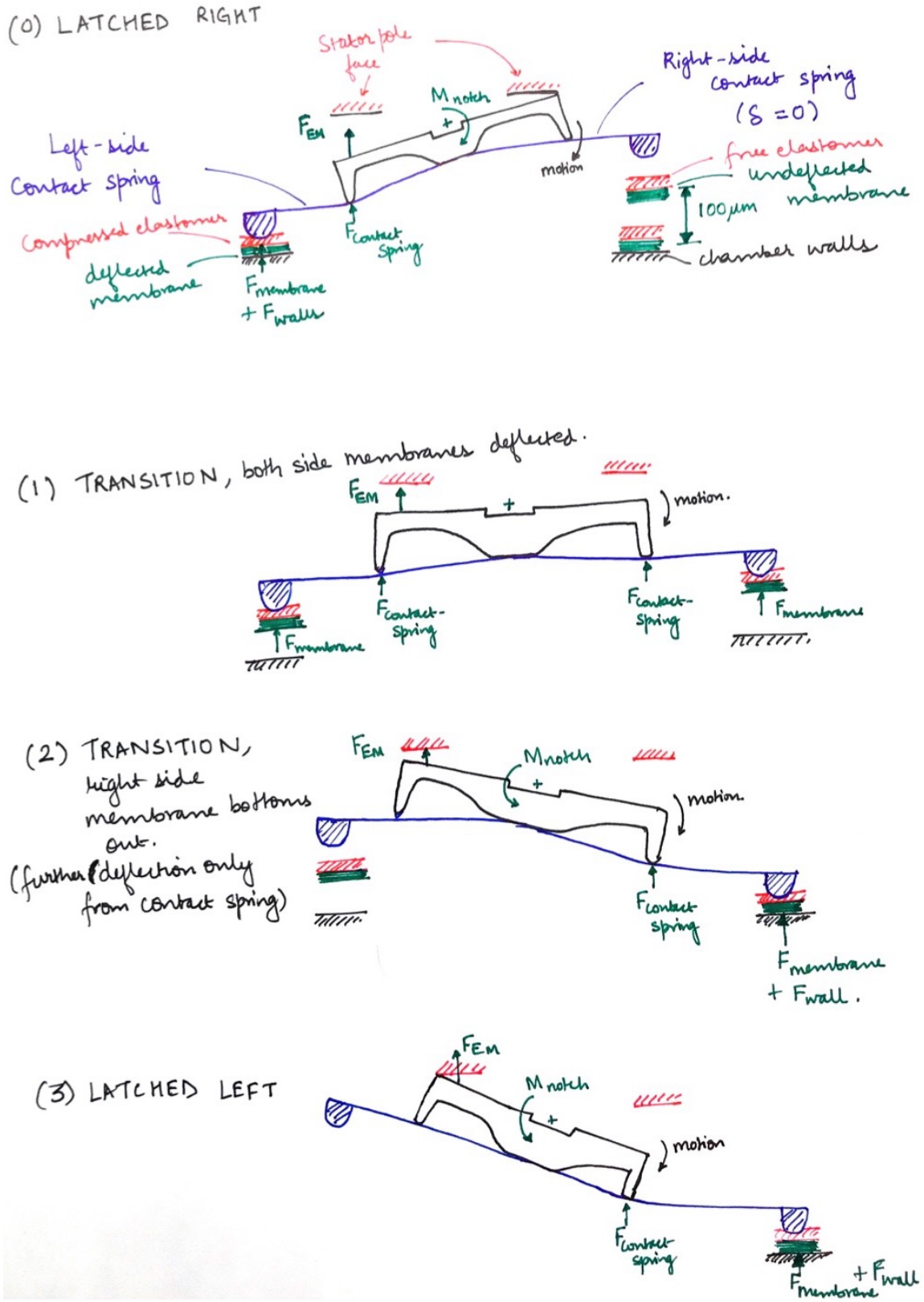

Figure 5-25: The regimes of operation within a rotor stroke, switching from contacting the right pole face to contacting the left pole face.

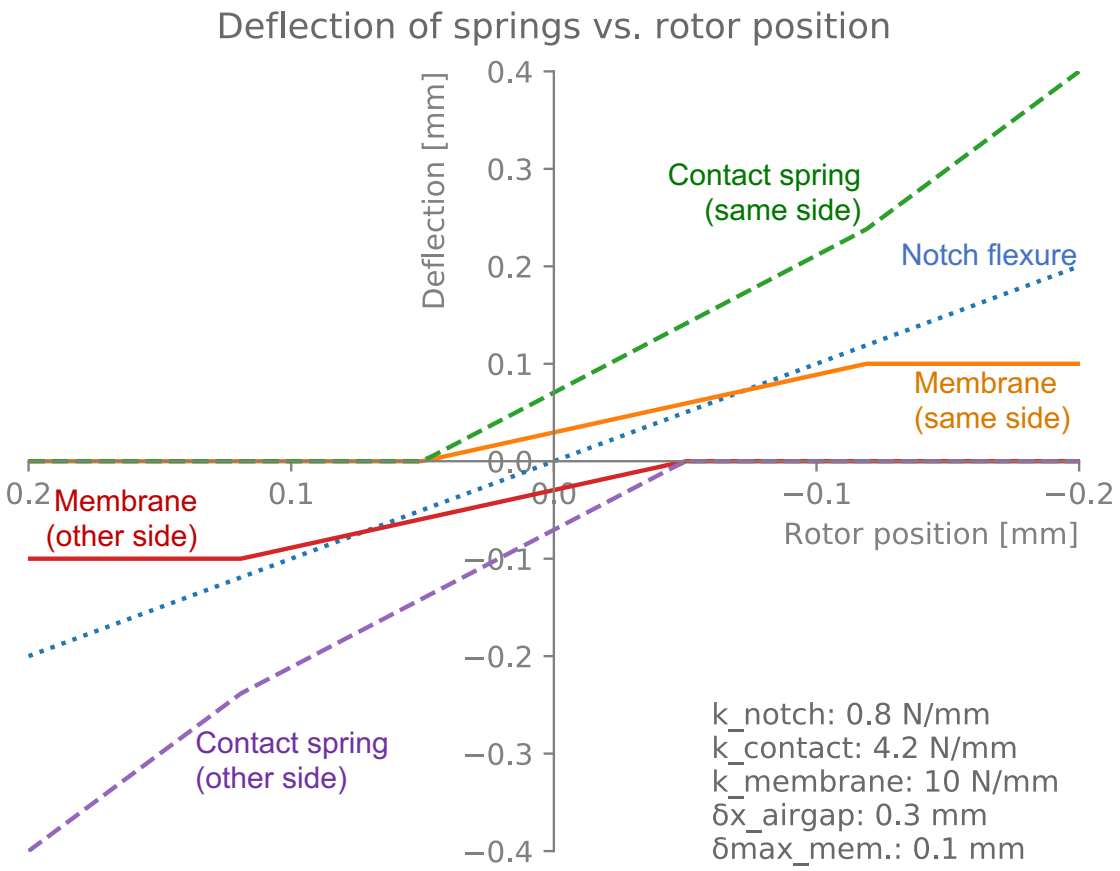

Figure 5-26: Deflection of springs during rotor switching from the right to the left pole face. When the rotor is latched to the right, the spring elements on the left are deflected. Membrane deflection saturates at 0.1 mm, the notch flexure moves along with the rotor and hence deflects an equivalent ±0.2 mm. Contact springs deflect 0.4 mm keeping push-button vertical at the end of rotor stroke. Note the larger displacements and hence deflections in the push-button and contact springs are due to the larger radius from the center of rotation as compared with the pole face.

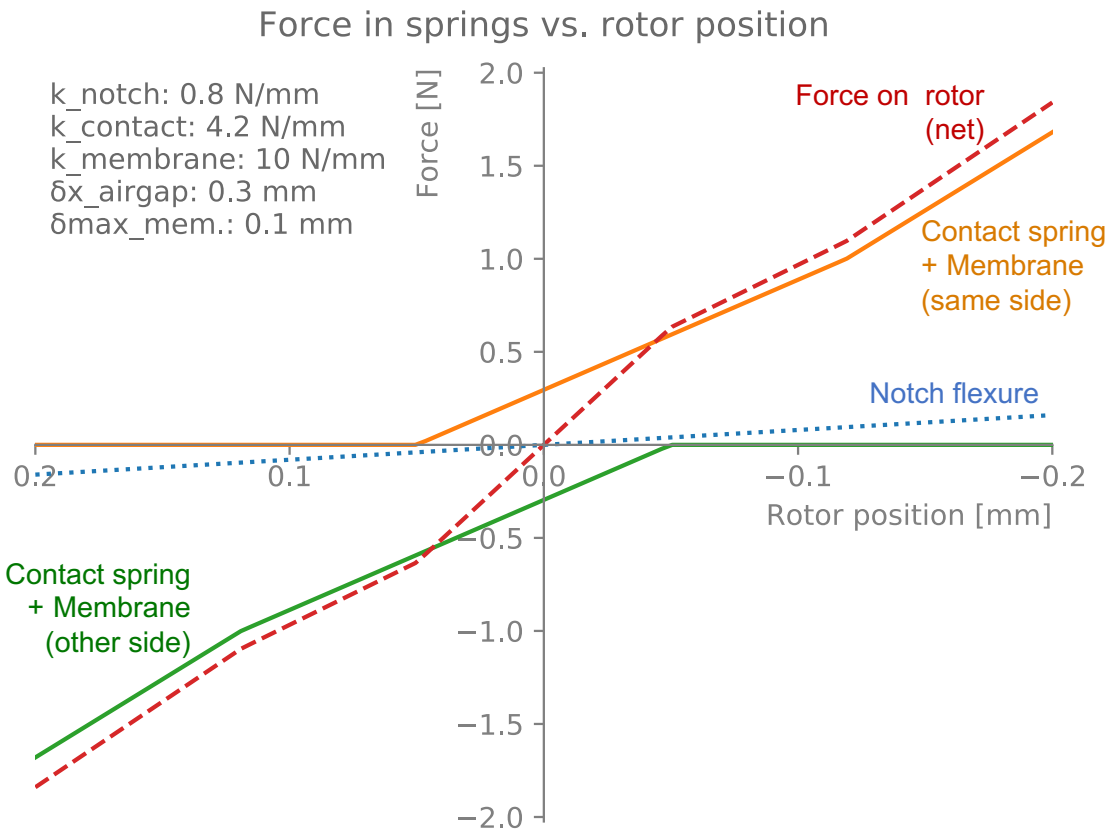

Figure 5-27: Corresponding forces in the springs and the total force on the rotor referred to the right pusher location. The maximum force on the rotor is 1.7 N at end of stroke.

in these spring elements is shown in Figure 5-27. All forces are referenced as if acting on the right side rotor pusher, with the up as the positive direction.

When the rotor is in contact with the right pole face, the springs on the left side are deflected which try to bring the rotor down. On the other hand, when the rotor is in the lower most position on the right side (in contact with the left pole face), the springs on the right side are deflected and try to push the rotor back up (Figure 5-25).

To simplify the modeling, symmetric deflections and stiffnesses on the left and right sides are considered. Figure 5-27 shows the maximum force on the membrane at the end of deflection to be about 1.7 N. The force due to the notch flexure (0.15 N) is small compared to the forces in other spring elements and could have been neglected from the model.

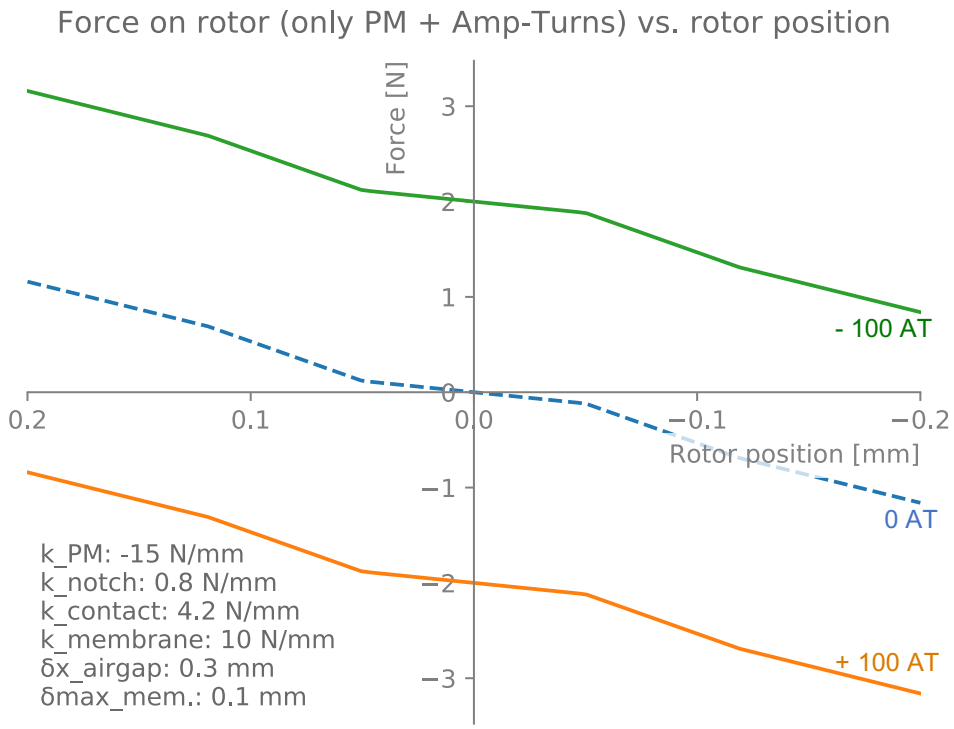

Figure 5-28: Net force on the rotor including the effect of the electromagnet (Figure 5-23 and the springs (Figure 5-27). The net latching force is reduced from 3 N (PM only) to about 1 N.

The spring forces can be superposed upon the electromagnetic forces, as modeled in Figure 5-23 to obtain the net force on the rotor as shown in Figure 5-28. When there is no current in the winding and the rotor is in contact with the top pole face, there is a net latching force of 1N. This is the buffer in force to accommodate variations in forces due to uncertainties in material properties, manufacturing and alignment. When there is a positive current of 100 Amp-turns in the winding, the net force becomes negative, which pulls the rotor down and causes it to move into latching on the other side. After the rotor crosses the neutral position, the net force is negative even if the current is turned off and the rotor will proceed to latch on the left side pole face.

Now that we have the net force on the rotor at every position in its stroke, we can find the motion parameters - position, velocity and acceleration of the rotor with time. We ignore damping and friction effects which would act to reduce the net force

on the rotor to get a rough estimate of the switching time.

The angular acceleration of the rotor is,

$$\alpha_{rotor} = \frac{F_{net_{rotor}} \frac{L}{2}}{I_{rotor}} \tag{5.10}$$

where, $F_{net_{rotor}}$ is the net force on the rotor at the right pusher, $L/2$ is approximately the radial distance of the pusher from the pivot point and I_{rotor} is the rotational moment of inertia of the rotor. Since the mass of the contact springs and the contact push-buttons is negligible compared to the rotor, only the rotor mass is considered in calculating the rotor moment of inertia. The rotor is approximated as a slender bar of mass m_{rotor} and length L, and its moment of inertia is,

$$I_{rotor} = \frac{m_{rotor} L^2}{12}. \tag{5.11}$$

The acceleration at the right pusher then is $\ddot{y} = \alpha_{rotor}(L/2)$. Given the net forces defined above, we now have an expression for the acceleration of the rotor at every point y in its stroke. The position as a function of time is found using the following set of equations.

$$\begin{aligned} \ddot{y} = \frac{d\dot{y}}{dt} = \frac{d\dot{y}}{dy}\frac{dy}{dt} = \dot{y}\frac{d\dot{y}}{dy} \\ \int_{v_0}^{v} \dot{y} \cdot d\dot{y} = \int_{y_0}^{y} \ddot{y} \cdot dy \\ \frac{v^2(y) - v^2(0)}{2} = \int_{y_0}^{y} \ddot{y} \cdot dy \end{aligned} \tag{5.12}$$

The initial velocity $v(0)$ is 0 and the right-hand side is numerically integrated to get velocity as a function of position $v(y)$. To find the position from velocity, we have,

$$v(y) = \frac{dy}{dt}. \tag{5.13}$$

Here, we integrate dt to get the time on the left-hand side and integrate $dy/v(y)$ to

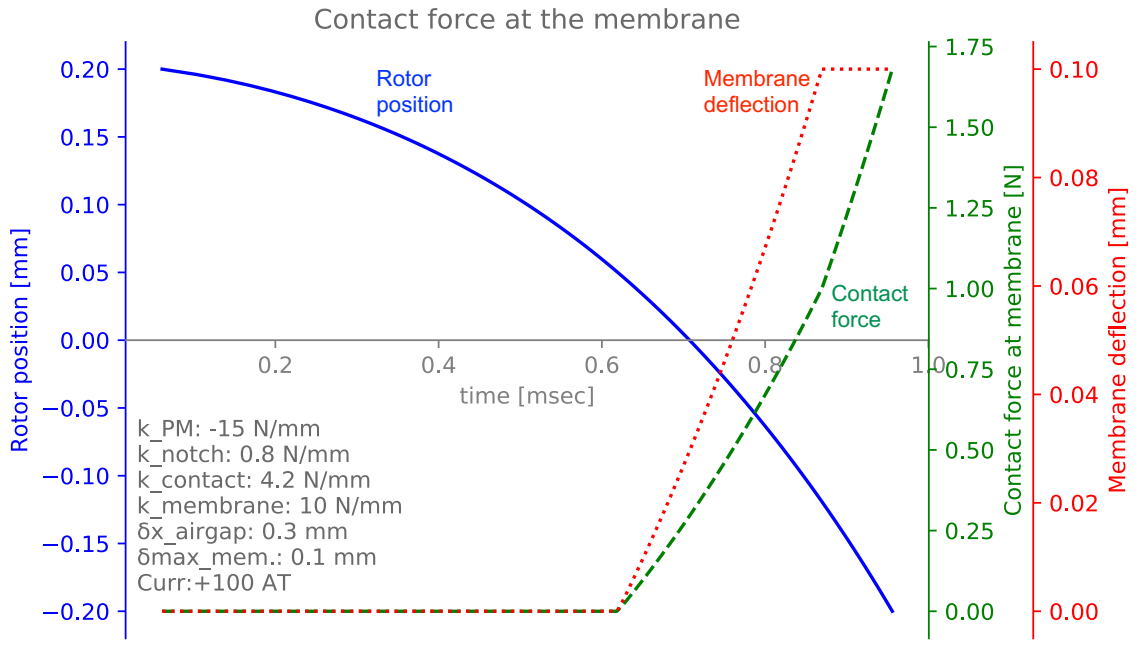

Figure 5-29: We assume that the rotor is initially latched to the right stator pole face. At time t=0, a current of 100 A-turns is applied in the winding, causing the rotor to begin to switch to the left side. Modeling predicts that the rotor should take about 1 msec for switching. The net force (sum of contact spring force and the electromagnetic (EM) force) acting on the rotor at the beginning of the stroke is small. The EM force rapidly increases as the rotor gets closer to the left side. This increasing force causes net acceleration of the rotor towards the other side and the velocity of the rotor keeps increasing. Rotor position is measured as displacement of the rotor measured at the right pusher. 0.2 mm stands for contact with the right pole face and -0.2 mm for contact with the left pole face.

get the position on the right hand side. That is,

$$\int_0^t dt = \int_{y_0}^{y} \frac{dy}{v(y)}. \tag{5.14}$$

Again, by numerically integrating the right-hand side, we get the time vector as a function of position, $t(y)$. Therefore, we now have position and time information along the rotor stroke.

A plot of the rotor position with time and the corresponding membrane deflection and contact force at the membrane is given in Figure 5-29. The model predicts that the stroke should be completed in about 1 msec. The maximum contact force on the membrane is around 1.7 N, under the reasonable assumption that the spring and the

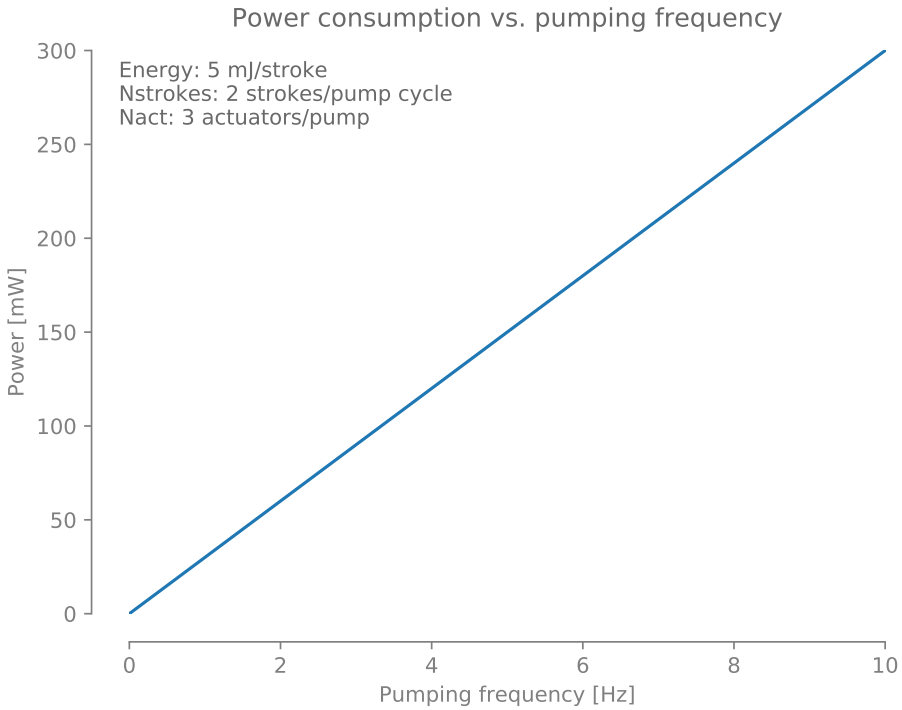

Figure 5-30: Modeled power consumption vs. pumping frequency for the designed EM actuators

push-buttons are massless.

Energy and Power estimates

We can get an estimate of the power consumption per stroke for the actuator. Each pulse would need to be $\Delta t \sim 2$ msec (conservative bound) based on the modeling of Section 5.3.2. The energy input to the actuator is by the current flowing through the winding. If there are 300 turns of wire, then 100 A-turns of current means 0.3 A of current, i flowing through the wire. As a conservative estimate, we assume $i = 0.5$ A if 150 A-turns are required.

We assume conservatively, a winding resistance of 10 Ω. We typically measure the resistance of same number of winding in similar actuators to be about 5–6 Ω. Then, the energy consumption per stroke is,

$$E = i^2 R \Delta t. \tag{5.15}$$

Substituting the values, we get, $E = 0.5^2 \times 1 \times 10^{-3} = 5$ mJ/stroke. We need 3 actuators (valve, pump, valve) for a pump channel. In each pumping cycle, every actuator undergoes two strokes - on and off. Then the power consumption is the product of, the number of actuators and the actuation frequency which is shown in Figure 5-30. In terms of power consumption, it is advantageous to operate the pump at lower frequencies. On the other hand, operating at higher frequencies allows for lower flow pulsatility. At 1Hz actuation, the predicted power consumption is about 30 mW per pump, which is significantly lower than the power consumption of 500 mW per pump for the existing 3-port pneumatic solenoid valves (SMC S070B-6CG). These valves are used to switch between pressure and vacuum for our pneumatic pumps and have a power consumption of 0.35 W per solenoid. Normally in a pump cycle, they are on approximately for half of the pumping cycle time.

5.4 Integration, Manufacturing and assembly of EM actuator pumps

This section describes integration, manufacturing and assembly of the actuator modules and their integration to make an EM pump.

5.4.1 Integration and assembly considerations

To enable pumping with the actuators, we need to locate the injection molded, bonded membrane pump test blocks (Chapter 3), also called the fluidic top-plates. We assemble the actuators such that the push-buttons can deflect the membranes by the desired amount, maintaining the desired deflection geometry of the various spring elements.

We need a rigid reference for the push-buttons, once the membrane is deflected to the chamber walls. Therefore, the plate holder has a thick beam to support the platform, which is shown in Figure 5-31. The plate holder has slots on either side of the beam and is elevated using rubber feet to allow for fluidic connections to the top

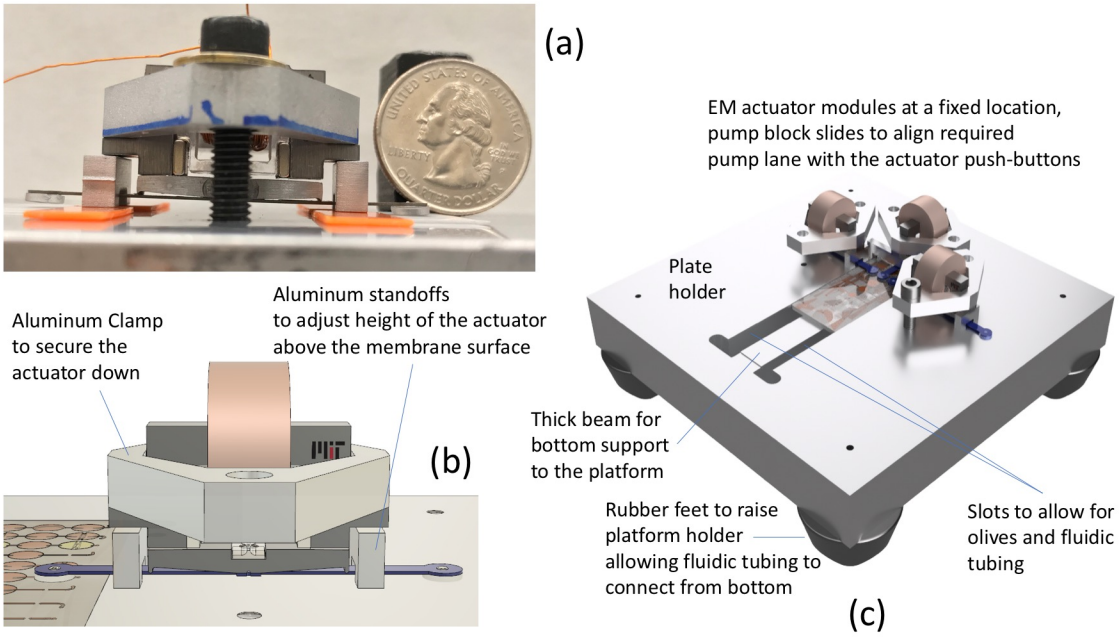

Figure 5-31: Integration of the EM actuator modules into the EM pump. (a) front view of the assembled actuator with the stator resting on aluminum standoffs. An aluminum clamp secures them to the plate holder using two bolts. (b) CAD model showing standoffs and clamps for clarity. (c) CAD model of the assembly showing the plate holder, the actuators and the fluidic top-plate

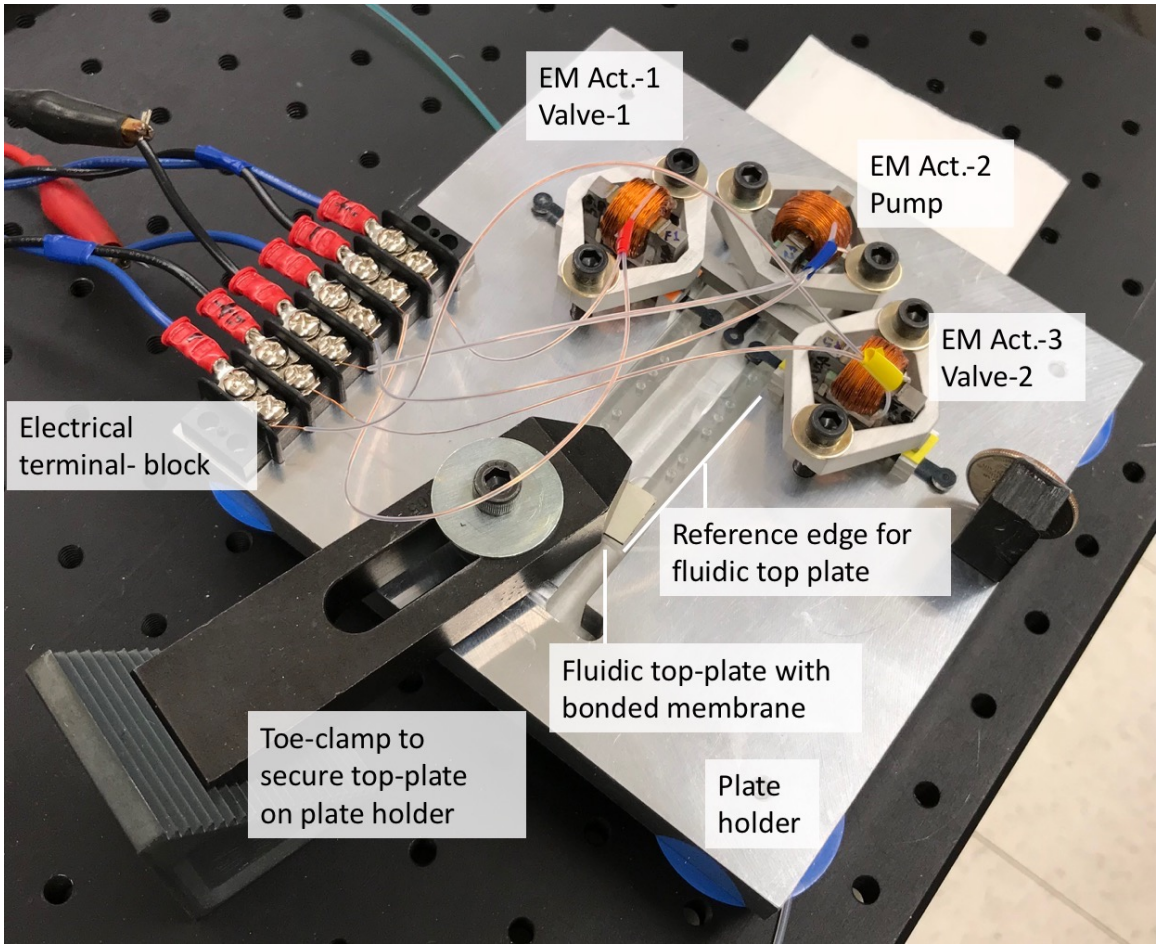

Figure 5-32: Assembled EM pump showing the plate holder, actuator modules, fluidic top-plate secured by a toe-clamp and electrical terminal blocks

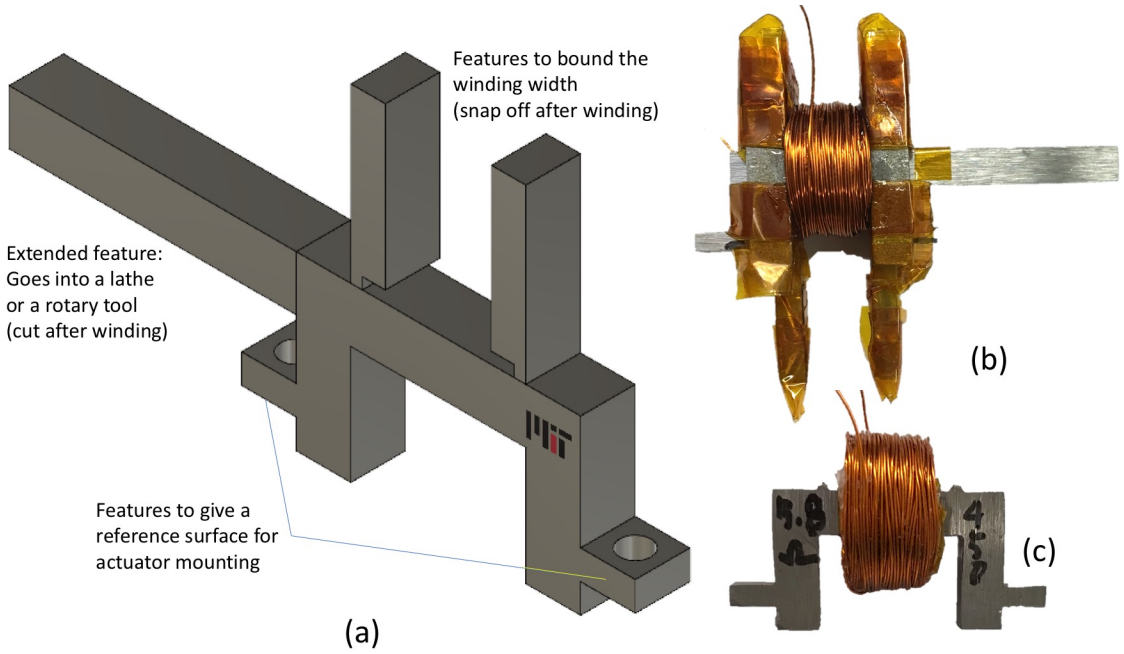

Figure 5-33: Stator modifications to facilitate easier assembly. (a) CAD model describing the modified features. (b) Stator after winding showing template to restrict the winding width. (c) Stator after winding, with the winding-support features removed.

plates from below. The pump block is secured using sandard toe-clamps as shown in Figure 5-32.

The actuator height above the membrane is determined by machined aluminum standoffs with shims. The whole actuator is secured with machined aluminum clamps using bolts which fix into threaded holes in the plate holder. (Figure 5-31). The parallelism of the rotor and the contact spring is achieved by machining flat the mating surfaces of the stand-offs and the stator. There is a clearance fit of the bolt within the holes of the clamps which allows minor adjustments of the actuator in the horizontal plane so as to fine align with the pumps/valve areas on the top plate.

The electromagnetic actuator elements contain design features for better performance and to make fabrication and assembly easier as described below:

1. Stator

   Due to the U-shaped stator design, winding it is a challenge as the coil can't be prewound and then slipped onto the stator, but must be wound in place.

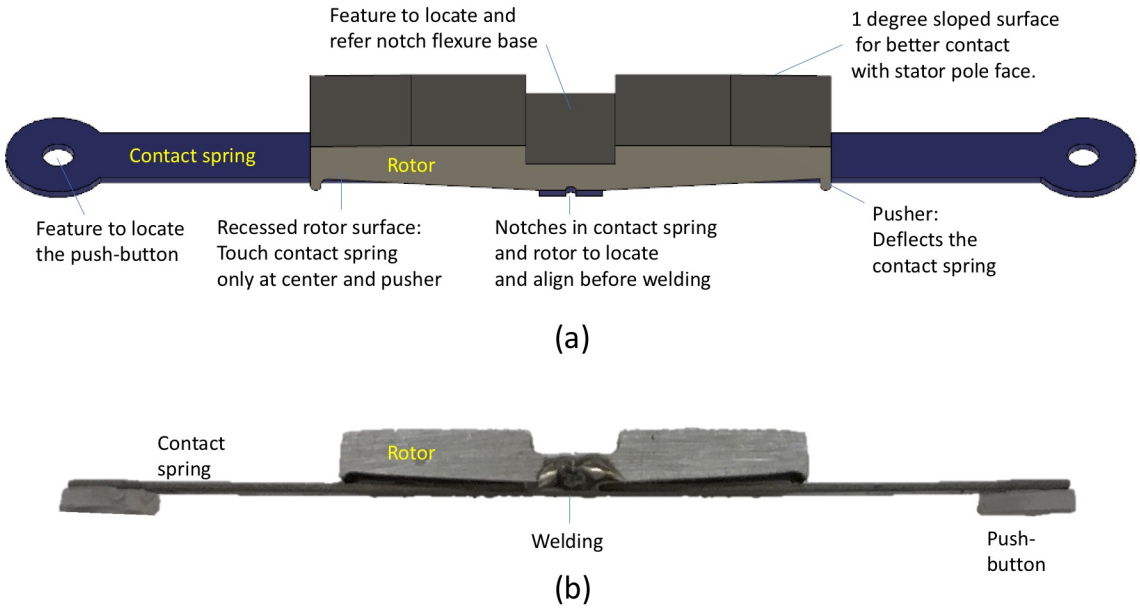

Figure 5-34: Rotor and contact spring showing details of the modifications to improve performance. (a) CAD model describing the various features. (b) Photograph of the assembly showing the push-buttons bonded to the contact spring and the contact spring micro-TIG welded to the rotor.

Therefore, the stator shape is modified as shown in Figure 5-33, which shows the modified features along with the stator after winding and after the removal of the support features. The winding width is smaller than the distance between the stator legs so as to accommodate the notch flexure. This is achieved during winding by using template bars which are secured at the required distance using kapton tape (Figure 5-33 (b)).

2. Rotor and Contact Spring

The faces of the rotor contacting the stator poles are angled to have better contact and minimize the air-gap between the rotor and the stator pole contact faces (Figure 5-34). The rotor also has a recessed surface at the bottom such that the rotor contacts the contact spring only at the center where the two are welded together and at the raised areas (pushers) on either side of the rotor. The rotor also has notch features to locate and align the contact spring before welding. The contact spring has corresponding notch features to locate on the

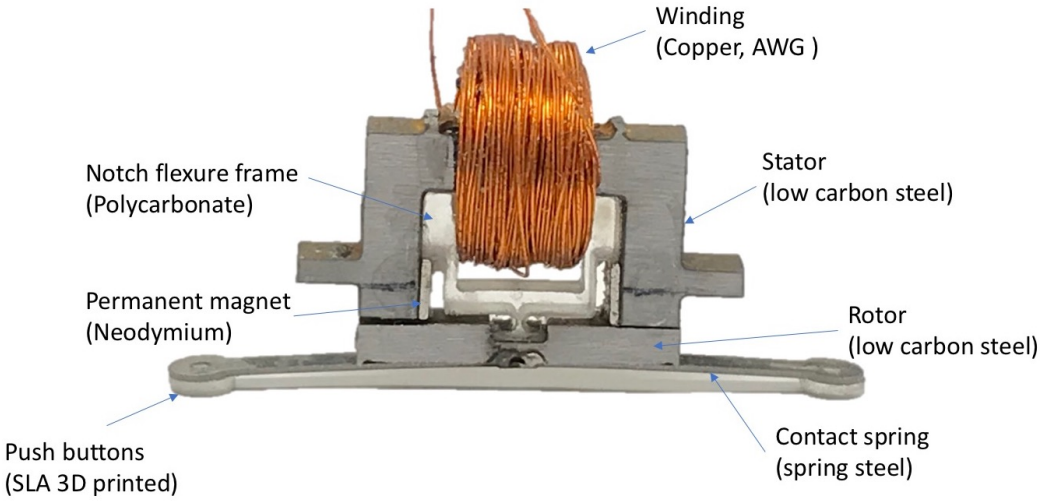

Figure 5-35: Assembled EM actuator module, including the rotor, notch flexure, contact spring and push-buttons.

rotor before welding (Figure 5-34), as well locating features to mount the push-buttons.

5.4.2 Manufacturing of the components

Table 5.2 lists the materials and the fabrication methods used to fabricate the various components.

5.4.3 Assembly of the EM actuator pump

The sequence of steps followed to assemble the EM actuator module and integrating them on the plate holder are described below:

1. The stator with the features as shown in 5-34 is cut from stock low-carbon steel sheet on a water-jet cutter. Then the stator pole faces and the stand-off resting faces are milled on a machine tool to be flat and parallel to each other. The template for winding is then attached using kapton tape and wound manually with the stator held in a rotating tool. For the final prototype, we wound 450 turns using AWG-30 winding wire. After winding, the extra features are removed, as shown in Figure 5-34, by snapping off or cutting on a band-saw.

Table 5.2: Component material and fabrication details

Component	Material	Source	Fabrication
Stator	3/16" Thick Low-Carbon Steel	McMaster-Carr	Water-jet, Milling
Rotor	3/16" thick low-carbon steel	McMaster-Carr	water-jet, milling
Permanent magnet	NdFeB N42 grade 3/16"x3/16"x1/16"	K&J Magnetics	—
Notch flexure	3/16" thick poly-carbonate	McMaster-Carr	Water-jet
Contact spring	0.015" thick 1095 spring steel	McMaster-Carr	Water-jet
Push-button	clear SLA resin	Formlabs, Inc.	SLA 3D-printing
Winding	enamel coated winding wire	McMaster-Carr	—
Platform holder	1/2" thick 6061 aluminum	McMaster-Carr	Milling
Actuator Standoff	1/8" thick 6061 aluminum	McMaster-Carr	Water-jet, Milling
Actuator Clamp	1/4" thick 6061 aluminum	McMaster-Carr	Water-jet
Elastomer layer	sorbothane, silicone	McMaster-Carr	—

2. The rotor is cut from stock low-carbon steel sheet on a water-jet cutter.The contact spring is cut from stock 1095 spring steel sheet on a water-jet cutter. The rotor and the contact spring surfaces are prepared for welding by sanding. They are then bonded together (Figure 5-34) using a micro-TIG welder (Sunstone 200i2 - Pulse Arc/Micro TIG Welder).

3. The notch flexure is cut from stock polycarbonate sheet on a water-jet cutter. The mating surfaces with the rotor and the stator are sanded, as preparation for bonding. First, the notch flexure is bonded to the rotor using cyanoacrylate (Henkel Loctite 4851 and Loctite 408) adhesive. Then, the permanent magnets are placed on the stator with the correct magnet orientation, with both permanent magnets' north pole pointing into the stator. The notch-flexure bonded to the rotor is then aligned in position in the stator. An equal gap of 0.2 mm is maintained between the rotor top-face and the stator pole faces using shim-stock. The notch flexure and the permanent magnets are then adhesively bonded using cyanoacrylate (Henkel Loctite 4851 and Loctite 408) at the same time to the stator and allowed to set. Now we have an assembled EM actuator module (Figure 5-1 and 5-35).

4. The plate holder is milled on a vertical milling machine. Rubber feet are attached to it at 4 corners to give an elevation. Actuator standoffs and clamps (Figure 5-31) are cut from stock aluminum sheet on a water-jet cutter. The bottom legs and top surface of the standoffs are milled flat and parallel on a machine tool.

5. The fluidic top plate is placed on the plate holder with one of its edges in contact with the reference edge on the plate holder (Figure 5-32). The electromagnetic actuator modules are then assembled on the plate holder. The required pump lane is aligned with the nominal center of the push-buttons and the top plate is secured with a toe-clamp (Figure 5-32). The actuators are then adjusted by hand to place the push-buttons over the center of the chambers.

6. Circular discs of 4–5 mm diameter are cut from layer of sorbothane (0.2 - 1 mm) using a knife or a die punch. This disc is then kept underneath the push-button for the valves with the help of forceps. A 4–5 mm circular disk is similarly cut from a thin layer of 0.050 mm silicone and kept under the pump push-button. A larger thickness is used for the valves as the valve deflection depth is smaller and we can thereby get a larger deflection from the contact springs. This is because of the reduced effect of tilt in the push-button with increasing elastomer layer thickness. It is the pressure within the elastomer region that deflects the membrane against the sealing lands and causes it to seal. That is, the elastomer acts as a hydrostatic equalizer for the pressure from the push-button. For the pump chambers, it is important to have a deterministic deflection stroke and therefore, the elastomer layer must be thinner.

7. The stators are positioned at the height required, with shims between the stator and the standoffs. The actuators are then secured in position using actuator clamps (Figure 5-36).

8. An electrical terminal block is attached to an edge of the plate holder (Figure 5-32). The winding leads are affixed to this terminal for easy connection to the amplifiers and to isolate them from any external strains. We now have a fully-assembled single lane electromagnetic pump!

5.5 Testing of the EM actuator

The EM actuators are tested independently, after assembly and before mounting on the plate holder, to measure the latching force and the current required to switch. For this, the actuator is mounted on its side, with the stator legs clamped using toe-clamps (Figure 5-37). A square wave excitation is applied at a low frequency, and the current gradually increased in amplitude till the rotor flips. The current at which the rotor first flips is the minimum current required to flip without any restoring force from deflection of the contact springs. The associated latching force is measured by

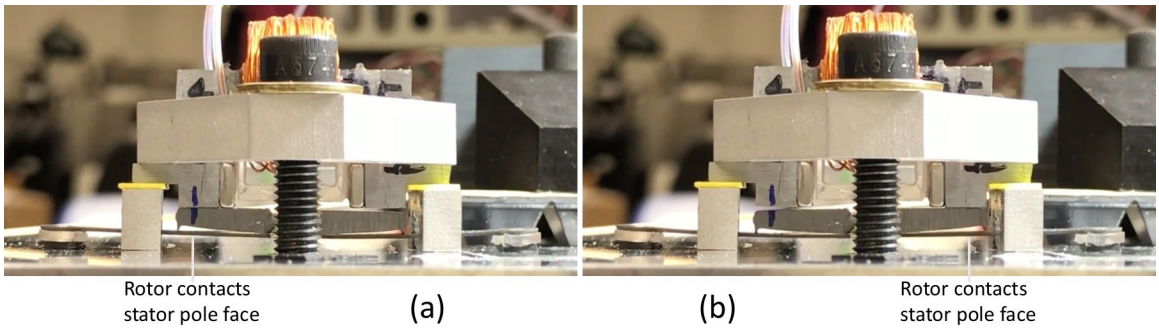

Figure 5-36: EM actuator module assembly for driving the valve, with the actuator height adjusted above the standoffs using shims (yellow). The 0.6 mm sorbothane layer is in black, below the push-button. The actuator is actuated and two states are shown:
(a) Rotor contacting the left stator pole face.
(b) Rotor contacting the right stator pole face.

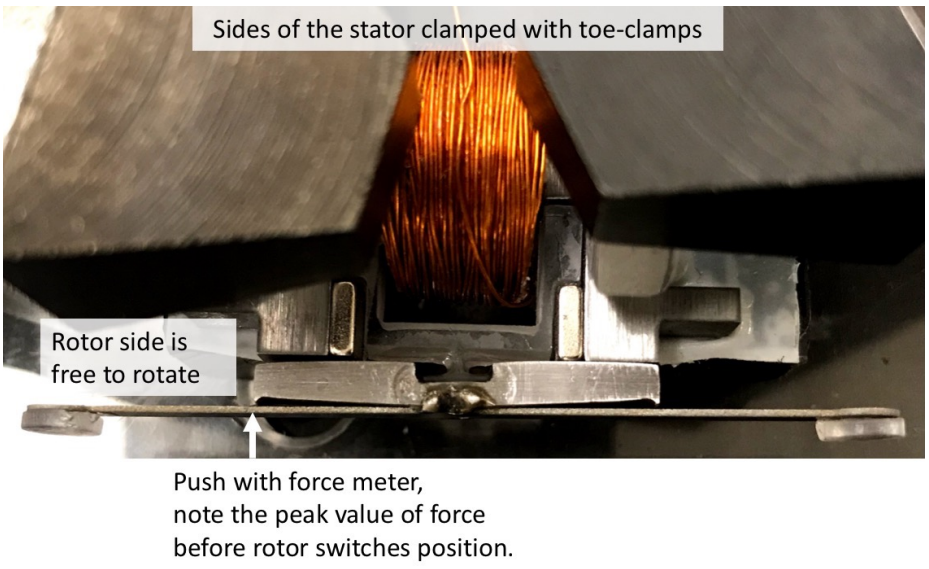

Figure 5-37: Setup for separate testing of EM actuators

pushing on the air-gap rotor side with air-gap slowly increasing force until the rotor flips (Figure 5-37). The threshold force at which the rotor just flips is the latching force.

For the actuators we built, there are 450 turns in winding. The winding resistance varies between 5.5–6 Ω. We observed threshold current to flip of 140–160 Amp-turns and a latching force between 4.3–4.7 N. The actuator inductance was measured to be about 15 mH, using Agilent 4284A Precision LCR Meter. The measurement frequency is 20 Hz, at a current level of 10 mA under the Ls-Rs function. At 100 mA current level, the inductance increases to about 23 mH.

We found a small variation in the minimum flipping current and the latching forces between the left and the right side. This is most likely due to asymmetry in manufacturing to assemble the permanent magnets. When the rotor is close to the pole face, even small differences in geometries and placement of the permanent magnet can cause an observable difference in forces.

For pumping, we mount the actuators and the fluidic top plate on the plate holder as described in Section 5.4.3. The setup is shown in Figure 5-38 with a close-up of the plate holder shown in Figure 5-32. The actuators run in a 6-step pumping sequence shown in Table 5.3. In each step of the sequence, there is change in state of one of the actuators. The actuation wave-forms are generated in National Instruments CompactRIO (NI cRIO-9076) running LabVIEW Real-Time. The software was developed using NI LabVIEW. The waveforms are output as analog voltage signals between -10 to +10 V. They go to PA10 linear amplifier which amplifies the signal by 2 times and this amplified voltage is the voltage across the winding. The voltage divided by the winding resistance is the average current when the actuator is turned on. This current gives rise to a net differential in the magnetic flux between the left and the right side stator pole face, causing the actuator to switch its state.

For pumping actuation we have 3 degrees of freedom. The actuation voltage and the duration of excitation are the two degrees of freedom available in the actuator module. For each pump stroke, we specify the duration that the pump stays in a particular state before moving to the next state(Table 5.3). This is the third degree

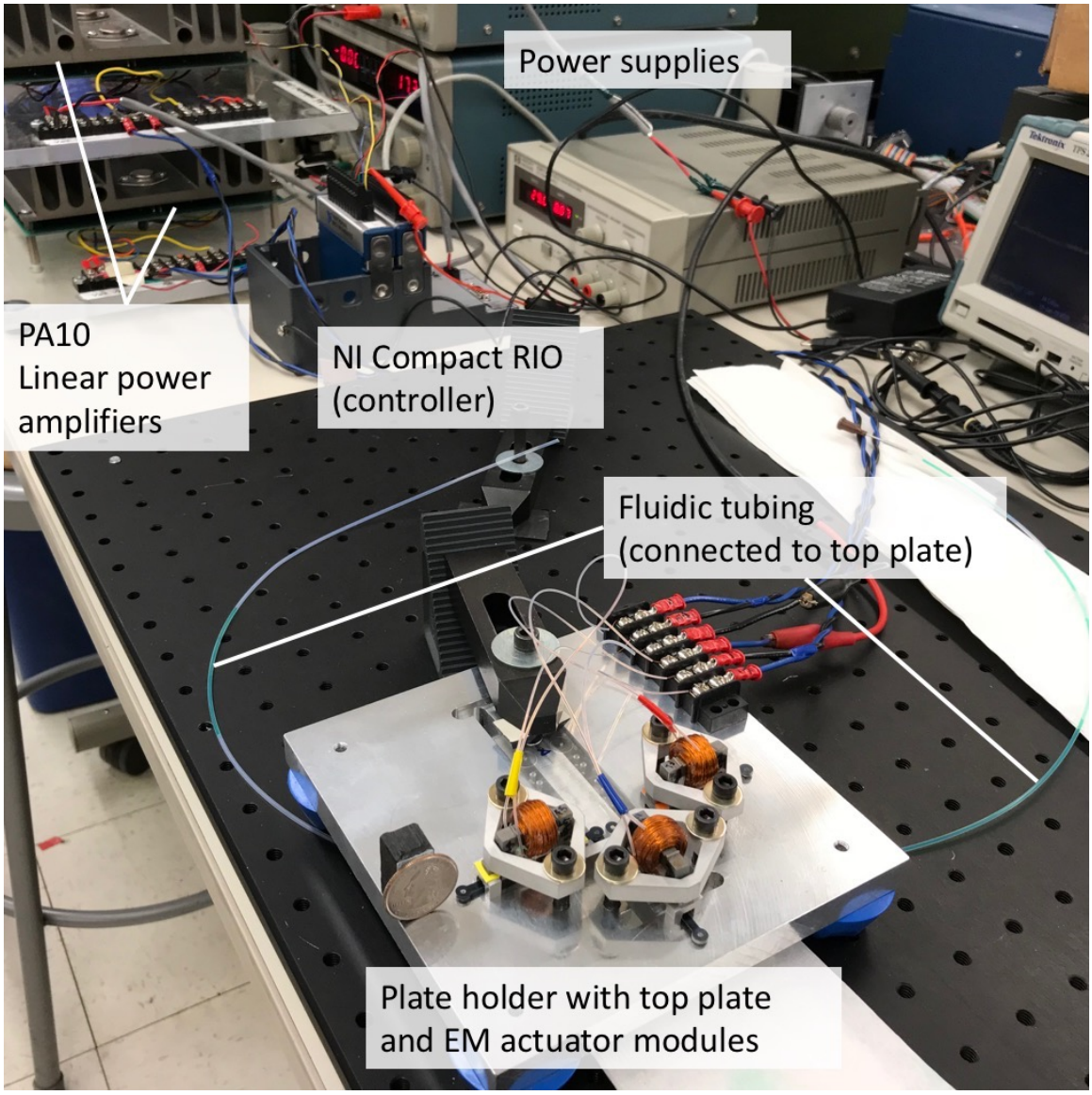

Figure 5-38: EM pump test setup showing the various elements. A close-up view of the plate holder with the EM modules is given in Figure 5-32.

Table 5.3: 6-step pump sequence for peristaltic diaphragm pumps with active valves. This sequence causes fluid flow in direction of valve-1 to valve-2. To reverse the flow, we can reverse the pumping sequence or switch the states between valve-1 and valve-2.

Step	Valve-1	Pump	Valve-2	Remarks
1	close	close	close	
2	**open**	close	close	
3	**open**	**open**	close	Suction stroke
4	close	**open**	close	
5	close	**open**	**open**	
6	close	close	**open**	Discharge stroke

of freedom. After the 6th step is completed, the system returns to step-1 and the cycle repeats.

We use lane-5 of the fluidic top-plate, which has mid-wall valves with a chamber diameter of 4 mm and depth of 0.075 mm, and a conical pump chamber with diameter of 5 mm and depth of 0.1 mm (Chapter 3). We test for valve sealing by switching the actuators to open or close the valve. When the valve is open, we push fluid through with a pressure-head and when the valve is actuated to a closed position, the valve stops the flow. Then we increase the pressure head till we see observable flow through the valve. The flow-rate is measured using the time taken to travel a given distance of a fluid-air meniscus though the connection tube (Figure 5-39). We find that the valves seal reasonably well up to a pressure of 60 kPa. This is an approximate value and more detailed experiments are in progress, but this value larger than our requirement of 20 kPa sealing pressure.

We demonstrate pumping with the suction side (inlet) at atmospheric pressure and with 0 back-pressure. Actuating at a 1 Hz pumping cycle, the volume discharged per cycle was found to be 0.45 µL/cycle. This is close to the maximum displaced volume possible of 0.48 µL for an intersection of a spherical cap of 15 mm radius with the conical pump chamber. The pumping sequence described in Table 5.3 is used with 340 ms for step-3 (suction stroke), 100 ms for step-6 (discharge stroke) and 15 ms for all other steps. We find that as we increase the frequency, the flow-rate per stroke reduces. This is likely due to the low stiffness of the diaphragm near the zero deflection point. The pump chamber therefore, is unable to generates a high

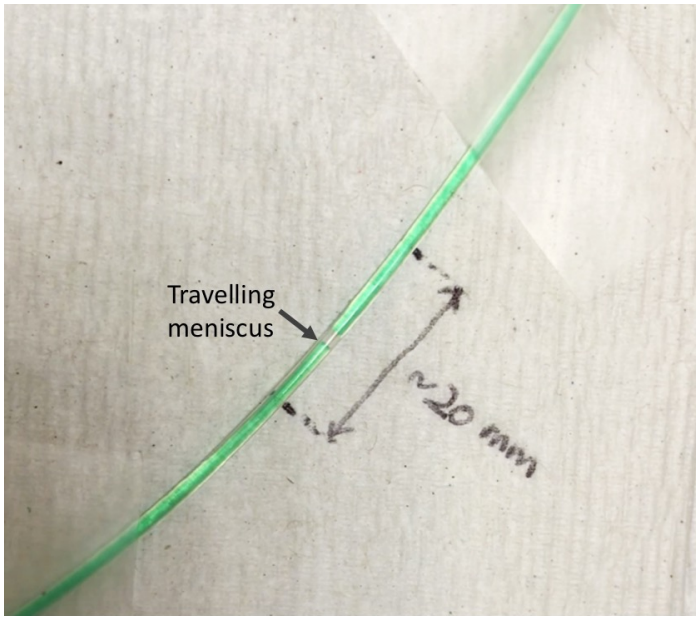

Figure 5-39: Traveling meniscus is tracked over time in the tube to measure flow-rate, given a known tube internal diameter.

suction pressure and hence a high suction flow-rate. Insufficient time in the suction step allows for only partial filling of the pump chamber. Thus, we believe that the flowrate is primarily limited by required to fill the pump chamber in the suction stroke, which is driven by the diaphragm stiffness. This is still work in progress and future possible directions are discussed in Chapter 9.

We find in our testing that for an actuation voltage above 8 V, we are able to switch for an excitation duration greater than or equal to 1 ms. The associated current through the winding for that short duration rises to about 0.4 A. The winding resistance is approximately 6 Ω. Therefore, the instantaneous power dissipation in the winding is about 1 W, and the energy consumption per stroke is $E = i^2Rt \approx 1$ mJ/stroke which is lower than our initial estimate of the energy (Section 5.3.2). At 1 Hz pump operation, the actuation frequency is 2 Hz and we have 3 actuators per pump which results in an average power consumption of $1 \times 3 \times 2 = 6$ mW per pump lane, which is low.

We measured the steady-state temperature rise of the EM pumps to be less than 0.1 °C at the actuator winding coils (Figure 5-40).The pump was run at a pumping frequency of 1 Hz (2 strokes per second for the actuator) for over 90 minutes. The

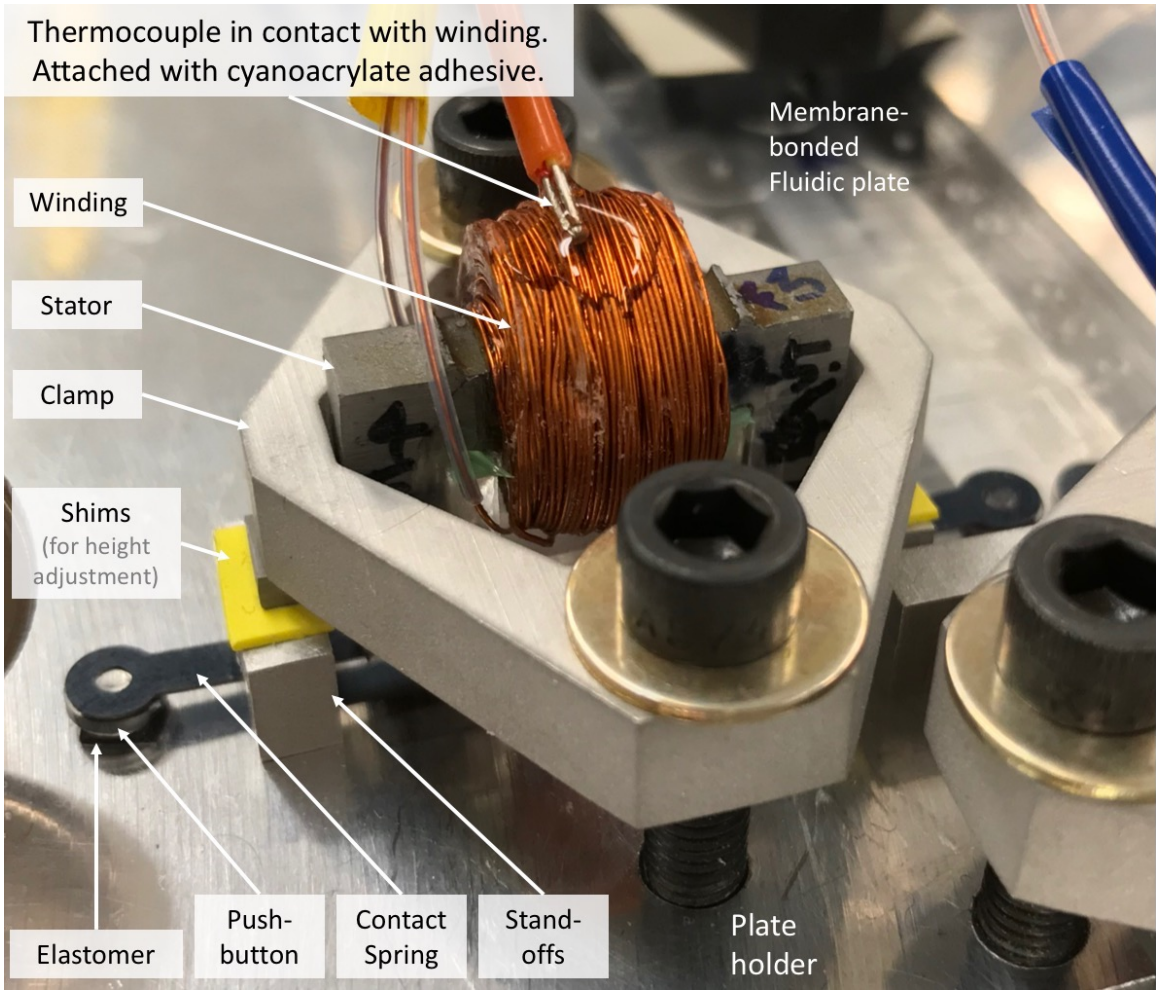

Figure 5-40: Measured temperature rise was less than 0.1 °C when running at 2 strokes/sec operation over 90 minutes. The Type-K thermocouple, with resolution of 0.1 °C is placed in contact with the top surface of the winding. A thick layer of glue of about 1mm is placed used to bond the thermocouple to the winding as well as insulate it from the surrounding environment. The ambient temperature was 22 °C throughout the experiment.

ambient room temperature was 22 °C thoughout the experiment. We used a thermocouple connected to a multimeter with 0.1 °C temperature resolution to measure the temperature. This makes the actuator suitable for use within a cell-culture incubator with very small effects on the nominal 37 °C temperature of the cell-culture medium, even for a platform using multiple actuators.

Preliminary tests with the actuator running for around 10^5 strokes (5 hours $\times$ 5 Hz $\times$ 2 strokes/actuation) show all the elements of the actuator performing well at the end of the test. More tests are on-going.

5.6 Results and Conclusions

Electromagnetic pumping at the micro-scale is a relatively unexplored area. A major challenge is the energy efficiency of these actuators on the micro-scale. For easier and faster fabrication and assembly, a scaled-up version of the electromagnetic pump is first developed as described herein. The pump uses a teeter-totter EM actuator having a low energy consumption of about 1 mJ/stroke. This is achieved by a latching design which requires only a short pulse of energy to switch its state and where springs store some of the actuator kinetic energy, which is then recovered in the reverse stroke.

In this chapter, we describe the design of the EM actuator and the design and fabrication considerations. We develop models to predict the EM actuator behavior, and finally describe the manufacturing and assembly of the actuator. We describe the integration of these actuators into an EM pump and present preliminary test results.

The preliminary test results are promising and show potential for this type of actuator for electromagnetic pumping. The actuators need to be made about 4 times smaller to enable integrated actuation of multiple pump lanes while fitting onto a single platform. Many of the principles described in this chapter can be used to guide the design as the actuator scales down. Work on this is in progress, and recommended future scope is described in Chapter 9.

Chapter 6

Spillway design for passive liquid leveling

- The work described in this chapter was done jointly with Luis R. Soenksen, a PhD student in our lab.

6.1 Introduction

Our MicroPhysiological System (MPS) platforms [2] have open wells in which various organ tissues are cultured. They also include a central reservoir, called the mixer (Figure 6-1). Common fluid-media recirculates in the platform by pumping from the mixer to all organ-MPSes, through pneumatic diaphragm micro-pumps, and then returns back to the mixer. This return of media to the mixer should maintain a definite steady-state volume in each organ-MPS and ensure that none of them run dry in operation, as well as preventing back-flow from the mixer to the organ-MPS.

This is achieved by the spillway feature which passively transport fluid from a source well (organ) to a sink well (typically the mixer) once the fluid level in the source well increases beyond a certain height. The drive for this transport comes from the hydro-static head of the fluid in the source well when it tries to rise above the desired height (Figure 6-2).

As shown in Figure 6-2, due to surface tension, there is a meniscus at the top

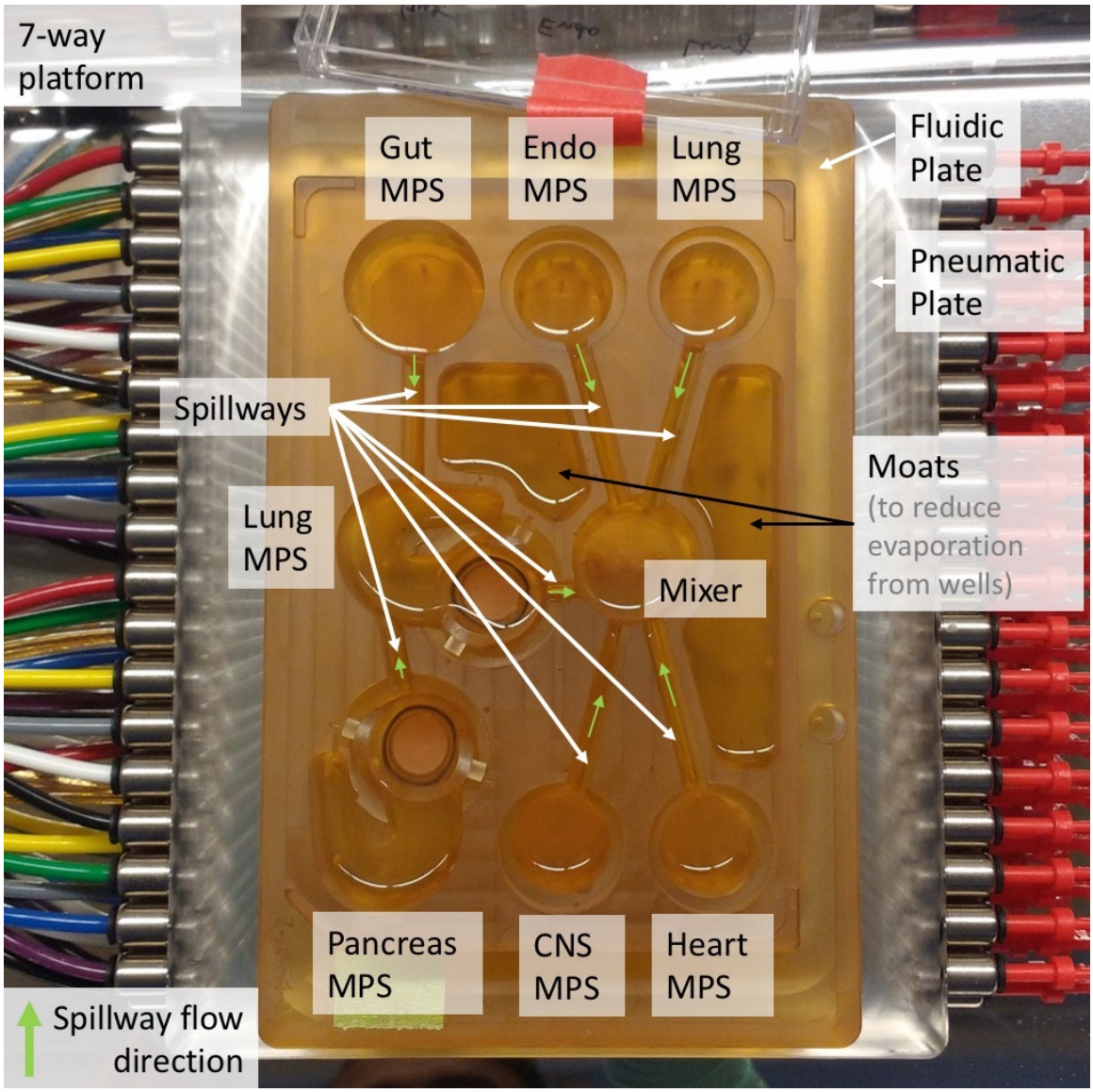

Figure 6-1: 7-way platform showing the various organ-MPSs and spillways which return flow from the organs to the mixer. Spillway flow directions are labeled with green arrows.

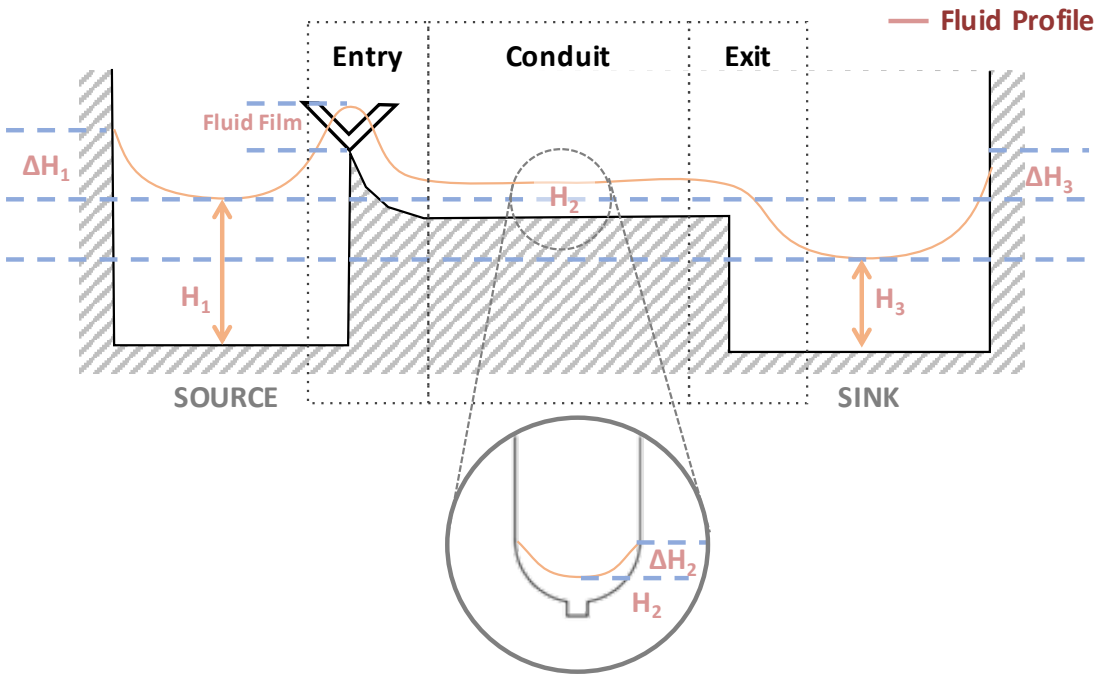

Figure 6-2: An earlier spillway configuration. Entry is the input geometry leading into the spillway conduit; exit is the output geometry leading into the sink well; conduit is the spillway channel geometry, connecting the entry to the exit. Height, H_1 is the fluid height at the source well, measured at the center of its meniscus; ΔH_1, ΔH_2, ΔH_3 represent the difference between fluid height at the lowest point in the meniscus and fluid height close to the walls due to meniscus effects. Height, H_3 is the fluid height at the sink well, measured at the center of its meniscus

layer of fluid in the well and therefore, the fluid height at the walls is higher than at the middle. This makes setting accurate height of the fluid within the source and sink wells a challenge. For this purpose, entry, conduit, and the exit features are important considerations. An earlier spillway geometry features a step + V-cut entry and then a step down + shallow circular conduit with a groove at the bottom which exits at the sink well, as shown in Figure 6-2.

This chapter describes the problems with the existing spillway designs. It proposes an improved design, and gives experimental results showing its performance improvement over the earlier design. The two major challenges are due to the high resistance to flow of the media through the conduit, and the coupling of fluid levels between the source and sink wells by the establishment of a continuous thin film. The improved spillway has a meniscus pinning groove at the desired height in the source well which leads into the spillway entrance, and which helps in maintaining a flatter meniscus. The spillway conduit connects the entry and exit, and uses a Spontaneous Capillary Flow (SCF) channel, which causes fluid to flow through without any external pressure drop. The spillway conduit is parallel to horizontal. The spillway exit uses a rounded exit geometry which thins the fluid film and causes it to break into droplets, due to surface tension destabilizing the thin film. Simultaneously, these droplets shed via gravity into the sink well, thereby decoupling the fluid heights between the source and sink wells (Figure 6-10).

6.2 Issues with the existing V-cut entry spillways

The earlier V-cut entry spillway geometry is shown in Figure 6-2. In operation, we observed the following difficulties with its performance:

1. Unstable spillway behavior leads to fluid build up.

   In the earlier spillway configuration, a continuous fluid film from source to the sink is necessary for proper spillway functioning. This film is easy to break by evaporation - on the exit side due to reduction of fluid height below the exit at the source well (Figure 6-5), in the conduit (Figure 6-4), and on the entry

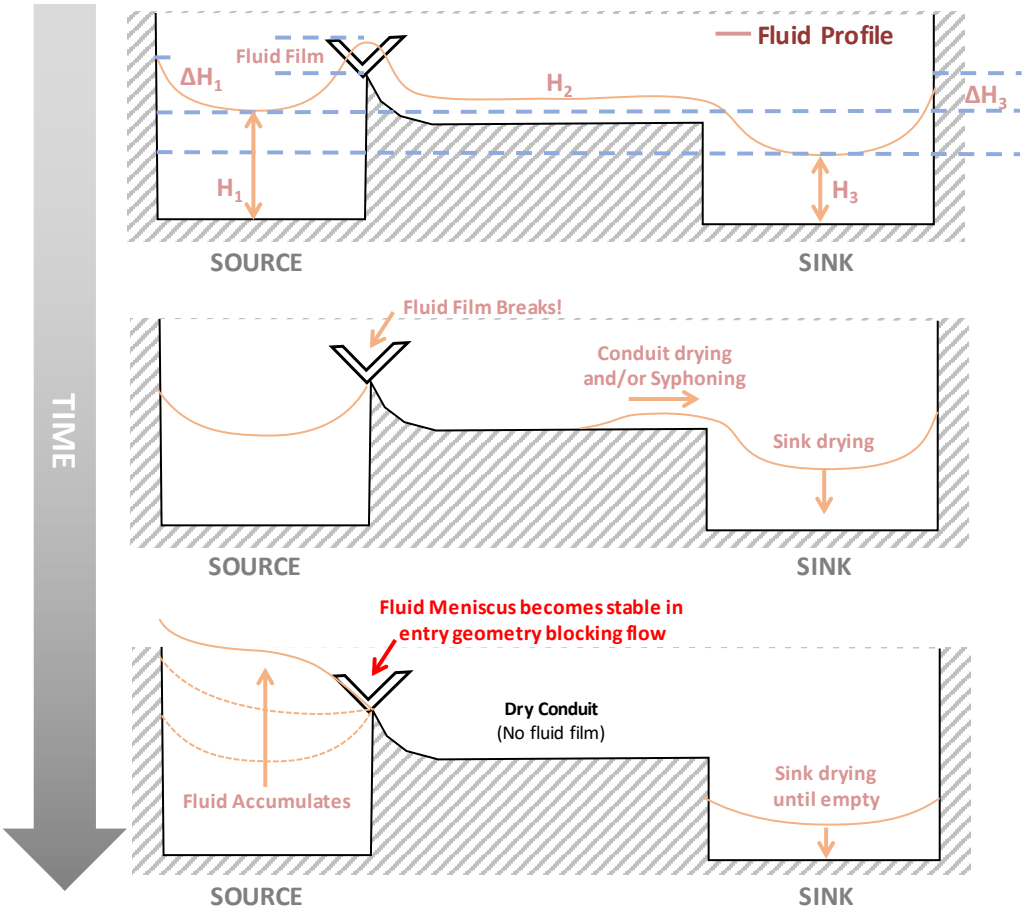

Figure 6-3: Spillway entry drying sequence and subsequent fluid accumulation in source well. If fluid film breaks and conduit dries, the increase of fluid level at the source seems to require less energy than to break the meniscus, create a new fluid film and restore flow into spillway and out to sink well. This appears to be a typical mode of failure for this earlier design, which leads to the drying out of the sink well, and excess volume in the source well.

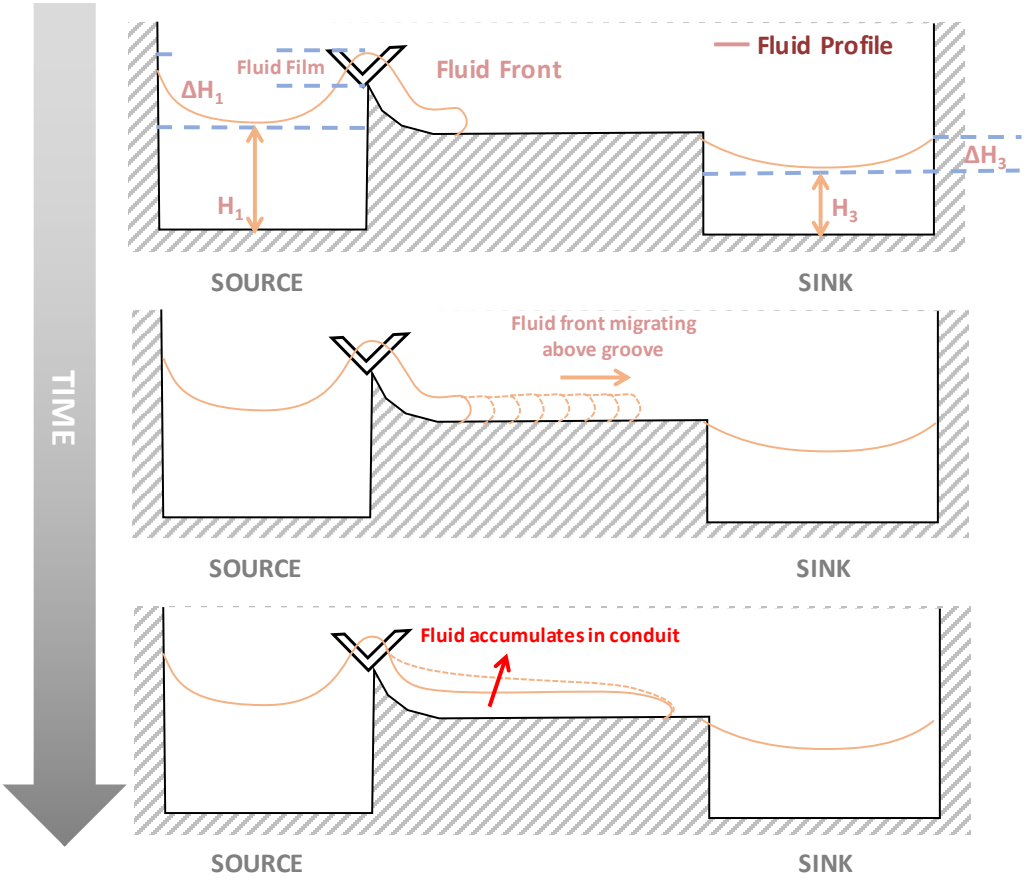

Figure 6-4: Spillway conduit behavior without prior priming or in case of spillway drying due to evaporation or fluid film disruption. If spillway conduit does not have a fully developed fluid film, the front forms a meniscus within the walls of the conduit. This meniscus advances slowly and accumulates fluid above the groove, leading to excess volume storage in the conduit.

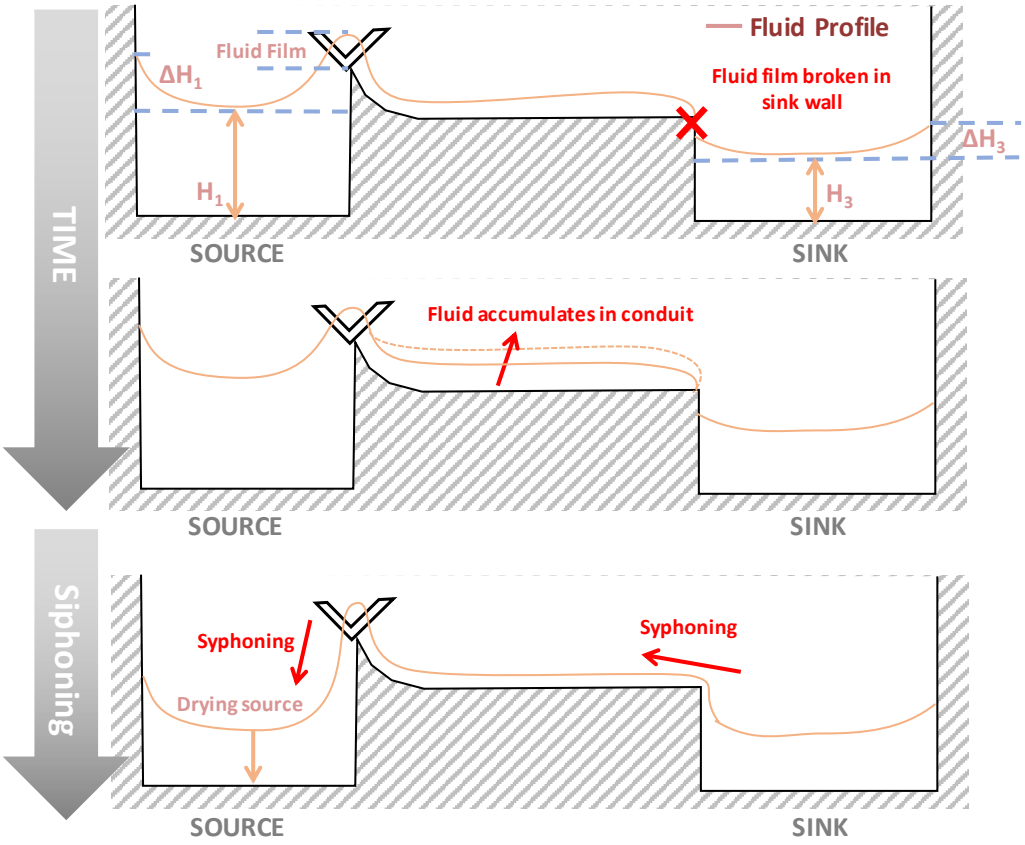

Figure 6-5: Spillway exit behavior, leading to fluid accumulation in conduit if fluid film is disrupted, and to siphoning effects if the fluid film is too stable. If the spillway exit does not have a fluid film in the vertical wall, fluid starts accumulating in the conduit and leads to spilling bursts. If fluid film is always present, siphoning between source and sink may happen even if the source fluid level is below sink level. The V-cut feature was intended to break siphoning effects, but was not always successful.

side by reduction of volume in the source well (Figure 6-3). If the fluid-film breaks at the entry, then there is fluid accumulation in the the well and after a significant increase in fluid height above the level of the V-cut the flow goes into the spillways again (Figure 6-3). This hysteritic height fluctuation occurs because, at the height of the V-cut, the fluid finds it more energetically favorable to accumulate in the source well than to enter the dry spillway, until it builds up to a level where gravity forces on the fluid are large enough to overcome surface tension. If the fluid film breaks at the spillway exit, then the fluid level builds up in the spillway conduit until the level is high enough that it goes through the exit again, as shown in Figure 6-5. As long as the entry and exit are wetted, the source and sink are in communication via the fluid film and the spilling behavior happens normally.

2. Poor control of source well height.

   The height of the fluid in the source well is controlled by the breakage of the fluid contact (meniscus) at the spillway entry. The earlier spillway design exhibited a large range of heights at which the fluid will connect to the spillway entry, driven by a combination of contact angle, surface tension and negative pressure due to the hydro-static head difference in the level between source and the sink. Once initiated, spilling into the spillways from the source to the sink only stops when the fluid film breaks at the entry of the spillways. This process was not sufficiently deterministic.

3. Siphoning action makes MPS volume retention have high variability.

   When there is a film connecting the source and the sink wells, the fluid transfer model is similar to a siphon [27]. The surface tension of the fluid connection forms the equivalent of a hose, which connects the two wells such that fluid can flow upward above the source well fluid height and then drain into the sink well. The meniscus at the walls helps make fluidic contact even when the mean fluid level in the wells is below the spillway entry or exit. The driving force for the flow is the fluid height difference between the source and the sink well. In this

siphon behaviour, higher level of fluid in the spillway does not prevent forward or backward flow between the wells. As an example, if we extract fluid from the source well, the reduction in height of the source well below the sink well causes fluid to flow back from the sink well into the source well (Figure 6-5 bottom). On the other hand, if we extract fluid from the sink well, it pulls in more fluid from the source well, reducing its volume even if the source well level drops below the spillway exit. The volume in each well at the end of an experiment is an important parameter to evaluate the concentration of analytes. Such volume varying behavior is unacceptable as it makes the volume measurements unreliable, and can also lead to the drying out of some MPS wells.

6.3 Requirements of passive levelling

The following are the requirements to achieve robust spillway operation,

1. Low variation of fluid height in the source well.

   Fluid should spill over at the exit of spillways, as soon as fluid in the source well crosses a predetermined height. Generally it is observed that the fluid level needs to increase higher to have enough pressure head to spill and then the fluid level in the source well drops. Over time, the height again increases and then after it crosses a threshold, it spills again. This intermittent operation causes a variation in the steady state height in the source well and should be minimized.

2. Spillways should operate consistently and hold a relatively small volume of fluid.

   The fluid volume held by the spillways is dead volume and thus should be minimized. The spillway performance should be robust against the range of conditions within the incubator while in operation, such as temperature and humidity variations, wetted and non-wetted regions, and range of fluid heights in the sink well. Fluid should also not accumulate in the spillways.

3. Spilling should be the most favorable event when fluid height increases above the level of the spillways.

If there are multiple pathways for the fluid once it raises beyond a certain level, the spilling should be the most favorable path and the fluid flow through the other pathways should be minimized.

4. Spilling should happen regardless of sink fluid level.

   Spilling should only depend on the fluid height in the source well and should happen the same way independent of the fluid height in the sink well. By design, the fluid level in the sink well should never be at or beyond the fluid level in the source well.

5. No siphoning

   Siphoning behavior, i.e., pulling of fluid from the source or the sink well when the fluid level in the other well reduces, should be avoided.

6.3.1 Ideal mode of operation of spillways

The ideal mode of operation of the spillways, which meets the design requirements would be,

1. As soon as the fluid level increases beyond a certain height in the source well, the fluid should enter the spillways.

2. Once it enters the spillways, the fluid should reach the spillway exit with minimal additional increase in fluid height in the source well,

3. The fluid should spill into the sink well at the exit, independent of the height of fluid in the sink well as long as this height is below the exit. This will minimize the fluid accumulation in the source well and the spillways.

4. At the end of every spilling event, the fluid film should break so that there is no coupling between the fluid height in the source well and the sink well. This will eliminate the siphoning effects.

6.4 Spillway designs

The design of spillways can be considered in three regions - the entry, conduit and the exit. All these three regions work together and result in the overall spilling behavior between the source and the sink.

6.4.1 Entry geometry

At the entry, we need two functions: (1) a relatively flat fluid meniscus, and (2) a low barrier to entry of fluid into the conduit.

A flat fluid meniscus is achieved by including a ring in the source well wall at the height at which we want the fluid level to be maintained. Geometric edges act as points of meniscus pinning [28]. We utilize this behavior by having a circular slot at the height we want fluid to maintain level in the source well as shown in Figure 6-10.

6.4.2 Conduit

The conduit should provide a self-wetting, low resistance path for the fluid from the spillway entry to exit.

This can be achieved by utilizing the effect of Spontaneous Capillary Flow (SCF) as described by Berthier and Brakke in [29] and [30]. SCF occurs when a liquid volume is moved spontaneously by the effect of capillary forces, without the help of auxiliary devices to create an external pressure drop. In SCF, as soon as fluid enters the fluid channel, it travels through the entire length of the channel. The flow rate is difficult to estimate and depends on the interaction between surface tension and viscosity effects. Berthier *et al.* in [30] derive a general law for determining the condition for SCF in micro-channels.

The general law for SCF in open micro-channels is that the generalized Cassie angle, θ^* be less than 90° [30]. The Cassie angle, θ^* was proposed by Cassie and

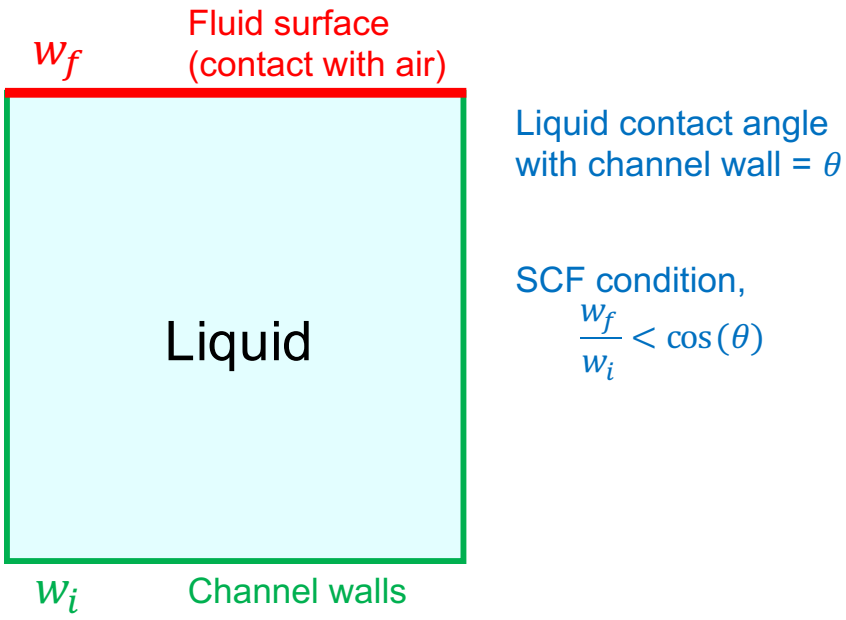

Figure 6-6: Conditions for Spontaneous Capillary Flow (SCF). Parameter, w_i is the area in contact with the channel walls, and w_f is the fluid surface area in contact with air.

Baxter in [31] and is given by

$$cos(\theta^*) = \sum_i f_i \, cos(\theta_i), \tag{6.1}$$

where f_i stands for the fraction of the area of the fluid in contact with each of the materials and θ_i is the corresponding contact angle of the liquid with each of the contact materials. By convention, the contact angle for liquid contact with air is taken to be π. If the channel consists of a homogeneous material and θ is the contact angle of the fluid with the channel material, w_i is the area in contact with the channel walls, and w_f is the area in contact with air (Figure 6-6), then the Equation

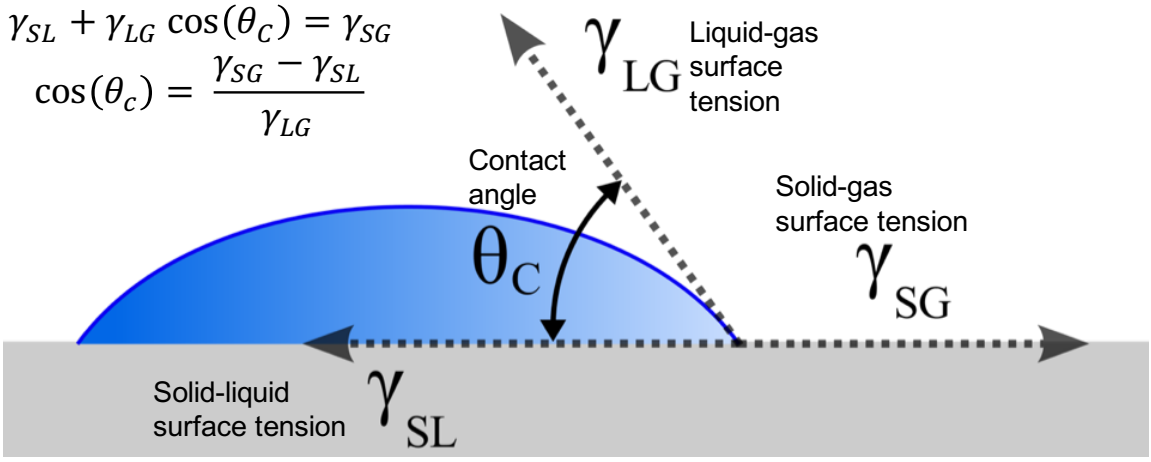

Figure 6-7: Contact angle between the fluid and a solid surface by force balance at the triple contact line.

6.1 simplifies to,

$$\begin{aligned} \theta^* &< \pi/2 \\ cos(\theta^*) &> 0 \\ w_i\ cos(\theta) + w_f\ cos(\pi) &> 0 \\ \frac{w_f}{w_i} &< cos(\theta). \end{aligned} \tag{6.2}$$

Equation 6.2 gives a simple equation to design the spillway conduit channels such that the flow is spontaneous. We need to know the contact angle the fluid media makes with polysufone to use the model.

Contact angle of fluid-media and polysulfone

The equilibrium contact angle reflects the relative strength of the liquid, solid, and gas/vapor molecular interactions. The geometry is shown in Figure 6-7) including the triple contact line region where the liquid, solid and gas interact.

Accurate measurement of contact angle is challenging as it depends on a number of factors such as, surface tension of the liquid (which depends on temperature), surface roughness of the substrate (which varies due to machining parameters of the machined

polyshulfone fluidic plates) and contact angle hysteresis. We measured the contact angle of the fluid media with polysulfone by putting small drops ($\sim 1-5\mu L$) on a flat polysulfone sample with a machined surface. We estimate the contact angle from pictures of the side profile of the drop contacting the surface (Figure 6-7). For initial contact, when the fluid media wets the surface for the first time, polysulfone behaves hydrophobically with contact angles between 70°-110°. After the first contact, there is a thin layer of media on the surface and on subsequent measurements, polysulfone behaves hydrophilically with contact angles between 30° to 60°. Though these are very approximate measurements, it gives us ball-park values of contact angles under various regimes of operation.

During the first contact, the fluid-pulysulfone contact is hydrophobic, with contact angle close to 90°. In that scenario, there is no ratio of free to contact surface areas which will lead to spontaneous capillary flow. After the first contact, the polysulfone surface behaves hydrophilic and we assume a contact angle of 60° for our calculations. According to Equation 6.2, we should at least have 2/3rd of the area in contact with the channel walls and at most 1/3rd of the area as free surface. We decided to use a rectangular geometry of 0.5 mm width and 1.5 mm depth, thereby having a free to wall-contact surface area ratio of 1/7 which is well within the regime for SCF.

We verified the SCF by 3D printing various channel geometries. The material used is clear SLA 3D printing resin from Formlabs, Inc. The contact angle of the 3D printed part with media is approximately in the range of 70° to 120°. After initial wetting, the contact angle reduces to 40° to 80°. Therefore, it is a reasonable substrate to evaluate spontaneous capillarity. We found the deep rectangular geometry shown in Figure 6-8 to perform reasonably well.

6.4.3 Exit geometry

At the exit, we want flow in the conduit to transition reliably to flow into the sink well. We want to do this, while not making a fluid connection with the sink well bulk fluid as that would couple the source and sink well. That coupling could potentially lead to siphoning.

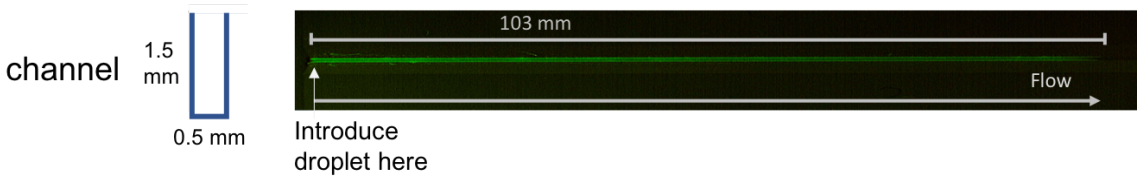

Figure 6-8: Spontaneous Capillary Flow (SCF) test. Add a 2 µL fluid droplet (water or media) with fluorescein in the channel and measure the distance wetted by the fluid in 5 minutes. Image on the right shows fluorescing liquid in the channel.

There are two primary spillway locations where the fluid film can be broken, either at the entry, or at the exit. At the entry, the fluid film breaks when the fluid height goes below the spillway entry and the meniscus of the fluid breaks and separates from the wall at the spillway entry point. The other location is at the exit. To break the film at the exit, we need to make the film unstable and shed into the sink well.

The rounded exit geometry shown in Figure 6-9 is one solution to break the film at the exit. This design spreads the fluid flow coming though the SCF conduit over a larger area thereby thinning the film, given the negative pressure due to gravity. This thin film is unstable [32] and breaks up and sheds into the sink well. Thereby, the design transports fluid to the sink well without having a contiguous contact between the source and sink wells. Figure 6-10 shows the new spillway design with modified entry, conduit and exit features.

6.4.4 Integration of entry, conduit, exit of the spillway

If the MPS has an oxygenation tail, like the liver as shown in Figure 6-11, then the presence of the the meniscus pinning groove in the well can short-circuit the flow of media from the oxygenation tail directly into the spillways without first going into the MPS. For a flat wall, with a 30° contact angle of the media with the wall surface, the meniscus can climb a distance of about 3 mm [32] vertically. This value is close to the capillary length which is the measure of relative importance between gravity and surface tension, $k^{-1} = \sqrt{\gamma/\rho g}$, where γ is the liquid surface tension, ρ is the density of the liquid and g is the acceleration due to gravity [32]. Such vertical climbing is a potential problem as any vertical well features such as the scaffold ears (Figure 6-11)

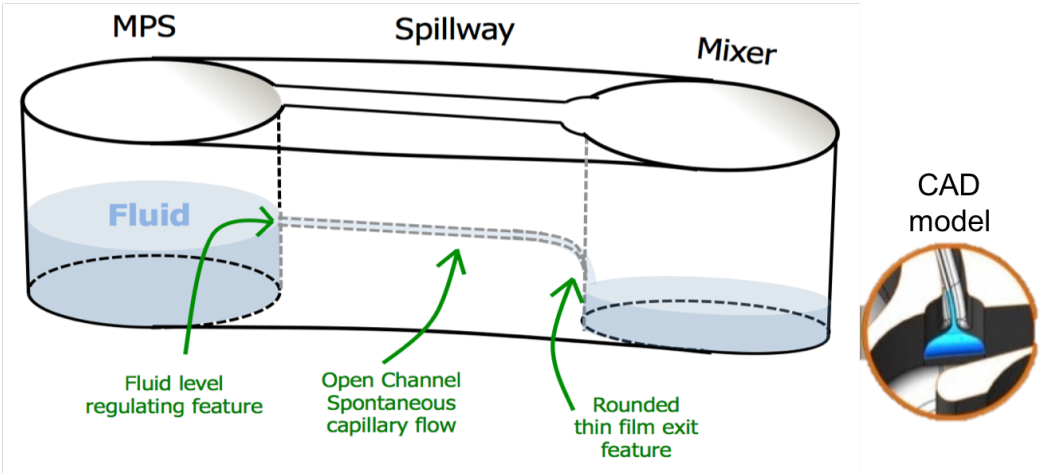

Figure 6-9: Our new design with rounded spillway geometry at the exit. In normal operation there is a fluidic connection from the entry well through Spontaneous Capillary Flow (SCF) until the fluid film breaks at the rounded exit feature. The fluid thins at the exit due to the larger area, and this thin film is unstable due to surface tension and thus breaks up into droplets and sheds into the sink well. Thereby, it transports media into the sink well, but without a fluid coupling between the source and the sink well.

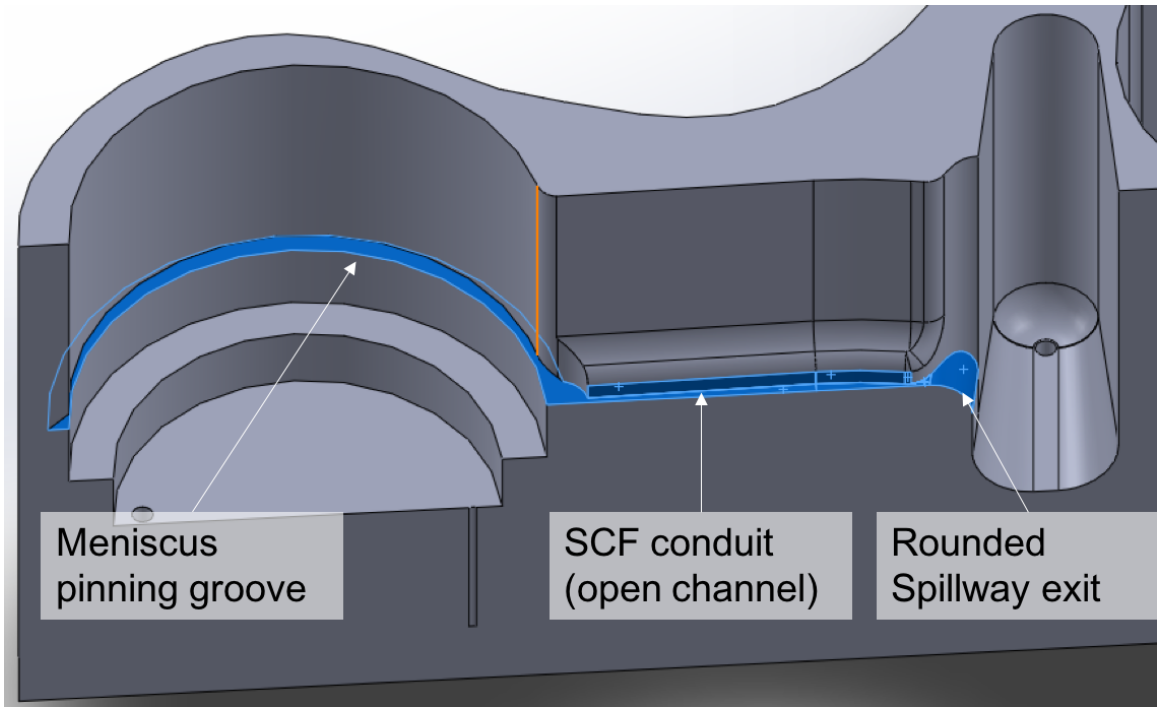

Figure 6-10: Modified spillway geometry with fluidic control features at the entry (meniscus pinning groove), conduit (SCF channel) and exit (rounded exit).

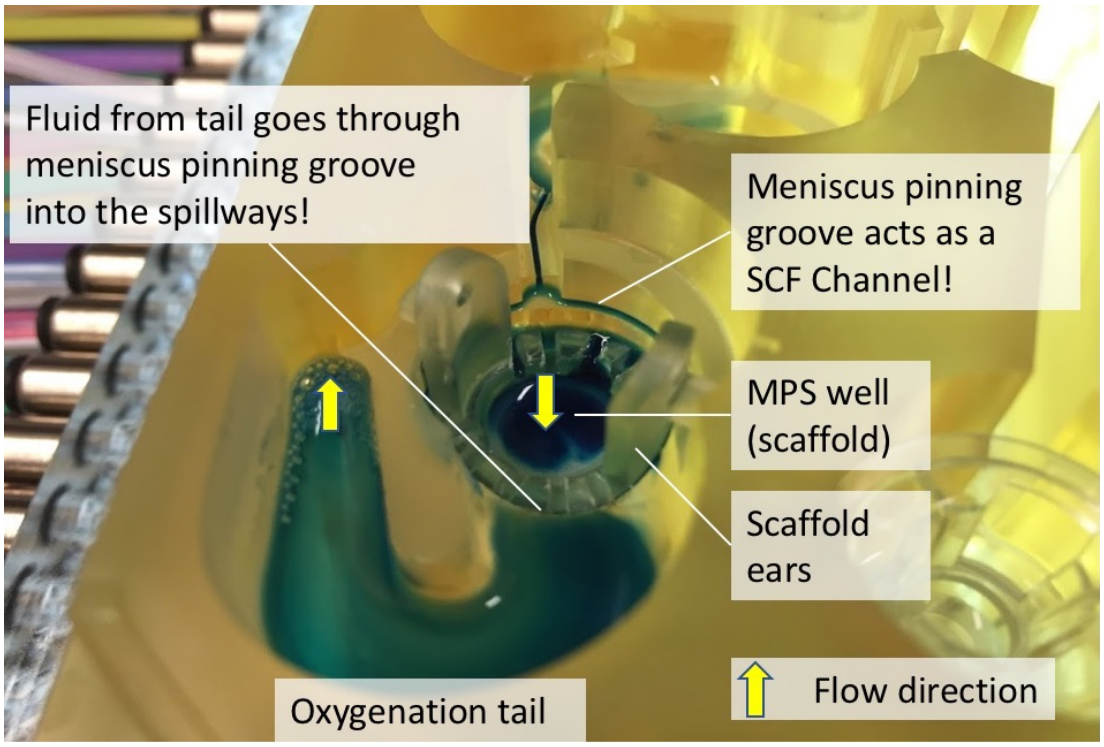

Figure 6-11: MPS with oxygenation tails should not have the meniscus pinning groove. The fluid can short-circuit the MPS and directly enter the spillways via the meniscus pinning groove.

can support capillary transport of the fluid from a lower level up to the meniscus capture groove. Therefore, for such organs, we avoid the meniscus pinning grove and give a direct spillway entry from the source well with no groove. The height of the spillway is correspondingly adjusted to hold sufficient volume in the source well. This blank wall design has a higher uncertainty of fluid height as compared to the wells with a meniscus pinning groove.

Another consideration is that the maximum fluid level in the sink well during operation should be below 3 mm from the lowest feature of the spillway exit. This is to ensure that the meniscus from the fluid in the sink well doesn't bridge the spillway exit, thereby making a continuous fluid chain from the source well to the sink well and coupling the source and sink fluid levels, like a siphon.

We made prototypes of the well geometries and of the spillways on a 3D printer to gauge the performance of various features (Figure 6-10). The scheme of pinning the fluid meniscus at the source well, its entry into a SCF conduit and then a rounded

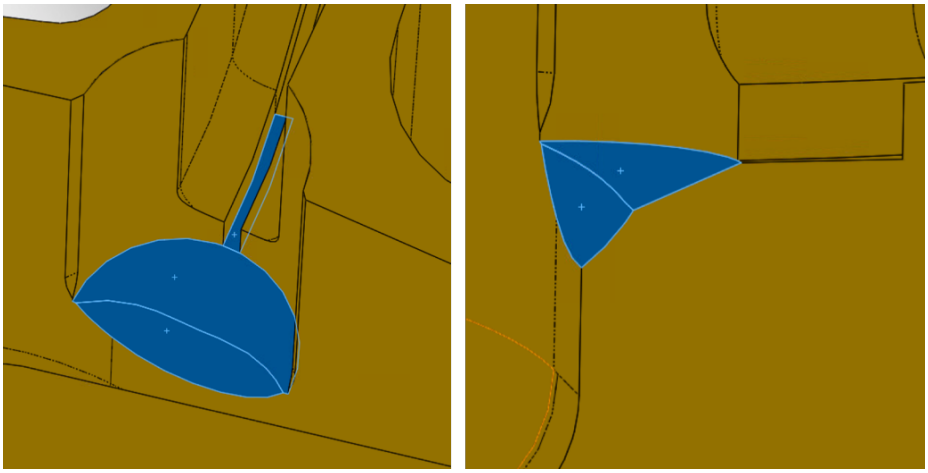

Figure 6-12: Modification to the round spillways exit for easier manufacturing. The modified exit geometry requires only a few passes of a drill and a milling tool compared to a series of milling passes with a ball end mill as shown in Figure 6-9 (inset).

exit geometry to make the film unstable and break the film showed promising results.

It is hard to manufacture the rounded spillway exit geometry via machining, (Figure 6-9 inset) as this would require a large number of passes with a ball-end mill. Therefore, we designed a modified geometry to a more vertical fall as shown in Figure 6-12. This geometry can be cut by a few passes of simpler milling tools. The performance of the modified spillway exit is not as good as the original rounded geometry, but is close and is much improved compared to the original V-cut spillway geometry.

An alternate idea shown in Figure 6-13 is to use gravitational head to transport fluid to the sink well once the fluid enters the spillways. The breaking point of the fluid film would then happen at the entry to the spillways. The sharp angle and long length of the diagonal tube from the source well into the conduit breaks the meniscus effectively. The end of the conduit uses a slanted tube going into the sink well. A benefit of this design is that the media in the source well can be sealed off by plugging of the inlet port to the spillways for isolation experiments, by using a screw plug. A downside to this design is that the open channel conduit can hold a larger volume of media as the level in the sink well increases. Ideally we would like a closed channel but that raises manufacturing issues with the machined fluid plates,

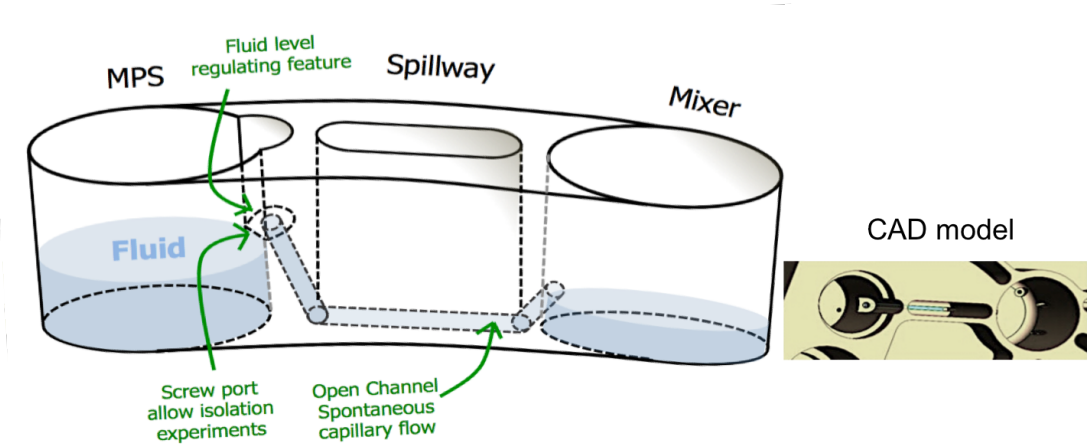

Figure 6-13: Diagonal hole spillway design developed with Luis Soenksen. The breaking of fluid film to prevent siphoning happens at the spillway entry point in the source well. A slanted tube carries the media into a Spontaneous Capillary Flow (SCF) open channel. The media then goes into the sink well again though through a diagonal tube. This design uses a screw port which can hold a screw-in plug to isolate the media in the source well for isolation experiments. Challenges are that the fluid height is controlled by how much the meniscus can climb the well walls in the source well and the potential for the fluid to rise in the open channel depending on the fluid heights in the source and sink wells.

as the indicated geometry cannot be machined. With a bonded, injection-molded manufacturing process this design could be feasible. Another downside is the higher uncertainty of the fluid height in the source well due to the meniscus climbing at the spillway entry.

6.5 Experiments

We manufactured two polysulfone fluidic plates with 7-organs on a single platform using the new spillway geometry for the rounded exit and the diagonal hole spillway designs. These plates were assembled with the existing pneumatic plates to actuate the diaphragm micro-pumps and transport media with the flow-rates used in the actual experiments. Media was added to each of the wells and the platforms were operated in the incubator for 48 hours with the usual cover on the platforms. The results for volume retention are shown graphically in Figure 6-14. The gray bars

denote the initial volume added into each well, and the blue and orange bars represent the volumes recovered from two replicates of the platform with the same spillway geometry. The diagonal spillway data is shown on the left and the round exit spillway data is shown on the right. The round exit spillway geometry performs reasonably well and the volumes recovered are within 20% of the initial added volumes. Ideally, the volumes should be the same as the initially added volumes and any volume deficit, due to evaporation, should be accommodated from the excess volume in the mixer.

Each design was tested independently for siphoning by filling media in the source well until it spills into the sink well, and then extracting media from either the source or the sink well. There was no change in fluid height in the other well implying no siphoning. Based on these results, the rounded exit spillway design was selected as the spillway design for the 10-way biological interaction studies as a part of the DARPA project milestones [2]. These spillway geometries performed adequately and contributed to the success of the experiments.

6.6 Conclusions

Passive fluid leveling of each MPS is an important design feature of the organs-on-chips platforms developed in our lab. This chapter describes the design of improved spillway geometries which satisfy the requirements of spillway operation during experiments.

A key challenge is to resolve the fluid coupling between the source and the sink well during spilling. The fluid meniscus climbs the walls of the wells due to surface tension effects. In the earlier design, a thin film of fluid creates a continuous chain from the source to the sink well. This changes the steady-state volumes of the source well and also leads to issues of siphoning.

We resolve this issue by designing features at the entry, conduit and the exit stages of the spillways. The spillways have a meniscus pinning groove, which helps in maintaining a flatter meniscus at the desired height in the source well leading into the spillway entrance. The spillway conduit includes a Spontaneous Capillary Flow

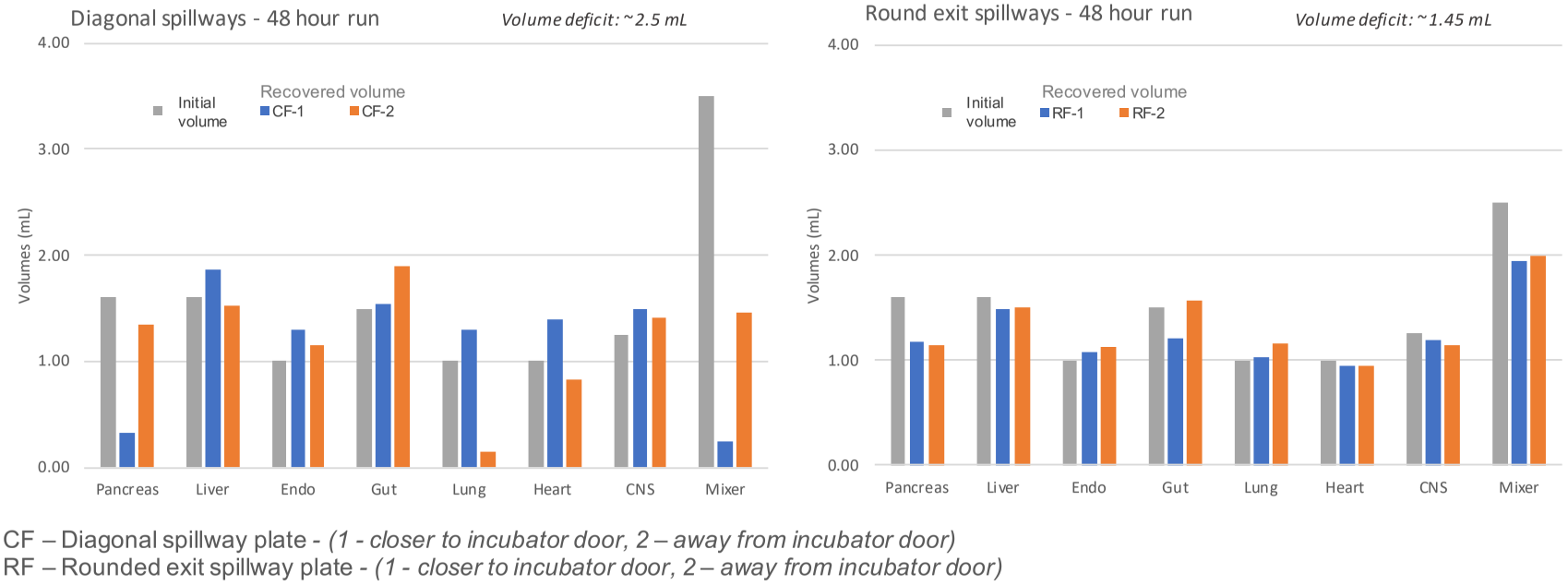

Figure 6-14: Volume retention tests for the two spillway designs. Round exit spillways are shown to maintain steady-state volumes in the MPSs reasonably well. On left is data for the diagonal spillways and on right is the data for the rounded exit spillways. The (gray) bars denote the initial volume added into each well, and the blue and orange bars represent the volumes recovered after 48 hours from two replicates of the platform with the same spillway geometry. The platforms are operated in the cell-culture incubator and numbers 1,2 represent the relative location of these platforms in the incubator; CF/RF-1 implies that these platforms are closer to the incubator door, CF/RF-2 implies that these platforms are inside, away from the incubator door. Diagonal spillways show a larger variation in the steady state volumes recovered. Ideally, the recovered volume should be the same as the added volume and the deficit, due to evaporation, should come from the mixer. The diagonal spillways show a larger deficit due to the accumulation of fluid in the conduits. For the round spillways, the volumes recovered are within 20% of the initial added volumes.

(SCF) channel, which causes the fluid to flow through without any external pressure drop, connecting the entry to the exit, even though the spillway is level. The spillway exit uses a rounded exit geometry which thins the fluid film and causes it to break apart by gravity and shed in to the sink well, thereby decoupling the fluid heights between the source and the sink wells, and avoiding siphoning.

Surface tension phenomena, especially at our millimeter scales scales are rather challenging as many of the characteristic geometric features on our platforms are of the order of the capillary length (k^{-1}) of around 3 mm. At this scale, both gravity and surface tension are important and this leads to complex phenomena. Viscosity is another parameter to consider when flows are involved. As an example, to predict the flow through the SCF channels, the flow from the pressure due to capillary forces is resisted by viscosity due to friction at the channel walls. The net result is that as the flow accelerates a terminal flow velocity is reached, which is the maximum flow velocity achievable in the channel without an external pressure drop. Moreover, surface tension effects depend on the surface properties of the substrate as well as temperature, which makes it difficult to analytically predict fluid behavior. Bounding calculations for getting a sense of the overall behavior and iterative testing of design ideas are pivotal to arriving at a feasible design. The use of 3D printing technology is very helpful in this regard, as a physical prototype can be quickly realized which can be iterated at a much faster pace as compared to conventional manufacturing practices. The new spillway designs worked well in the DARPA 10-way experiments.

Chapter 7

Interconnection of 7-way and 3-way platforms for the 10-way experiments

7.1 Introduction

For drug development and personalized medicine, one of the major challenges is to test physiological response of various drugs earlier in the development cycle with greater precision and speed. This requires the ability to mimic the relevant human multi-organ physiology in-vitro. One approach to Micro-Physiological Systems (MPS) are those developed in our program at the Center for Gynepathology Research (CGR) at Massachusetts Institute of Technology (MIT) led by Prof. Linda Griffith. These systems physiologically mimic the form and behavior of tissues of a given organ (http://physiomimetics.mit.edu/). The MPS systems are housed in open wells in a platform as shown in Figure 7-1. This version is the 10-way platform, which provides 10 wells for tissues. Media circulates among the organs transporting nutrients and other chemicals from a central reservoir (mixing chamber) to each organ as well as among organ systems, thereby mimicking the physiological circulation between those organ systems. As shown in the Figure 7-1, we use two interconnected n-way platforms where n=7 and n=3. Here, "n" stands for the number of organ systems which are fluidically connected on a platform. The 7-way and 3-way together form the 10-way system. Figure 7-2 shows the circulation for a 10-way interaction. The fluid transport

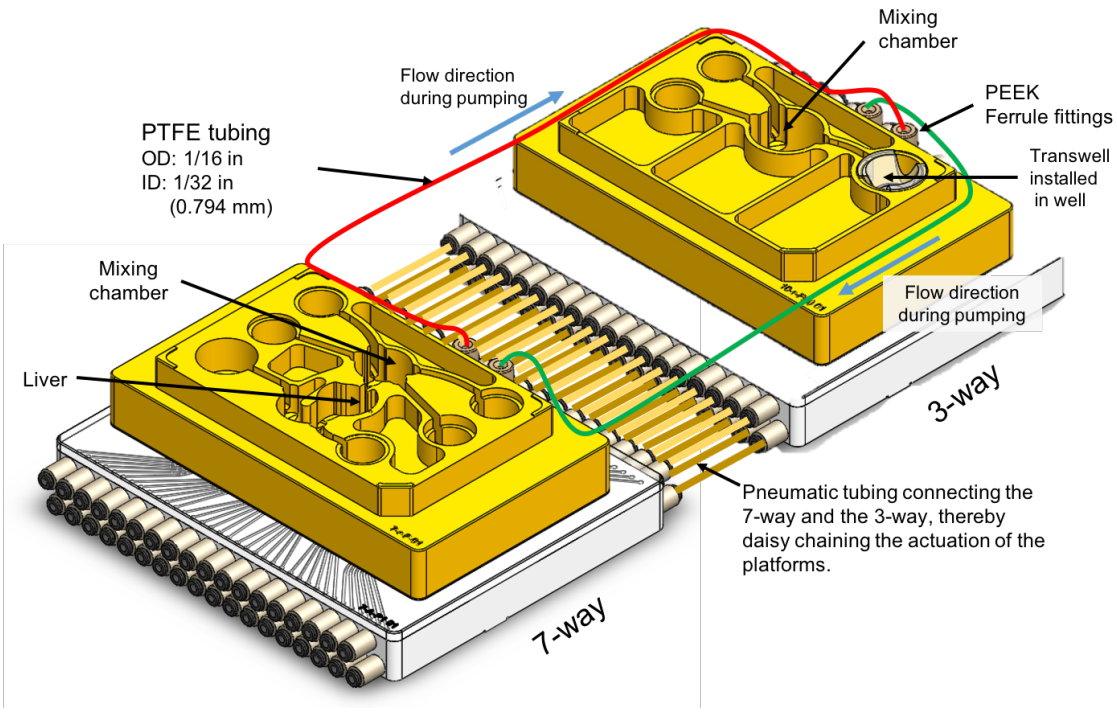

Figure 7-1: 10-way hardware showing the 7-way and the 3-way platform daisy chained with the interconnect tubing. The 7-way and the 3-way are connected together with two lengths of PTFE tubing. The flow directions are shown. In operation, a sequence of pumping between the platforms is followed by a duration of passive self-leveling.

from the central reservoir (mixer), to each of the organs is by pumping the media using on-board diaphragm pumps which are pneumatically actuated [5],[33]. For the 7-way, there are a total of 17 pumps with 12 independently controllable channels which can run one or more pumps in parallel [2]. The fluid level between each MPS on a platform is maintained passively using spillway features which are described in greater detail in Chapter 6.

We present the design of a system to maintain a net circulating interconnection flow-rate ($Q_{connect}$) of 1 µL/s and simultaneously maintain the fluid level between the 7-way and the 3-way platform which together constitute the 10-way platform. To achieve this, the mixers of the two platforms are connected using two lengths of PTFE tubing. We use a repeating sequence of pumping from one platform to another for a certain duration followed by a duration of passive hydro-static levelling. A $Q_{connect}$ of 1 µL/s is accomplished and the volume difference between mixers is maintained

within 1 mL at steady state operation. It is found that the fluid resistance due to the internal channels and the tubes primarily determine the steady-state volume difference during operation. The various considerations in setting up the system are laid out and a model to predict the levelling dynamics and the steady state volume difference between the mixers is developed and experimentally validated.

7.1.1 Requirements for the 10-way experiments

For the 10-way experiments that were a part of the final milestone of the DARPA project, the goals were to demonstrate 10-way interaction on platform for 28 days and also to study toxicity in the 10-way interaction (Figure 7-3). This required that the platforms support tissue structures for 10-MPSs and that the physiological flow partitioning between them is as modeled by the Translational Systems Pharmacology (TSP) team, which a part of our lab.

We had two options - either to spin a new revision of larger platforms which could fit 10 MPSes on a single platform or to reuse the existing 7-way platforms that had been recently used, to demonstrate 7-way interaction.

A new platform spin would incur a significant additional time and cost required. Therefore, we decided to explore the option to reuse the 7-way by daisy chaining it with another 3-way platform. The challenge here is that the two platforms need to communicate with each other in such a way that the physiological flow-partitioning mimics the flow-partitioning as if all the organs were on a single platform. Figure 7-3 shows the flow schematic within each platform and between the platforms. The percentages represent the percentage of the mixing flow Q_{mix} going to each organ from the mixer. The flowrates and the MPS volumes are given in the legend beside the schematic. Modelling done by the TSP team, as shown in Figure 7-4 shows that, physiologically the system with the daisy chained platforms connected with a flow-rate of greater than $Q_{connect}$ of $1\mu L\,s^{-1}$ is equivalent to that of all organs on a single platform. As the $Q_{connect}$ increases the model-2 concentrations which represents interconnected chained 7-way and 3-way platforms approaches the concentrations of model-1 which represents all MPSes on a single platform.

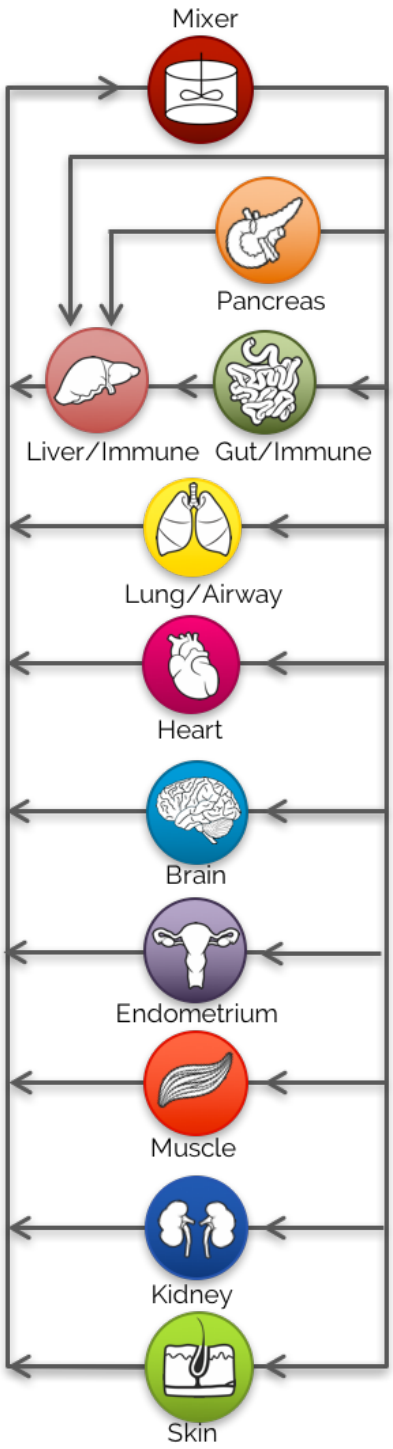

Figure 7-2: This schematic shows the interconnection of the various tissue organs. The flow from the mixer mimics the systemic circulation. Media is pumped from the mixer to the organs and returns back though spillway features. To stuy the effects of oral drug administration, the spillways for the gut and pancreas drain into the liver, before draining back to the mixer. Image by Emily Geishecker, a project manager in our lab for the DARPA project.

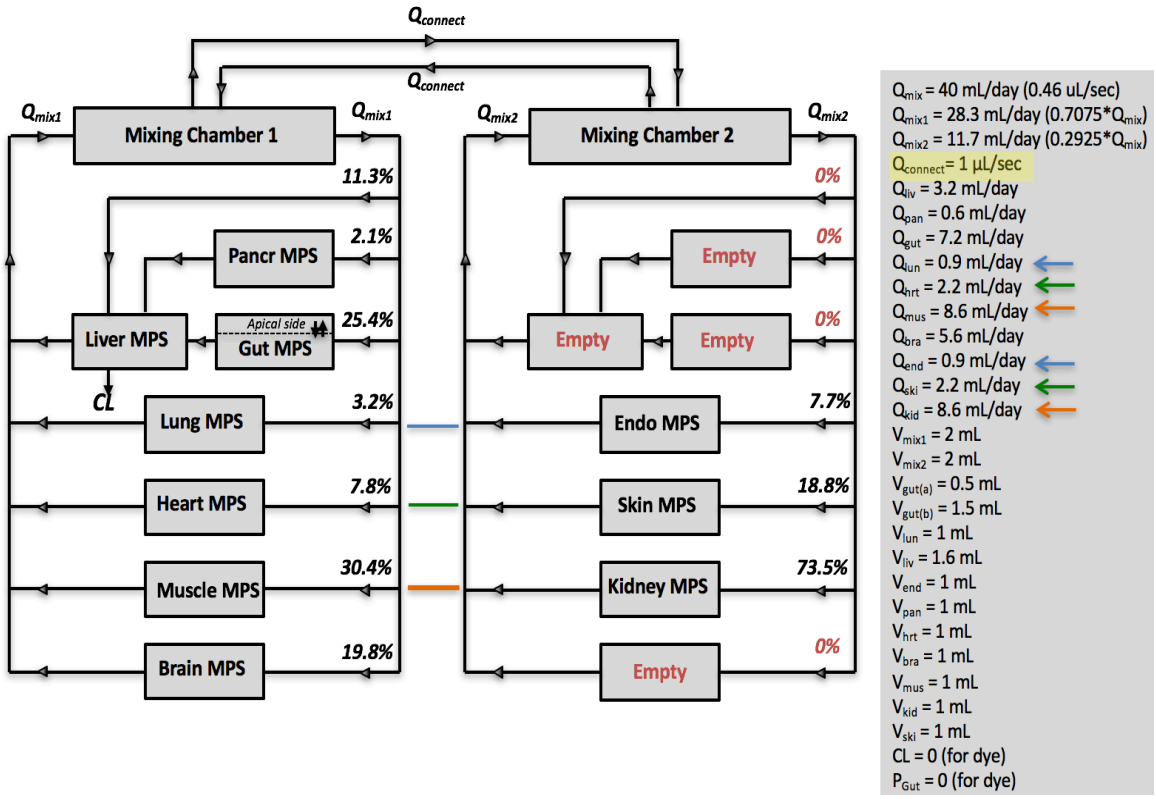

Figure 7-3: 10-way flow schematic showing the physiological flow partitioning between the various MPSs and also between both the platforms [2]. As shown, the Lung and Endo (blue), Heart and Skin (green) and the Muscle and Kidney (orange) MPSs are daisy chained to have the same flow-rates, with a flow-rate, $Q_{connect}$, between the platforms. Modelled by the Translational Systems Pharmacology team, which is a part of our lab.

7.1.2 Configuration of the platforms for the 10-way

To achieve a net circulating interconnect flowrate between platforms, we need to be able to pump media from each platform to the other at the $Q_{connect}$ flow-rate. This would mean two pumps running simultaneously pumping in opposite directions. Their volume flow-rates would need to be matched exactly to ensure that there in no net accumulation of fluid in one mixer. Since generally, there will be some variation in the two flow-rates and these platforms have to run days without intervention, we need some method to reduce the net accumulation.

One possible system is a closed loop control of fluid volume - using sensors to measure volumes in each platform and adjusting the pump flow-rates accordingly

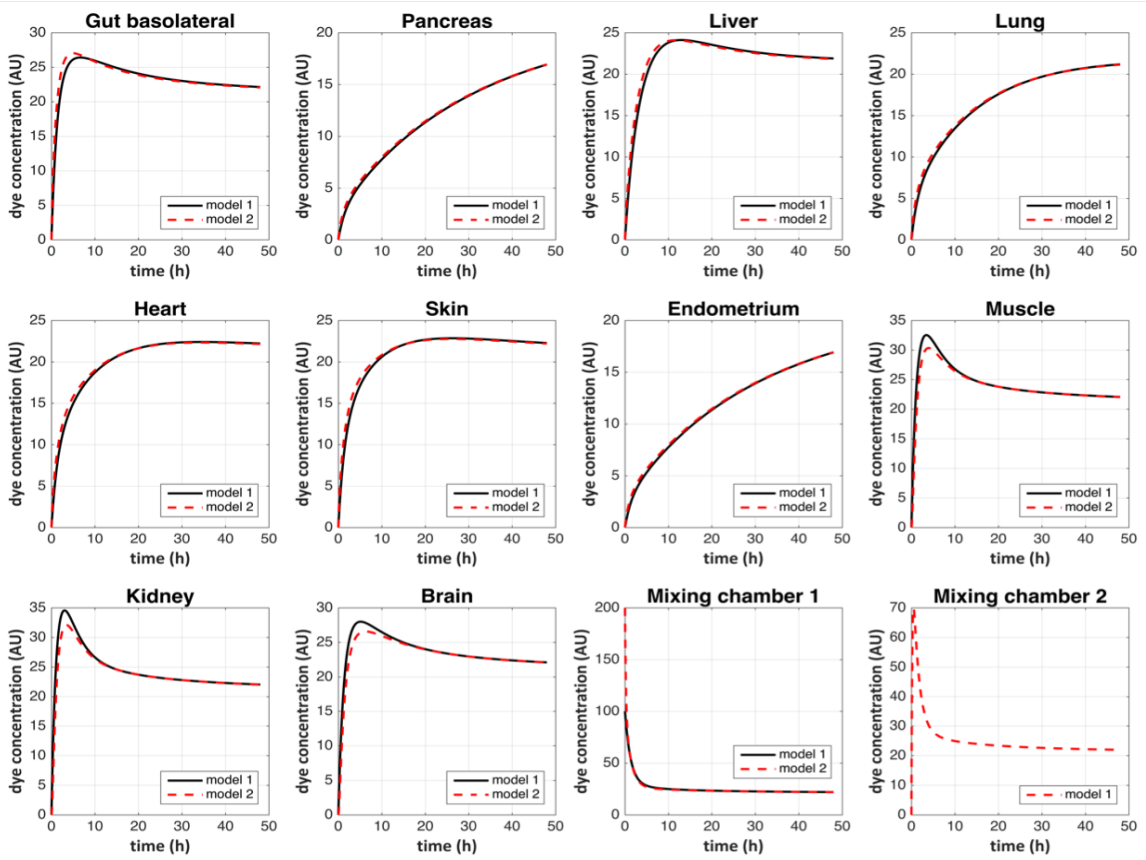

Figure 7-4: 10-way drug mixing comparison for different flow models. Model-1 stands for all MPSs on a single platform and Model-2 stands for a 7-way and a 3-way platform as shown in Figure 7-1 and Figure 7-3 with a with a net circulating interconnect flow-rate, $Q_{connect}$ of $1 \mu L\, s^{-1}$. This shows that using interconnected 7-way and 3-way platforms with the mixers interconnected $Q_{connect}$ of at least $1 \mu L\, s^{-1}$ is equivalent to all 10 MPSs on a single platform. Modelled by the Translational Systems Pharmacology team, which is a part of our lab.

to get net interconnect flow rate of at-least $Q_{connect}$. This would require additional sensors and software to run the closed loop control. A simpler method could be to make use of gravity to level the fluid volume in the two platforms. Fluid is pumped at a rate faster than $Q_{connect}$ between the two platforms for a certain duration. Any fluid accumulation results in a difference in fluid height, that creates a net gravitational pressure head to drives the fluid to flow from the platform in which the fluid height is higher to the one in which it is lower. This period is called leveling. Therefore, there is a duration of active pumping and passive leveling, while still maintaining a net interconnect flow-rate of $1\, \mu Ls^{-1}$ This is the method that we followed and is

Table 7.1: Details of interconnect equipment used to connect the 7-way and the 3-way fluidically with a net circulating interconnect flowrate, $Q_{connect}$ of at least 1 µLs^{-1}.

Item	Specifications	Qty.	Source
Tubing	Tefzel (ETFE) Tubing 1/16" OD x .030" ID	2 x 300mm	IDEX H&S
Ferrules	Super Flangeless One-Piece Fitting 1/4-28 Flat-Bottom, for 1/16" OD	4	IDEX H&S

described in greater detail below.

The platforms are connected together using interconnect tubing connected to the flow ports by the side of the platforms as shown in Figure 7-1. The two platforms are interconnected using Teflon or FEP tubing with ferrule connectors. The two ports connect via. onboard pumps to the mixers of each platform.

The additional hardware required for the interconnection is given in Table 7.1. To achieve the net $Q_{connect}$ between the platforms, fluid is pumped between the two mixers faster than $Q_{connect}$ for a certain duration (pumping), which leads to net accumulation of volume in one of the mixers. It is then allowed to level, driven by gravitation head between the mixers for a certain duration (levelling). The whole cycle is repeated continuously and eventually the system reaches a steady state volume difference between the two mixers and maintains it on average thereafter. In subsequent sections, the requirements, modelling, pumping scheme and experimental results are discussed.

7.2 Requirements of the interconnect system

In this section we discuss the objectives and considerations for the interconnection between the 7-way and 3-way platforms.

7.2.1 Objectives

1. Achieve a net $Q_{connect}$ between mixers of at least 1µL s^{-1}.

   This requires the pumping rate between the two mixers during the pumping

phase be high enough so that the to total volume transferred divided by the cycle duration (pumping + levelling) is equal to $1\mu L\,s^{-1}$. More details are considered and analyzed in Section 7.3.

2. Maintain at least 1mL volume in each mixer such that no mixer dries out.

   The mixers act as a reservoir to pump media to various organs and which is returned passively via the spillway feature. It is important that the mixers always have media in them, otherwise we risk lowering the steady state volumes in the MPSes. Initial volume added in each mixer is 2.5 mL, therefore, the maximum steady state volume difference allowable is 2.5 mL - 1 mL = 1.5 mL. Keeping a buffer of 0.5 mL, the target steady state volume difference is 1 mL. The system should be capable of running at least 48 hours without intervention. More details are considered in Section 7.2.2 and 7.3

3. Minimize evaporation loss through the tubing

   This is primarily based on the tubing material and surface area and thickness of the tubing. The materials selected for the tubing are Teflon and FEP because they are inert to drug adsorption, have low leaching and are bio-compatible. Also, compared to most common plastics, they are highly moisture impermeable. In the cell-culture incubator, where these platforms are operated, the relative humidity is close to 90% which further reduces the evaporation of fluid through the tubing walls.

7.2.2 Considerations

The pneumatic membrane pumps used in the platforms are actuated with pressures of ± 40 kPa. Due to manufacturing tolerances in the pump geometries, and the uncertainties in membrane deflection, there is a spread of up to 20% in the stroke volume pumped per stroke [2]. Hence, if fluid is pumped out from each mixer continuously at the same set-point flow-rate, then due to the slight difference in flow-rates between the two pumps, there will be net accumulation of fluid in one of the mixers.

This is a concern as one of the mixers would then go dry after some time. The system should be capable of running at least 48 hours in the cell-culture incubator without intervention. Therefore, an operating scheme involving a duration of pumping (pumping duration) followed by a duration in which both the pumps are held in an open state (levelling duration) is employed. In the levelling duration, the pumps act as a conduit through the interconnect tubing fluidically connecting the two mixers

Successful levelling driven by gravity requires that there is a continuous fluid column connecting one mixer to another. This is just like in a siphon [27]: through the interconnect tubing, the fluid has to rise above the height level of the fluid in the mixer and then drain into another mixer. The fluid in the portion which is above the height of the mixer fluid level is at a pressure lower than atmosphere and therefore, more prone to form bubbles which once formed, break the fluid chain and stop siphoning. Any bubbles in the tube have the potential to break the fluid chain and therefore, it is important to always pump out from each mixer so that the fluid in the interconnect tubing and connections is under positive pressure during pumping and the surface tension of the fluid aids in sealing. On the other hand, if the pumps are run such that they suck the fluid from the other mixer, there is a high risk for air to be drawn into the fluid from the fittings and other sealing areas due to system negative pressures leading to the failure of leveling. it is It is also important to minimize the fluid rise height as much as possible because, during the levelling phase, the system above the fluid level will be under negative pressure.

7.3 Modeling the interconnect behavior

Figure 7-5 shows the connection from one mixer to another which consists of interconnect tubing and internal conduit from the mixer to the ports. The internal conduits have a diameter of 0.4 mm as shown in Figure 7-6. Table 7.2 lists the important parameters used in the modeling.

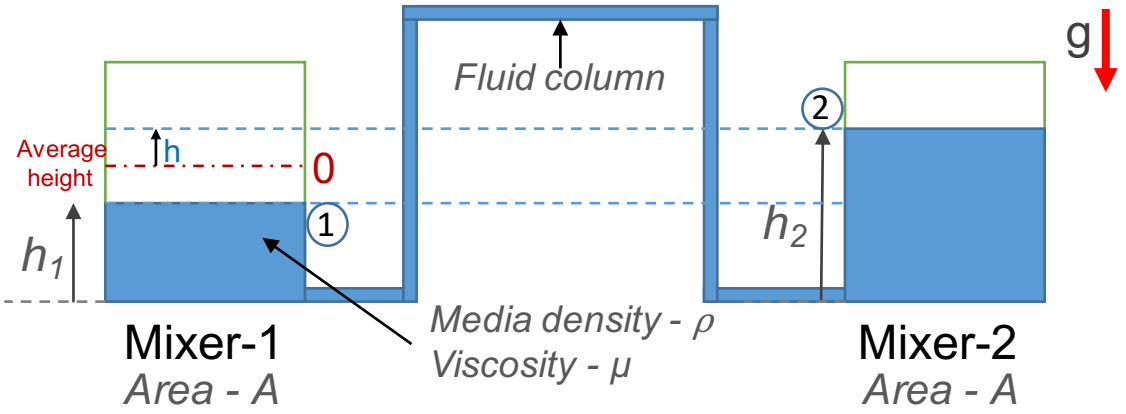

Figure 7-5: Schematic for levelling between two mixers. Fluid in mixer of platform-2 (mixer-2) has a higher fluid level at the end of the pumping duration, compared to the fluid level in mixer-1. The connection between the mixers is through the interconnect PTFE tubing (Figure 7-1) and the internal fluid channels of each platform. The fluid heights in the wells are measured from the bottom of the wells as reference. When the system is allowed to come to equilibrium, the fluid level in each mixer will reach the average height between the two mixers, marked in red. Two mixers have across sectional area A and this the fluid volume is the product of A and the fluid height in each mixer. For example, the fluid volume in mixer-1 is $A \times h1$.

7.3.1 Bounds for the pumping and leveling time between the two mixers

Pumping time

All the volume contained in the fluid column should be cleared and then some more volume should be pumped every pumping phase as the direction of flow during the leveling phase is non-deterministic. Thus, to avoid cases where at steady state,

Table 7.2: Parameters used for modeling the leveling behavior between the two mixers.

Parameter	Symbol	Units
Length of tube	L_{tube}	mm
Inner diameter of tube	D_{tube}	mm
Length of internal conduit	$D_{conduit}$	mm
Diameter of internal conduit	$L_{conduit}$	mm
Fluid column volume	V_{col}	mm^3=μL
Pumping flow-rate	$Q_{pumping}$	$\mu L\, s^{-1}$
Interconnect flow-rate	$Q_{connect}$	$\mu L\, s^{-1}$

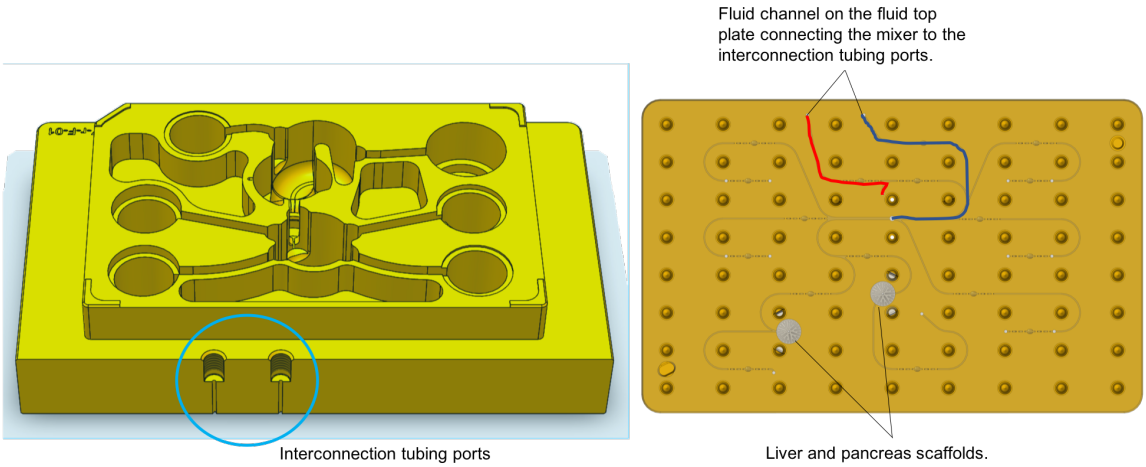

Figure 7-6: 7-way platform with internal fluid conduits - mixer to ports. In the left picture, the internal conduits are within the blue circle going below from the fluid ports and in the right picture, the internal conduits are shown by red and blue line connecting to the mixer. The scaffolds are machined into the fluid top plate for the liver and pancreas MPS to create a uniform, laminar flow for the perfusion of these tissues in the wells. More details abut the fluid top plate can be found in [2].

the entire volume pumped from one mixer returns back every cycle and no volume transfers to the other mixer, the volume in the tube should at least be cleared once.

1. Minimum pumping time required to clear all the volume of media in the fluid column is

$$t_{pumping\_min} = \frac{V_{col}}{Q_{pumping}}, \tag{7.1}$$

where V_{tube} is the volume of fluid contained in the column given by,

$$V_{tube} = \frac{\pi}{4}(D_{tube}^2 L_{tube} + D_{conduit}^2 L_{conduit}). \tag{7.2}$$

2. Maximum pumping time allowable is based on 20% error between pump flow-rates and the volume difference allowable per cycle (ΔV) between the mixers, i.e.,

$$t_{pumping\_max} = \frac{\Delta V_{mixer}}{(0.2)Q_{pumping}}. \tag{7.3}$$

Levelling time

1. The lower bound for the levelling time depends on the levelling dynamics of

the interconnect system. The requirements for the leveling time come from the maximum allowable steady-state volume difference requirements and the time-constant of leveling. For a given steady-state volume difference, the leveling time can be reduced as the leveling time-constant reduces. Conversely, as the leveling time-constant reduces, for a given leveling time, the system would reach a lower steady-state volume difference.

2. Upper bound for levelling time maintaining at-least nominal $Q_{connect}$ is,

$$t_{levelling\_max} = t_{pumping}\left(\frac{Q_{pumping}}{Q_{connect}} - 1\right). \tag{7.4}$$

Based on the above, we should minimize the volume contained in the tube to minimize the pumping time required to clear the tube, pump with maximum possible $Q_{pumping}$, and give the maximum time allowable for levelling while maintaining the nominal $Q_{connect}$ value. A spreadsheet with these calculations was made which allows for easy evaluation of various what-if scenarios.

7.3.2 Levelling dynamics

We look at the behavior of the system in the levelling duration. Figure 7-7 shows an equivalent electrical schematic of the flow model between the two mixers. There is an initial difference in height of the fluid in the two mixers which reduces over time. Figure 7-5 shows the schematic and Table 7.2 list the important variables.

Assumptions and considerations

1. The flow develops quickly compared to the time constant of levelling such that the flow in the tube is in the fully developed Hagen-Poiseuille flow regime. In the tube, the diffusion of momentum by viscosity happens in the order of $\tau_{diff} = D_{tube}^2/\nu$. For a tube of 1 mm, this is is of the order of 1 µs and therefore, the flow is assumed to be fully developed in further analysis.

2. The datum for height measurement is from the average height between the two mixers, which will be the final level of the fluid in the two mixers after a long

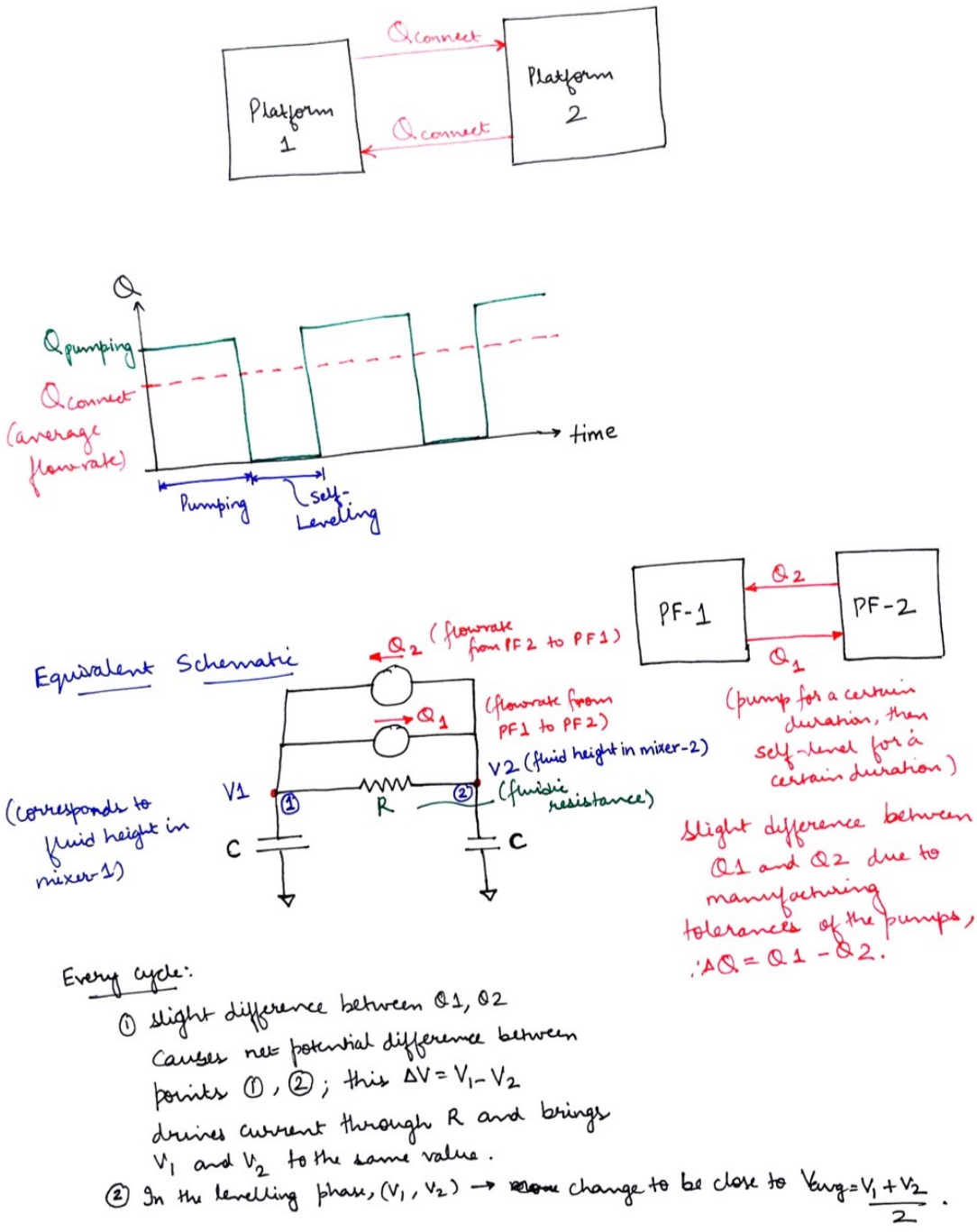

Figure 7-7: We need an net interconnection flowrate between the platforms of $Q_{connect}$.The onboard pumps on both platforms are actuated with the same parameters. They have a $\pm 10\,\%$ variation in flowrates due to manufacturing tolerances of the pumps. To stabilize the volumes such that one of the platforms does not accumulate too much volume, the pumps are run at a higher flowrate ($Q_{pumping}$) than the $Q_{connect}$, and then allowed to self-level (both pumps are will all valves open and act as conduits for fluid flow), still achieving an average flowrate of $Q_{connect}$. An equivalent schematic using circuit elements is shown in the lower half of the figure.

time ($t \to \infty$).

3. The diameter of mixer is much larger than the diameter of the tubes. Therefore, the fluid velocity in the mixers is small and the rate-of-change of fluid velocity in the mixers can be assumed to be zero.

The flow can be analyzed using the unsteady Bernoulli equation [34], which states:

$$\int_1^2 \rho \frac{\partial v_s}{\partial t} ds + \left(P + \frac{1}{2}\rho v_s^2 + \rho g h \right)_2 - \left(P + \frac{1}{2}\rho v_s^2 + \rho g h \right)_1 = 0. \tag{7.5}$$

This equation results from integrating the Euler equation along a streamline - $\int_1^2 ds$. Here, P is the hydrostatic pressure, ρ is the density of the fluid, v_s is the average fluid velocity in the tube and conduit, g is the acceleration due to gravity, and z is the height with reference to a datum.

Using conservation of mass, we can find the relations for the fluid flow-rate in each region of flow. The flow-rate in the mixer is given by the product of the mixer cross-section area and the rate of change of fluid height which should be equal to the product of the cross-section area and the fluid velocity in the interconnect tube and the internal channels. Since we are using two interconnect tubing to connect the mixers, the flow-rate (Q) is equally divided between both the tubes. Therefore, flowrate is,

$$Q = A\frac{dh}{dt} = 2\frac{\pi D^2}{4} v_s. \tag{7.6}$$

Here, A is the cross-sectional area and h is the height of the fluid in the mixer, D is the diameter and v_s is the flow velocity of the tube or conduit.

We can integrate the unsteady term piece-wise and stitch it together using the conservation of mass at the boundaries. Since the flow-velocity along the tube and along the conduit is constant and since the rate-of-change of flow velocity is zero in each of the mixers, the unsteady term can be taken out of the integration and the contribution is only from the internal conduits of length $L_{conduit}$, which are equal in

both platforms and the interconnect tubing of length L_{tube}. Therefore, we get,

$$\int_1^2 \rho \frac{\partial v_s}{\partial t} ds = 2\rho \left(\frac{\partial v_s}{\partial t} \right)_{L_{conduit}} \int_0^{L_{conduit}} ds \; + \; \rho \left(\frac{\partial v_s}{\partial t} \right)_{L_{tube}} \int_0^{L_{tube}} ds. \tag{7.7}$$

The integral of path length is the length of the tube/conduits. Also, from Eq. 7.6, we can get the unsteady term as a function of h. Therefore,

$$\int_1^2 \rho \frac{\partial v_s}{\partial t} ds = 2\rho L_{conduit} \left(\frac{\partial v_s}{\partial t} \right)_{L_{conduit}} + \rho L_{tube} \left(\frac{\partial v_s}{\partial t} \right)_{L_{tube}} \tag{7.8}$$

and,

$$\int_1^2 \rho \frac{\partial v_s}{\partial t} ds = \sum_{sections} \rho L_{sec.} \left(\frac{\partial v_s}{\partial t} \right)_{L_{sec.}} = \frac{2\rho A}{\pi} \sum_{sections} \left(\frac{L}{D^2} \right)_{sec.} \frac{\partial^2 h}{\partial t^2}. \tag{7.9}$$

The parameters inside the bracket represent those values for each section of the fluid column.

There will be energy loss due to viscosity of the fluid at the walls of the tubing and internal conduits which results in a loss of pressure head between points 1 and 2. This can be estimated from the Hagen-Poiseuille equation for a tube of diameter D and length L as,

$$\Delta P_{friction} = \frac{128 \mu L Q}{\pi D^4}. \tag{7.10}$$

Since we have two tubing connected between the platforms, the flow-rate is equally divided between the tubes and the total resistance is halved. Summing piece-wise over each section of the flow, the energy deficit between points 2 and 1 (Ref. Figure 7-5) due to friction loss is,

$$\Delta P_{friction} = -\frac{64 \mu A}{\pi} \left(\sum_{sections} \left(\frac{L}{D^4} \right)_{sec.} \right) \frac{\partial h}{\partial t}. \tag{7.11}$$

Fluid surfaces in both mixers are exposed to the atmosphere above them hence the static pressure is the same as the atmospheric pressure. The fluid velocity at the two fluid levels in the mixers should be the same, again by conservation of mass. The

height of the two mixers are related such that if h reduces by a certain δh at point 2, the height of fluid at point 1 raises by δh as well. Hence, $h_2 - h_1 = 2h$ for all time, where h is measured from the average height of the top surfaces of the fluid in the two mixers as shown in Figure 7-5.

Thus, the unsteady Bernoulli equation can then be rewritten as:

$$\frac{2\rho A}{\pi}\left(\sum_{sections}\left(\frac{L}{D^2}\right)_{sec.}\right)\frac{\partial^2 h}{\partial t^2} + 2\rho g h + \frac{64\mu A}{\pi}\left(\sum_{sections}\left(\frac{L}{D^4}\right)_{sec}\right)\frac{\partial h}{\partial t} = 0. \quad (7.12)$$

Table 7.3: Values of parameters of levelling model

Parameter	Symbol	Value	Units
Length of tube	L_{tube}	300	mm
Inner diameter of tube	D_{tube}	0.4 - 1.6	mm
Area of Mixer	A	320	mm^2
Length of internal conduit	$L_{conduit}$	100	mm
Conduit inner diameter	$D_{conduit}$	0.4	mm
Density of water	ρ	1000	kg/m^3
Dynamic viscosity of water	μ	0.8×10^{-3}	Pa s
Acceleration due to gravity	g	9.81	m/s^2

We can look at the relative scaling of various terms and their relative magnitudes. The parameters values for the platforms are given in Table 7.3. Doing the calculations for a nominal $D_{tube} = 1$ mm we get,

$$\tau_2^2 \frac{\partial^2 h}{\partial t^2} + \tau_1 \frac{\partial h}{\partial t} + h = 0. \quad (7.13)$$

The first term is from inertia of the fluid in the tubing and the conduit with $\tau_2^2 = 20$, the second term is from the damping due to friction with $\tau_1 = 2500$ and the third term is from the stiffness due to gravitational pressure head.

We non-dimensionalize the equation with respect to h and t, such that $h = h_0\, h^*$ and $t = \tau_1\, t^*$. $h*$ and $t*$ are non-dimensional variables which are normalized and vary from 0 to 1, i.e. they are of order unity - $\mathcal{O}(1)$. Applying the non-dimensionalization to Eq. 7.13 we get,

$$\frac{\tau_2^2}{\tau_1^2}\frac{\partial^2 h^*}{\partial t^{*2}} + \frac{\partial h^*}{\partial t^*} + h^* = 0. \quad (7.14)$$

All the dimensionless derivative terms should be of order $\mathcal{O}(1)$ when the scaling for h, t is correct. Comparing the dimensionless coefficients of the dynamic terms, the coefficient of the damping term is 1 while the coefficient of the inertia term is $\mathcal{O}\left(\frac{\tau_2^2}{\tau_1^2}\right) \ll 1$, since $\tau_2 \ll \tau_1$. Therefore, the inertia term can be neglected. Therefore, solving the first order differential equation,

$$\tau \frac{\partial h}{\partial t} + h = 0, \tag{7.15}$$

we get,

$$h = h_0 \, \mathrm{e}^{(-t/\tau)} \tag{7.16}$$

where, τ is the self-levelling time-constant (in seconds) in which height (h) reduces to a value of $1/e$ times h_0. The expression for τ is then given by,

$$\tau = \frac{32\mu A}{\pi \rho g} \left(\sum_{sections} \left(\frac{l}{D^4} \right)_l \right) \tag{7.17}$$

and h_0 is the initial height difference between the two mixers.

τ is most sensitive to the diameter of the tube and internal channels and since the internal channels have an ID of 0.4 mm, they contribute the maximum fluidic resistance in the system and largely determine the value of τ.

7.3.3 Mode of operation - steady state height difference

As shown in Figure 7-8 - in pumping mode, the average height difference (h) of the fluid level in the two mixers increases linearly due to the constant difference in pump flow-rates. Then, in self-levelling mode, the height difference reduces exponentially, based on the self-levelling time-constant (τ). Before the height difference is able to return to zero, the next pumping sequence begins and the height difference increases again leading to a greater height difference than the previous step. Due to the larger height difference at the beginning of this self-levelling step, the initial height decrease rate is larger and more volume is transferred during the self-levelling phase but there is net increase in fluid height this cycle as well, although a smaller increase than the

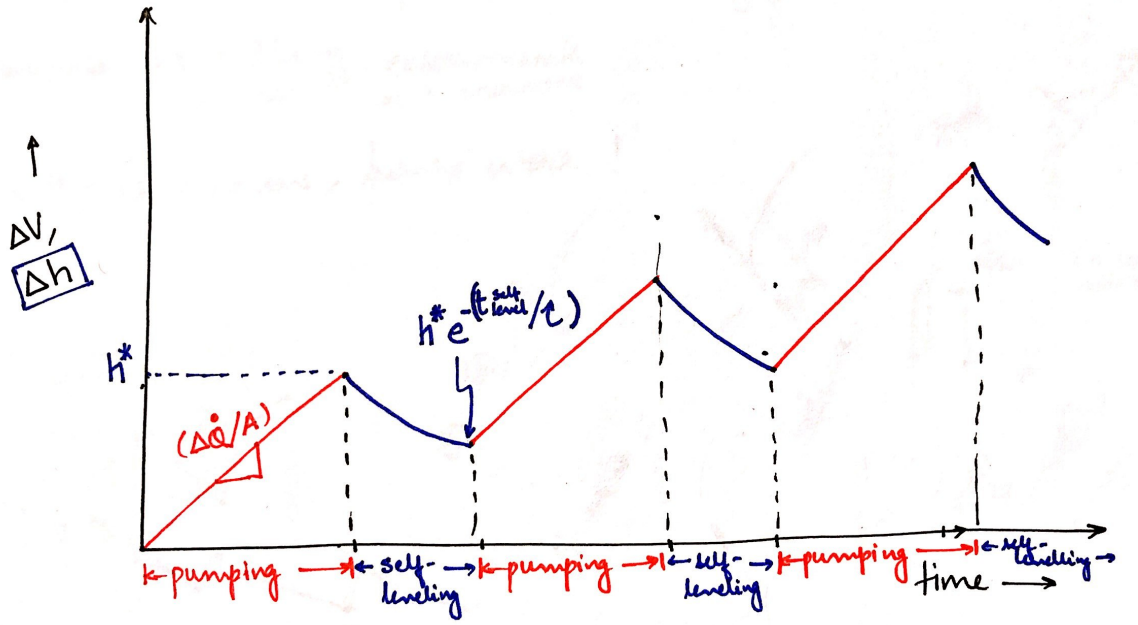

Figure 7-8: Self-levelling operation. Every pumping step, the volume difference linearly increases due to a difference in pump flow-rates (ΔQ). The area of the mixer is A, therefore the height difference increases between the mixers by ($\Delta Q/A$). Every self-leveling step the volume exponentially decreases from the value at the end of the pumping step by a factor of $exp(t_{self-leveling}/\tau)$. τ is the self-leveling time constant of the system as defined in Equation 7.17. One pumping step and one self-leveling step together is defined as one cycle. The self-leveling would take a long time to return back to 0 height difference. In a self-leveling step, before the system can return to a height difference at the beginning of the pumping step of that cycle, a new pumping step of the next cycle begins. Therefore, every cycle, there is net increase in the height difference. At each cycle there is net volume accumulation, which is smaller than the accumulation in the previous cycle. This sequence continues till the system reaches a steady state height difference (Figure 7-9).

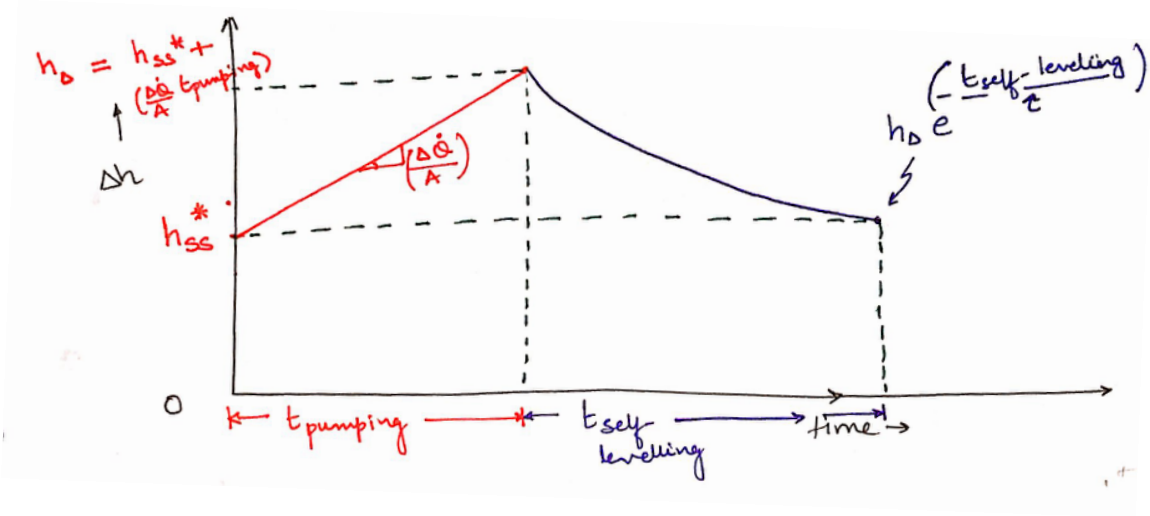

Figure 7-9: Self-levelling - Steady state operation. At steady state, the volume increase during pumping is matched by the volume reduction during self-levelling and there is no net change in the volume difference, as averaged over time.

previous step. This continues till a steady state is reached as can be seen in Figure 7-9. The steady state is attained when the height difference increase in the pumping step is the same as the height difference reduction in the self-levelling step.

The steady state height difference can be estimated by,

$$h_{SS} = \frac{\delta h \, \lambda}{1 - \lambda}. \tag{7.18}$$

Here, δh is the height difference every pumping portion of operation due to the difference in pump flow-rates and λ is the fraction by which the height during every self-leveling step, i.e.

$$\delta h = \frac{\Delta Q \; t_{pumping}}{A}, \tag{7.19}$$

and,

$$\lambda = \mathrm{e}^{-(t_{levelling}/\tau)}. \tag{7.20}$$

7.3.4 Time to reach steady state

The self-levelling over each sequence can be modelled as as a geometric progression. For the first cycle, during pumping, the height increases by δh and then reaches $\lambda \; \delta h$ at

the end levelling. At the end of the second cycle, the height now reaches $(\lambda\ \delta h + \delta h)\lambda$. This process continues and thus, the height after n cycles can be written as,

$$h_n = \delta h \sum_{i=1}^{n} \lambda^i. \tag{7.21}$$

At the limit of $n \to \infty$ this value converges to the steady state height difference - h_{SS} which we obtained in Eq. 7.18.

To evaluate what the value of n should be to reach 99% of steady state value, we have

$$h_n = 0.99 h_{SS}. \tag{7.22}$$

By substituting the value for h_{SS} and solving for n, we get,

$$\lambda^n = (1 - 0.99), \tag{7.23}$$

and,

$$n = \left\lceil \frac{\log 0.01}{\log \lambda} \right\rceil. \tag{7.24}$$

Then, the time required to reach 99% of steady state value would be,

$$t_{SS} = n(t_{pumping} + t_{levelling}). \tag{7.25}$$

7.3.5 Modeling results

The leveling behavior was modelled for three tubing diameters - 1/64 in (0.397 mm), 1/32 in (0.794 mm) and 1/16 in (1.588 mm) and is shown in Figure 7-10. The predicted volume difference between mixers for a 400s pumping and 600s levelling cycle, with a $Q_{pumping}$ of 2.5 µL/s are also shown.

The steady state volume difference is correlated with the time constant which is proportional to the fluidic resistance. When the tube diameter is larger by at least 1.7 times the diameter of the internal channel, then the resistance from the tube section is 10 times smaller than the resistance from the internal channels and only

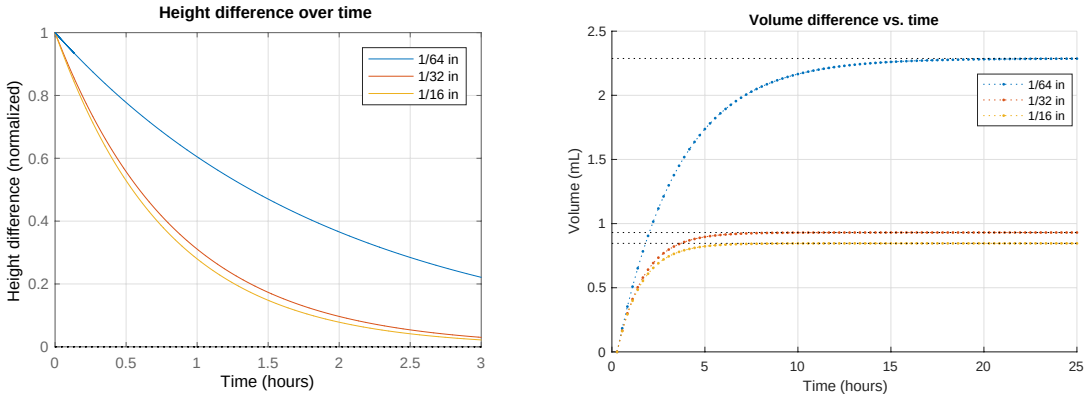

(a) Leveling time-constant. **(b)** Volume difference.

Figure 7-10: Levelling behavior for different tubing diameters.

Table 7.4: Parameters for different tubing diameters.

Parameter	Units	1/64"	1/32"	1/16"
Time to clear pipe volume	sec	50	140	500
Levelling time constant (τ)	hr	1.9	0.8	0.7
Steady state volume difference	mL	2.2	0.9	0.8
No. of cycles to 99% steady-state	-	54	24	22
Time to 99% steady-state	hr	15	7	6

Conditions: $t_{pumping} = 400$ sec, $t_{levelling} = 600$ sec, $Q_{pumping} = 2.5$ µL/s

the contribution from the internal channels is significant. If the tube diameter is of the order of the internal channel diameter, then contribution due to both sections add up.

The requirement for the biology experiments is that at-least 1 mL fluid volume remains in each mixer. Since the initial holding volumes of the mixers are 2.5 mL, using the 1/32 in diameter tubing is optimal considering the time required to clear the tube as well as the steady state volume difference which is less than 1 mL.

As the platforms were already fabricated, the internal channel diameter could not be modified. If we increase the internal channel diameter to be the order of 1/32 in (0.794 mm), then the leveling time constant τ would be reduced to 0.1 hr, the steady state volume difference would be 0.16 mL and the time to reach 99% stabilization would be reduced to less than 1 hour.

Based on the modeling, 1/32 in diameter tubing of 300 mm length is selected.

The selected operating parameters are: $t_{pumping}$ = 400 sec, $t_{levelling}$ = 600 sec, $Q_{connect}$ = 2.5 µL/s which meets the requirements of a $Q_{connect}$ of 1 µL/s

7.4 Experiments

The system is setup as described in Section 7.1.2 and as shown in Figure 7-11. 1% Bovine Serum Albumin (BSA) solution which is very similar to the media used in actual biological experiments in terms of density and viscosity is used as the test fluid. 2.5 mL of 1% BSA was added to each mixer and are run at operating parameters described in Section 7.3.5 in a cell-culture incubator. At the end of 48 hours, the recovered volumes are measured.

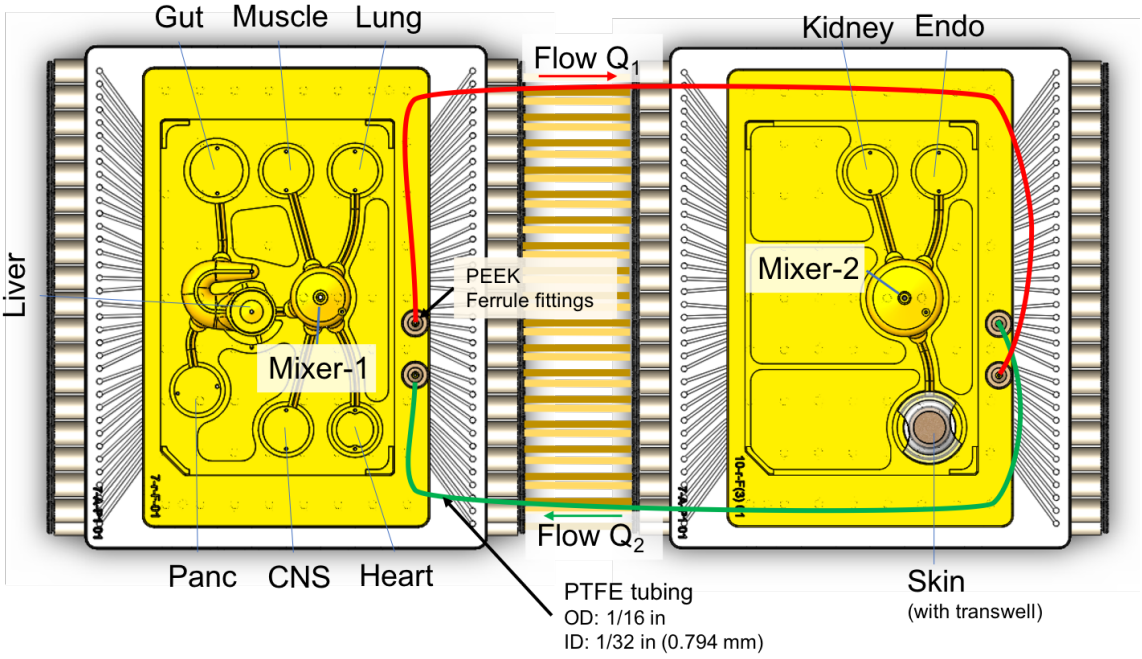

Figure 7-11: Top view of platforms interconnected.

The tests were repeated several times and in each case, the steady-state volume difference between the mixers was consistently found to be between 0.5 mL to 1 mL for the 1/32 in diameter tubing. The variation in the steady state volume difference is primarily due to the variation in the pumps between different platforms. When we experimented with 1/64 in diameter tubing, we found that the volume in one of the

mixers would become dangerously low and start drawing in air-bubbles through the pumps into various MPSes. In many cases, the mixer would even dry out. This in agreement with the predictions from the model.

Therefore, the experimental results agree very well with the model developed and this system was used for the biology exeperiments for the 10-way interaction.

7.5 Results and Conclusions

A cost effective method to utilize the existing 7-way and 3-way platform hardware for the 10-way experiments was described. A system for maintaining a net inter-connection flow-rate ($Q_{connect}$) of 1 µL/s between two platforms and simultaneously maintaining the fluid level between the two was designed. To achieve this, the mixers of the two platforms were connected using PTFE tubing. A repeating sequence of pumping from one platform to another for a certain duration followed by a duration of allowing for hydro-static levelling was utilized.

A $Q_{connect}$ of 1 µL/s is accomplished and the volume difference between mixers is maintained within 1 mL at steady state operation. It is found that the fluid resistance due to the internal channels and the tubes primarily determine the steady-state volume difference during operation. The various considerations in setting up the system were laid out and a model to predict the levelling dynamics and the steady state volume difference between the mixers was developed. The model was experimentally verified and is in close agreement with the experimental observations.

The method and the modelling outlined can be used in a situation where there is a need to understand the levelling dynamics between two chambers connected by a tube or where there is a need to provide net mixing flow-rate between two modules while simultaneously maintaining steady state volumes or both. If the inertial terms are significant compared to the damping term in Eq. 7.13, then we will need to solve a second-order partial differential equation to get the fluid height, with the appropriate boundary conditions - initial fluid height of h_0, initial fluid velocity of 0. We can expect to get a decaying-sinusoidal expression for the average fluid height

difference, h.

The DARPA 10-way experiments were conducted using the described system configuration and operating parameters and the milestones were successfully met in the first attempt within schedule. More details of the DARPA milestone experiments can be found in [2].

Chapter 8

Tubing selection to resolve condensation issue in platforms

8.1 Introduction

MicroPhysiological Systems (MPS) mimic the relevant human multi-organ physiology in-vitro. One approach developed in our lab uses an open-well system to culture various tissue systems [2]. It circulates a common fluid-media between the organs using pneumatic diaphragm micro-pumps [5]. The diaphragm is the active element for these pumps and its stability is important to achieve reliable long-term operation. These platforms generally operate inside a cell-culture incubator with a controlled atmosphere with a temperature of 37 °C, 5% CO_2 concentration and 95% relative humidity (RH) [35].

During long-duration experiments in the cell-culture incubator, water droplets were found in the pneumatic channels of these platforms as shown in Figure 8-1. Such droplets can interfere with the proper operation of the polymeric pump diaphragms due to the much larger viscosity of water as compared to air. We also had increased incidences of failures of the switching solenoids some of which showed signs of rusting on some of the steel parts. The switching solenoids switch between pressure and vacuum and this actuation signal travels through flexible plastic tubing through quick-disconnect couplings (Colder Products Company, MN) and then to the platform

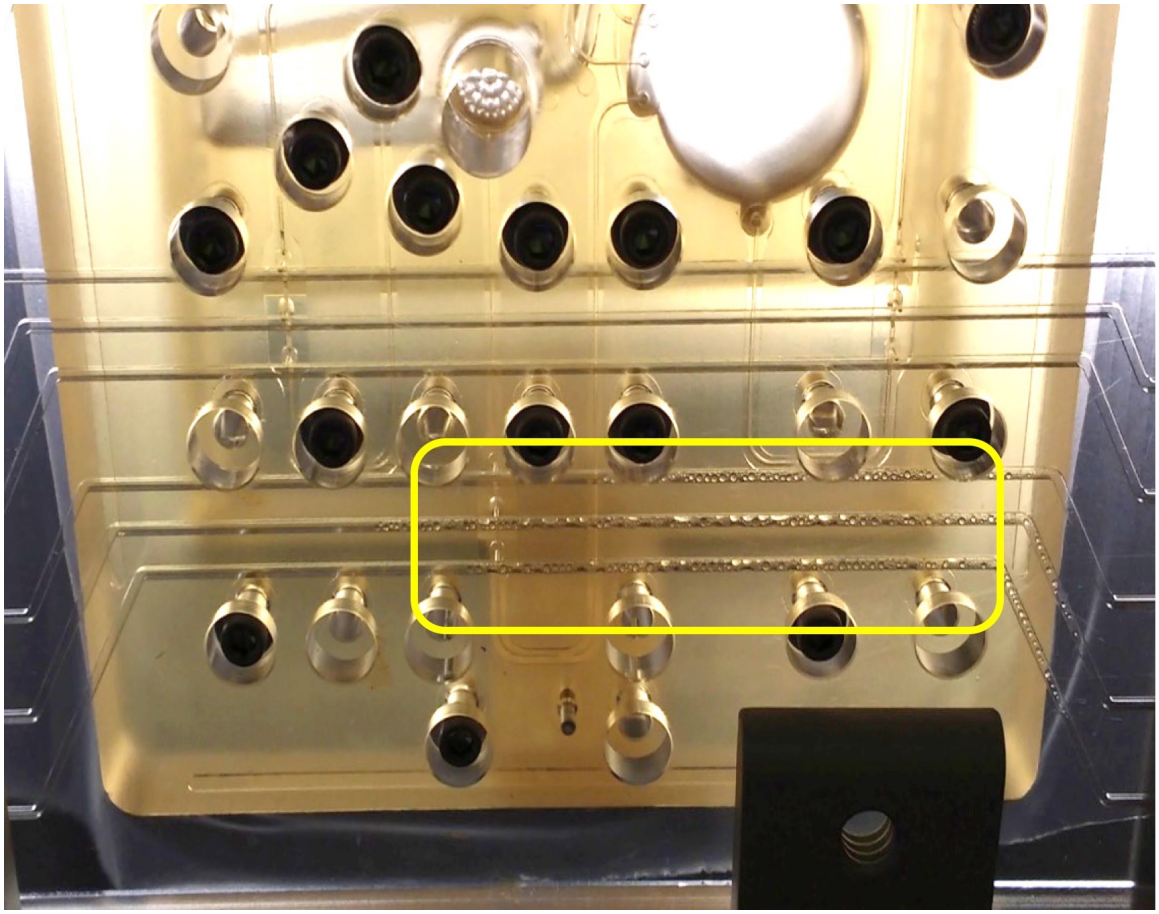

Figure 8-1: Condensation in the platform pneumatic channels. These channels supply pressure and vacuum from the switching solenoids to the diaphragms of the micro-pump for their actuation.

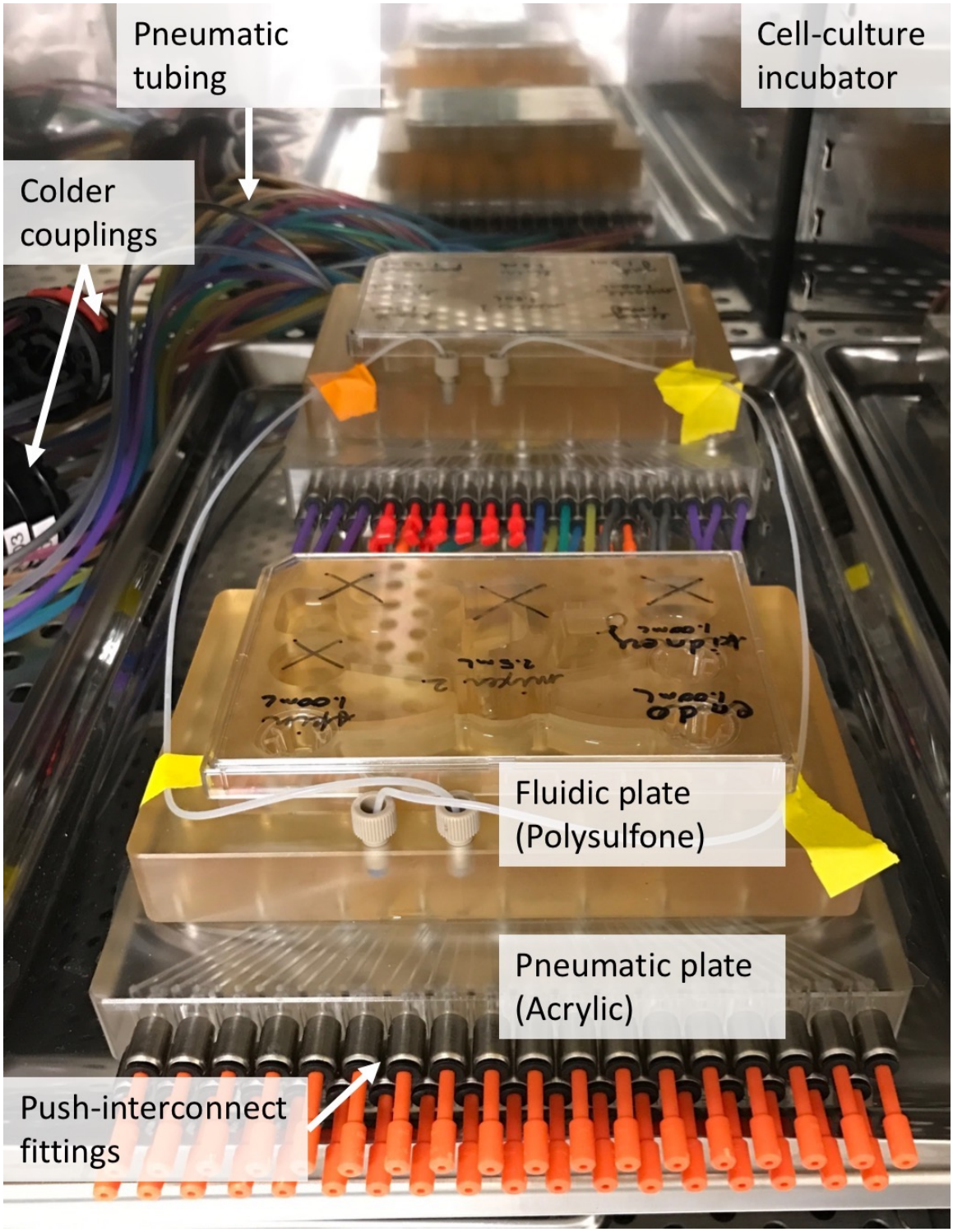

Figure 8-2: Platform setup inside the cell culture incubator. The pneumatic tubing connects to the pneumatic plate through push-interconnect fittings which lead into pneumatic channels which connect to the diaphragm of the micro-pumps.

pneumatic channels to switch the pneumatic side of the diaphragm under pressure or vacuum (Figure 8-2). This is the chain of actuation of the pneumatic diaphragm micro-pumps.

This chapter describes the steps taken to identify the source of water in the pneumatic channels, and the steps taken to resolve the issue. We determined that inside the incubator, water-vapor permeates through the originally used PolyUrethane (PU) pneumatic tubing and condenses. This condensate remains and is seen as water droplets in the pneumatic channels. We thus selected an alternate material, Poly-Olefin Elastomer (POE) which has low water-vapor permeability and which resolved this issue. Though seemingly simple, such condensation can cause significant reliability problems.

8.2 Problems with water in pneumatic channels

Water droplets are a potential problem as these can be transported upstream, towards the solenoids. When the pneumatic channel is under vacuum, the water droplets can rise up to the solenoids, damaging them as they have very small orifices and small steel moving parts which are specified for dry air operation only. It can also potentially go into the line vacuum tubing which can damage the vacuum pumps if left unchecked. The liquid shuttles every pressure/vacuum stroke and can potentially corrode away particles from the solenoids or platform channel. This can clog the ports, blocking airflow, or damage the membrane, compromising its integrity and performance. Compromised membrane integrity is a serious issue as it can potentially lead to contamination of the tissue cultures. Water can also clog the on-platform pneumatic channels and thereby interfere with the pump operation.

Therefore, there is a need to ensure that the pneumatic channels on platform run dry, within the incubator despite the near 100% relative humidity environment. This should be achieved, ideally by removing the source of water droplets, or at least by quickly removing them from the lines as soon as they are formed.

8.3 Identification of the source of water droplets

Water droplets in the pneumatic channels are the end state. Phenomenologically, to see water droplets in the pneumatic channel we need a source of water and a pathway for water transport into the pneumatic channel from the source. The potential sources of water could be:

1. High relative humidity of the line pressure which could be condensing in the pneumatic channels over time.

2. Fluid transport through the diaphragm thickness, from the fluidic side into the pneumatic side.

3. Water vapor transport from the high relative humidity incubator environment into the pneumatic channels. There are multiple regions in the pneumatic line which are within the incubator environment - plastic tubing, quick disconnect couplings, the acrylic base into which the pneumatic channels are machined, and the pneumatic channel end fittings which connect with the pneumatic tubing.

To identify the source of water, we conduct experiments keeping only one of the potential sources and isolating the others.

1. For relative humidity of the source line pressure, we ran the platforms on the bench, with room temperature of 24 °C and relative humidity of 30–60%. The pumps were operational for 48 hours, with no fluid on the fluidic side. We did not find any condensation in the pneumatic channels, indicating that the line pressure system is probably not a major source of water in the pneumatic channels.

2. To test the fluid transport through the diaphragm thickness, from the fluidic side to the pneumatic side, we again conducted experiments on the bench. This time, we used inline desiccants such as the Speedaire disposable air filter/dryer which lowers the dew point to -40 °F (-40 °C) to ensure dry air goes into the platform. We again did not find any condensation in the pneumatic channels

after 48 hours indicating that transport through the membrane is probably not a major source of water in the pneumatic channels.

3. To test if water vapor from the high relative humidity atmosphere in the incubator is the source, we ran the platforms inside the incubator with in-line desiccants for the pneumatic lines and no fluid on the fluidic side for 48 hours. We found water droplets in the pneumatic channel indicating that the water vapor in the high relative humidity atmosphere in the incubator is definitely the source.

After having identified water vapor in the incubator atmosphere as the source, we still need to identify the pathway for the entry of water into the pneumatic channels. As discussed above, there are four potential points for water vapor entry - plastic tubing, quick-disconnect couplings, the acrylic base into which the pneumatic channels are machined, and the end fittings which connect with the pneumatic tubing. We need to test each of the elements to identify the major sources. Water vapor either enters through some air-gaps in the material or permeates through the polymer material.

8.4 Permeability of polymers

Although all polymers are permeable to fluids to some extent, the range varies widely depending on the nature of the polymer and the fluid [36]. The "solution-diffusion" mechanism is commonly used to describe permeation of small molecules through polymer membranes. It consists of five steps [37]:

1. Diffusion of the small molecules from the environment to the surface of the polymer,

2. Solution (sorption) of small molecules into the membrane at the side of higher potential (pressure, concentration, etc.),

3. Molecular diffusion of the molecules in and through the membrane,

4. Release (desorption) of the diffused molecules from the solution at the opposite side into the liquid or gas phase at lower potential, and

5. Diffusion of the small molecules away from the surface into the environment at the opposite side.

The term permeation describes the overall mass transport of the gas or liquid penetrating across the membrane, whereas the term diffusion describes the movement of those small molecules inside the bulk of the polymer. Usually, the molecular diffusion through the polymer membrane is the slowest and, thus, the rate-determining step in the permeation process. Gas permeation through a non-porous, dense polymer membrane is usually described by the following equation, [37]

$$P = DS \tag{8.1}$$

where, P is the permeability, D is the diffusion coefficient, which characterizes the mobility of dissolved gas molecules and S is the solubility coefficient, which characterizes the affinity between the diffusing gas and the polymer material. P depends on the materials of the polymer-gas system, along with the pressure (which influences S) and the temperature (which influences D and S).
P has units of,

$$\frac{amount\ of\ gas \times membrane\ thickness}{membrane\ area \times time \times pressure}.$$

In SI units, this translates to $\mathrm{mol\,m^{-1}s^{-1}Pa^{-1}}$. The total amount of gas transported to the other side therefore is directly proportional to the membrane area, time, and partial pressure-difference of the gas on the two sides and inversely proportional to the membrane thickness. For liquid and vapor permeability, the vapor transmission rate for vapors is independent of the pressure differential across the membrane. This is because the vapor pressure for a liquid is a function of the liquid temperature [38]. The permeability over a wide range of pressures is almost constant and therefore, the pressure term is not mentioned in the units describing P for liquids and vapors. Thus, for water vapor permeability, P is commonly expressed in $\mathrm{g\,mm\,m^{-2}day^{-1}}$.

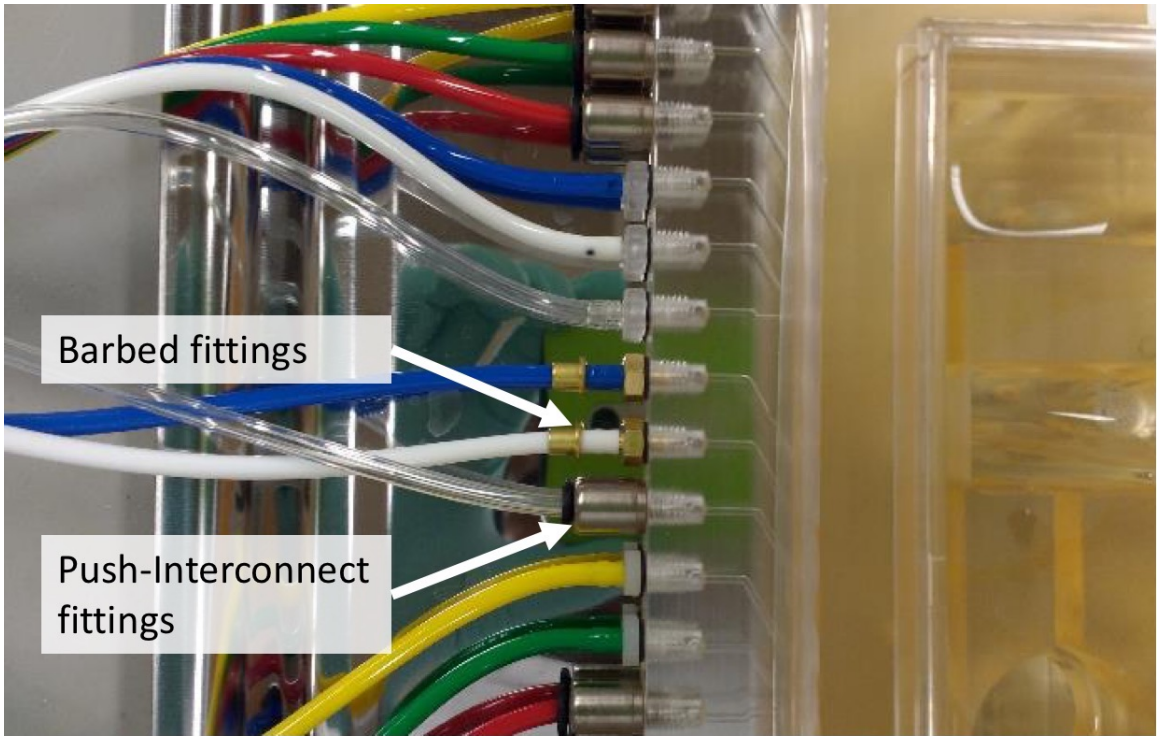

Figure 8-3: Push-Interconnect and barbed fittings are tested for water vapor permeation through the tubes. Push-Interconnect fittings are commonly used for their ease of use, though barbed fittings result in a much tighter seal.

8.5 Identifying source of water vapor entry into the pneumatic channels

We take each element one by one to analyze if it is the source of water vapor entry into the pneumatic channels.

1. Pneumatic channel end fittings

   Usually, the platforms use Push Interconnect (PI) fittings for connection of the pneumatic channels with the pneumatic tubing (Figure 8-3). These make it easier to connect and disconnect the pneumatic tubes compared to other fittings such as barbs and compression fittings. On the other hand they are also more prone to leaking. Therefore, we tested the platforms with barbed connectors instead of the push interconnect fittings. We ran the platforms in the incubator for 48 hours without water on the fluidic side and with in-line desiccants for the

pneumatic lines. We still found condensation in the pneumatic lines, indicating that the major source of water vapor entry is something else.

2. Acrylic base

   Analysis of the acrylic base independently is challenging as permeability depends on the applied pressure difference and to apply a difference in pressure, we require the pneumatic tubing connected to the platform. As a partial test, the platform with all the pneumatic connections sealed and no fluid on the fluidic side was kept in the incubator for 72 hours. There was no condensation indicating that the acrylic base is probably not the major source.

3. Pneumatic tubing

   We used the pneumatic polyurethane tubing used for the pneumatic connection from the switching solenoid to the platforms. We took around 300 mm of transparent tubing and sealed off one of the ends by melting and crimping the walls together. We then connected them to the quick-disconnect couplings inside the incubators and ran the regular actuation cycle for the solenoids for 48 hours. We found condensation in the tube (Figure 8-4) which indicates definitively that the pneumatic tube and/or the colder coupling is the major point of entry of water vapor into the pneumatic channels.

4. Colder connectors

   It is challenging to test independently between the colder connector and the tubing. Therefore, a custom high relative-humidity setup was made for more analysis as described below.

8.6 Desktop high relative humidity setup

We made a desktop high relative humidity setup, which is shown in (Figure 8-5). The principle used is that a closed environment with water will eventually reach a humidity level of 100% RH. In that state of water-vapor saturation, the water-vapor

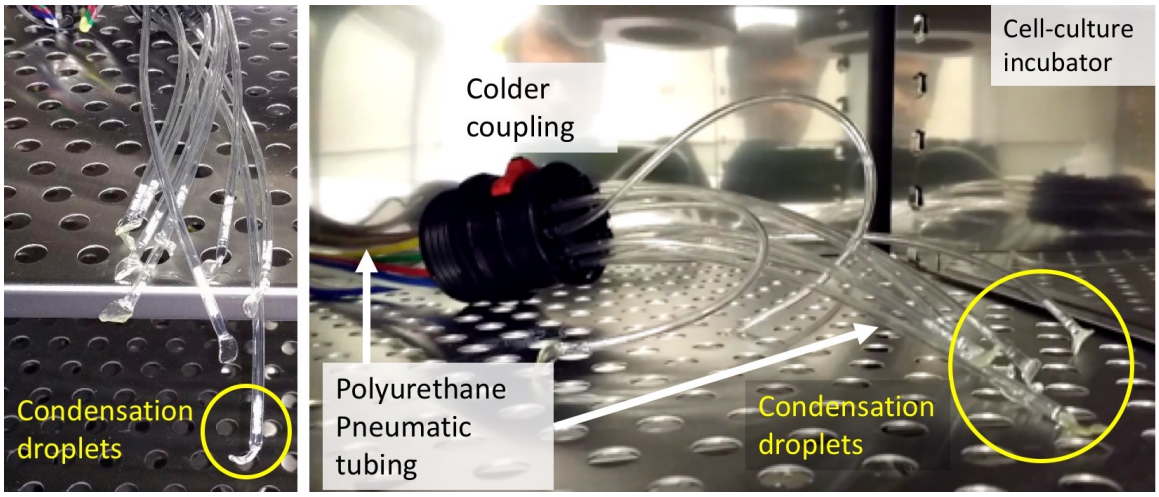

Figure 8-4: Tests with polyurethane tubing in the cell-culture incubator show condensation droplets inside the tubing, indicating that water vapor entry though the tubing is a major cause.

above the water surface in equilibrium with the bulk liquid. The process of reaching saturation can be sped up if the temperature of water is increased as this leads to an increase in vapor pressure. A limit is when the vapor pressure of water becomes equal to the atmospheric pressure, at which point the liquid begins to boil.

The setup (Figure 8-5) consists of an air-tight food storage container with water and a frame to hold test samples above the water level. The container is placed on a hot plate to slightly increase the water temperature to around 35-40 °C. A thermometer is used to measure the water temperature and set the heating power. The hot plate has a magnetic stirrer and the magnetic stir bar is placed in the water inside the container to get a more homogeneous temperature distribution. A cutout is made from the side to allow for pneumatic tubes into the container. Leaving the setup running for about an hour shows condensation droplets at the walls indicating that the environment inside is saturated, with a relative humidity of 100% RH.

Tests with polyurethane tubing placed inside the high RH setup, and with the quick-disconnect (Colder) couplings placed outside the airtight container showed condensation in the tubes (Figure 8-6). Thus, we identified the tubing as the source of water vapor entry into the pneumatic channels.

The mechanism is that water vapor permeates through the tubing walls. When

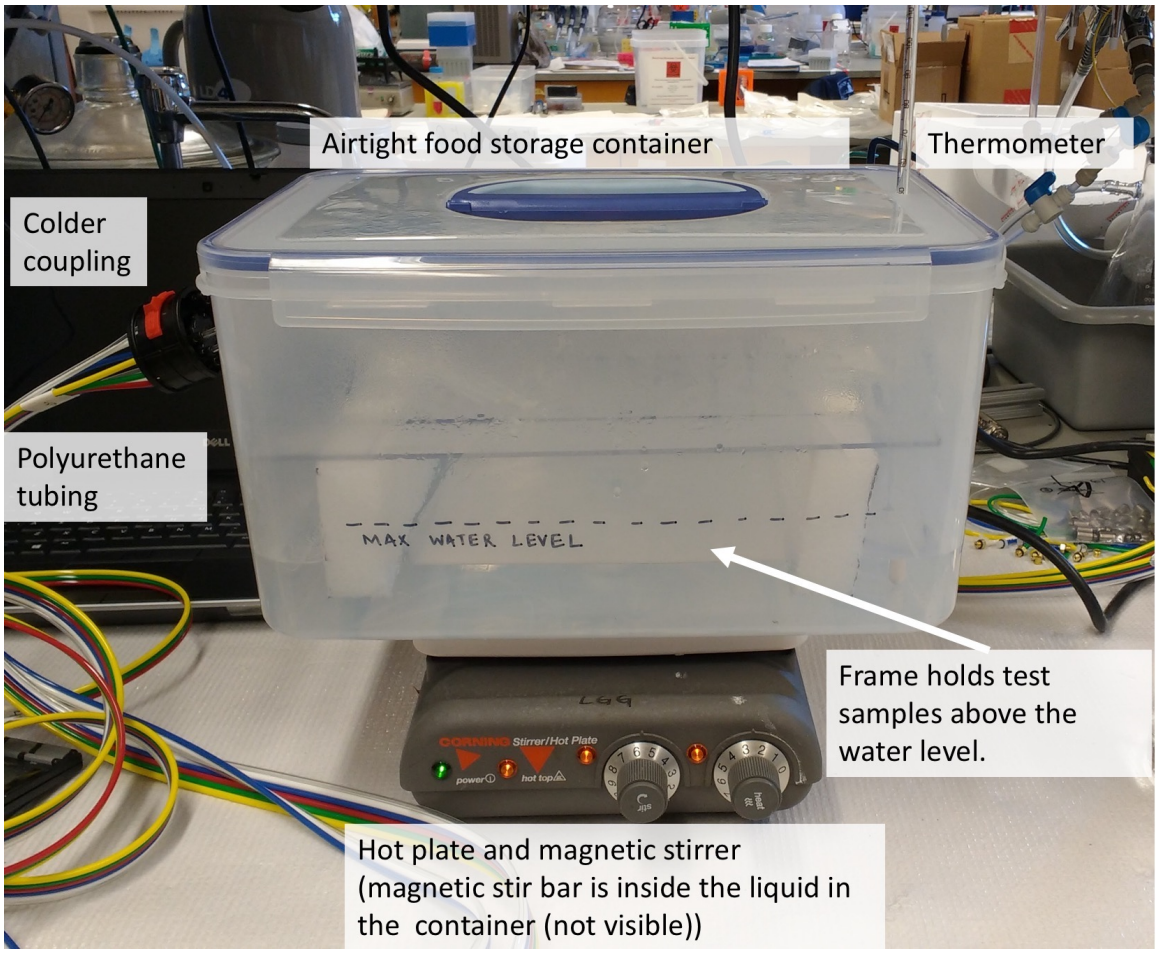

Figure 8-5: High relative humidity setup

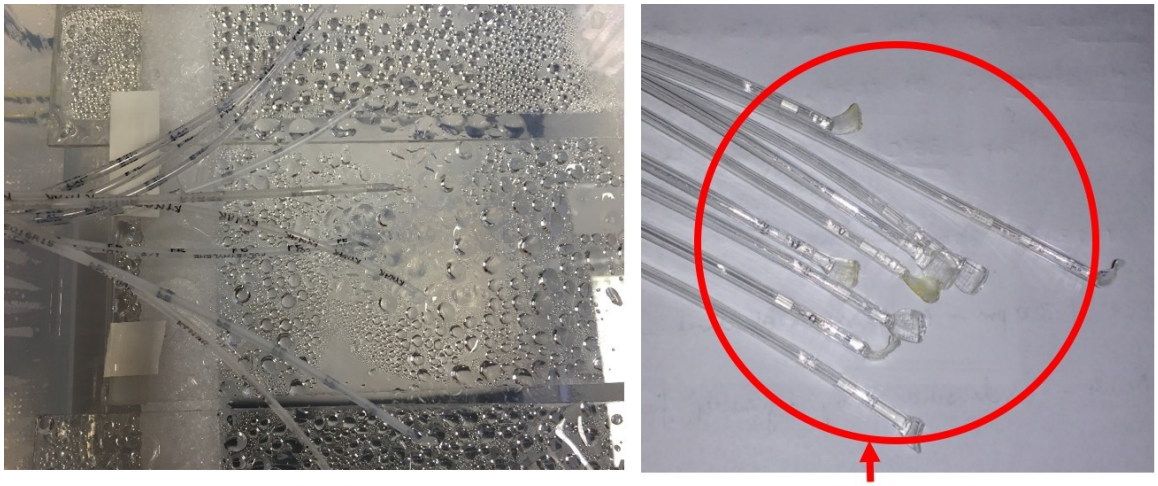

Tubes inside the high RH setup
(*condensation droplets on the wall due to high RH*)

Condensation in tubes
(*high reflectivity regions are due to water*)

Figure 8-6: Condensation observed in the tubing placed inside the high relative humidity setup

the pressure switches to vacuum inside the tubing, it is associated with adiabatic expansion of air and hence, cools down the inside of the tube causing the water vapor to condense and be seen as water droplets in the tube. These water droplets can travel both upstream and downstream which supported by our initial observation of water droplets inside the pneumatic channel.

Therefore, the problem statement now is to identify a tubing material which is relatively impermeable to water vapor within the operating conditions. We still don't know about the quick-disconnect (Colder) couplings and test for them once we identify an impermeable tubing material.

8.7 Low water-vapor permeability tubing selection

We explored various tubing materials. In general, the physical and chemical properties of polymers can vary significantly lot to lot, in manufacturing and between manufacturers. For comparison of nominal values, we extracted information from [37] which is shown in Table 8.1. Common grades of plastic tubing material available are evaluated. Apart from water vapor impermeability, the tubing must also be flexible for easy installation and handling. The material should be soft (low durometer) to be able to work with barbed fittings for the quick-disconnect (Colder) couplings and should be rated for pressure/vacuum up to $\pm$100 kPa.

From Table 8.1, we find that Fluorinated EthylenePropylene (FEP) would be the ideal material in terms of water vapor impermeability. Unfortunately, it doesn't work with barbed connectors and it was hard to find this material in multi-color options, which are required for connecting the many lines. We decided to explore the performance of other materials and obtained samples of Polyethylene (PE), Polyolefin Elastomer (POE), PolyVinyl Chloride (PVC), and Kynar® to test in the high RH setup. Nylon is very rigid and was not evaluated, further it can be seen in Table 8.1 that Polyurethane (PU) has a high water vapor permeability, which supports our observation of problems with this material in our setup.

Testing the vapor permeability for the different materials, we find no condensation

Table 8.1: Comparison of various tubing materials for water-vapor permeability [$g\,mm\,m^{-2}day^{-1}$]. Water-vapor permeability data extracted from [37]. Except PVC which needs to be reinforced for vacuum use, all other tubing materials are directly suitable for pressure/vacuum up to ±100 kPa.

Material	Water-vapor permeability	Fitting
Fluorinated Ethylene Propylene (FEP)	0.2	Push-interconnect compression
Polyethylene (PE)	0.4	Push-interconnect compression
Nylon	0.4	Push-interconnect compression
PolyOlefin Elastomer (POE)	0.4	Push-interconnect compression barbs
PolyVinyl Chloride (PVC)	0.9	Barbs
Kynar® PolyVinyliDene Fluoride (PVDF)	1.0	Push-interconnect compression
Polyurethane (PU)	2.0	Barbs push-interconnect

in PE and POE. In all others, there were visible water droplets inside the tubing. Out of the two, since POE works with barbed connections, it was chosen as the tubing material for the pneumatic connections.

To test the quick-disconnect (Colder) connectors, we kept Colder connectors with POE tubing inside the high RH setup for 48 hours running a standard pumping cycle and found no condensation indicating that the Colder couplings seal well against water vapor entry.

We replaced the polyurethane pneumatic tubing in an incubator with POE and

ran the platform with water on the fluid side with push-interconnect fittings on the pneumatic plate for 4 weeks non-stop and found no condensation in the pneumatic channels.

This solution was replicated to all of our incubators and we have not faced the issue of water droplets in the pneumatic channels since.

8.8 Conclusions

Water free operation of the pneumatic channels is important for long term reliability of pneumatic diaphragm micro-pumps. In this chapter, we describe the steps taken to identify and resolve the issue of water in the pneumatic channels when platforms were run in the incubator.

We find that the the mechanism of water entry is through the permeation of water vapor through the PolyUrethane (PU) tubing. This water-vapor then condenses due to the reduced temperature from expansion of air when switching from pressure to vacuum. This condensate remains in the tube and is seen as water in the pneumatic channels.

An alternate tubing material, PolyOlefin Elastomer (POE) was identified which has a low water-vapor permeability of around 0.4 $gmmm^2day^1$. It also meets other criteria for handling and pressure/vacuum ranges. After changing the pneumatic tubing to POE in the cell-culture incubators, the issue was resolved.

Polymers are very versatile and with this versatility, comes a large range of physical and chemical properties between polymers which can be tweaked to get the desired behavior. Therefore, careful selection of polymers based on the environment, structural and dynamics loads, and stability is essential to ensure long-term, reliable operation.

Chapter 9

Conclusions and suggestions for future work

9.1 Conclusions

Microphysiological (MPS) systems, also called organs-on-chips are platforms that simulate the activities, mechanics and physiological responses of entire organs and organ systems. On-platform pumps provide greater flexibility and design freedom and are a key feature of such platforms. It is desirable that these platforms be portable and energy efficient. For greater adoption of these platforms by the wider community, there is a thrust in the field to make these platforms low cost and single-use to reduce the sterilization and setup time and effort (Chapter 3).

This thesis describes the design and development of a scaled-up version of an electromagnetic (EM) pump (Chapter 5). It uses electrical energy which can be supplied by a battery and is therefore portable. The EM pump uses a teeter-totter EM actuator having a low energy consumption of about 1 mJ/stroke. Running at 1 Hz pumping frequency, that translates to a power consumption of 6 mW (total) for 3 actuators, one each for a set of valve-pump-valve. We experimentally verified the steady-state actuator coil temperature rise to be less than 0.1 °C, confirming negligible heating in the winding due to this low power consumption. This makes the EM pump suitable to be used within a cell-culture incubator with very small effects on

the nominal 37 °C temperature of the cell-culture medium, even for a platform using multiple actuators. The actuator's low energy consumption is achieved by a latching design which requires only a short pulse of energy to switch its state and where springs store some of the actuator kinetic energy, which is then recovered in the reverse stroke. In addition, we explore concepts for pumping and valves (Chapter 4). This thesis also describes the development of injection-molded, single-use platforms with onboard diaphragm micro-pumps (Chapter 3). It describes various valve and pump geometries and a model to predict large deflections of polymer diaphragms (Chapter 2). We integrate the EM actuators with these platforms, demonstrating pumping at a flowrate of 0.45 µL/stroke, no measurable temperature rise, valve sealing up to 60 kPa, and a pumping frequency of 1 Hz, limited by diaphragm behavior (Chapter 5).

Further, this thesis describes improvements in passive leveling between MPSes on a platform using improved spillway designs (Chapter 6). It also presents a method to fluidically interconnect two platforms and maintain fluid level between them (Chapter 7). It also describes the selection of polymer material for pneumatic tubing to resolve the condensation issue in pneumatic channels of the diaphragm micro-pumps (Chapter 8).

The testing of the EM pump is in progress. Preliminary results are encouraging, and show potential for EM pumping at the microscale. The EM pump needs to be characterized in more detail. The EM actuators also need to be made about 4 times smaller for integrated actuation of multiple pump lanes while fitting onto a single platform.

9.2 Suggestions for Future Work

This section details ideas and concepts for further work building on the work already described in this thesis.

9.2.1 Diaphragm design for micro-pumps

While our developed model reasonably predicts deflections of diaphragms over a wide range of deflections, the model is valid only in those cases where the diaphragm deflection is not constrained externally. For the valve chambers, the diaphragm deflection is constrained by the sealing lands. For the pump chambers, the diaphragm deflection is constrained by the chamber walls beyond which the deflected volume does not change. Our model gives bounding values for the forces and pressures to first make contact with the pump and valve chambers. To accurately know the final stress state of the membrane, we need to model the diaphragm deflection and stress state once it makes contact with the chamber walls and model the contact progression with increasing driving pressure. We can then predict the long term performance of the membrane knowing the stress and strain information of the diaphragm during actuation.

For accurate prediction of the diaphragm behavior, especially long-term performance, the properties of the diaphragm should also be accurately measured. Polymers can vary greatly in their properties lot-to-lot, even from the same manufacturer. Therefore, accurate measurement is the best way to obtain data on the properties of diaphragm materials. Another confounding factor is the friction state of the diaphragm with the chamber walls. Low friction will allow for slip between the diaphragm and chamber surface and therefore only constrain the deflection normal to the diaphragm surface in contact. High friction values on the other hand, will constrain in-plane as well as normal deflection of the diaphragm surface in contact with the chamber walls. For initial prototypes, the bounding values and calculations as described in Chapter 2 are sufficient. The life of the diaphragm needs to be tested after fabrication. The more advanced analysis may be useful to optimize the parameters and as a complement to extensive testing under various conditions, once a product is developed and is being scaled up for volume manufacturing.

This can potentially be done using dynamic, non-linear Finite Element Analysis (FEA). This problem is presumably too complex to model analytically.

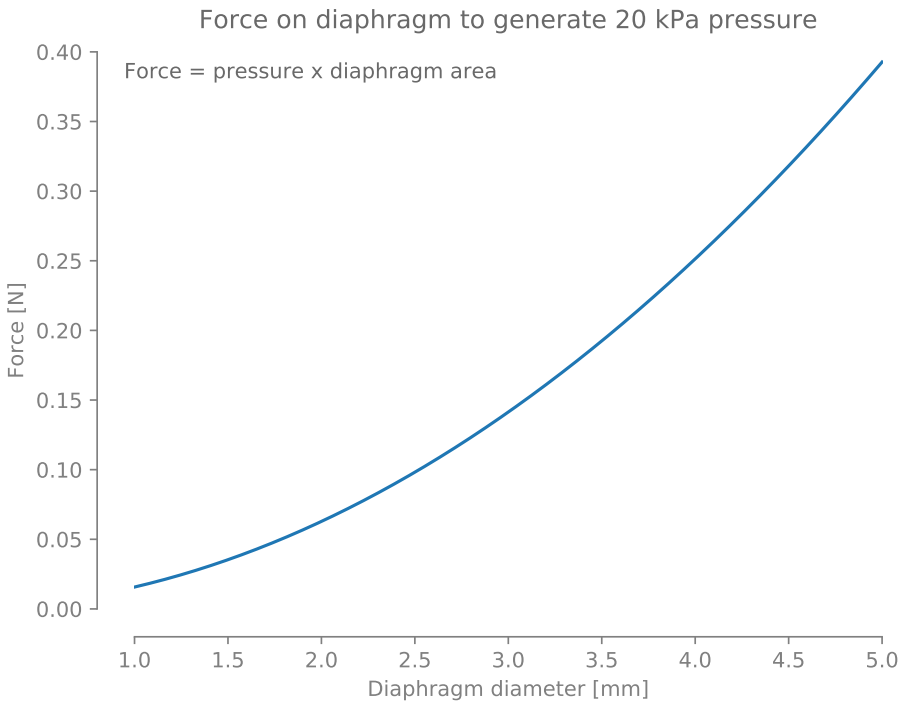

Figure 9-1: The force required to generate a given pressure quadratically increases with increasing diameter.

9.2.2 Electromagnetically actuated diaphragm micro-pump

The actuator developed and tested in Chapter 5 of this thesis is a scaled up version for ease of fabrication and testing. The actuators need to be made about 4 times smaller for integrated actuation of multiple pump lanes while fitting onto a single platform. Many of the principles described in Chapter 5 can be used to guide the design as the actuator scales down.

We should move towards using more flexible membranes and then have some other means to provide a quick return to the diaphragm. This would enable working with smaller diameters and drastically reduce the force requirement. For example, to generate 20 kPa back-pressure with a 3mm diaphragm, the force requirement is only about 0.15 N if the force required to deflect the diaphragm is negligible.

As shown in Figure 9-1, the actuation force increases quadratically with increasing diameter of the diaphragm. For example, the force requirement, just to increase pressure to 20 kPa in a constrained volume of fluid through a 5 mm diaphragm is,

force = pressure×area = 0.4 N. Thus, going to a smaller diameter reduces the force requirement to generate a given pressure.

On the other hand, the diaphragm stiffness drastically increases with decreasing diaphragm diameter for the same thickness of the diaphragm (Section 2.1.1). Hence, the force required for a given deflection increases with decreasing diameter. In our current pumps, the return of the diaphragm is through this "self-stiffness" of the diaphragm. Therefore, the total force requirement is 1 N for a 5 mm diameter diaphragm against 20 kPa of back-pressure. These two requirements of larger diameter to reduce force requirement to deflect the membrane and smaller diameter to reduce the force required for a given pressure requirement contradict each other.

One solution to provide the return force for the diaphragm is to bias the diaphragm deflection as shown in Figure 9-2. This approach uses vacuum to pull the diaphragm away from the pump chambers when the actuator is not pushing on the diaphragm. Other ways to increase the diaphragm stiffness, especially near the zero deflection point, are shown in Figure 9-3. If we use a more flexible membrane material such as Elastomeric Cyclic Olefin Copolymer (E-COC), which has a Young's modulus of 50 MPa compared to 1300-1500 MPa for the COC membrane used in our present designs, we can greatly reduce the force required for diaphragm actuation. As shown in Figure 9-4, for a 3 mm diameter diaphragm, the force required for the membrane deflection of 0.1 mm is about 0.04 N.

Then, the total force including the force to pressurize the fluid and to deflect the membrane is about 0.2 N. In addition, the actuator will need to overcome the spring element or vacuum which brings the diaphragm back to the neutral position. Assuming symmetric loading in both directions, we get a total force requirement of 0.4 N. With a factor of 1.5, for the additional spring deflection, the force requirement from the actuator is 0.6 N, which is less than the present 1 N.

Bounding calculations for permanent magnet and winding

For a surface with normal magnetic field B, the magnetic stress normal to the surface, acting on a ferromagnetic material to bring the two surfaces close together

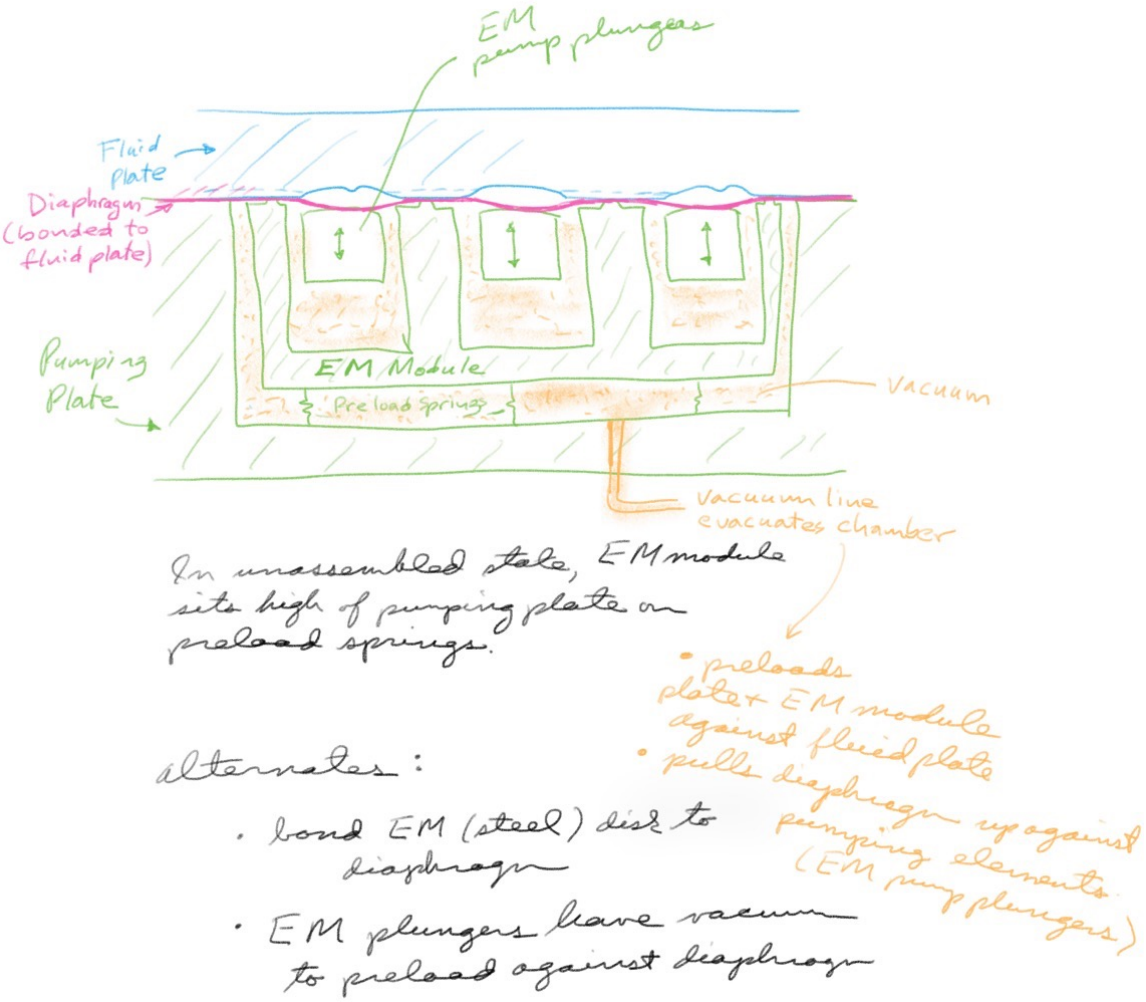

Figure 9-2: Vacuum preload for the diaphragm. The diaphragm (magenta) is bonded to the fluid plate (blue). The fluid plate is is preloaded against the pumping plate (green) using vacuum (orange). The vacuum is provided through channels in the pumping plate. When unassembled, the EM modules rest within the pumping plate on the preload springs. When the fluid plate is assembled and vacuum is applied, the pumping plate and the fluid plate come into contact and push on each other. In addition, the vacuum pulls the fluid plate towards the EM modules and the vertical position is controlled by the contact between lands of the EM module and the fluid plate surface. In operation, vacuum pulls the diaphragm away from the pump and valve chambers and towards the EM actuators. In operation, the EM actuator pushes the diaphragm towards the chamber walls and the diaphragm return is by the vacuum preload.

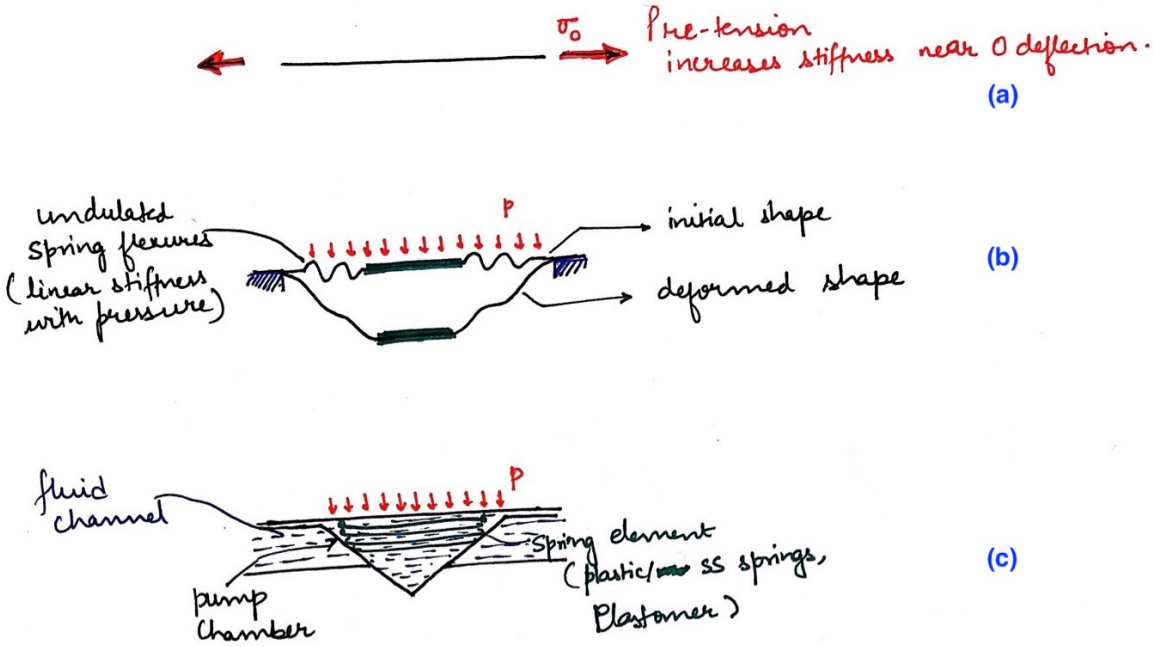

Figure 9-3: Other options to increase diaphragm stiffness so as to give faster fluid refill. (a) Increasing pre-tension in the diaphragm increases membrane stiffness, especially at the 0 deflection point. This leads to a greater suction pressure and faster suction stroke of the pump chamber. Unfortunately, this also increases the overall force requirement for deflection of the diaphragm. (b) Undulated spring features make the diaphragm deflection linear with increasing pressure. This results in a greater stiffness at zero deflection and at the same time, reduces the overall force for deflections greater than the diaphragm thickness. (c) Placing some spring elements on the fluidic side, immersed in the fluid, also can assist the diaphragm for quicker return in the suction stroke. A challenge is material selection which meets the bio-compatibility and drug-adsorption requirements, as well as assembly and possible reuse issues.

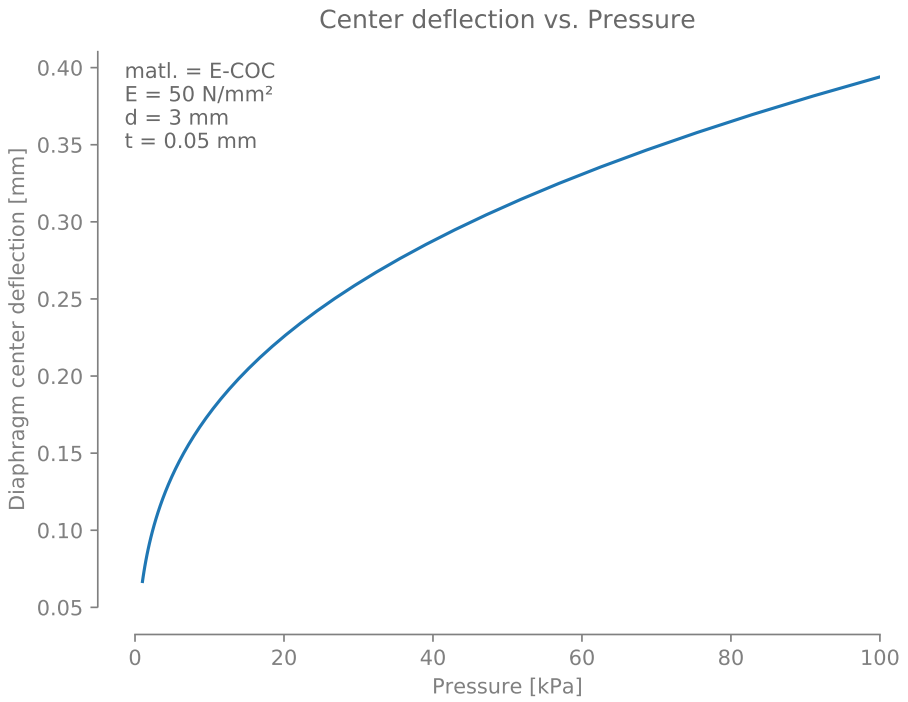

Figure 9-4: E-COC membrane has much lower stiffness compared to regular COC membrane. The pressure required for 0.1 mm diaphragm deflection is only around 5 kPa, which translates to a force of 0.04 N for a 3 mm diaphragm. This data is generated from the Timoshenko model described in Chapter 2. The initial diaphragm tension is assumed to be 0.

is given by [39],

$$P_{magnetic} = \frac{B^2}{2\mu_0} \tag{9.1}$$

where, μ_0 is the permeability of free space and equal to $1.257 \times 10^{-6}\,\mathrm{NA}^{-2}$.

For a field of 1 T, normal at the surface of a permanent magnet, this stress calculates to $P_{magnetic} \approx 0.4\,\mathrm{MPa}$. For 0.6 N of force, the pole face area required is thus $0.6/0.4 = 1.5\,\mathrm{mm}^2$.

The winding magnetic field counteracts this latching B-field from the permanent magnet. Figure 9-5 shows a schematic with the rotor latched on the left pole face. Assuming a relative permeability of low carbon steel to be $\mu_r = 1000$, and maximum winding current density, J_{max} of $10\,\mathrm{A/mm}^2$ for a short pulse, we can roughly estimate the winding area required. For simple estimate, we can assume the relative permeability of the low-carbon steel to have an infinite permeability compared to the

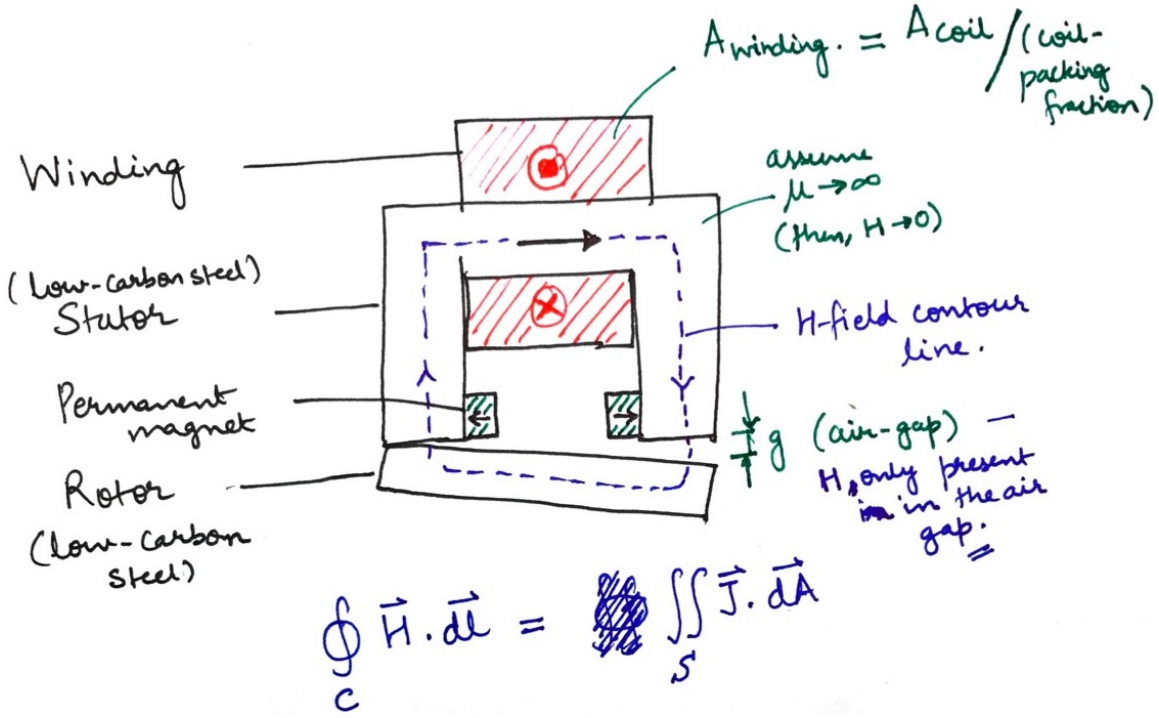

Figure 9-5: A schematic of the actuator to get rough estimates of the winding area. The rotor is latched to the left pole face. The winding current drives an H-field which counteracts the B-field on the left side pole face causing the rotor to flip. The stator and rotor are assumed to have an infinite permeability. Therefore, the H-field inside them is 0. Most of the H-field in the magnetic circuit is then in the air-gap. We can find the winding area using Ampere's law.

air-gap. Then, the H-field inside the low-carbon steel material (stator and rotor) is negligible and most of the drop in H occurs at the air-gap (g). In our scaled up actuator, we consider an air-gap of 0.4 mm. Assuming we have the same air-gap, then using Ampere's law [39],

$$\oint_C H \cdot dl = \iint_S J \cdot dA \tag{9.2}$$

We can use Equation 9.2, to get an estimate of the winding area required. To get a B-field of 1T, the H-field in the air gap should be $H = B/\mu_0 \approx 800\,\text{A/mm}$. Then, the required coil area is given by,

$$A_{coil} = \frac{H \cdot g}{J_{max}} \tag{9.3}$$

Substituting the values, we get $A_{coil} = 800 \times 0.4/10 = 32\,\text{mm}^2$. Assuming a coil packing fraction of 0.5, the winding area then becomes $A_{winding} = 64\,\text{mm}^2$

With a B-field of 0.6 T, the magnet area required becomes about $4\,\text{mm}^2$ and the winding area $A_{winding}$ becomes about $38\,\text{mm}^2$. The total number of Amp-turns is then approximately 200 Amp-turns. One way of reducing the amp-turn requirement is to have a larger area of the stator at the winding and focus that flux with a smaller area at the pole faces. The reduction in area increases the B-field to keep the flux constant, and since the normal force varies quadratically with B-field and linearly with area, the total force at the pole faces should then increase until the B-field within the low-carbon steel saturates.

9.2.3 Suggestions for design with reduced actuator size

A few suggested concepts are given in Figure 9-6. By making the stator smooth and curved, without sharp corners, we can simplify the coil winding. In addition, the actuator can be made more compact by keeping the pusher only on one side and folding the other side of the rotor to have a 90° included angle as shown in Figure 9-6. The pole surface area can be reduced compared to the stator cross-section area at the winding to focus the magnetic flux and therefore amplify the B-field. The approximate dimensions can be about 15-20 mm for each edge of the rotor and the contact spring can be about 30-40 mm. This would give a winding length of about 20 mm (circumference of the quarter circle). Smaller actuators should have a lower inertia and hence exhibit faster dynamics.

These are preliminary concepts and more design options need to be generated and evaluated with the modeling developed as described in Chapter 5 to design the EM actuators with a smaller foot-print.

9.2.4 Spillway design for passive liquid leveling

The spillway conduits exhibit spontaneous capillary flow due to having a generalized Cassie angle (θ^*) less than 90° [30]. The designs to date used a rectangular

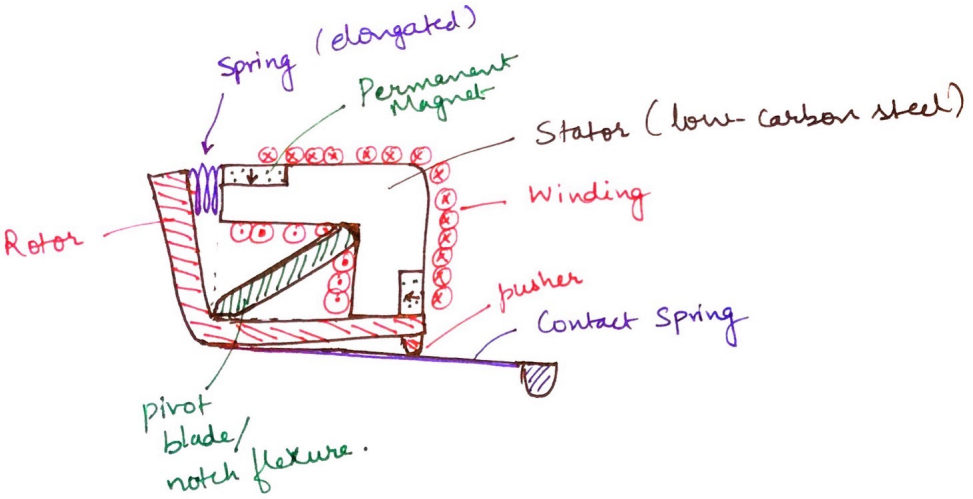

(a) Concept-1

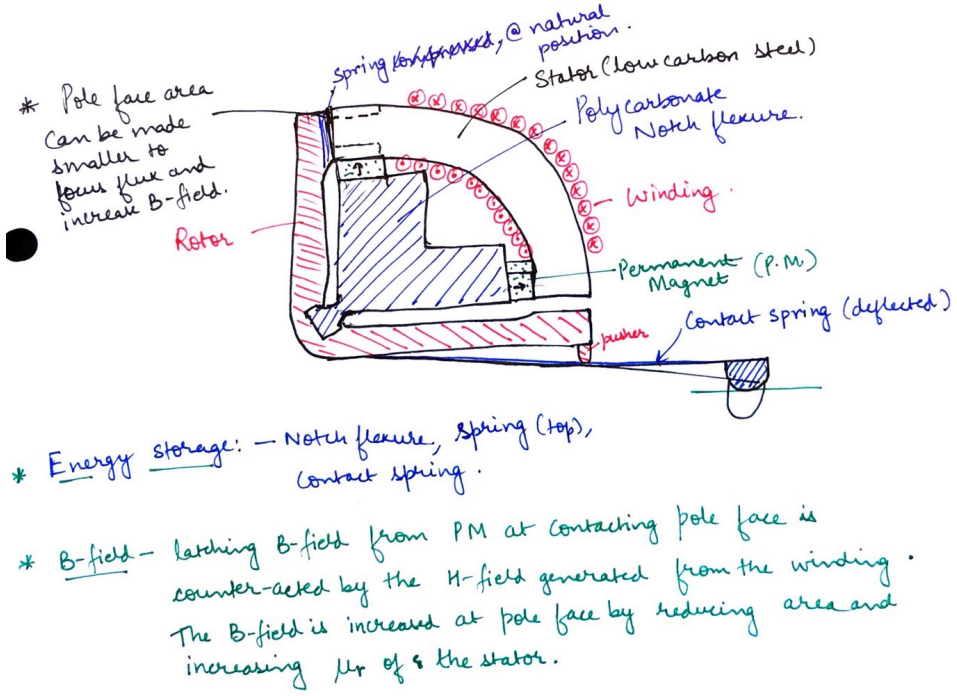

(b) Concept-2

Figure 9-6: Concepts for smaller EM Actuators. (a) Using a rigid blade as a pivot simplifies the pivot design. The radius on the rotor provides the rolling contact. The tension spring (elongated) on top pulls the rotor to the top pole face when the contact spring is not loaded. (b) Using a notch flexure. Making the stator without sharp bends makes it easier to wind. The magnet can potentially be embedded within the stator geometry by making a cut-out, to reduce the pole face area compared to the the area at the winding, to amplify the B-field. Pusher is only needed on one side to make contact with the membrane. The other side can store energy in a small spring which elongates when the rotor moves away from the pole face. The stator, PM and notch flexure (or pivot blade) can be bonded together.

cross-section channel with a high aspect ratio of 3:1 to achieve spontaneous capillary flow, as described in Chapter 6.

A V-groove is capable of exhibiting capillary filaments, also called Concus-Finn filaments, depending on the contact angle and the channel corner geometry [40]. Formation of capillary filaments in such a groove requires the contact angle (θ) between the fluid and the channel substrate to generally be less than 45°. If α is the V-groove half angle, then the condition for a filament to form is,

$$\theta < \frac{\pi}{2} - \alpha. \tag{9.4}$$

Capillary filaments would allow for fast capillary filing of the spillway conduits and hold lower captive volumes. Dry polysulfone surface behaves hydrophobically with contact angles around 90° (Section 6.4.2). Then there can be no formation of filaments. Once the surface is primed (already wet with a thin fluid layer or with some proteins to increase hydrophilicity), the contact angle is in the range of 30°–60°. Assuming contact angle of 60°, we can achieve SCF with filament formation for V-groove half angles less than 30°. Therefore, we manufacture and test a V-groove with 60° included angle at the corner.

Our initial tests with a prototype V-groove for the spillway conduit with a 60° included angle show encouraging results once the spillways are primed. We observed filament formation along the groove bottom and low volume accumulation at steady state compared to the rectangular channels. More tests are necessary to verify their reliability in long term operation. The rectangular channel spillway conduits retain fluid and do not evaporate in operation. The same needs to be evaluated for the V-groove spillways. Another possibility is to have multiple parallel v-grooves. The analysis for such systems is also described by Berthier et al., in [40].

9.3 Summary

In closing, this thesis has contributed ideas for an energy-efficient electromagnetic actuator for diaphragm micro-pumps. Preliminary test results are promising and suggest the potential of electromagnetic pumping at the micro-scale. In addition, the thesis describes designs of pumps and valves suitable for injection-molded, single-use platforms and a model to predict the large deflection of diaphragms used in micro-pumps.

We have worked on pumping systems and overall hardware development for the MPS platforms, and thereby established promising new mechatronic technologies for creating novel organs-on-chip platforms and devices.

Bibliography

[1] E.-M. Dehne, T. Hasenberg, and U. Marx, "The ascendance of microphysiological systems to solve the drug testing dilemma." *Future science OA*, vol. 3, no. 2, p. FSO185, jun 2017. [Online]. Available: http://www.ncbi.nlm.nih.gov/pubmed/28670475http://www.pubmedcentral.nih.gov/articlerender.fcgi?artid=PMC5481853

[2] C. D. Edington, W. Li, K. Chen, E. Geishecker, T. Kassis, and L. R. Soenksen, "Interconnected Microphysiological Systems for Quantitative Biology and Pharmacology Studies," *Scientific Reports*, In Press.

[3] Y. S. Zhang, "Engineering challenges in microphysiological systems," *Future Science OA*, vol. 3, no. 3, p. FSO209, aug 2017. [Online]. Available: http://www.future-science.com/doi/10.4155/fsoa-2017-0049

[4] N. Shanks, R. Greek, and J. Greek, "Are animal models predictive for humans?" *Philosophy, ethics, and humanities in medicine : PEHM*, vol. 4, p. 2, jan 2009. [Online]. Available: http://www.ncbi.nlm.nih.gov/pubmed/19146696http://www.pubmedcentral.nih.gov/articlerender.fcgi?artid=PMC2642860

[5] W. Inman, K. Domansky, J. Serdy, B. Owens, D. Trumper, and L. G. Griffith, "Design, modeling and fabrication of a constant flow pneumatic micropump," *Journal of Micromechanics and Microengineering*, vol. 17, no. 5, pp. 891–899, may 2007. [Online]. Available: http://stacks.iop.org/0960-1317/17/i=5/a=007?key=crossref.2c6ef790667cd3917e053887817e3eef

[6] M. K. Small, J. J. Vlassak, and W. D. Nix, "Re-examining the bulge test: Methods for improving accuracy and reliability," *J. Mater. Res*, vol. 7, p. 1553, 1992.

[7] H. Becker, "One size fits all?" *Lab on a Chip*, 2010. [Online]. Available: http://pubs.rsc.org/en/content/articlepdf/2010/lc/c005380p

[8] Timoshenko. S and S. Woinowsky-Krieger, *Theory of Plates and Shells*, 2nd ed. McGraw-Hill, New York, 1959. [Online]. Available: https://archive.org/details/TheoryOfPlatesAndShells

[9] W. K. Schomburg, "Membranes," in *Introduction to Microsystem Design. RWTHedition, vol 1.* Springer, Berlin, Heidelberg, 2011, pp. 29–52. [Online]. Available: http://link.springer.com/10.1007/978-3-642-19489-4{_}6

[10] P. Lin and S. D. Senturia, "Thin Films: Stresses and Mechanical Properties II," *Mater. Res. Soc. Symp. Proc.*, vol. 188, 1990.

[11] S. Way, "S. Way, Trans. ASME, vol. 56, p. 627, 1934,No Title," *Trans. ASME*, vol. 56, p. 627, 1934.

[12] Y. Zhang, "Large deflection of clamped circular plate and accuracy of its approximate analytical solutions," *Article . SCIENCE CHINA Physics, Mechanics & Astronomy China-Phys. Mech. Astron*, vol. 59, no. 59, pp. 624 602–624 602, 2016. [Online]. Available: https://link.springer.com/content/pdf/10.1007/s11433-015-5751-y.pdf

[13] E. W. Weisstein, "Spherical Cap." [Online]. Available: http://mathworld.wolfram.com/SphericalCap.html

[14] ASTM International, "ASTM D882: Standard Test Method for Tensile Properties of Thin Plastic Sheeting," West Conshohocken, PA, p. 12, 2012. [Online]. Available: http://www.astm.org/cgi-bin/resolver.cgi?D882

[15] microfluidic ChipShop, "microfluidic ChipShop Catalog," 2016. [Online]. Available: http://www.microfluidic-chipshop.com/index.php?pre_cat_open=209

[16] C. K. Byun, K. Abi-Samra, Y.-K. Cho, and S. Takayama, "Pumps for microfluidic cell culture." *Electrophoresis*, pp. 245–257, 2013. [Online]. Available: http://www.ncbi.nlm.nih.gov/pubmed/23893649

[17] P. Woias, "Micropumps - summarizing the first two decades," *Proceedings of the SPIE - The International Society for Optical Engineering*, vol. 4560 BT -, pp. 39–52, 2001. [Online]. Available: http://dx.doi.org/10.1117/12.443069

[18] B. D. Iverson and S. V. Garimella, "Recent advances in microscale pumping technologies: a review and evaluation," *Microfluidics and Nanofluidics*, vol. 5, no. 2, pp. 145–174, 2008. [Online]. Available: http://link.springer.com/10.1007/s10404-008-0266-8

[19] D. J. Laser and J. G. Santiago, "A review of micropumps," *Journal of Micromechanics and Microengineering*, vol. 14, no. 6, pp. R35–R64, jun 2004. [Online]. Available: http://stacks.iop.org/0960-1317/14/i=6/a=R01?key=crossref.137857bfcf5ea513064ec576b484af8f

[20] N.-T. Nguyen, X. Huang, and T. K. Chuan, "MEMS-Micropumps: A Review," *Journal of Fluids Engineering*, vol. 124, no. 2, p. 384, jun 2002. [Online]. Available: http://fluidsengineering.asmedigitalcollection.asme.org/article.aspx?articleid=1429524

[21] T. Kassis, P. M. Perez, C. J. W. Yang, L. R. Soenksen, D. L. Trumper, and L. G. Griffith, "MICCS: A Fully Programmable Multipurpose Integrated Cell Culture System," *bioRxiv*, p. 192047, nov 2017. [Online]. Available: https://www.biorxiv.org/content/early/2017/11/25/192047

[22] A. K. Au, H. Lai, B. R. Utela, and A. Folch, "Microvalves and Micropumps for BioMEMS," *Micromachines*, vol. 2, no. 4, pp. 179–220, may 2011. [Online]. Available: http://www.mdpi.com/2072-666X/2/2/179/

[23] V. Tandon, W. S. Kang, A. J. Spencer, E. S. Kim, E. E. L. Pararas, M. J. McKenna, S. G. Kujawa, M. J. Mescher, J. Fiering,

W. F. Sewell, and J. T. Borenstein, "Microfabricated infuse-withdraw micropump component for an integrated inner-ear drug-delivery platform," *Biomedical Microdevices*, vol. 17, no. 2, 2015. [Online]. Available: http://link.springer.com/10.1007/s10544-014-9923-8

[24] V. Tandon, W. S. Kang, T. A. Robbins, A. J. Spencer, E. S. Kim, M. J. McKenna, S. G. Kujawa, J. Fiering, E. E. L. Pararas, M. J. Mescher, W. F. Sewell, and J. T. Borenstein, "Microfabricated reciprocating micropump for intracochlear drug delivery with integrated drug/fluid storage and electronically controlled dosing," *Lab Chip*, vol. 16, no. 5, pp. 829–846, 2016. [Online]. Available: http://xlink.rsc.org/?DOI=C5LC01396H

[25] A. Geipel, A. Doll, F. Goldschmidtboing, P. Jantscheff, N. Esser, U. Massing, and P. Woias, "Pressure-Independent Micropump with Piezoelectric Valves for Low Flow Drug Delivery Systems," *19th IEEE International Conference on Micro Electro Mechanical Systems*, no. January, pp. 786–789, 2006. [Online]. Available: http://ieeexplore.ieee.org/document/1627917/http://ieeexplore.ieee.org/lpdocs/epic03/wrapper.htm?arnumber=1627917

[26] H. Soemers, *Design Principles for Precision Mechanisms*. Enschede, the Netherlands: T-Point Print VoF, 2010. [Online]. Available: http://www.t-pointprint.nl/?page_id=218

[27] A. Potter and F. H. Barnes, "The siphon," *Physics Education*, vol. 6, no. 5, pp. 362–366, sep 1971. [Online]. Available: http://iopscience.iop.org/article/10.1088/0031-9120/6/5/005

[28] W.-J. A. de Wijs, J. Laven, and G. de With, "Wetting forces and meniscus pinning at geometrical edges," *AIChE Journal*, vol. 62, no. 12, pp. 4453–4465, dec 2016. [Online]. Available: http://doi.wiley.com/10.1002/aic.15341

[29] J. Berthier and K. A. Brakke, *The Physics of Microdoplets*. John Wiley & Sons, Inc, 2012. [Online]. Available: https://www.wiley.com/en-us/The+Physics+of+Microdroplets-p-9780470938805

[30] J. Berthier, K. A. Brakke, and E. Berthier, "A general condition for spontaneous capillary flow in uniform cross-section microchannels," *Microfluidics and Nanofluidics*, vol. 16, no. 4, pp. 779–785, apr 2014. [Online]. Available: http://link.springer.com/10.1007/s10404-013-1270-1

[31] A. B. D. Cassie and S. Baxter, "Wettability of porous surfaces," *Trans. Faraday Soc.*, vol. 40, no. 0, pp. 546–551, 1944. [Online]. Available: http://dx.doi.org/10.1039/TF9444000546

[32] P.-G. de. Gennes, F. Brochard-Wyart, and D. QueÌĄreÌĄ, *Capillarity and wetting phenomena : drops, bubbles, pearls, waves*, 1st ed. Springer, 2004.

[33] S. W. Inman, "Development of a high throughput 3D perfused liver tissue bioreactor," Ph.D. dissertation, Massachusetts Institute of Technology, 2006. [Online]. Available: https://dspace.mit.edu/handle/1721.1/35670?show=full

[34] Gareth McKinley, "Unsteady Bernoulli Equation," *2.25 Advanced Fluid Mechanics F2013 (Massachusetts Institute of Technology: MIT OpenCourseWare)*, 2013. [Online]. Available: https://ocw.mit.edu/courses/mechanical-engineering/2-25-advanced-fluid-mechanics-fall-2013/inviscid-flow-and-bernoulli/

[35] B. Hildreth, "Manipulating Relative Humidity in Cell Culture | Baker Co." [Online]. Available: https://info.bakerco.com/blog/manipulating-relative-humidity-in-cell-culture/

[36] Polymerdatabase.com, "Permeability of Polymers." [Online]. Available: http://polymerdatabase.com/polymerphysics/Permeability.html

[37] L. W. McKeen, *Permeability Properties of Plastics and Elastomers*, 4th ed. William Andrew 2017, 2016. [Online]. Available: https://www.sciencedirect.com/science/book/9780323508599

[38] L. K. Massey and Plastics Design Library., *Permeability properties of plastics and elastomers : a guide to packaging and barrier materials*. Plastics Design Library, 2003.

[39] H. A. Haus and J. R. Melcher, *Electromagnetic Fields and Energy*. Prentice Hall Books, 1989. [Online]. Available: http://web.mit.edu/6.013_book/www/book.html

[40] J. Berthier, K. A. Brakke, and E. Berthier, "Capillary Filaments," in *Open Microfluidics*. Hoboken, NJ, USA: John Wiley & Sons, Inc., aug 2016, pp. 57–89. [Online]. Available: http://doi.wiley.com/10.1002/9781118720936.ch2